UAB
Universitat Autònoma de Barcelona

s-Block metal-mediated Hydroelementation

Irina Bozhinovska

s-Block metal-mediated Hydroelementation

Irina Bozhinovska

Ph.D. Thesis

Ph.D. in Chemistry

Supervisors:

Prof. Dr. Agustí Lledós (UAB),

Prof. Dr. Gregori Ujaque (UAB)

Prof. Dr. Matthias Westerhausen (FSU)

Departamento de Química

Facultat de Ciències

Universitat Autònoma de Barcelona

Institute for Inorganic and Analytical Chemistry

Faculty of Chemistry and Earth Sciences

Friedrich-Schiller-Universität

2025

Universitat Autònoma de Barcelona
Department of Chemistry

s-Block metal-mediated Hydroelementation

Irina Bozhinovska

Doctoral Thesis

PhD in Chemistry

Doctoral Advisors:

Prof. Dr. Agustí Lledós (UAB),

Prof. Dr. Gregori Ujaque (UAB)

Prof. Dr. Matthias Westerhausen (FSU)

2025

s-Block metal-mediated Hydroelementation

Dissertation

in Partial Fulfilment of the Requirements for the Degree of

“doctor rerum naturalium (Dr. rer. nat.)”

Submitted to the Council of the Faculty of Chemistry and Geosciences

of the Friedrich Schiller University Jena

by Irina Bozhinovska

born on 09.11.1996 in Kumanovo, Republic of Macedonia

This page intentionally left blank

Memòria presentada per aspirar al
Grau de Doctor per Irina Bozhinovska

Irina Bozhinovska

Vist i plau

Prof. Dr. Agustí Lledós (UAB),

Prof. Dr. Gregori Ujaque (UAB)

Prof. Dr. Matthias Westerhausen (FSU)

Contents

Acknowledgements

This doctoral thesis represents the culmination of a joint research effort carried out under a cotutelle agreement between the Universitat Autònoma de Barcelona (UAB) and Friedrich-Schiller-Universität (FSU). The collaborative nature of this project has been instrumental in shaping the research and providing a comprehensive educational experience that spans both institutions.

I would like to express my deepest gratitude to the European Union for their generous funding through the Horizon 2020 research and innovation programme. This project was made possible by the Marie Skłodowska-Curie actions (MSCA) grant agreement No. 860322, which enabled this international collaboration and supported my research endeavours. The support provided by this grant has been crucial in advancing my studies and achieving the objectives of this thesis. Thank you to Italmatch and the entire team for the valuable industrial placement opportunity, which has significantly expanded my skills and experience in the industry

Additionally, I would like to expand my gratitude to my three supervisors: Professor Agustí Lledós and Dr. Gregori Ujaque at the Universitat Autònoma de Barcelona (UAB), and Professor Matthias Westerhausen at Friedrich-Schiller-Universität (FSU). I am profoundly grateful to them for giving me the opportunity to carry out this research within their esteemed groups and for the invaluable guidance and support they have provided throughout this journey.

Over the past four years, I have learned so much under their mentorship, benefiting from their vast knowledge and experience. Their commitment to my professional growth has been remarkable, and I am truly thankful for all the time and effort they have dedicated to helping me develop as a researcher. Their positivity and encouragement regarding the progress of the project have been incredibly motivating, even during the challenging phases of my research. Thank you all for being such an integral part of this journey and for contributing to my development as a researcher and as an individual.

I also like to extend my sincere gratitude to Professors Vladimir Ivanovski, Ljubco Pejov, Stefica Ujcic, and Aleksandra Korunovska for their unwavering support

throughout my academic journey, beginning in high school and continuing through my time abroad. Your mentorship has been crucial at every stage, from early guidance to valuable feedback during my studies.

I am deeply grateful for your ongoing support, insight, and belief in my potential.I would like to thank everyone involved in the CCIMC network, from other supervisors to my fellow 14 ESRs (with special thanks to Anastasiia, Wimonsiri, Paven, Max and Joel). Starting this journey during the pandemic and in a new country, followed by moves to two other countries, it was crucial to have a supportive community to share experiences with. Over the past four years, our opportunities to travel, meet in person, and enjoy these moments together have been invaluable. These experiences have not only enriched my professional growth but have also created lasting memories and friendships. I am grateful for the collaborative spirit that has made this journey both fulfilling and memorable.

I would like to express my heartfelt gratitude to my Macedonian friends (Angjela and Tijana), for being a constant source of joy and support throughout this journey. Your endless stream of humour and catching ups have been truly invaluable. These moments of laughter provided much-needed breaks and kept me grounded. I also to extend this thanks to my friends in the UK (Nan, Chloe, Yusra, Maymuna, Luke, and Sammy) for being such an integral part of my journey. Your organization of much-needed breaks back to the UK, along with your endless supply of humor and eagerness for new adventures, has filled my life with unforgettable memories from my undergraduate days through to my doctorate.

I would like to extend my heartfelt thanks to the people in my computational group (Iker, Wen Juan, Bernant and Andres) for their support and for teaching me the basics of computational chemistry. Your patience and the welcoming, laughter-filled environment you provided made learning an enjoyable experience. I am also deeply grateful for your help in teaching me the language, which has greatly enriched my experience and interactions. The positive atmosphere and the invaluable skills I gained during my time with you will always be remembered. I also want to express my sincere gratitude to the research group in Germany (Miles, Paul, Bahareh and Benjamin) for their guidance and collaboration during my lab work. Your expertise and dedication

I want to also say heartfelt thanks to my uncle for helping me move to the UK, which was the first step in my journey. Your support at that moment made it possible for me to start my academic adventure and laid the foundation for everything that followed

In conclusion, I want to express my deepest gratitude to my mom and dad for their unwavering support throughout this journey. Your trust in me and your encouragement have been the foundation upon which I built my academic career. Despite the challenges of living in different countries after spending so many years together, your support never wavered. These experiences have made the time we spent together during holidays and special occasions even more meaningful and cherished. Your belief in my dreams and your constant support have been a source of immense strength. The distances between us only served to highlight the value of our time together and deepened my appreciation for the moments we could share. Thank you for being my steadfast supporters and for celebrating my successes with me, no matter how far apart we were. Significantly enhanced my learning and contributed greatly to my development as a researcher.

I am deeply grateful to Dr. Jonathan Kenneth Bartley, who supervised me both during my undergraduate thesis and my research stay at Cardiff University, for giving me the initial spark to start my journey and for including me in a publication six years after completing my degree.

Lastly, I want to dedicate this thesis to the memory of my beloved granddad. Although he is no longer with us, his influence and wisdom continue to inspire me every day.

Thank you all from the bottom of my heart!!!

List of figures:

List of schemes:

List of tables:

Abbreviations

Abbreviation	Description
Å	Ångström (10-10 m)
ACF	Adiabatic connection formula
ACS	Active catalytic species
Alk	alkyl
AO	Atomic orbital
aq.	aqueous
Ar	any aromatic group
B3LYP	Becke's three parameter, Lee-Yang-Parr exchange-correlation functional
δ	chemical shift
Bp.	Boiling point
Br	broad
c	concentration
C_6D_6	deuterated benzene
cat.	catalytic
$CDCl_3$	Deuterated chloroform
conv.	conversion
CT	charge transfer
Cy	Cyclohexyl
d	doublet (NMR)
DCM	dichloromethane
DFA	Density Functional Approximation
DFT	Density Functional Theory
DIBAL-H	diisobutylaluminium hydride
EAO	electron accepting orbital

ECP	effective core potential
EDG	electron donating group
ee	enantiomeric excess
eq. equiv.	Equivalent
EWG	Electron withdrawing group
GTO	gaussian-type orbital
h	hours
HF	Hartree-Fock
HMDS	Bis(trimethylsilyl)amine- $N(SiMe_3)_2$
H-HMDS	Bis(trimethylsilyl)amide - $HN(SiMe_3)_2$
HOMO	Highest occupied molecular orbital
HSAB	Hard and soft acids and bases
IBO	Intrinsic bond orbital
ICP	Intersystem crossing process
IR spectroscopy	Infrared Spectroscopy
KS	Kohn-Sham
L	Ligand
LCAO	linear combination of atomic orbitals
LDA	Local Density Approximation
LSDA	Local Spin Density Approximation
LUMO	Lowest unoccupied molecular orbital
M	unspecified metal
m	multiplet (NMR)
M-HMDS	metalated
m/z	mass to charge ratio
Me	methyl
MeCN	acetonitrile
Mes	mesityl
MHz	Megahertz
min	Minute
mL	mililiters
MM	Molecular mechanics

mmol	milimol
MO	Molecular orbital
Mp	Melting point
MP2	Møller–Plesset perturbation theory of second order
MS	mass spectrometry
^{n}J	coupling constant over n bonds
NMR	Nuclear magnetic resonance
Nu	nucleophile
OLED	organic light emitting diode
PCM	Polarizable Continuum Model
PES	Potential Energy Surface
Ph	Phenyl
Ppm	parts per million
q	quartet (NMR)
QM	Quantum Mechanics
quant.	Quantitative
RESP	restricted electrostatic potential
s	singlet (NMR)
sat.	saturated
SDD	Stuttgart-Dresden effective core potential
SPE	single point energy
T	temperature
t	time
t	triplet (NMR)
tBu	tert-butyl
TEP	Tolman electronic parameter
THF	tetrahydrofuran
TLC	thin layer chromatography
TMEDA	N,N,N’,N’ -tetramethyleethylendiamine
TMS	trimethylsilyl
UV-VIS	ultraviolet-visible spectroscopy
$\tilde{\nu}$	wavefunction

Abstract

This thesis is dedicated to advancing the understanding and development of reactions that produce organophosphorous compounds through a comprehensive combination of experimental and computational methodologies. The central focus is on the addition of phosphorous(III) and phosphorous(V) species to unsaturated hydrocarbons *via* hydrophosphination and hydrophosphorylation reactions, notable for their atom-economic formation of P–C bonds. These transformations are crucial for the efficient synthesis of organophosphorous compounds but involve significant kinetic and electrostatic challenges, necessitating the use of catalysts for successful execution.

This thesis explores the use of alkali metal-based catalysts for hydrophosphination and hydrophosphorylation reactions, highlighting their advantages of non-toxicity, abundant availability, and environmentally friendly properties. Among these, metal bis(trimethylsilyl)amides (M-HMDS, where M = Li, Na, and K; HMDS = $N(SiMe_3)_2$) have shown particular effectiveness. The reaction outcomes are significantly influenced by the choice of alkali metal and the steric properties of the phosphorous-bound substituents. However, it should be noted that there is no fundamental understanding of electronic and steric control for these reactions, particularly regarding predictive experimental and theoretical capability, due to the absence of directing d-orbitals in these metals.

Aiming to form stereo- and regioselective P–C bonds *via* alkali metal-catalysed reactions, this work adopts a comprehensive approach that combines experimental and theoretical methods. This strategy aims to elucidate the mechanistic steps involved in these reactions, identify the key factors governing stereo- and regioselectivity, and ascertain the most suitable alkali metal for these processes. The integration of experimental and theoretical approaches provides insight into which steps influence regio- and stereoselectivity and enables us to understand why these reactions do not happen with several combinations of alkali cation and P-bound substituents.

The thesis begins with an introductory chapter that provides a brief overview of s-block metal catalysis. The second chapter details the computational methodology employed. DFT calculations were performed using the B3LYP functional, complemented by Grimme's D3BJ correction to account for dispersion effects. The

experimental solvent (THF) was modelled using both a continuum model (SMD) and a hybrid cluster-continuum model, incorporating several THF solvent molecules. This methodology was applied to study the addition of P(III) and P(V) compounds to unsaturated hydrocarbons and the subsequent oxidation of the formed products. The light-induced formation of the [2+2] adduct was analysed using Time-Dependent DFT (TD-DFT) with CAM-B3LYP for improved agreement with UV-vis spectra, while the Harvey group's program was utilized to locate minimum energy crossing points (MECP) between singlet and triplet states.

In the first chapter of the results section of this thesis, computational methods were used to elucidate the reaction mechanisms of the Pudovik reaction, employing M-HMDS (M = Li, Na, and K) as a catalyst. This work builds on previous experimental results published by Prof. Westerhausen's group at Jena University. The research aimed to investigate how variations in alkali cations (decreased reactivity for smaller congeners) and the nature of the P-bound group (R = Mes, Mes/Ph, Ph, OEt, and Cy) influenced the intricacies of the reaction processes, as well as the factors governing the regio- and stereoselectivities of the reaction. This study sought to uncover the complexity of these mechanisms and proposed a detailed description of each step involved, with the formation and deactivation of active species being the essential first step for the reaction to occur. In this chapter, we proposed mechanisms concerning the formation of *Z*- and *E-isomer*ic mono-hydrophosphorylated products, bisphosphorylated products, and 2-benzyl-1-mesityl-5,7-dimethyl-2,3-dihydrophosphindole 1-oxide.

In the subsequent chapter, we investigated the addition of mesityl phosphine to 1,4-diphenylbutadiyne, promoted by the same catalysts (M-HMDS; M = Li, Na, and K) as in the previous chapter. This reaction yielded 1-mesityl-2,5-diphenyl phosphole as the sole product, with quantitative conversion verified by ^{31}P NMR spectroscopy. In this chapter, we proposed a mechanism for the formation of 1-mesityl-2,5-diphenyl phosphole and computed the Gibbs energy profile for its formation. The reactivity trend observed here mirrored that of the previous chapter: K-HMDS displayed the highest reactivity, Na-HMDS showed intermediate reactivity, and Li-HMDS exhibited limited reactivity in both hydrophosphination and hydrophosphorylation reactions. Notably, DFT calculations confirmed the same correlation between the chemical hardness of the alkali metals and their catalytic activity, as observed experimentally in both this

chapter and the previous one. Additionally, the formation and deactivation of the active species were identified as key steps determining the different reactivities observed among the catalysts in this chapter.

Finally, in the last chapter of this thesis, we integrated experimental results with computational analysis to elucidate the underlying reaction mechanisms for the oxidation of 1-mesityl-2,5-diphenylphosphole, synthesized in the previous chapter, and its subsequent dimerisation into a [2+2] adduct under visible light irradiation. Additionally, comparative computations for the [4+2] Diels-Alder cycloaddition were performed to provide a broader contextual understanding of these processes.

Overall, this thesis demonstrates the *via*bility of using alkali metal-based catalysts for the addition of P(III) and P(V) compounds to unsaturated hydrocarbons, achieving the formation of new P-C compounds in an atom-efficient manner. The research offers important experimental and mechanistic insights into the electronic and steric factors that affect these reactions and emphasizes the critical role of selecting the appropriate M-HMDS catalysts. Both theoretical and experimental findings confirmed that these cations are not merely "spectator" species but play a crucial role in the outcome of these reactions. Their involvement should be considered at each step of the reaction process. These findings advance the development of sustainable synthetic methodologies for organophosphorous compounds and provide fresh perspectives on the reactivity of alkali metal catalysts, setting the stage for future research aimed at improving the efficiency and scope of these catalytic processes in organic synthesis.

Keywords: Organophosphorous compounds, hydrophosphination, hydrophosphorylation , alkali- based catalysts, Density Functional Theory (DFT), Pudovik reaction, 1-mesityl-2,5-diphenylphosphole, [2+2] photodimerisation of phosphole oxides

Resumen

Esta tesis tiene como objetivo avanzar en la comprensión y desarrollo de reacciones que producen compuestos organofosforados mediante un enfoque integral que combina metodologías experimentales y computacionales. El enfoque central radica en la adición de especies de fósforo(III) y fósforo(V) a hidrocarburos insaturados a través de reacciones de hidrofosfonilación y hidrofosforilación, que se distinguen por su formación de enlaces P–C con economía atómica. Estas transformaciones son cruciales para una síntesis eficiente de compuestos organofosforados, pero involucran retos cinéticos y electrostáticos significativos, lo que requiere el uso de catalizadores para una exitosa ejecución.

Esta tesis explora el uso de catalizadores basados en metales alcalinos para reacciones de hidrofosfonilación e hidrofosforilación, destacando sus ventajas como la no toxicidad, abundancia y propiedades respetuosas con el medio ambiente (excluyendo el berilio). Entre estas, las bis(trimetilsilil)amidas de metales (M-HMDS, donde M = Li, Na, y K; HMDS = N(SiMe3)2) han demostrado ser particularmente efectivas. Los resultados de la reacción están significativamente influenciados por la elección del metal alcalino y las propiedades estéricas de los sustituyentes unidos al fósforo. Sin embargo, cabe señalar que aún no hay una comprensión profunda del control electrónico y estérico para estas reacciones, particularmente en lo que respecta a la capacidad predictiva tanto experimental como teórica, entre otras cosas debido a la ausencia de orbitales d directores en estos metales.

Con el objetivo de formar enlaces P–C estereoespecíficos y regioselectivos a través de reacciones catalizadas por metales alcalinos, este trabajo adopta un enfoque integral que combina métodos experimentales y teóricos. Esta estrategia tiene como objetivo dilucidar las etapas del mecanismo involucradas en estas reacciones, identificar los factores clave que gobiernan la estereo- y regioselectividad, y determinar el metal alcalino más adecuado para estos procesos. La integración de enfoques experimentales y teóricos proporciona información sobre qué pasos influyen en la regio- y estereoselectividad y permite comprender por qué estas reacciones no ocurren con varias combinaciones de cationes alcalinos y sustituyentes unidos al fósforo.

La tesis comienza con un capítulo introductorio que proporciona una breve visión general de la catálisis de metales del bloque s. El segundo capítulo detalla la metodología computacional empleada. Se realizaron cálculos DFT utilizando el funcional B3LYP, complementados por la corrección D3BJ de Grimme para tener en cuenta los efectos de dispersión. El disolvente experimental (THF) fue modelado utilizando un modelo de continuo (SMD) y un modelo híbrido de clúster-continuo, incorporando varias moléculas de disolvente de THF. Esta metodología se aplicó para investigar la adición de compuestos de P(III) y P(V) a hidrocarburos insaturados y la posterior oxidación de los productos formados. La formación inducida por la luz del aducto [2+2] fue analizada utilizando DFT Dependiente del Tiempo (TD-DFT) con CAM-B3LYP para mejorar el acuerdo con los espectros UV-vis, mientras que se utilizó el programa del grupo de Harvey para localizar los puntos de cruce de energía mínima (MECP) entre estados singlete y triplete.

En el primer capítulo de la sección de resultados de esta tesis, se utilizaron métodos computacionales para dilucidar los mecanismos de reacción de la reacción de Pudovik, empleando M-HMDS (M = Li, Na, y K) como catalizador. Este trabajo se basa en resultados experimentales previos publicados por el grupo del Prof. Westerhausen en la Universidad de Jena. La investigación tenía como objetivo investigar cómo las variaciones en los cationes alcalinos (disminución de reactividad para los congéneres más pequeños) y la naturaleza del grupo unido al fósforo (R = Mes, Mes/Ph, Ph, OEt y Cy) influían en la complejidad de los procesos de reacción, así como en los factores que gobernaban la regio- y estereoselectividad de la reacción. Este estudio buscó desentrañar la complejidad de estos mecanismos y propuso una descripción detallada de cada paso involucrado, siendo la formación y desactivación de especies activas el primer paso esencial para que la reacción ocurra. En este capítulo, se proponen mecanismos relacionados con la formación de productos monohidrofosforilados *Z* y *E*-isómeros, productos bisfosforilados y 2-benzil-1-mesityl-5,7-dimetil-2,3-dihidrofosfindol-1-óxido.

En el capítulo siguiente, se investiga la adición de fosfina mesityl a 1,4-difenilbutadiyno, promovida por los mismos catalizadores (M-HMDS; M = Li, Na y K) que en el capítulo anterior. Esta reacción produjo 1-mesityl-2,5-difenil fosfol como único producto, y la conversión cuantitativa fue verificada utilizando espectroscopia de RMN de ^{31}P. En este capítulo, se propone un mecanismo para la formación de 1-mesityl-2,5-

difenil fosfol y se computa el perfil de energía de Gibbs para su formación. La tendencia de reactividad observada reflejó la del capítulo anterior: K-HMDS mostró la mayor reactividad, Na-HMDS mostró reactividad intermedia y Li-HMDS exhibió reactividad limitada tanto en reacciones de hidrofosfanilación como de hidrofosforilación. Notablemente, los cálculos DFT confirmaron la misma correlación entre la dureza química de los metales alcalinos y su actividad catalítica, como se observó experimentalmente en este capítulo y en el anterior. Además, se identificaron la formación y desactivación de las especies activas como pasos clave que determinan las diferentes reactividades entre los catalizadores en este capítulo.

Finalmente, en el último capítulo de esta tesis, se combinan resultados experimentales con análisis computacional para dilucidar los mecanismos de reacción subyacentes a la oxidación de 1-mesityl-2,5-diphenylphosphole, sintetizado en el capítulo anterior, y su posterior dimerización en un aducto [2+2] bajo irradiación de luz visible. Además, se llevan a cabo cálculos comparativos para la ciclación Diels-Alder [4+2] para proporcionar una comprensión contextual más amplia de estos procesos.

En general, esta tesis demuestra la viabilidad del uso de catalizadores a base de metales alcalinos para la adición de compuestos de P(III) y P(V) a hidrocarburos insaturados, logrando la formación de nuevos compuestos P–C con economía atómica. La investigación ofrece importantes perspectivas experimentales y mecanísticas sobre los factores electrónicos y estéricos que afectan estas reacciones y enfatiza el papel crítico de seleccionar los catalizadores adecuados de M-HMDS. Tanto los hallazgos teóricos como experimentales confirmaron que estos cationes no son meramente especies "espectadoras", sino que desempeñan un papel crucial en el resultado de estas reacciones. Su participación debe considerarse en cada paso del proceso de reacción. Estos hallazgos avanzan el desarrollo de metodologías sintéticas sostenibles para compuestos organofosforados y proporcionan nuevas perspectivas sobre la reactividad de los catalizadores de metales alcalinos, sentando las bases para futuras investigaciones destinadas a mejorar la eficiencia y el alcance de estos procesos catalíticos en la síntesis orgánica.

Palabras clave: compuestos organofosforados, hidrofosfanilación, hidrofosforilación, catalizadores a base de metales alcalinos, Teoría del Funcional de la Densidad (DFT),

reacción de Pudovik, 1-mesitil-2,5-difenilfosfol, fotodimerización [2+2] de óxidos de fosfol.

Resum

Aquesta tesi es dedica a avançar en la comprensió i el desenvolupament de reaccions que produeixen compostos organofosforats mitjançant una combinació completa de metodologies experimentals i computacionals. L'enfocament central és l'addició d'espècies de fòsfor(III) i fòsfor(V) a hidrocarburs insaturats mitjançant reaccions d'hidrofosfonilació i hidrofosforilació, notables per la seva formació d'enllaços P-C des del punt de vista de l'economia atòmica. Aquestes transformacions són crucials per a la síntesi eficient de compostos organofosforats, però impliquen importants reptes cinètics i electrostàtics, cosa que requereix l'ús de catalitzadors per a una execució reeixida.

Aquesta tesi explora l'ús de catalitzadors basats en metalls alcalins per a reaccions d'hidrofosfanilació i hidrofosforilació, destacant els seus avantatges tant de no toxicitat com abundància, i propietats respectuoses amb el medi ambient. Entre aquests, les bis(trimetilsilil)amides metàl·liques (M-HMDS, on M = Li, Na, i K; HMDS = N(SiMe3)2) han demostrat una eficàcia particular. Els resultats de la reacció estan significativament influenciats per l'elecció del metall alcalí i les propietats estèriques dels substituents units al fòsfor. Tanmateix, cal tenir en compte que no hi ha una comprensió fonamental del control electrònic i estèric per a aquestes reaccions, especialment pel que fa a la capacitat predictiva experimental i teòrica, a causa principalment de l'absència d'orbitals d directors en aquests metalls.

Amb l'objectiu de formar enllaços P-C estereo- i regioselectius mitjançant reaccions catalitzades per metalls alcalins, aquest treball adopta un enfocament integral que combina mètodes experimentals i teòrics. Aquesta estratègia pretén elucidar les etapes dels mecanismes implicats en aquestes reaccions, identificar els factors clau que governen l'estereo- i la regioselectivitat, i determinar el metall alcalí més adequat per a aquests processos. La integració dels enfocaments experimentals i teòrics proporciona informació sobre quins passos influeixen en la regio- i estereoselectivitat i ens permet entendre per què aquestes reaccions no es produeixen amb diverses combinacions de catió alcalí i substituents units a P.

La tesi comença amb un capítol introductori que ofereix una breu visió general de la catàlisi de metalls de bloc s. El segon capítol detalla la metodologia

computacional emprada. Els càlculs DFT es van realitzar utilitzant el funcional B3LYP, complementat per la correcció D3BJ de Grimme per tenir en compte els efectes de dispersió. El dissolvent experimental (THF) es va modelar utilitzant tant un model continu (SMD) com un model híbrid de clúster continu, incorporant diverses molècules de dissolvent THF. Aquesta metodologia es va aplicar per estudiar l'addició de compostos de P(III) i P(V) a hidrocarburs insaturats i la posterior oxidació dels productes formats. La formació induïda per la llum de l'adducte [2+2] es va analitzar mitjançant DFT dependent del temps (TD-DFT) amb CAM-B3LYP per millorar la concordança amb els espectres UV-vis, mentre que el programa del grup Harvey es va utilitzar per localitzar punts de creuament d'energia mínima (MECP) entre els estats singlet i triplet.

En el primer capítol de la secció de resultats d'aquesta tesi, es van utilitzar mètodes computacionals per elucidar els mecanismes de reacció de la reacció de Pudovik, emprant M-HMDS (M = Li, Na, i K) com a catalitzador. Aquest treball es basa en resultats experimentals anteriors publicats pel grup del professor Westerhausen a la Universitat de Jena. La recerca tenia com a objectiu investigar com les variacions en els cations alcalins (disminució de la reactivitat per a congèneres més petits) i la naturalesa del grup unit a P (R = Mes, Mes/Ph, Ph, OEt, i Cy) van influir en les complexitats dels processos de reacció, així com els factors que governen les regio- i estereoselectivitats de la reacció. Aquest estudi va intentar descobrir la complexitat d'aquests mecanismes i va proposar una descripció detallada de cada pas implicat, sent la formació i desactivació d'espècies actives el primer pas essencial perquè es produeixi la reacció. En aquest capítol, proposem mecanismes relacionats amb la formació de productes monohidrofosforilats isomèrics Z i E, productes bisfosforilats i 1-òxid de 2-benzil-1-mesitil-5,7-dimetil-2,3-dihidrofosfindol.

En el capítol següent, investiguem l'addició de fosfà de mesitil a 1,4-difenilbutadií, promoguda pels mateixos catalitzadors (M-HMDS; M = Li, Na, i K) que en el capítol anterior. Aquesta reacció va produir 1-mesitil-2,5-difenil fosfol com a únic producte, amb una conversió quantitativa verificada per espectroscòpia de RMN de ^{31}P. En aquest capítol, proposem un mecanisme per a la formació d'1-mesitil-2,5-difenil fosfol i calculem el perfil d'energia de Gibbs per a la seva formació. La tendència de reactivitat observada aquí va reflectir la del capítol anterior: el K-HMDS va mostrar la reactivitat més alta, el Na-HMDS va mostrar una reactivitat intermèdia i el Li-HMDS va mostrar una reactivitat limitada tant en les reaccions d'hidrofosfanilació com

d'hidrofosforilació. Cal destacar que els càlculs de DFT van confirmar la mateixa correlació entre la duresa química dels metalls alcalins i la seva activitat catalítica, tal com s'ha observat experimentalment tant en aquest capítol com en l'anterior. A més, la formació i desactivació de les espècies actives es van identificar com a passos clau que determinen les diferents reactivitats observades entre els catalitzadors en aquest capítol.

Finalment, a l'últim capítol d'aquesta tesi, vam integrar els resultats experimentals amb l'anàlisi computacional per elucidar els mecanismes de reacció subjacents per a l'oxidació de l'1-mesitil-2,5-difenilfosfol, sintetitzat al capítol anterior, i la seva posterior dimerització en un adducte [2+2] sota irradiació de llum visible. A més, es van realitzar càlculs comparatius per a la cicloaddició de Diels-Alder [4+2] per proporcionar una comprensió contextual més àmplia d'aquests processos.

En general, aquesta tesi demostra la viabilitat d'utilitzar catalitzadors basats en metalls alcalins per a l'addició de compostos P(III) i P(V) a hidrocarburs insaturats, aconseguint la formació de nous compostos P-C de manera eficient des del punt de vista de l'economia atòmica. La investigació ofereix importants coneixements experimentals i mecanístics sobre els factors electrònics i estèrics que afecten aquestes reaccions i emfatitza el paper crític de seleccionar els catalitzadors M-HMDS adequats. Tant les troballes teòriques com les experimentals van confirmar que aquests cations no són només espècies "espectadores", sinó que tenen un paper crucial en el resultat d'aquestes reaccions. La seva implicació s'ha de tenir en compte en cada pas del procés de reacció. Aquestes troballes fan avançar el desenvolupament de metodologies sintètiques sostenibles per a compostos organofosforats i proporcionen noves perspectives sobre la reactivitat dels catalitzadors de metalls alcalins, preparant el terreny per a futures investigacions destinades a millorar l'eficiència i l'abast d'aquests processos catalítics en la síntesi orgànica.

Paraules clau: compostos organofosforats, hidrofosfonilació, hidrofosforilació, catalitzadors basats en àlcalins, teoria funcional de la densitat (DFT), reacció de Pudovik, 1-mesitil-2,5-difenilfosfol, fotodimerització [2+2] d'òxids de fosfol

Zusammenfassung

Diese Dissertation ist der Förderung des Verständnisses und der Entwicklung von Reaktionen gewidmet, die organophosphorhaltige Verbindungen durch einen umfassenden Ansatz erzeugen, der experimentelle und rechnergestützte Methoden kombiniert. Der zentrale Fokus liegt auf der Addition von Phosphor(III)- und Phosphor(V)-Spezies zu ungesättigten Kohlenwasserstoffen über Hydrophosphination und Hydrophosphorylation, die sich durch ihre atomökonomische Bildung von P–C-Bindungen auszeichnen. Diese Transformationen sind entscheidend für die effiziente Synthese von organophosphorhaltigen Verbindungen, beinhalten jedoch erhebliche kinetische und elektrostatische Herausforderungen, die den Einsatz von Katalysatoren für eine erfolgreiche Durchführung erforderlich machen.

Diese Thesis untersucht die Verwendung von Katalysatoren auf Basis von Alkalimetallen für Hydrophosphination- und Hydrophosphorylation-Reaktionen und hebt deren Vorteile von Nicht-Toxizität, reichhaltiger Verfügbarkeit und umweltfreundlichen Eigenschaften hervor. Unter diesen haben sich Metallbis(trimethylsilyl)amide (M-HMDS, wobei M = Li, Na, und K; HMDS = $N(SiMe_3)_2$) als besonders effektiv erwiesen. Die Reaktionsprodukte werden erheblich durch die Wahl des Alkalimetalls und die sterischen Eigenschaften der an Phosphor gebundenen Substituenten beeinflusst. Es sollte jedoch angemerkt werden, dass es kein grundlegendes Verständnis für die elektronische und sterische Kontrolle dieser Reaktionen gibt, insbesondere hinsichtlich der prädiktiven experimentellen und theoretischen Fähigkeiten, aufgrund der Abwesenheit von dirigierenden d-Orbitalen in diesen Metallen.

Mit dem Ziel, stereo- und regioselektive P–C-Bindungen über alkali-metallkatalysierte Reaktionen zu bilden, verfolgt diese Arbeit einen umfassenden Ansatz, der experimentelle und theoretische Methoden kombiniert. Diese Strategie zielt darauf ab, die mechanistischen Schritte, die an diesen Reaktionen beteiligt sind, zu erläutern, die Schlüsselfaktoren zu identifizieren, die die Stereo- und Regioselektivität steuern, und das am besten geeignete Alkalimetall für diese Prozesse zu bestimmen. Die Integration experimenteller und theoretischer Ansätze bietet Einblicke, welche Schritte die Regio- und Stereoselektivität beeinflussen, und ermöglicht es uns zu verstehen,

warum diese Reaktionen mit mehreren Kombinationen von Alkalikationen und P-gebundenen Substituenten nicht stattfinden.

Die Dissertation beginnt mit einem einführenden Kapitel, das einen kurzen Überblick über die Katalyse mit s-Blockmetallverbindungen bietet. Das zweite Kapitel beschreibt die verwendete rechnerische Methodik im Detail. DFT-Berechnungen wurden unter Verwendung des B3LYP-Funktionals durchgeführt, ergänzt durch Grimmes D3BJ-Korrektur zur Berücksichtigung von Dispersionseffekten. Das experimentelle Lösungsmittel (THF) wurde sowohl mit einem Kontinuum-Modell (SMD) als auch mit einem hybriden Cluster-Kontinuum-Modell modelliert, das mehrere THF-Lösungsmittelmoleküle einbezieht. Diese Methodik wurde angewendet, um die Addition von P(III)- und P(V)-Verbindungen an ungesättigte Kohlenwasserstoffe sowie die anschließende Oxidation der gebildeten Produkte zu untersuchen. Die lichtinduzierte Bildung des [2+2]-Addukts wurde mit zeitabhängiger DFT (TD-DFT) unter Verwendung von CAM-B3LYP analysiert, um eine verbesserte Übereinstimmung mit UV-vis-Spektren zu erzielen, während das Programm der Harvey-Gruppe verwendet wurde, um minimale Energieübergangspunkte (MECP) zwischen Singulett- und Triplett-Zuständen zu lokalisieren.

Im ersten Kapitel des Ergebnisteils dieser Arbeit wurden computergestützte Methoden verwendet, um die Reaktionsmechanismen der Pudovik-Reaktion zu erhellen, wobei M-HMDS als Katalysator eingesetzt wurde. Diese Arbeit baut auf früheren experimentellen Ergebnissen auf, die von der Gruppe von Prof. Westerhausen an der Universität Jena veröffentlicht wurden. Die Forschung zielte darauf ab, zu untersuchen, wie Variationen in den Alkali-Kationen (verringerten Reaktivität für kleinere Kongenere) und die Natur der P-gebundenen Gruppe (R = Mes, Mes/Ph, Ph, OEt und Cy) die Feinheiten der Reaktionsprozesse sowie die Faktoren, die die Regio- und Stereoselektivitäten der Reaktion bestimmen, beeinflussten. Diese Studie wollte die Komplexität dieser Mechanismen aufdecken und schlug eine detaillierte Beschreibung jedes beteiligten Schrittes vor, wobei die Bildung und Deaktivierung aktiver Spezies der wesentliche erste Schritt für das Eintreten der Reaktion war. In diesem Kapitel wurden Mechanismen hinsichtlich der Bildung von *Z*- und *E-isomer*en mono-hydrophosphorylierten Produkten, bisphosphorylierten Produkten und 2-benzyl-1-mesityl-5,7-dimethyl-2,3-dihydrophosphindol 1-oxid vorgeschlagen.

Im nachfolgenden Kapitel untersuchten wir die Addition von Mesitylphosphan zu 1,4-Diphenylbutadiin, gefördert durch dieselben Katalysatoren (M-HMDS; M = Li, Na und K) wie im vorherigen Kapitel. Diese Reaktion ergab 1-Mesityl-2,5-diphenylphosphol als das einzige Produkt, und die quantitative Umwandlung wurde mittels ^{31}P NMR-Spektroskopie verifiziert. In diesem Kapitel schlugen wir einen Mechanismus für die Bildung von 1-Mesityl-2,5-diphenylphosphol vor und berechneten das Gibbs-Energieprofil für seine Bildung. Der hier beobachtete Reaktivitätstrend spiegelte den des vorherigen Kapitels wider: K-HMDS zeigte die höchste Reaktivität, Na-HMDS wies eine mittlere Reaktivität auf, und Li-HMDS zeigte eine begrenzte Reaktivität sowohl in Hydrophosphanylierungs- als auch in Hydrophosphorylierungsreaktionen. Bemerkenswerterweise bestätigten DFT-Berechnungen die gleiche Korrelation zwischen der chemischen Härte der Alkalimetalle und ihrer katalytischen Aktivität, wie sie experimentell sowohl in diesem Kapitel als auch im vorherigen beobachtet wurde. Darüber hinaus wurden die Bildung und Deaktivierung der aktiven Spezies als entscheidende Schritte identifiziert, die die unterschiedlichen Reaktivitäten der Katalysatoren in diesem Kapitel bestimmen.

Schließlich haben wir im letzten Kapitel dieser Dissertation experimentelle Ergebnisse mit computergestützter Analyse integriert, um die zugrunde liegenden Reaktionsmechanismen für die Oxidation von 1-Mesityl-2,5-diphenylphospholen, die im vorherigen Kapitel synthetisiert wurden, und deren anschließende Dimerisierung zu einem [2+2]-Addukt unter sichtbarem Licht zu erläutern. Darüber hinaus wurden vergleichende Berechnungen für die [4+2] Diels-Alder-Cycloaddition durchgeführt, um ein umfassenderes Verständnis dieser Prozesse zu ermöglichen.

Insgesamt zeigt diese Dissertation die Machbarkeit der Verwendung von alkalimetallbasierten Katalysatoren für die Addition von P(III)- und P(V)-Verbindungen an ungesättigte Kohlenwasserstoffe und erreicht die Bildung neuer P–C-Verbindungen auf eine Atom-effiziente Weise. Die Forschung bietet wichtige experimentelle und mechanistische Einblicke in die elektronischen und sterischen Faktoren, die diese Reaktionen beeinflussen, und betont die entscheidende Rolle der Auswahl der geeigneten M-HMDS-Katalysatoren. Sowohl theoretische als auch experimentelle Ergebnisse bestätigten, dass diese Kationen nicht lediglich „Zuschauer“-Spezies sind, sondern eine entscheidende Rolle für den Ausgang dieser Reaktionen spielen. Ihre Beteiligung sollte in jedem Schritt des Reaktionsprozesses berücksichtigt werden. Diese

Ergebnisse fördern die Entwicklung nachhaltiger synthetischer Methoden für organophosphorhaltige Verbindungen und bieten neue Perspektiven auf die Reaktivität von alkali-metallkatalysatoren, wodurch der Weg für zukünftige Forschungen geebnet wird, die darauf abzielen, die Effizienz und den Umfang dieser katalytischen Prozesse in der organischen Synthese zu verbessern.

Schlüsselwörter: Organophosphorverbindungen, Hydrophosphanylierung, Hydrophosphorylierung, Alkalimetall-basierte Katalysatoren, Dichtefunktionaltheorie (DFT), Pudovik-Reaktion, 1-Mesityl-2,5-diphenylphosphol, [2+2]-Photodimerisierung von Phospholoxiden

Chapter 1: Introduction

1.1. Catalysis

1.1.1. Basic concepts and origin

Catalysis is a phenomenon recognized since ancient times, although its theory and characteristics were not well understood until much later. Today, catalysis plays a crucial role in the production of most chemicals used by society. The term "catalysis" was proposed in 1835 by the Swedish chemist Jöns Jakob Berzelius (1779-1848). In an attempt to explain a series of chemical reactions and decompositions he wrote:[1–3]

"…*the property of exerting on other bodies an action which is very different from chemical affinity. By means of this action, they produce decomposition in bodies and form new compounds into the composition of which they do not enter"*.

"*This new force, which was unknown until now, is common to organic and inorganic nature. I do not believe that this is a force entirely independent of the electrochemical affinities of matter; I believe, on the contrary, that it is only a new manifestation, but since we cannot see their connection and mutual dependence, it will be easier to designate it by a separate name. I will call this force catalytic force. Similarly, I will call the decomposition of bodies by this force catalysis, as one designates the decomposition of bodies by chemical affinity analysis*".

Therefore, Berzelius employed the idea of catalysis to unify various phenomena that could not be clarified by the prevailing notion of reactions driven solely by chemical affinity. Initially, the term was purely descriptive because Berzelius intentionally avoided attempting to elucidate the nature of catalysis. Specifically, he referred to a "catalytic force" as a new phenomenon, while stressing his anticipation of explaining its operation within the framework of electrochemical theory.

At present, IUPAC (International Union of Pure Appl. Chem.) defines catalyst as:[4]

"*A substance that increases the rate of a reaction without modifying the overall standard Gibbs energy change in the reaction; the process is called catalysis. The catalyst is both a reactant and product of the reaction*".

Notably, the current definition is similar to the one provided by Ostwald in 1895: [5]

"A catalyst is a substance that accelerates the rate of a chemical reaction without being part of its final products".

Therefore, a catalyst alters the rate of a reaction but does not affect the thermodynamic equilibrium between reactants and products. In simpler terms, in a catalysed reaction, the activation energy changes whilst the Gibbs energy ($\Delta G^{\ddagger}$) remains unaffected (see **Figure 1.1**).[6]

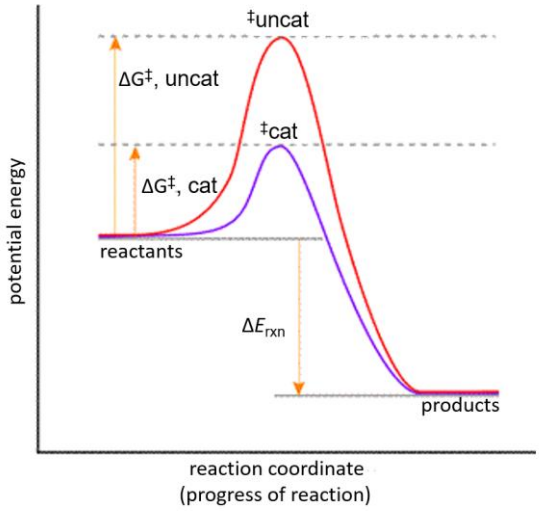

Figure 1.1.: General schematic representation of a reaction profile for an uncatalysed (*red curve*) and catalysed (*purple curve*) reaction.[6]

In addition to examining how catalysts influence reaction equilibrium, it is essential to introduce *Le Chatelier's Principle*.[7] This principle states that if a dynamic equilibrium of a system is disturbed by changing conditions, the equilibrium position will shift to counteract the disturbance and establish a new equilibrium. Typically, catalysts do not affect the position of the equilibrium since they accelerate both the forward and reverse reactions equally, helping the system reach equilibrium faster without altering its position. However, in some cases, catalytic species can influence

equilibrium by modifying reaction pathways or the stability of intermediates, which can lead to changes in product concentrations.

Le Chatelier's Principle helps to explain how changes in temperature, pressure, or concentrations of reactants or products can influence reaction equilibrium. Even when a catalyst is present, any shifts in equilibrium caused by external factors (like temperature or pressure changes) still occur, but the catalyst itself does not directly trigger these shifts. Instead, catalysts facilitate the attainment of equilibrium by lowering the energy barriers for both the forward and reverse reactions, allowing the system to reach equilibrium more quickly. Therefore, while catalysts typically do not alter the position of equilibrium, Le Chatelier's Principle reminds us that changes in external conditions can still affect equilibrium, even in catalysed reactions.

1.1.2. Energy Barriers: Insights into Transition State Stability

Catalysts facilitate reactions by lowering the activation energy barriers required for the reaction to proceed. The activation energy is the energy barrier that molecules must overcome to reach the transition state and ultimately convert into products. By lowering energy barriers, catalysts enable for molecules to reach the transition state more easily, thereby speeding up the reaction kinetics without being consumed or altered in the process.[5] The transition state is a fleeting, high-energy state where bonds are simultaneously in the process of breaking and forming. Catalysts interact transiently with the molecules in the transition state.[8]

Generally, the catalyst binds with one or more reactants and maintains this binding throughout the transition state (TS) of the catalytic process. During this process, when the product detaches, it either directly regenerates the original catalyst or produces a species that will eventually reform to the original catalyst. As a result, catalysts can be utilised in smaller quantities relative to the reactants, optimizing their efficiency in chemical reactions.

Catalysts can reduce the energy of the highest-energy transition state by interacting with and stabilizing a structure that resembles the transition state of the uncatalysed reaction.[8] Alternatively, they may also present an entirely different reaction pathway. The former is common in enzyme-catalysed processes, where the catalyst stabilizes

a transition state like that of the uncatalysed reaction, thereby lowering the overall energy barrier.[9],[10] Organometallic compounds, on the other hand, frequently utilise catalysts that drive reactions through a series of steps. Each of these steps has a reduced activation energy compared to the uncatalysed reaction. As a result, although the reaction progresses in multiple stages, the catalyst lowers the activation energy needed for each individual step.[5]

1.1.3. The steps of the catalytic cycle

The series of steps involved in a catalytic reaction is commonly referred to as the catalytic cycle, as illustrated in **Figure 1.2**. This sequence is often depicted in a cyclic form because the starting point of the process coincides with the ending point of the reaction. This cyclic representation highlights the continuous nature of catalysts, which facilitate reactions by repeatedly binding to reactants, lowering activation energies, and returning unchanged to initiate further reaction cycles.[11]

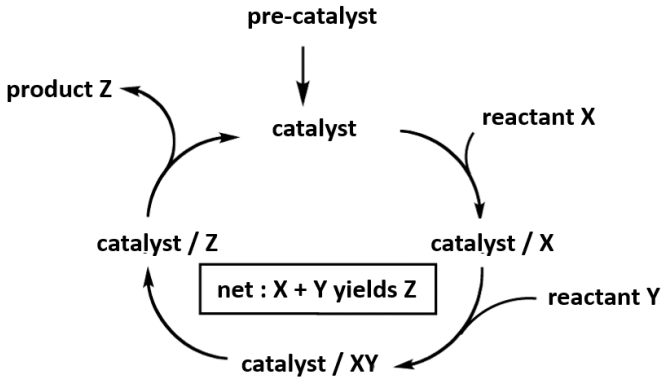

Figure 1.2.: General representation of a catalytic cycle

When catalysts are used in reactions, they often start as inactive precursors that transform into active catalytic species. These active species participate directly in the catalytic cycle, facilitating reactions by lowering activation energies and enhancing reaction rates. Throughout this cycle, the catalytic species undergoes transformations and reactions, promoting the conversion of reactants into products while regenerating itself for continued use.[10]

However, challenges can arise in the catalytic cycle. Competing reactions may lead to the formation of inactive species or byproducts that can deactivate the catalyst over time, reducing its efficiency. Managing these side reactions is crucial to prolonging catalyst's lifespan and maintaining optimal reaction performance.[11] Understanding and optimisation of the catalytic cycle i.e., formation, activity and the deactivation of the catalytic species are essential for maximising the effectiveness of catalysts in industrial processes and chemical synthesis.

The following sections will describe the nature of the catalysts used, particularly the roles of s-block metals in catalytic cycles. They will examine different reaction pathways facilitated by these catalysts, emphasizing their ability to enhance reaction rates and efficiencies. Detailed case studies and experimental results will illustrate the practical applications, setups, and outcomes of each catalytic reaction. Additionally, challenges such as catalyst deactivation and side reactions will be addressed, along with strategies to overcome them. This comprehensive overview will offer insights into the mechanisms, benefits, and practical implications of the catalytic reactions studied in this thesis.

1.2. Alkali metal-based catalysis of unsaturated bonds

The use of s-block metal-based catalysis has significantly increased in recent years, driven by their remarkable ability to facilitate a wide variety of reactions.[12,13] This broad applicability stems from their abundant availability, cost-effectiveness, and low toxicity, with the notable exception of highly toxic beryllium.[9] Particularly appealing is their role in hydrofunctionalisation reactions, which involve the addition of H–E bonds (E = P in this thesis) across multiple bonds such as alkenes and alkynes. These reactions are atom-efficient, enabling the chemo-selective formation of new C–P bonds. The hydrofunctionalisation of alkynes, as depicted in **Scheme 1.1**, serves as an example, yielding *E*- and *Z-isomer*s. In this thesis, we will focus on the alkali metal-mediated reactions of hydrophosphorylation and hydrophosphination.

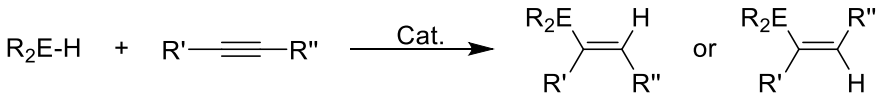

Scheme 1.1: Hydrofunctionalisation of alkynes

These reactions present considerable challenges, due to the inherent unfavorability of a base lone pair approaching the electron-rich π-system of an unsaturated bond.[14] Additionally, the entropic penalty associated with intermolecular hydrofunctionalisation makes these processes highly disfavoured.[15] Overcoming these hurdles requires a catalyst to reduce the high activation barrier and facilitate the reaction.[16]

s-Block metal-based catalysts achieve catalysis by deprotonating the protic substrate to generate highly nucleophilic species capable of adding to the carbon atoms of unsaturated bonds, thereby forming new C–E bonds. Nonetheless, the outcome of these reactions strongly depends on the nature of the alkali metal and the type of P-bound substituents. Notably, the outcome of the reaction will also depend on the R-group attached onto the unsaturated bonds of alkynes and alkanes, however this is out of scope for this thesis.[17,18] Hitherto, it has been observed that when P-bounded group is an aryl group, *E*/*Z-isomer*ization readily occurs in solution, complicating the isolation of a specific isomer. This phenomenon can be explained by charge delocalization, which weakens the C=C double bond of the alkenyl group.[19,20] This will be discussed more into detail in **Scheme 1.4**.

It should be noted that there is no fundamental understanding of electronic and steric control for these reactions, particularly in terms of predictive capability, because alkali metals lack directing d-orbitals. Moreover, the limited exploration of these elements can be attributed to several challenges, including their short-lived reactivity, pronounced sensitivity to air and moisture, and a lack of synthetic expertise. Consequently, their use has largely been confined to controlled laboratory environments, highlighting the need for more comprehensive investigations.[8,10,14]

With the aim of forming stereo- and regioselectivity C-E bonds *via* alkali-metal catalysed reactions, this thesis focuses on a combined approach involving experimental and computational methods to determine the mechanistic steps of the catalytic cycle by which these reactions ensue, to identify and underline the decisive factors

which govern the stereo- and regio-selectivity of the products and to ascertain which alkali metal is the most suited one to be utilised as part of the catalyst.

The atomic sizes and charges of s-block elements result in highly electropositive cations with Lewis acidic properties, often paired with nucleophilic anions. These features enable interactions with the π-bonds of unsaturated compounds, a prerequisite for hydroelementation reactions. In hydrofunctionalisation, such interactions are crucial for bringing nucleophilic species into close proximity with the π-bonds of alkynes.[17,21] This coordination facilitates substrate activation, allowing the metal catalyst to efficiently promote the desired functionalisation reactions.[22]

Computational calculations of s-block metal-promoted processes offer a promising approach to addressing key questions about these reactions. However, this area has received comparatively less attention than the extensively studied transition metal-catalysed systems. Unlike transition metals, which guide reactions through orbital overlap interactions described by the Dewar-Chatt-Duncanson model, s-block metal interactions with electron-rich sites (Lewis bases) are primarily non-directional and ionic in nature.[23]

Additionally, it is worth noting that s-block metals exhibit redox inertness due to their inability to undergo oxidative addition and reductive elimination reactions, which are characteristic of transition metals.[14] Consequently, the catalytic mechanisms involving s-block metals differ fundamentally from the catalytic mechanisms of transition metal-based catalysts.[16] Depending on the nature of the catalyst rather than the nature of the metal, a radical mechanism might proceed.[21] **Scheme 1.2** depicts a general catalytic cycle for the hydroelementation of alkynes with substrates containing H-P bonds; (hydrophosphination or hydrophosphorylation).

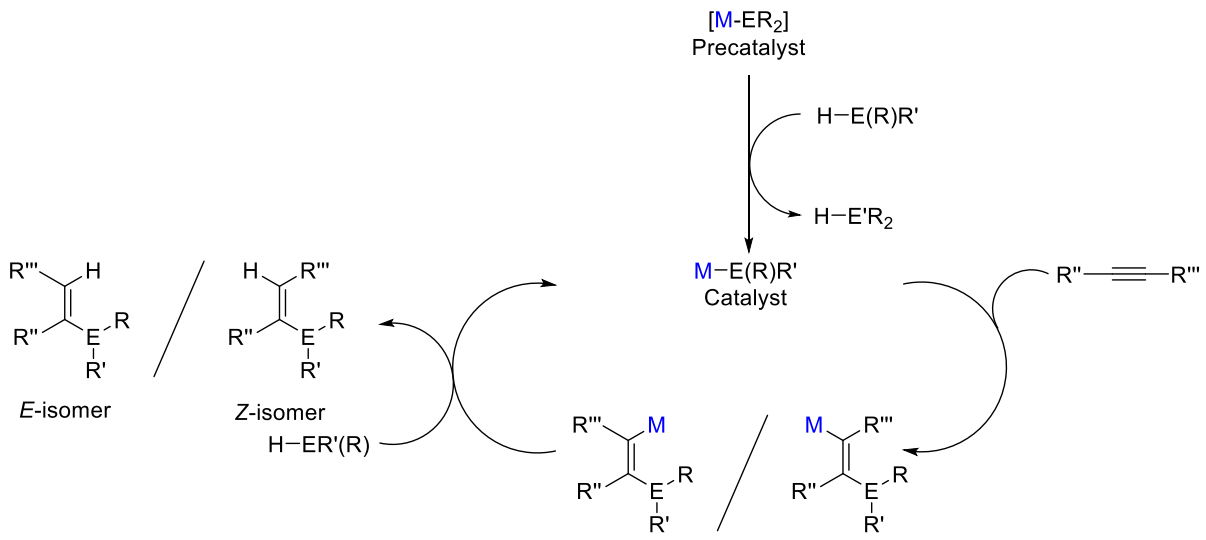

Scheme 1.2: General catalytic cycle for hydroelementation of alkynes. This cycle will be extended to substrates containing H-P bonds, specifically in the processes of hydrophosphination and hydrophosphorylation. Adapted from ref.24

Depending on the nature of the catalyst rather than the nature of the metal, a radical mechanism might proceed.[21] Additionally, obtaining experimental evidence for these reactions is particularly challenging due to the difficulty in characterising and isolating key intermediates. Therefore, it is not surprising that both experimental and computational studies on s-block mediated reactions are relatively limited.[25,26]

An example of the application of s-block metals in catalysis includes hydrophosphinylation and hydrophospholyation. This methodology has been explored by various research groups, including notable work by the Westerhausen group and recent contributions from the He*via* group (see **Scheme 1.3**). These studies demonstrate the versatility of s-block metals in catalysing reactions involving π-system activation, showcasing their potential in synthetic organic chemistry and materials science.[22,27,28]

a) Westerhausen (2011)

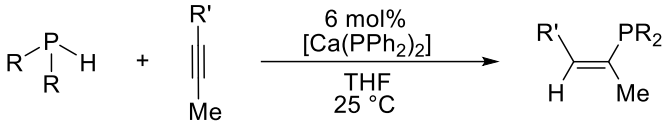

b) Westerhausen (2020)

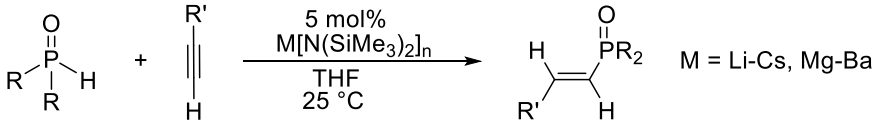

c) Hevia (2022)

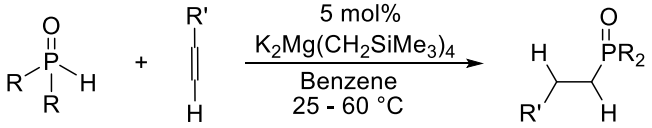

Scheme 1.3: Hydrophosphination and hydrophosphorylation of unsaturated compounds *via* s-block metal-based catalysts.

In **Scheme 1.3**, three distinct s-block metal-mediated hydrophosphination and hydrophosphorylation reactions of unsaturated compounds *via* s-block metal-based catalysts are depicted. Under (*a*), we depicted an example from the Westerhausen group in which they presented successful heterobimetallic potassium magnesiate catalyst for the catalytic hydrophosphinylation of styrenes, exploiting s-block cooperativity.[28] Under (*b*) is presented a latter study by the same group in which they studied alkali- and alkaline-earth metal amides [M{N(SiMe$_3$)$_2$}$_n$; M = group 1 (n=1), M = group 2 (n=2)] for the hydrophosphinylation of arylacetylenes, with heavy alkali-metal amides proving to be the most effective catalysts, while lighter metals exhibited poor activity.[27] Lastly, under (*c*), He*via et al.* investigated the heterobimetallic K/Mg complex, a very effective catalyst for the hydrophosphination of substituted alkynes (R–C≡C–R, R = Me, Ph).[22] With these three examples, we get a glimpse into the diverse world of alkali-metal-mediated hydrophosphinylation and hydrophosphorylation reactions. As it may be observed, these reactions generally favour the formation of anti-Markovnikov

addition products, with only a few exceptions.[21,22,25] This selectivity arises from the stabilisation of the transition states during the addition step, which effectively directs the reaction towards the anti-Markovnikov pathway.

In 2018, the Westerhausen group investigated intermolecular hydrophosphorylation of various alkynes (R_1–C≡C–R_2), utilising the same active catalytic species, K-P(O)R_2, as in the hydrophosphorylation reaction explored in **Chapter 5**. While this study employed KH as the catalyst instead of M-HMDS (M = Li, Na, and K), they successfully generated the same active species, K-P(O)R_2. Since both systems share the same active catalytic species and involve the same substrates undergoing addition reactions, we will discuss their proposed mechanism for the thermal isomerisation as determined from the NMR studies in the Scheme below. Notably, a mechanism for formation was proposed, though it was not confirmed through NMR studies in the paper. In **Chapter 5**, we propose the same mechanistic steps for the formation of the alkenylphosphineoxides.

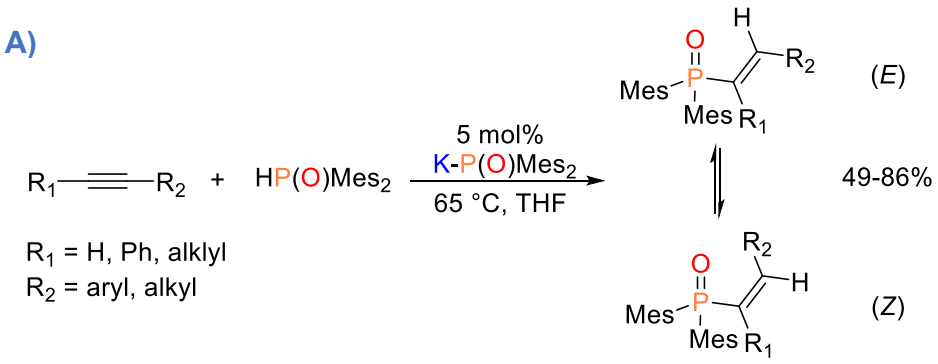

B)

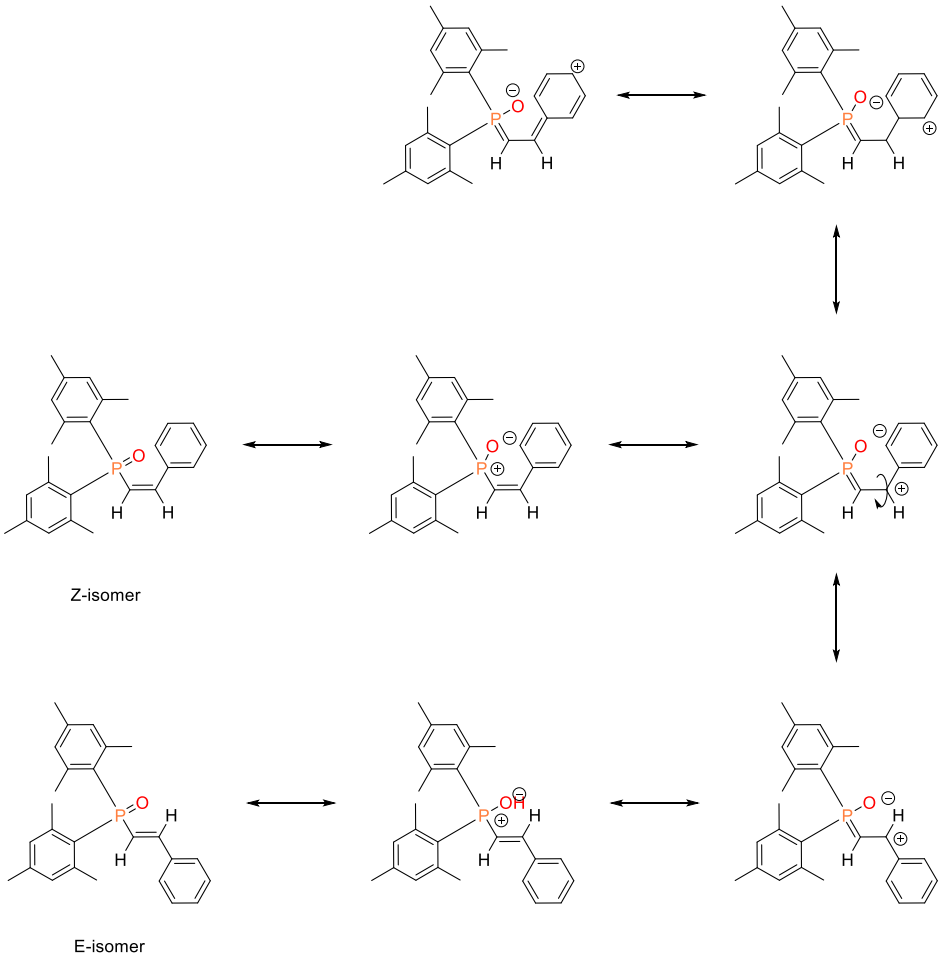

Scheme 1.4: KP(O)Mes$_2$-catalytzed hydrophopshorylation reaction on alkynes. De-aggregation depicted for trimethylsiliyl subsituted alkyne substrate.

The thermally driven *E/Z* isomerisation observed in alkenyldimesitylphosphineoxides bearing a conjugated aryl substituent at the β-position of the alkenyl moiety has been attributed to delocalisation of positive charge across the P–C═C–aryl segment and it has been described in **Scheme 1.4.**, which weakens the C═C bond and facilitates isomerisation. Crystallographic studies support this rationale, showing a nearly coplanar arrangement between the phenyl ring and the adjacent alkenyl fragment. Notably, such isomerisation proceeds thermally, rather than photochemically. The E/Z ratio in these systems is also influenced by both the steric demand of the P-bounded substituent and the polarity of the solvent, indicating that subtle electronic and environmental factors modulate the isomerisation equilibrium. Importantly, in contrast to many classical transformations involving phosphorous-containing

species, straightforward Brønsted acid–base interactions appear to play a minor role in this type of isomerisation process.[14,21,24]

In the following section, we will discuss alkaline mediated reactions with $M\{N(SiMe_3)_2\}_n$ as catalyst in more detail.

1.2.1. Catalysis by alkaline M-HMDS

In this thesis, alkali metal bis(trimethylsilyl)amides (hexamethyldisilazanides, M-HMDS) were selected as catalysts for hydrophosphination and hydrophosphorylation reactions. Successful examples of their use were provided in the previous section; however, we will now delve deeper into their role as catalysts and explore them in more detail. It should be noted that these complexes are not the actual active forms of the catalysts but the precursors which would partly generate the active species.[29–31] They facilitate the generation of alkali metal phosphinites and phosphonates, which act as the ultimate nucleophiles *i.e.* the active catalytic species. This occurs through the deprotonation and metalation of phosphineoxides to form alkali metal phosphinites, and the metalation of phosphines to form alkali metal phosphonates, respectively. Alkali metal bis(trimethylsilyl)amides are highly soluble in common organic reagents, ensuring homogenous reaction conditions that are conducive to controlled and efficient catalytic processes. Moreover, their widespread availability on a large scale makes them practical choices for industrial applications and large-scale synthetic chemistry.[28,32,33] **Scheme 1.5** illustrates an example of the hydrophosphorylation reaction of unsaturated compounds using alkaline M-HMDS catalysts. In this thesis, we will take a closer look at the outcome of this reaction in **Chapter 4**, while hydrophosphination reactions of unsaturated compounds promoted by alkaline M-HMDS catalysts will be discussed in **Chapter 5**.

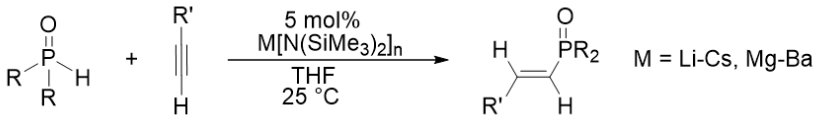

Scheme 1.5: Example of hydrophosphorylation of unsaturated compounds *via* alkaline M-HMDS catalysts. [28]

However, in solution, M-HMDS complexes undergo aggregation and solvation processes, which complicate the precise determination of their chemical speciation in solvents. The degree of aggregation and solvation is solvent-dependent, as different solvents can influence the extent of these processes.[29,34–36] The formation of the active catalytic species is only possible when the complexes are in their disaggregated form, as only this form can proceed to generate the active species. Thus, it is crucial to choose the correct solvent, as the solvent plays a key role in preventing aggregation and ensuring the formation of the disaggregated, active catalytic species.

It is also important to note that the active form of the catalyst (alkali metal phosphinites and alkali metal phosphonates) as well as the M-HMDS catalyst tend to encounter issues with aggregation and solvation, depending on the solvent. Moreover, the current literature on this topic is scarce. Additionally, alkali metal phosphinites exhibit tautomerism, which further influences the concentration of the active catalytic species in the solution. An experimental and computational study by Montchamp *et al.* on the tautomerism of alkali metal phosphinites suggests that the direct P,O-proton transfer proceeds through a strained three-membered ring.[37] However, this will be discussed further in detail in the relevant subsection later in the thesis. The degree of aggregation and solvation depends on several factors, including the alkali metal, the solvent, the concentration in the solution, and the P-bonded group in the nucleophile. Hence, for accurate studies, freshly prepared alkali metal phosphinites and phosphonates must be used.

Furthermore, the interaction between the s-block cation and the π-systems present in the system will be dependent on the ion itself, with lithium cation preferable mode of interaction with the π-system from the triple bonds, to the potassium with a preferred mode of coordination with the π-system of phenyl rings.[34,38] On the other

hand, sodium cation is present with middle of the road preferred mode of coordination.[38,39] These interactions are primarily electrostatic in nature, governed by Coulomb's law, which dictates that the strength of ionic interactions is proportional to the dielectric constant (ε) of the medium and the distance between charges.[40]

Solvent effect also play a crucial role, as they can significantly influence these interactions by altering the dielectric environment.[40] Considering the predominance of ionic interactions in these complexes, achieving stereo- and regioselective outcomes in reactions can be challenging. Different metal ions dictate the formation of distinct products due to their varied preferences for interaction and differences in ionic radii.[27,28]

1.2.4.2. Phosphole Formation *via* Cycloaddition of 1,3-Diynes with primary phosphines

The cycloaddition of 1,3-diynes with primary phosphines to form 1,2,5-trisubstituted phospholes can be viewed as a special form of hydrophosphorylation (see **Scheme 1.6**), thus we decided to make it into one of the research topics for this thesis. We explored alkali metal-mediated hydrophosphorylation in the **Chapter 5**. The catalyst-mediated addition of P–H bonds to the alkyne moieties in 1,3-diynes results in the formation of phosphole rings, following a mechanism akin to hydrophosphorylation of alkynes. Notably, despite the common use of alkali metal-based catalysts, alkali M-HMDS catalysts have not been explored for this specific reaction.

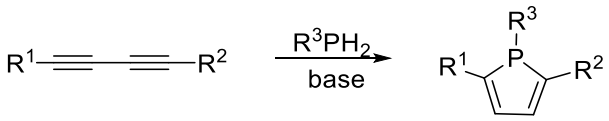

Scheme 1.6: Synthesis of phospholes from diynes.

Phospholes are considered derivatives of cyclopentadiene, consisting of a five-membered unsaturated ring with a single phosphorous heteroatom.[41,42] Unlike pyrrole,

thiophene, and even weakly aromatic furan, phospholes exhibit diminished aromaticity. This reduction is due to the increased pyrimidization at the phosphorous atom, which weakens the aromatic character compared to other heteroaromatic compounds (see **Scheme 1.7**).[43–45]

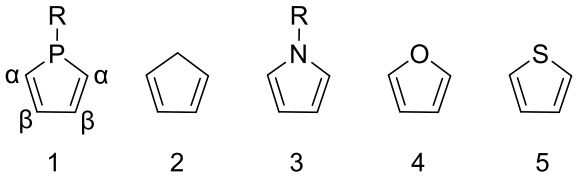

Scheme 1.7: Phosphole and its analogous compounds.

The chemistry of phospholes presents a fascinating area for exploration, largely due to the unique capabilities of the phosphorous atom to engage in various bonding modes and oxidation states.[46–49] Phospholes are characterized by distinct electronic properties, resulting from the reduced hybridization and absence of sp-hybrid orbitals on the phosphorous atom. Consequently, the C-P bonds in phospholes primarily form through π-electrons, imparting a strong s-character to the lone pair on phosphorous. This configuration leads to hyperconjugation between the intracyclic diene and the exocyclic σ*(P–R) bonds, contributing to the aromaticity of the phosphole ring and leaving the lone pair available for further chemical reactivity.[50]

The versatile nature of phospholes is particularly advantageous in the synthesis of various derivatives, which can exhibit unique photophysical properties. These properties make phospholes and their derivatives promising candidates for use in optoelectronic devices, such as organic light-emitting diodes (OLEDs) and photovoltaic cells, as well as in coordination chemistry, where they can act as ligands to form stable complexes with transition metals.[49,51–54]

The majority of computational studies on phospholes concentrate on their aromaticity, the calculation of their inversion barriers, and their potential for forming Diels-Alder products. These areas, while significant in the context of phosphole chemistry, are not the focus of our research. Notably, numerous reviews are available in the

literature are available and provide comprehensive overview on these properties of phospholes.

1.2.2. Alkali metal-mediated formation of phospholes

Hitherto, the synthesis of phospholes appears to be predominantly driven by lithium-ion-based catalysts, suggesting a distinct catalytic role for lithium in these transformations.[46,55] This limited body of work highlights the need for further computational studies to enhance our understanding of the phosphole formation mechanism. These studies notably implemented lithium-based catalysts, further emphasising their importance in driving the reaction.

Notably, in the mechanism it is suggested the formation of phosphaallylic intermediates, which, depending on the reaction conditions transform either to phosphetes or the corresponding phospholes. Building on these findings, it is essential to consider the potential formation of their constitutional isomers, phosphetes, when examining the mechanism of phosphole formation. Phosphetes feature a four-membered heterocyclic motif with an exocyclic methylene unit and can be constructed *via* a rearrangement in the coordination sphere of transition metal fragments. As the reaction progresses, contingent to the reaction's conditions conversion will proceed either to phospholes or analogous phosphetes (see **Scheme 1.8**).

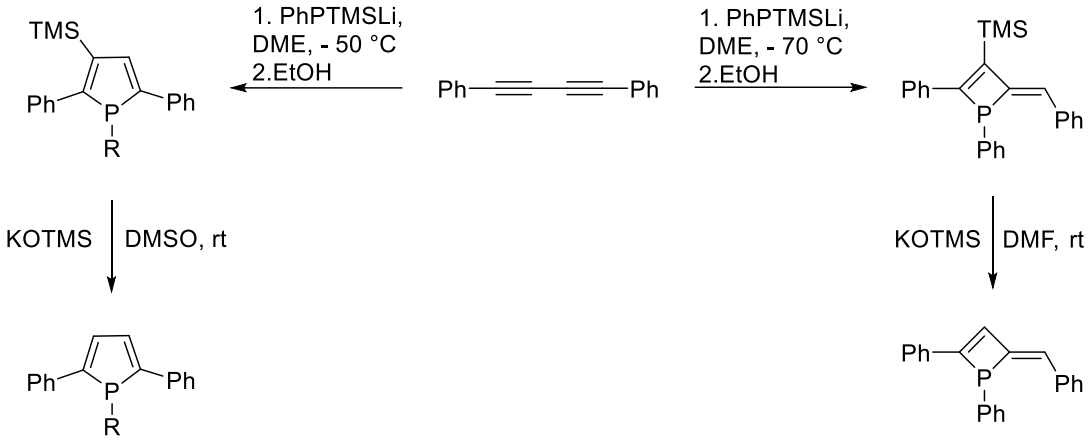

Scheme 1.8: Synthesis of β-silyl phosphole and the corresponding phosphete and their desilylation to β-H phosphetes β-H phosphole.[56]

Since our focus is on phospholes and their formation, we will not review the postulated reaction mechanism for the formation of phosphetes, however, detailed discussion regarding this aspect can be found in the respective paper.[56]

Notably, the synthesis of phospholes bearing germyl and stannyl substituents was reported by the same research group in two sequential studies, the latter of which (published in 2023) proposed a DFT mechanism for their formation, in a manner similar to their previous work.[56] It is important to note that the mechanisms presented in both studies did not include explicit lithium cations, but instead relied on a "naked" anionic system. This computational simplification, while practical, introduces certain assumptions regarding the nature of the reactive intermediates and the influence of metal coordination.

In their proposed mechanism, the key step involves the nucleophilic addition of a phosphanide anion (PhPTMSLi) to a 1,4-diphenylbutadiyne backbone. This step proceeds with an activation barrier of 8.6 kcal mol^{-1}, followed by a silyl group migration that stabilises the resulting vinyl anions. A more stable C−Si bond forms as the P−Si bond is cleaved, with the negative charge becoming delocalised over a 1-phosphaallylic π-system. This rearrangement occurs *via* a low-energy transition state (0.9 kcal mol^{-1}), resembling an SN_2-type mechanism in which the silicon atom adopts a pentacoordinate geometry.

Regardless of the substituent present on the phosphole, the formation of the *Z*-intermediate will be initial. This isomer will tend to isomerise into its less stable *E*-counterpart by 0.6 kcal mol^{-1}, driven by steric constraints that prevent the *Z-isomer* from engaging in ring closure. In contrast, the *E-isomer* can undergo intramolecular cyclisation *via* nucleophilic attack on the neighbouring alkyne unit, leading to the formation of either a phosphole or a phosphete, depending on the specific carbon atom involved in the attack. The final step of the mechanism was postulated to be a protonation event. While this transformation was not investigated through computational means, the protonated product was experimentally confirmed.

Due to the absence of any observed spontaneous ring opening of the phosphole or the phosphete during the reaction, it can be concluded that the corresponding anionic species are likely trapped during the quenching step. Research has demonstrated that the protonation step plays a critical role in determining the overall reaction outcome, emphasising its importance in the mechanistic pathway. Interestingly, the anionic ring-closed intermediates exhibit lower stability in comparison to their phosphaallylic precursors, raising questions regarding the thermodynamic driving force for the cyclisation. Nevertheless, the irreversible nature of the protonation step appears to shift the equilibrium towards product formation, securing the final heterocyclic framework.

1.2.2.1. Oxidation of phospholes

Phospholes undergo diverse reactions, particularly chalcogenation processes, with oxidation to phosphole oxides being the most prominent.[57–59] These compounds can also engage in Diels-Alder reactions, showcasing their versatility in cycloaddition chemistry, as well as polymerisation reactions, demonstrating their potential for functionalisation. In **Chapter 6**, we delved into the experimental and computational aspects of the oxidation of the phosphole, synthesized in **Chapter 5**, culminating in the serendipitous [2+2] dimerisation of the newly formed phosphole oxide. This exploration encompassed a detailed analysis of the oxidation process, examining the conditions required for efficient oxidation and the resulting structural changes in the phosphole molecule.

1.2.2.2 Side reaction of phospholes and phosphole oxides

Phospholes and phosphole oxides exhibit interesting reactivity, particularly in the context of photochemical cycloaddition reactions. These compounds can undergo dimerisation *via* [2+2] and [4+2] additions, often influenced by factors such as oxidation and complexation. While the aromaticity of phospholes and their derivatives plays a role in these processes, it is not the focus of this thesis. Instead, in this section will introduce specific [2+2] and [4+2] photoreactions of phospholes and phosphole oxides. Before proceeding into the discussion, it is important to note that phospholes and phosphole oxides may also undergo Diels-Alder reactions, allowing for the formation of fused polycyclic systems.[54,60–62] These reactions are valuable for modifying the electronic properties and stability of phosphole-based compounds.[45,59,63,64] While studies have demonstrated the potential of phospholes in Diels-Alder reactions, no such products were obtained experimentally in this thesis. However, we did briefly explore the formation of Diels-Alder adducts using DFT calculations. Thus, further discussions on studies related to this aspect will be addressed in the relevant subsection of the thesis.

According to Keglevich *et al.* experimental findings, phospholes are stable for a couple of days, but phosphole oxides under the same conditions rearrange to form 7-phosphanorbornene.[65–67] The instability of phospholes can partly be explained because of weak antiaromaticity. The weak aromaticity is switched upon oxidation to a medium antiaromatic character due to transformation of $\sigma^3 \rightarrow \sigma^4$ of the P atom. In this study the [2+2] adduct was not observed. Notably, in this thesis we did not explore the aspect of aromaticity of phospholes and its derivates, however there are several papers published on this topic. [45,67–70]

In 1969 Nelson *et al.* presented for the first time, a [2+2]-dimer obtained by irradiating a 1,2,5-triphenylphosphole.[68] From the initial data, the stereochemistry of the cyclobutane ring and the ‘’head-to-tail’’, the orientation of the dimer couldn’t be determined (see **Scheme 1.10**).

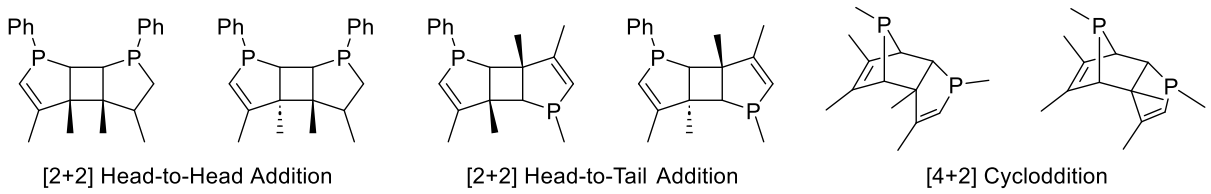

Scheme 1.9: Possible isomers generated *via* cycloaddition from photocycloadditions with $Ru(DMPP)_2L]PF_6$ complexes. [70]

According to experimental data dimerisation in this instance is reversible if higher intensity of light is applied. Attempts to trap the excited intermediate with additional olefins or acetylenes have proved futile, despite using ten-fold molar excesses of trapping agent for the example above. Hence, it can be concluded that these systems have a strong propensity for photodimerization.[68,71] Although dimerisation is typically a rapid process, as mentioned for all systems, intermediates have been detected by ^{31}P NMR for some other phosphole oxides.[72–74]

Upon oxidation or complexation, the phosphorous lone pair on the phosphole ring exhibits a strong tendency to undergo dimerisation *via* [4+2] cycloaddition, leading to the formation of fused polycyclic structures. The substitution pattern of the phosphole ring plays a crucial role in determining the dimerisation behaviour, as lower substitution typically results in a less stable monomeric species, which is more prone to undergo dimerization. Moreover, the nature of the substitution on the phosphorous atom can further influence the reactivity, potentially altering the stability of both the monomer and the resulting dimer. The [2+2] dimerisation relies on the UV radiation, with the most eminent case of *cis*-$(phosphole)_2Mo(CO)_4$ complexes. Duffy *et al.* in 2011 reported another dimerization, in this instance the slight change in the structure of a biphosphole derivative's structure causes a full switch from [4+2] to [2+2] dimerization.[71]

In 2013, Marinetti *et al.* subjected compound (Rp)-5 ((5R)-2-((Z)-5-(Benzo[c]phenanthren-2-yl)oct-4-en-4-yl)-5-((1S,2R,5S)-2-isopropyl-5-methylcyclohexyl)-5H-benzo[b]phosphindole 5-oxide) to photochemical cyclodehydrogenation under standard conditions with iodine (I_2) as an oxidant in the presence of propylene oxide.[75] This reaction yielded (Rp)-5-azahelicene. Interestingly, the reaction did not halt at the formation of (Rp)-5 but proceeded to further photochemical [2+2] cyclization

of the phosphoindole moieties, resulting in a head-to-head dimeric structure. This cyclization reaction is depicted in **Scheme 1.11**. Six years later, the same group discovered that helical phosphinamides could also undergo [2+2] cyclization.[76] They demonstrated that this cyclization could be achieved using sunlight radiation in both solid-state and solution forms, as well as *via* X-ray MoK$_\alpha$ radiation. However, attempts to induce cyclization using CuK$_\alpha$ radiation, were unsuccessful.

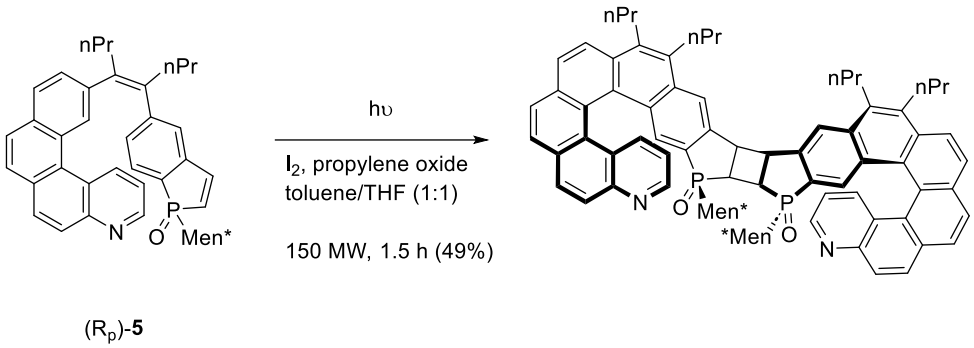

(R_p)-**5**

Scheme 1.10: Photochemical synthesis of dimeric bi-heterohelicenes.

The first [2+2]-dimer of phosphole oxide was reported by Arp *et al.* in 2021.[77] This product is analogous to the phosphole dimer previously presented by Nelson *et al.*[68] Unlike Nelson's work, Arp's synthesis of the [2+2] dimer did not involve the prior synthesis of the analogous phosphole, making the discovery accidental. Their research focused on exploring the boundaries of phosphine oxide carriers, and they achieved the selective formation of the phosphole dimer by reacting 1,2,5-triphenylphosphole with the water adduct of di(hydroperoxy)adamantane. From a stereochemical perspective, the P=O groups in the dimer are oriented on the same side of the ring system, forming hydrogen bonds with other identical molecules. This structural arrangement plays a crucial role in the dimer's stability and properties.

Having provided background on alkali metal-based catalysts in hydrophosphorylation and phosphination, with a specific focus on phosphole formation and subsequent oxidation leading to dimerization, which are the reactions explored in this thesis, we can now proceed to the final remarks of this chapter. These reactions highlight the diverse reactivity of alkali metal-based catalysts, opening up new opportunities for their

use in chemical synthesis and material science, which will be explored throughout the thesis.

1.3. Final remarks

As a summary, hydrofunctionalisation of alkynes and other π-systems is predominantly catalysed by acids, bases, or metals, with occasional instances of radical mechanisms. Various metal catalysts can effectively activate π-systems *via* phosphines or phosphine oxides, facilitating these reactions.

In a typical catalytic cycle, the initial step involves the attack of a phosphanide (for hydrophosphination and hydrophosphination) or phosphinite (for hydrophosphorylation) at an alkyne or cumulene, forming an intermediate with a reactive metal-carbon bond. This organometallic complex deprotonates the protic substrate, regenerating the catalyst and producing the desired product. Increased Brønsted acidity accelerates protonation, but reduced Lewis basicity necessitates harsher conditions for the nucleophilic attack on multiple bond systems.

The effectiveness of s-block metal-mediated hydrofunctionalisation of alkynes and heterocumulenes depends on several factors. The stability of catalysts is crucial; s-block metal phosphanides are stable, allowing for the preparation of stock solutions. In contrast, alkali metal phosphinites are less stable, often disproportioning into soluble phosphanide and insoluble phosphinate. Metal ions play a vital role through their charge and radius, determining the electrostatic attraction to Lewis basic π-systems. The highly reactive metal-carbon bonds formed in intermediates facilitate substrate deprotonation.

The solvent used in these reactions must act as a Lewis base to ensure solubility of metal ions while being hemilabile to open coordination sites for substrate activation. These reactions are regioselective, generally yielding anti-Markovnikov products, but lacks stereoselectivity, producing E- and *Z-isomer*s. Subsequent E/Z isomerization complicates the separation and isolation of specific isomers.

Substituents on substrates affect conversion rates through their electronic properties and bulkiness. Heavily shielded substrates can hinder hydrofunctionalisation reactions. The rate-determining step is postulated to be the approach of an anionic

species to an electron-rich π-system, with rapid protonation of the intermediate organometallic complex making the pKa values of substrates less significant. Additionally, hydrofunctionalisation reactions require an inert and moisture-free atmosphere to avoid the occurrence of radical reactions and the disruption of both radical and ionic pathways.

This overview highlights the crucial aspects of s-block metal catalysis in hydrofunctionalisation reactions, emphasizing the roles of catalyst stability, metal ion characteristics, solvent effects, and reaction conditions in determining the efficiency and outcome of these transformative processes.

Bibliography

1. Wisniak, J. The History of Catalysis. From the Beginning to Nobel Prizes. *Educación Química* **21,** 60–69 (2010).
2. Henry M. Leicester, H. S. K. *A Source Book in Chemistry*. (Harvard University Press, 1965).
3. Berzelius, J. J. *Ann. Chim. Phys*. (1836).
4. *The IUPAC Compendium of Chemical Terminology: The Gold Book*. (International Union of Pure and Applied Chemistry (IUPAC), 2019).
5. Atkins, P. W. & De Paula, J. *Physical chemistry*. (W.H. Freeman, 2010).
6. Sinar Mashuri, S. I., Ibrahim, M. L., Kasim, M. F., Mastuli, M. S., Rashid, U., Abdullah, A. H., Islam, A., Asikin Mijan, N., Tan, Y. H., Mansir, N., Mohd Kaus, N. H. & Yun Hin, T.-Y. Photocatalysis for Organic Wastewater Treatment: From the Basis to Current Challenges for Society. *Catalysts* **10,** 1260 (2020).
7. Blundell, S. & Blundell, K. M. *Concepts in thermal physics*. (Oxford University Press, 2010).
8. Novas, B. T. & Waterman, R. Metal-Catalyzed Hydrophosphination. *ChemCatChem* **14,** (2022).
9. Greenwood, N. N. & Earnshaw, A. *Chemistry of the elements*. (Butterworth-Heinemann, 1997).
10. Steinborn, D. *Fundamentals of organometallic catalysis*. (Wiley-VCH, 2012).
11. Shriver, D. F.; Atkins, P. Inorganic Chemistry,Oxford University Press. (2014).
12. Harder, S. From Limestone to Catalysis: Application of Calcium Compounds as Homogeneous Catalysts. *Chem. Rev.* **110,** 3852–3876 (2010).
13. Zhang, L., Bai, S. & Zheng, L. Magnesium-Catalyzed Regioselective Hydrophosphinylation of Alkenes with Diarylphosphine Oxides. *Organometallics,* **42** (2023).
14. Krieck, S. & Westerhausen, M. Kudos and Renaissance of s-Block Metal Chemistry. *Inorganics,* **5,** 17 (2017).
15. Krieck, S. & Westerhausen, M. *Early Main Group Metal Catalysis*, 123–149 (Wiley, 2020).
16. *Early main group metal catalysis: concepts and reactions*. (Wiley-VCH, 2020).
17. Koshti, V., Gaikwad, S. & Chikkali, S. H. Contemporary avenues in catalytic PH bond addition reaction: A case study of hydrophosphination. *Coord. Chem. Rev.* **265,** 52–73 (2014).
18. Hirano, K. & Miura, M. Recent advances in diphosphination of alkynes and alkenes. *Tetrahedron Lett.* **58,** 4317–4322 (2017).
19. Al-Shboul, T. M. A., Volland, G., Görls, H., Krieck, S. & Westerhausen, M. Oxidation Products of Calcium and Strontium Bis(diphenylphosphanide). *Inorg. Chem.* **51,** 7903–7912 (2012).
20. Härling, S. M., Krieck, S., Görls, H. & Westerhausen, M. Influence of 18-Crown-6 Ether Coordination on the Catalytic Activity of Potassium and Calcium Diarylphosphinites in Hydrophosphorylation Reactions. *Inorg. Chem.* **56,** 9255–9263 (2017).
21. Beletskaya, I. P., Nájera, C. & Yus, M. Catalysis and regioselectivity in hydrofunctionalization reactions of unsaturated carbon bonds. Part III. *Russ. Chem. Rev.* **90,** 70–93 (2021).
22. Platten, A. W. J., Borys, A. M. & Hevia, E. Hydrophosphinylation of Styrenes Catalysed by Well-Defined s-Block Bimetallics. *ChemCatChem* **14,** e202101853 (2022).
23. Housecroft, C. E. *Inorganic chemistry*. (Pearson, 2018).
24. Banerjee, I. & Panda, T. K. Recent advances in the carbon–phosphorus (C–P) bond formation from unsaturated compounds by s- and p-block metals. *Org. Biomol. Chem.* **19,** 6571–6587 (2021).
25. Byrne, K. M., Robertson, S. D., Mulvey, R. E. & Krämer, T. Mechanistic Insight into Alkali-Metal-Mediation of Styrene Transfer Hydrogenation: A DFT Study. *ChemCatChem* **16**, (2024).

26. Al-Shboul, T. M. A., Pálfi, V. K., Yu, L., Kretschmer, R., Wimmer, K., Fischer, R., Görls, H., Reiher, M. & Westerhausen, M. Catalytic synthesis of vinylphosphanes via calcium-mediated intermolecular hydrophosphination of alkynes and butadiynes. J. Organomet. Chem. **696,** 216–227 (2011).
27. Fener, B. E., Schüler, P., Ueberschaar, N., Bellstedt, P., Görls, H., Krieck, S. & Westerhausen, M. Scope and Limitations of the s-Block Metal-Mediated Pudovik Reaction. *Chem. Eur. J.* **26,** 7235–7243 (2020).
28. Woltornist, R. A. & Collum, D. B. Aggregation and Solvation of Sodium Hexamethyldisilazide: Across the Solvent Spectrum. *J. Org. Chem.* **86,** 2406–2422 (2021).
29. Rabe, G. W., Yap, G. P. A. & Rheingold, A. L. Synthesis and X-ray Crystal Structure Determination of the First Potassium Salt of a Primary Phosphane: $[KP(H)Mes^*]_x$. *Inorg. Chem.* **36,** 1990–1991 (1997).
30. Ojeda-Amador, A. I., Martínez-Martínez, A. J., Robertson, G. M., Robertson, S. D., Kennedy, A. R. & O'Hara, C. T. Exploring the solid state and solution structural chemistry of the utility amide potassium hexamethyldisilazide (KHMDS). *Dalton Trans.* **46,** 6392–6403 (2017).
31. Fener, B. E., Schüler, P., Görls, H., Liebing, P. & Westerhausen, M. Alkaline-earth metal dimesitylphosphinites and their ether adducts – A structural study in solution and in the crystalline state. *Z. Anorg. Allg. Chem.* **649,** (2023).
32. Fener, B. E., Schüler, P., Pröhl, F. E., Görls, H., Liebing, P. & Westerhausen, M. s-Block Metal Base-Catalyzed Synthesis of Sterically Encumbered Derivatives of Ethane-1,2-diyl-bis(diphenylphosphineoxide) ($dppeO_2$). Organometallics (2024).
33. Mulvey, R. E. & Robertson, S. D. Synthetically Important Alkali-Metal Utility Amides: Lithium, Sodium, and Potassium Hexamethyldisilazides, Diisopropylamides, and Tetramethylpiperidides. *Angew Chem Int Ed* **52,** 11470–11487 (2013).
34. Spivey, J. A. & Collum, D. B. Potassium Hexamethyldisilazide (KHMDS): Solvent-Dependent Solution Structures. *J. Am. Chem. Soc.* **146,** 17827–17837 (2024).
35. Henderson, K. W., Dorigo, A. E., Liu, Q.-Y. & Williard, P. G. Effect of Polydentate Donor Molecules on Lithium Hexamethyldisilazide Aggregation: An X-ray Crystallographic and a Combination Semiempirical PM3/Single Point *ab Initio* Theoretical Study. *J. Am. Chem. Soc.* **119,** 11855–11863 (1997).
36. Janesko, B. G., Fisher, H. C., Bridle, M. J. & Montchamp, J.-L. P(═O)H to P–OH Tautomerism: A Theoretical and Experimental Study. *J. Org. Chem.* **80,** 10025–10032 (2015).
37. Armstrong, D. R., Davidson, M. G., Garcia-Vivo, D., Kennedy, A. R., Mulvey, R. E. & Robertson, S. D. Monomerizing Alkali-Metal 3,5-Dimethylbenzyl Salts with Tris(*N* , *N* -dimethyl-2-aminoethyl)amine (Me_6 TREN): Structural and Bonding Implications. *Inorg. Chem.* **52,** 12023–12032 (2013).
38. Davidson, M. G., Garcia-Vivo, D., Kennedy, A. R., Mulvey, R. E. & Robertson, S. D. Exploiting σ/π Coordination Isomerism to Prepare Homologous Organoalkali Metal (Li, Na, K) Monomers with Identical Ligand Sets. *Chem. Eur. J.* **17,** 3364–3369 (2011).
39. Heddle, T. *Calculations in Fundamental Physics* 167–186 (Elsevier, 1971).
40. Bange, C. A. & Waterman, R. Challenges in Catalytic Hydrophosphination. *Chem. Eur. J.* **22,** 12598–12605 (2016).
41. Katritzky, A. R. *Comprehensive heterocyclic chemistry III*. (Elsevier, 2008).
42. Leung, S. Y.-L., Evariste, S., Lescop, C., Hissler, M. & Yam, V. W.-W. Supramolecular assembly of a phosphole-based moiety into nanostructures dictated by alkynylplatinum(II) terpyridine complexes through non-covalent Pt···Pt and π–π stacking interactions: synthesis, characterization, photophysics and self-assembly behaviors. *Chem. Sci.* **8,** 4264–4273 (2017).

43. Egan, W., Tang, R., Zon, G. & Mislow, K. Low barrier to pyramidal inversion in phospholes. Measure of aromaticity. *J. Am. Chem. Soc.* **92,** 1442–1444 (1970).
44. Delaere, D., Dransfeld, A., Nguyen, M. T. & Vanquickenborne, L. G. Theoretical Study of the Structure−Property Relationship in Phosphole Monomers. *J. Org. Chem.* **65,** 2631–2636 (2000).
45. Roesler, F., Bruhn, C. & Pietschnig, R. Asymmetrically Substituted Phospholes as Ligands for Coinage Metal Complexes. *Molecules* **27,** 3368 (2022).
46. Matano, Y. Org. Redox Syst.: Synth. Prop. Appl. 477–501 (Wiley, 2016).
47. Matano, Y. & Imahori, H. Design and synthesis of phosphole-based π systems for novel organic materials. *Org. Biomol. Chem.* **7,** 1258 (2009).
48. Matano, Y. Synthesis and Structure-Property Relationships of Phosphole-Based π Systems and Their Applications in Organic Solar Cells: Synthesis and Structure-Property Relationships of Phosphole-Based π Systems and Their Applications in Organic Solar Cells. *Chem. Rec.* **15,** 636–650 (2015).
49. Berlin, K. D. Phosphorus−Carbon Heterocyclic Chemistry: the Rise of a New Domain *J. Am. Chem. Soc.* **124,** 10628–10629 (2002).
50. Joly, D., Tondelier, D., Deborde, V., Geffroy, B., Hissler, M. & Réau, R. Phosphole-based π-conjugated electroluminescent materials for OLEDs. *New J. Chem.* **34,** 1603 (2010).
51. Johannsen, T., Golz, C. & Alcarazo, M. α-Cationic Phospholes: Synthesis and Applications as Ancillary Ligands. *Angew. Chem. Int. Ed.* **59,** 22779–22784 (2020).
52. Klintuch, D., Kirchmeier, A., Bruhn, C. & Pietschnig, R. Synthetic access and luminescence tuning in a series of β-H and β-silyl substituted phospholes. *Dyes Pigm.* **180,** 108443 (2020).
53. Dinadayalane, T. C., Gayatri, G., Sastry, G. N. & Leszczynski, J. Competitive Diels−Alder Reactions: Cyclopentadiene and Phospholes with Butadiene. *J. Phys. Chem. A* **109,** 9310–9323 (2005).
54. Roesler, F., Kovács, M., Bruhn, C., Kelemen, Z. & Pietschnig, R. Phosphetes via Transition Metal Free Ring Closure – Taking the Proper Turn at a Thermodynamic Crossing. *Chem. Eur. J.* **27,** 9782–9790 (2021).
55. Roesler, F., Kovács, M., Bruhn, C., Kelemen, Z. & Pietschnig, R. Moving on from Silicon to the Heavier Tetrels: Germyl- and Stannyl-Substituted Phosphole Derivatives. *Organometallics* **42,** 793–802 (2023).
56. Mathey, F. The organic chemistry of phospholes. *Chem. Rev.* **88,** 429–453 (1988).
57. Ji Ram, V., Sethi, A., Nath, M. & Pratap, R. in *The Chemistry of Heterocycles* 457–468 (Elsevier, 2019).
58. Iaroshenko, V. *Organophosphorus Chemistry: From Molecules to Applications*. (Wiley, 2019).
59. Bachrach, S. M. & Perriott, L. M. Theoretical exammation of the Diels–Alder reaction of 1,3-butadiene with cyclopentadiene and 2 *H* -phosphole. *Can. J. Chem.* **74,** 839–850 (1996).
60. Dinadayalane, T. C., Geetha, K. & Sastry, G. N. Ab Initio and Density Functional Theory (DFT) Study on [1,5] Sigmatropic Rearrangements in Pyrroles, Phospholes, and Siloles and Their Diels−Alder Reactivities ′. *J. Phys. Chem. A* **107,** 5479–5487 (2003).
61. Tomioka, H., Miura, S. & Izawa, Y. Synthesis and photochemical reaction of diels-alder adduct of phosphole oxide and cyclopentadiene. *Tetrahedron Lett.* **24,** 3353–3356 (1983).
62. König, N., Godínez-Loyola, Y., Yang, F., Laube, C., Laue, M., Lönnecke, P., Strassert, C. A. & Hey-Hawkins, E. Facile modification of phosphole-based aggregation-induced emission luminogens with sulfonyl isocyanates. *Chem. Sci.* **14,** 2267–2274 (2023).
63. Deschamps, E., Ricard, L. & Mathey, F. ChemInform Abstract: Toward Polyphospholes: Synthesis and Structure of an α-Linked Quaterphosphole. *ChemInform* **25,** no-no (2010).

64. Kollár, L. & Keglevich, G. *P* -Heterocycles as Ligands in Homogeneous Catalytic Reactions. *Chem. Rev.* **110,** 4257–4302 (2010).
65. Mucsi, Z. & Keglevich, G. Why are Phosphole Oxides Unstable? The Phenomenon of Antiaromaticity as a Destabilizing Factor. *Eur J Org Chem* **2007,** 4765–4771 (2007).
66. Mattmann, E., Mathey, F., Sevin, A. & Frison, G. De-aromatizing Phosphole. *J. Org. Chem.* **67,** 1208–1213 (2002).
67. Barton, T. J. & Nelson, A. J. Heterocyclopentadiene photochemistry. *Tetrahedron Lett.* **10,** 5037–5040 (1969).
68. Solgi, L., Mirjafary, Z., Mokhtari, J. & Saeidian, H. Phosphole aromaticity enhancement by electron pumping through Schleyer hyperconjugative aromaticity: A comprehensive DFT study. *Chem. Phys. Lett.* **821,** 140472 (2023).
69. Ji, H., Nelson, J. H., DeCian, A., Fischer, J., Li, B., Wang, C., McCarty, B., Aoki, Y., Kenney, J. W., Solujic, L. & Milosavljevic, E. B. [2 + 2] Photocycloadditions of [(η5-C5H5) Ru(DMPP)2L]PF6 complexes. *J. Organomet. Chem.* **529,** 395–408 (1997).
70. Duffy, M. P., Lin, Y., Ting, L. Y. & Mathey, F. Intramolecular [4+2] versus [2+2] cycloadditions in P–X–P-linked biphospholes (X = O, S). *New J. Chem.* **35,** 2001 (2011).
71. Keglevich*, G., Toke, L., B□cskei, Z. & Harmat, V. Steric hindrance in the synthesis and properties of the dimer of 1-(2,4,6-Tri-tert-butylphenyl)phosphole 1-oxide. *Heteroat. Chem.* **8,** 527–531 (1997).
72. Quin, L. D. & Wu, X. Products derived from oxidations of 3,4-dimethyl-1-phenylphosphole-1-oxide: A 3-phenyl-5,6-dimethyl-2,3-oxaphosphabicyclo[2.2.2]octene-3-oxide derivative as a precursor of phenyl metaphosphonic anhydride. *Heteroat. Chem.* **2,** 359–367 (1991).
73. Keglevich, G., Quin, L. D., Böcskei, Z., Keserü, G. M., Kalgutkar, R. & Lahti, P. M. Phospholes with reduced pyramidal character from steric crowding III NMR and X-ray diffraction studies on 1-(2,4,6-tri-isopropylphenyl)-3-methylphosphole. *J. Organomet. Chem.* **532,** 109–116 (1997).
74. Yavari, K., Retailleau, P., Voituriez, A. & Marinetti, A. Heterohelicenes with Embedded P-Chiral 1 *H* -Phosphindole or Dibenzophosphole Units: Diastereoselective Photochemical Synthesis and Structural Characterization. *Chem. Eur. J.* **19,** 9939–9947 (2013).
75. Febvay, J., Demmer, C. S., Retailleau, P., Crassous, J., Abella, L., Autschbach, J., Voituriez, A. & Marinetti, A. Phosphahelicenes with (Thio)Phosphinic Acid and Ester Functions by the Oxidative Photocyclisation Approach. *Chem. Eur. J.* **25,** 15609–15614 (2019).
76. Arp, F. F., Ashirov, R., Bhuvanesh, N. & Blümel, J. Di(hydroperoxy)adamantane adducts: synthesis, characterization and application as oxidizers for the direct esterification of aldehydes. *Dalton Trans.* **50,** 15296–15309 (2021).

Chapter 2: Scope and motivation for this thesis

This thesis uses both theoretical and experimental methods to examine the alkali metal-mediated formation of new compounds with P-C bonds, taking into account the information in the introduction and identifying the areas that need more research in the literature. The benefits of these reactions, such as their 100% atom economy, low catalyst cost, and utilisation of abundant and non-toxic metals, led to the selection of this topic. Furthermore, our work intends to investigate the role of alkali metal cations, both in terms of their influence on reaction outcomes and the factors that govern regio- and stereoselectivity, whereas a large portion of the existing research on this topic has focused on transition metal-based catalysts.

In this work we incorporated two alkynes/diynes to aid us in this aim: diphenylbutadiyne and phenylacetylene. We made the choice to use alkynes as they are richer with π-electron than alkenes hence, this would lead to increased electrostatic repulsion of the nucleophile. The use of alkynes would also facilitate the addition across the C≡C triple bond much more easily than across C=C double bonds. Additionally, the alkynes tend to form considerably weaker π-interactions amongst the alkyne and the metal centre of the catalyst. This interaction in itself is the driving force for the activation of the C≡C triple bond for a subsequent nucleophilic attack as, rather than a suppressor like in the instance on alkenes. This reaction will also be governed by the less sterically hindered attack from the nucleophile. Additionally, this reaction yield new compounds with P-C bonds, which may be implemented as regents are ligands for a wide range of organic and inorganic transformation. The aims of this research together with brief overview of the motivations for doing the research given here, are stated below.

Objective 1: *Ab initio* study of postulated mechanism of action for alkali metal-mediated Pudovik reaction for the addition across phenylacetylene and diphenylbutadiyne with a variety of di(organiyl)phosphineoxides

Objective 2: A combined experiential and theoretical study in the alkali metal-mediated hydrophosphination of diphenylbutadiyne.

Objective 3: A combined experiential and theoretical study on the [2+2] homodimerisation in P(V) derivates of 2,4-disubstituted phospholes

Chapter 3: In silico methods

At various levels of accuracy, computational chemistry allows the possibility to model and study varying chemical systems with different degrees of molecular complexity. This chapter offers an overview of the computational methods utilised in this thesis and a general explanation of the quantum mechanics behind them and how they are implemented in exploring chemical reactions.

The first section of this chapter delivers a quick overview of the origins and the fundamental principles of quantum mechanics. This is followed by how computational chemists apply quantum mechanics with its approximations to explore chemical reactions and how it allows us to acquire important information about chemical reactions. This chapter closes with a quick overview of the methods implemented throughout the thesis. Furthermore, the goal of this chapter is to present only a picture of the fundamental notions, approximations, methods, and ideas that underpin them rather than to provide an extensive description.

3.1. Introduction to Quantum Mechanics

3.1.1. Origin and Foundational Principles

Quantum mechanics is a fundamental theory in physics that describes the physical properties of compounds on the scale of atoms and subatomic particles. The inability to replicate some findings using the laws of classical mechanics results from the so-called *quantum realm*. In Physics and Chemistry, this phrase refers to the point at which quantum mechanical effects become significant. The discovery of the quantum realm was the most prominent driving force for developing this new theory in the first half of the last century. However, it is vital to remember that, despite their differences, quantum and classical mechanics are not mutually exclusive. The circumstances where quantum and classical mechanics concur are known as the *correspondence limit* or *classical limit*. All objects must abide by the rules of quantum mechanics per the *correspondence principle* between quantum and classical mechanics. According to the same principle, classical mechanics is only an approximation for larger systems.[1]

The *discretization of magnitudes* of physical quantities (such as energy), which argues that magnitudes may only have quantized or discrete values, is one of the fundamental concepts in quantum physics. Two additional fundamental ideas derived from QM are the *wave-particle duality*, which asserts that every particle possesses both wave and particle characteristics, and the *uncertainty principle*. In 1927, Werner Heisenberg formulated the uncertainty principle, which would later become one of QM's fundamental principles.[2] This principle establishes an inherent limitation to the degree of accuracy with which specific pairs of the fundamental properties of a particle, such as the momentum and position, may be determined concurrently, i.e., the more accurately one property is calculated, the more adversely the other one can be ascertained. Consequently, QM can only offer a range of probabilities for where a particle may be using its momentum, and the momentum probability of a particle. We can describe this range of possibilities using a *wavefunction* (Ψ). This function depends

on the quantum state at the "moment" of the measurement. As a result, the value does contain some uncertainty.

On the other hand, we have *eigenstates*, which describe specific states with an explicit value of a distinct measurable property. However, a system rarely exists in an eigenstate of the observable that interests us. The wavefunction will, however, instantly be an eigenstate of the observable if we perform a measurement of that observable. This thesis won't cover the discussion of *wavefunction collapse* in detail. The discussion on this matter can be found in quantum mechanics books[1-3].

3.1.2. The Schrödinger Equation.

The *Schrödinger equation* is a linear partial differential equation with an akin role to *Newton's second law* in classical mechanics, i.e., it defines the evolution of the wavefunction in time of a system. [3]

$$i\hbar \frac{\partial}{\partial t} \Psi(x,t) = \hat{H}\Psi(x,t) \tag{2.1}$$

Where $\hat{H}$ is the *Hamiltonian,* an operator that describes how this wavefunction should vary in time and corresponds to the value of the system's total energy. This operator is defined as the sum of the operator for the potential $(\hat{V})$ and the kinetic $(\hat{T})$ energies.

$$\hat{H} = \hat{V} + \hat{T} \tag{2.2}$$

Relativistic effects are disregarded in the Hamiltonian's general definition. It is important to note that for the first three rows of the periodic table ($Z < 36$), these effects are often insignificant.[4] The contributions of other operators, like those describing orbital-orbital, spin-spin, and spin-orbital couplings, are also disregarded as they are typically relatively minor. The *Hamiltonian operator* has a set of states known as eigenstates, whose eigenvalues are equal to their corresponding energies. The spatial and time dependences of the wave function for these states may be addressed independently if we assume that the Hamiltonian does not incorporate time. This assumption suggests that the system is conservative as its energy level stays constant.

$$\Psi(x,t) = \int(t)\Psi(x) \tag{2.3}$$

The Schrödinger Equation may be defined as follows if we presume that the wavefunction $\Psi(x)$ is an eigenstate of the Hamiltonian:

$$i\hbar \frac{1}{f(t)}\frac{\partial f(t)}{\partial t} = \frac{1}{\Psi(x)}\hat{H}\Psi(x) = E \tag{2.4}$$

The newly introduced E constant in this equation is the sum of the system's energies in the quantum states specified by the wave function. Solving the differential equation (2.4) gives the solution (2.5).

$$f(t) = e^{-iEt/\hbar} \tag{2.5}$$

and

$$\hat{H}\Psi(x) = E\Psi(x) \tag{2.6}$$

The *time-independent Schrödinger Equation* can be written as shown in Eq. (2.6). Given that the time dependence is always an exponential function of the type described by Eq. (2.5), it is essential to remark that Eq. (2.6) can also be viewed as the spatial component of the time-dependent Schrödinger equation (2.1). As a result, the Hamiltonian's eigenstates can be described as:

$$\Psi(x,t) = e^{-iEt/\hbar}\Psi(x) \tag{2.7}$$

These eigenstates are known as stationary states as they generate probability distributions independent of time, and consequently, their properties are independent of time. The stationary state with the lowest energy value is referred to as the *ground state*, while the other *stationary states* are known as *excited states*.

The time-independent Schrödinger equation is the focus of most of the techniques used to examine chemical reactions, so henceforth, the equation (2.6) shall be referred to as the "*Schrödinger equation*".

3.2. Application of Theory to Reactivity

Implementing quantum mechanics in studying reactivity has yielded the discovery of multiple approximations. These approximations enable estimating values for numerous molecular properties. In the proceeding sections an attempt to summarize the frequent approximations we make when implementing quantum mechanics to analyse chemical reactions. This section only serves as an introduction to how we approach such analysis and is not intended to be a thorough recapitulation of the theoretical ways to study reactivity.

3.2.1. The Born-Oppenheimer Approximation and the Concept of Electronic Structure

The Schrödinger equation for the hydrogen atom may be solved analytically, but it has limitations, and the same cannot be said for heavier atoms. To simplify the procedure for solving the Schrodinger equation for molecular systems, we adopt the# *Born–Oppenheimer* approximation.[1,5] The addition of this approximation allows us to divide the Schrödinger equation into two parts: one part that defines the nuclear wavefunction, with the energy from the electronic wavefunction acting as a potential energy and the second part which defines the electronic wavefunction for a fixed nuclear geometry. The two following assumptions constitute the foundation for the Born-Oppenheimer approximation:

- *The nuclear coordinates enter the electronic wavefunction as parameters only, while for the electronic subsystem, the nuclear momenta are not relevant as they describe the translational motion of the molecule as a whole.*

- *The total wavefunction can, therefore, be factored into electronic and nuclear terms.*

$$\Psi_{tot}\,(R,r) = \Psi_{el}\,(R,r)\,\Psi_{nuc}\,(R) \qquad (2.8)$$

(The sets of nuclear and electronic coordinates are defined by R and r, accordingly.

These two assumptions are based on the high mass ratio between nuclei and electrons, which culminates in the nuclei moving slower than the electrons. Since the ratio is: $\frac{m_{^1H}}{m_{e-}} \approx 1836$ for the lightest nuclei, ^1H or the proton, we can argue that this is an adequate estimation.

The two steps that comprise the Born-Oppenheimer approximation will be discussed further below. We will begin first by writing out the complete Schrödinger equation for the specified molecule:

$$\hat{H}_{tot}\Psi_{tot}\,(R,r) = E_{tot}\Psi_{tot}\,(R,r) \tag{2.9}$$

The *Hamiltonian* operator consists of five contributions to the system's total energy. The *H* can be expressed in the following form:

$$\hat{H}_{tot} = \hat{T}_{tot} + \hat{V}_{tot} = (T_{el} + T_{nuc}) + (V_{ne} + V_{ee} + V_{nn}) \tag{2.10}$$

With each of the terms defined as:

$$\hat{T}_{el} = -\frac{1}{2}\sum_{i}^{n}\nabla_i^2 \qquad \text{Electronic kinetic energy} \tag{2.11}$$

$$\hat{T}_{nuc} = -\frac{1}{2}\sum_{K}^{N}\frac{1}{M_K}\nabla_k^2 \qquad \text{Nuclear kinetic energy} \tag{2.12}$$

$$\hat{V}_{ee} = \sum_{i<j}^{n}\nabla_i^2 \qquad \text{Coulombic electron} - \text{electron repulsion energy} \tag{2.13}$$

$$\hat{V}_{en} = -\sum_{i}^{n}\sum_{K}^{N}\frac{Z_K}{r_{ik}} \qquad \text{Coulombic nuclear} - \text{electron attraction energy} \tag{2.14}$$

$$\hat{V}_{nn} = \sum_{k<1}^{n}\frac{Z_k Z_k}{r_{ik}} \qquad \text{nuclear} - \text{nuclear repulsion energy} \tag{2.15}$$

where *l* and *k* run over all nuclei, and j and i over electrons. The number of the nuclei and the electrons in the above equations are expressed as N and n correspondingly. The internuclear distance is denoted as r_{kl}, the electron-nuclei distance as r_{ik},

and the electron-electron distance as r_{ij}. The terms M and Z represent the mass and the charge of the nuclei.

Assuming that electrons are moving in the potential of fixed nuclei, and that they are faster that the latter we can exclude the term for nuclear kinetic energy from the above equation. Additionally, it is important that the repulsion among the nuclei may be regarded as constant. The electronic Hamiltonian may be defined now as:

$$\hat{H}_{el} = \hat{T}_{el} + \left(\hat{V}_{ne} + \hat{V}_{ee} + \hat{V}_{nn}\right) = \hat{T}_{el} + \hat{V} \tag{2.16}$$

Applying the electronic Hamiltonian to the electronic wavefunction will facilitate the electronic state of the molecule via the following equation:

$$\left(\hat{T}_{el} + \hat{V}\right)\Psi_{el}(R,r) = U_n(R)\Psi_{el}(R,r) \tag{2.17}$$

In the above equation the term U_n represents the sum of the potential and electronic energy with the nuclei at fixed coordinates. Since U_n is contingent on nuclear coordinates, a distinctive electronic wavefunction and a different electronic energy for each nuclear position will be generated. Solving Eq. (2.17) providing us with the resolution for one of the steps in the Born-Oppenheimer approximation.

Solving the electronic Schrödinger equation puts us one step closer to solving the complete Schrödinger equation. The second step can be achieved by applying the complete Hamiltonian onto the nuclear wavefunction.

$$\left(\hat{T}_{el} + \hat{T}_{nuc} + \hat{V}\right)\Psi_{nuc}(R) = E_{tot}\Psi_{nuc}(R) \tag{2.18}$$

The electronic Hamiltonian thus, may be approximated by its average value since electrons move significantly more quickly than nuclei. Thus, allowing the above equation to transfer into:

$$\left(\hat{T}_n + U_n(\mathrm{R})\right)\Psi_n(R) = E_{tot}\Psi_n(R) \tag{2.19}$$

The adiabatic potential or U_n can be obtained as a solution of the electronic Schrödinger equation. In the instance of a fixed nuclear configuration, this potential equals the sum of the coulombic repulsion between the nuclei and the electronic

energy. *Potential Energy Surface*, or PES, is the adiabatic potential determined for various nuclear geometries.

Particularly, the nuclei travel on a potential energy surface generated by solving the electronic Schrödinger equation in the Born-Oppenheimer approximation. This idea that the nuclei moved on a potential energy surface sparked the development of techniques for resolving the electronic Schrödinger equation. These approaches enable the extraction of molecular properties that can be extremely valuable in further investigation of chemical reactions and are collectively known as *electronic structure calculations*.

3.2.2. The Potential Energy Surface (PES)

The potential energy surface (PES) represents the term U_n derived from the Born-Oppenheimer approximation by solving the electronic Schrödinger equation (2.17) for array of nuclear coordinates. Consequently, solving the electronic Schrödinger equation for all an array of nuclear configurations yields the complete PES. However, since it is a 3N-6-dimensional space (where N represents the number of atoms), constructing the entire PES for molecules consisting of more than 3 to 4 atoms is nearly impossible.

A common approach in computational chemistry is to limit the calculations to the chemically relevant region as to allow extraction for pertinent data. From a chemical standpoint, the PES points where the energy is stationary relative to the nuclear coordinates are the most enticing. Specifically, first-order saddle points and minima. The first-order saddle points (or *transition states,* TSs) are points on the PES which correspond to a maximum in one direction and minima in the rest. A 3D representation of PES is depicted in **Figure 3.1**.

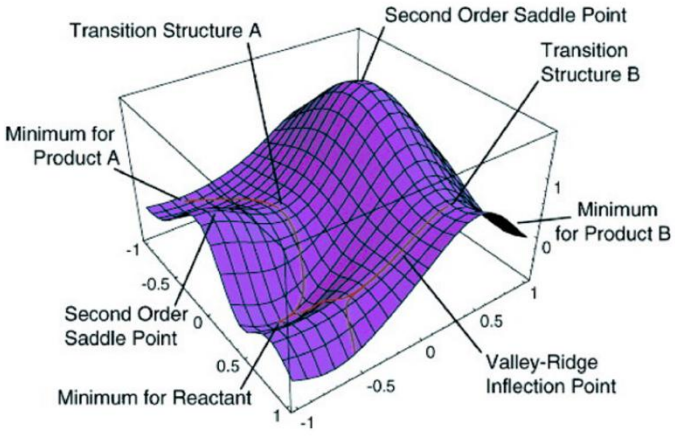

Figure 3.1.: Example of 3D-representation of PES[6]

They provide an estimation of the reactions barrier when transitioning from one to another minima. On the contrary, the changes in PES starting from the points corresponding minima are positive in all direction of the PES and as such they predict the nuclear configuration of a molecules. Additionally, they might be observed as reaction intermediates or stable products. Hence, when we investigate a postulated mechanism and the kinetics of it for a particular reaction, we look for the reaction minima's' and the transition states that connect these minima on the PES. Identifying these stationary locations is not straightforward and necessitates the selection of suitable methodology that strikes the balance among the computational cost and accuracy. Before embarking onto the exploration of the PES profile we would need to make the selection for the level of theory (e.g., Quantum Mechanics or/both Molecular Mechanics QM/MM), the approximation method (e.g., DFT, Hartree-Fock, MP2), the basis sets (e.g., double-ζ, pseudo- or polarization functions) and the model of the solvent (e.g., continuum vs explicit solvent). [7]

Extraction of the reaction energy (ΔE) and the energy barriers ($\Delta E^{\ddagger}$) may be perfromed from the PES profile upon location of the energy minima and the related transition states. It should be noted that above mentioned potential energies are not accurate for group of molecules (i.e., reactions), only for single molecules. Utilization of statistical thermodynamics is prerequisite to determine the thermodynamic properties of a group of molecules, which may later be compared with experimental values. Due to it being a complex process and as this methodology was not implemented in

this thesis this section will not be covered in is this thesis. However, there are several great books covering this subject in detail.[4,7,8]

The *Gibbs energy* in solution (G_S), as we shall see in the next chapters, is one of the most common thermodynamic parameters that we compute for further comparison with the experimental value. Measuring the thermodynamic attribute is not possible as there is no “Gibbs-meter”. Hence, when we are discussing "experimental Gibbs energies" we should be cognizant that they are not exactly experimental values. The "experimental Gibbs energies" are always founded on theoretical models. Consequently, despite what the name might suggest these energies are equally theoretical as the other Gibbs energies we calculate. Estimating the entropic contribution for a solute in gaseous phase allows us to approximate the "experimental Gibbs energies". This method generally yields good results despite it being a rough estimation. The exceptions are the estimation for associative and dissociative processes as the rotational and translational contributions to entropy are overstated in gaseous phase. This overestimation originates from the molecules' reduced ability to move and rotate freely in solution phase in comparison to gas phase, due to the presence of solvent molecules. Notably, when calculating the dissociative process in both liquid and gas phases the dissociation of molecules should also be accounted as it is a highly favourable process. Associative processes, on the other hand, are less favourable. In the last decades multiple approaches have been created and suggested for tacking this problem.[9,10] Another approach to combat the overestimation of entropy suggest considering only vibration contribution to the entropy. However, using this approach greatly underestimates the entropy.[11,12] Ziegler et al. proposed another approximation based on the *Wertz model*.[13–15] Even though this approximation doesn’t overestimation or underestimates the entropy, it necessitates prior knowledge of reference quantities, but they aren’t always attainable. Another approximation proposed by Martin et al.[16], suggests reproducing the condensed phase by calculating the Gibbs energies in gas phase but at high pressure. In this audit the authors stated that calculating the Gibbs energy at pressure: $p = \rho_w RT$ provides an accurate estimation. In the aforementioned formula, ρ_w corresponds to the solvent's experimental density, R denotes the ideal gas constant, and T represents the temperature. Since it entails modifying the standard state (T= 298.15 K and p = 1 atm), but it permits emulating the solvent's constraints over the free motion of the particles, this is likewise a crude approximation.

There are additional techniques (such as molecular dynamics simulations and Monte-Carlo-based techniques) that might theoretically yield superior Gibbs energy estimates. These techniques are typically only suitable for tiny systems as they are typically computationally expensive and slow.

3.2.2.1. Minimum Energy Crossing Point (MECP)

A myriad of reactions will proceed without any change in the electronic state when forming and breaking bonds but solely with redistribution of the electronic wave function. Nonetheless, in the instances when the reaction occurs without explicit contact, and the species contains unpaired electrons, the structural alteration will induce a change in the total electronic spin. This phenomenon is known as spin forbidden process. However, this process may be permitted depending on the size of the *spin-orbit coupling* (SOC). This behaviour is typical for reactions involving metal complexes, and they are also known as *spin-forbidden reactions*. [17]

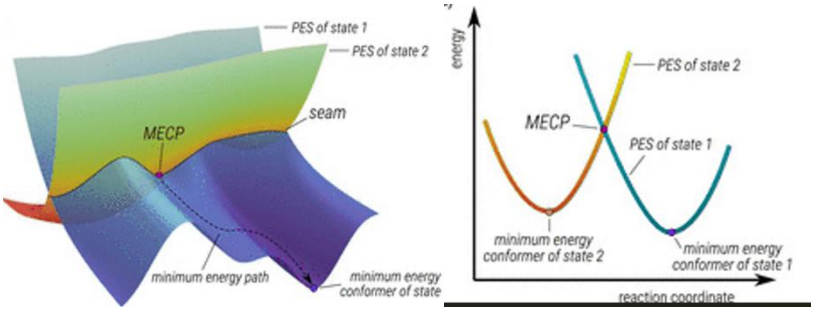

Figure 3.2.: (a) Schematic representation of the energy crossing seam between two electronic states. (b) One-dimensional representation of an MECP between two electronic states. [18]

Since spin-forbidden steps entail the change of some species' spin-state, determining the reactivity of a process, including spin-forbidden steps, is more complex than assessing the reactivity of a typical adiabatic reaction. To explain such reactions, one might envision having two PESs corresponding to the two spin states. This process is presented in **Figure 3.2**: (a) Schematic representation of the energy crossing seam between two electronic states. (b) One-dimensional representation of an MECP between two electronic states by two intersecting lines. When a modification to the species structure moves the system into the zone where the two surfaces meet, and

the SOC permits a transfer from one to the other, a spin shift can proceed. This transformation can be *diabatic* or *adiabatic*, depending on the strength of the SOC.

In the instance of low SOC, the transformation has a probability of p, as shown in **Figure 3.1**. However, in the presence of a strong SOC, the crossing area has a mixed-spin nature, allowing the system to go to the lowest mixed-spin surface. (**Figure 3.2**). As a result, the crossing of two diabatic surfaces is avoided, and the behaviour is more reminiscent of a spin-allowed reaction.

In most cases, the SOC is not powerful enough to significantly alter the energy between a diabatic and an adiabatic state. Therefore, finding a *crossover point* between the two PES is beneficial for describing the reaction process. Although it is not a stationary point, this point is called the *minimum energy crossing point* (MECP) and may be found using standard computational methods.[19] The use of this approach in this thesis may be found in Chapter 6.

3.2.3. Introduction into Approximative methods

The electronic Schrödinger equation (2.17) may be precisely solved in the case of one-electron systems, such as the H_2^+ molecule, but this is not the case for many-electron systems. Typical remark for the Schrödinger equation in such case is that it cannot be solved precisely due to it being a many-body interaction problem. More precisely it means that solving the problem of N-interacting electrons as a sum of N one-electron problems is not possible because of the electron-electron repulsive interactions. To tackle this obstacle several approaches have been developed to grapple with this electronic problem using various approximations.[20] The approximate methods for solving the electronic Schrödinger equation tend to be divided into two main categories: those based on the electron density and those based on the wavefunction. *The Hartree-Fock* (HF) technique is perhaps the most essential within the first class of methods, as the greatest number of methods are built on modifications to this method. On the other hand, methods based on electron density have rapidly been growing in popularity as they produce good results at economical computational cost. All the calculations in this thesis were done using techniques based on the electron density. Consequently, the next section will be dedicated to defining these approaches and the approximations that are used to create them.

3.3. The Density Functional Theory (DFT)

Solving the electronic Schrödinger equation (2.17) with the help of wavefunction methods entails calculating the wavefunction for a set of nuclear coordinates. However, the wavefunction is a function of 3N spatial coordinates with additional N spin variables, where N represents the number of electrons. Hence, the electronic Schrödinger equation can be solved for monoelectronic systems; nonetheless, the same cannot be said for many-electron systems due to increased complexity. This issue may be solved by implementing an alternative approach known as Density Functional Theory (DFT). The basis of this method is the electronic properties of the electron density, as opposed to the wavefunction. The key advantage of this approach is that it simplifies the issue by making the electron density dependant only on the three spatial coordinates (x,y,z).

The electron density $\rho(\overrightarrow{r_1})$ is expressed as the multiple integral over all electron spin variables and all except one spatial coordinate,

$$\rho(\overrightarrow{r_1}) = N \int \dots \int |\Psi\ (\vec{x}_1, \vec{x}_2, .., \vec{x}_n)|^2\ ds_1 d\vec{x}_2 \dots d\vec{x}_N \qquad (2.20)$$

given that,

$$d\vec{x}_i = ds_i d\vec{r}_i \qquad (2.21)$$

The electron density constitutes the probability of locating any of the *N* electrons inside the volume element $d\vec{r}_1$ but with arbitrary spin, whilst the remaining $N-1$ electrons have undefined locations. The spin in this is defined by Ψ. The probability density $\rho(\overrightarrow{r_1})$ is widely recognised solely as electron density. As electrons are indistinguishable from each other, the probability of locating any electron at a certain position is just N times that of detecting one specific electron. Thus, $\rho(\overrightarrow{r_1})$ is a non-negative function based on just three spatial coordinates that integrates to the total number of electrons and vanishes at infinity.

$$\rho(\vec{r} \rightarrow \infty) = 0, \qquad (2.22)$$

$$\int \rho(\vec{r}_1) d\vec{r}_1 = N \tag{2.23}$$

3.3.1. The Hohenberg-Kohn Theorems

The major theoretical pillars upon which present-day density functional theories are postulated are the theorems established in a fundamental paper by Hohenberg and Kohn.[21] The authors presented two theorems in this publication. The first theorem reads, directly quoting from Hohenberg and Kohn's publication:

"The external potential $V_{ext}(\vec{r})$ is (to within a constant) a unique functional of $\rho(\vec{r})$; since, in turn, $V_{ext}(\vec{r})$ fixes H we see that the full many-particle ground state is a unique functional of $\rho(\vec{r})$ ".

The authors proved the first theorem by demonstrating that two distinct $V_{ext}(\vec{r})$ cannot produce the same ground-state electron density, i.e., the external potential $V_{ext}(\vec{r})$ is defined solely by the ground state density. Consequently, derived from this principle, the system's ground-state properties are governed by its electron density. It is important to note that as the total ground state energy is a function of the ground state electron density, so must its components be. As a result, the expected value of the system's energy may be conveyed as:

$$E[\rho] = T[\rho] + V_{ee}[\rho] + V_{ne}[\rho] \tag{2.24}$$

Separating the terms that are universal or independent from the terms for external potential, we obtain the following Eq.2.25:

$$E[\rho] = T[\rho] + V_{ee}[\rho] + V_{ne}[\rho] = F_{HK}[\rho] + \int \rho_r V_{ne} d\vec{r} \tag{2.25}$$

The *Hohenberg-Kohn functional* $F_{HK}[\rho]$ amasses all the independent terms from the above equation.

$$F_{HK}[\rho] = T[\rho] + V_{ee}[\rho] \tag{2.26}$$

The Schrödinger equation can be solved precisely according to Eq. 2.25 only if we know the $F_{HK}[\rho]$. Additionally, as F_{HK} is a functional that is entirely independent of the system, it is equally effective to any molecule regardless of size. Unfortunately, things rarely turn out to be as simple as they first appear, and this situation is no exception. The fundamental issue in this case is that the exact form of the functional $F_{HK}[\rho]$ is unknown. As a result, the DFT faces a significant obstacle in finding an explicit formulation for this unknown functional, which also serves as the theory's weakest link. From the above equations, it can be concluded that the ground state density is, in theory, adequate to acquire all the properties of interest. To be assured that a given density is the ground state density we seek, we must implement the second *Hohenberg-Kohn theorem*.

According to the second theorem, the functional $F_{HK}[\rho]$, which supplies the system's ground state energy, delivers the *lowest energy* if and only if the input density is genuinely the ground state density. The second theorem, in simple terms, states:

Simply applying the established variational principle for wavefunctions to the situation at hand results in the following equation:

$$E_0 \leq E[\tilde{\rho}] = V_{ee}[\tilde{\rho}] + V_{ne}[\tilde{\rho}] + T[\tilde{\rho}] \tag{2.27}$$

In the above equation the density $\tilde{\rho}(\vec{r})$ depicts the trial density that describes a trial Hamiltonian, trial external potential and a trial wavefunction. It is important to note that the last equation yields energy equal to or higher than the exact energy of the system. Obtaining the electron density, which will minimise the energy, is the only way to get the precise energy of the system.

$$\left[\frac{\partial E[\,\rho\,]}{\partial\,\rho}\right] = 0 \tag{2.28}$$

In summary, the second Hohenberg-Kohn principle formulates the variational principle. Nonetheless, depicting the outcome must be done conscientiously to avoid overinterpretation. Most common wavefunction-based methods, like the HF method, are solely variational. Hence, the energy's expected value indicates the quality of the trial wave function, this implies that the higher the energy, the worse the estimation of the ground state wavefunction is. Nonetheless, in the instance where the exact

expression for the functional is not known this is not the case. The variational principle established by the second Hohenberg-Kohn theorem applies solely to the unknown exact functional. Consequently, the energy produced by a trial functional has no relevance in that regard.

3.3.2. The Kohn-Sham Method

As previously stated, the most significant disadvantage when attempting to solve a system of N electrons using DFT is the inability to precisely describe the functional $F_{HK}[\rho]$. Using an approximation equation for this functional and approximately solving the N-electron problem provides a strategy to get around this obstacle. Assuming the approximation functional $F_{HK}[\rho]$, it will yield us the system's energy. The necessity to determine an approximate approximation for $F_{HK}[\rho]$ prompted the creation of the *Thomas-Fermi-Dirac* (TFD) and *Thomas-Ferm*i (TF)methods. [22–24] These two approaches are commonly regarded as predecessors of present-day DFT. Additionally, they constitute the underlying basis for creation of the renowned *Kohn-Sham* (KS) method.[25] This latter is based on revisions of the TF and TFD methods and is also recognised as the second crucial paper of present-day DFT. Hence, before we discuss the *Kohn-Sham* method, let's first make an overview of these two methods.

The general expression for the energy functional in the TF and TFD methods is: (2.24),

The term $\mathrm{T}[\rho]$ that equates to the kinetic energy of the N-electron system may be replaced via the pertaining functional $\mathrm{T_{TF}}[\rho]$ for the uniform non-interacting electron gas. The second term $\mathrm{V_{ee}}[\rho]$, which corresponds for the electron-electron repulsion is substituted by the exchange energy $\mathrm{K}[\rho]$ and the coulombic repulsion among a pair of electrons $\mathrm{J}[\rho]$. [16] It should be noted, that term for the exchange energy is added solely in the TFD method. Considering, the aforementioned approximations the equation for the energy functional for the TFD method is as follows:

$$E_{TDF}[\rho] = T_{TF}[\rho] + J[\rho] + K[\rho] + V_{ne}[\rho] \qquad (2.30)$$

Having successfully established the formula for the energy functional, we may now examine the terms appearing in it. In both methods the terms $\mathrm{J}[\rho]$ and $V_{ne}[\rho]$ may

be simply derived from their classical formulations as they are analysed in classical way in both the TFD and TF methods.

$$V_{ne}[\rho] = -\sum_{a}^{M} \int \frac{Z_a \rho(\vec{r})}{|R_a - \vec{r}|}\, d\vec{r} \tag{2.31}$$

$$J[\rho] = \frac{1}{2} \iint \frac{\rho(\overrightarrow{r_1})\rho(\overrightarrow{r_2})}{|\overrightarrow{r_1} - \overrightarrow{r_2}|}\, d\overrightarrow{r_1} d\overrightarrow{r_2} \tag{2.32}$$

For the term $T_{TF}[\rho]$ and $K[\rho]$ the following equations can be derived in instance of non-interacting gas of electrons:

$$T_{TF}[\,\rho\,] = C_F \int \rho^{5/3}(\vec{r}) d\vec{r} \tag{2.33}$$

$$K[\rho] = -C_X \int \rho^{4/3}(\vec{r}) d\vec{r} \tag{2.34}$$

with,

$$C_F = \frac{3}{10}\,(\,3\pi^2\,)^{2/3} = 2.8712 \tag{2.35}$$

and

$$C_X = \frac{3}{10}\left(\frac{3}{\pi}\right)^{1/3} = 0.7386 \tag{2.36}$$

The expression for the energy functional in the TFD (2.30), therefore, may be obtained by including the equations for $T_{TF}[\rho]$, $J[\rho]$, $K[\rho]$, and $V_{ne}[\rho]$ in the equation for the energy functional.

$$E_{TFD}[\rho] = C_F \int \rho^{5/3}\,(\vec{r}) d\vec{r} + \frac{1}{2} \iint \frac{\rho(\overrightarrow{r_1})\rho(\overrightarrow{r_2})}{|\overrightarrow{r_1} - \overrightarrow{r_2}|}\, d\overrightarrow{r_1} d\overrightarrow{r_2}$$

$$- C_X \int \rho^{4/3}\,(\vec{r}) d\vec{r} - \sum_{a}^{M} \int \frac{Z_a \rho\,(\vec{r})}{|\,R_a - \vec{r}\,|} d\vec{r} \tag{2.37}$$

The energy functional in the TF method may be written as the above equation but with omitted $K[\rho]$ term.

As all of terms, included in the energy functional (2.37) in the *TD* and *TFD* methods are explicit functionals of the electronic density, the issue of the N-electron system is streamed lined. The approximations these methods for the kinetic energy factor are overly simplified, these two methods fail tremendously. Kohn and Sham in 1965 recognised that it would be better to focus on determining the kinetic energy as precisely as possible, as determining accurately the kinetic energy through an explicit functional of the density is futile.[25] The fundamental notion that they suggested was to determine the kinetic energy of a non-interacting reference system with a density identical to that one of an interacting system using the Slater determinant.[26] This is a determinant that defines the wave function of a multi-fermionic system in QM. By changing sign following the exchange of two electrons (or other fermions), it fulfils the anti-symmetry criteria and the Pauli principle.

$$T_s = -\frac{1}{2}\sum_{i}^{N}\langle\varphi_i\ |\nabla^2|\ \varphi_i\rangle \tag{2.38}$$

Despite sharing the same density, the kinetic energy of interacting system does not match the kinetic energy of the non-interacting system. Kohn and Sham combined this and the previous approximation from the universal functional and coined a new term $E_{HK}[\rho]$ (Eq.2.26). Hence, the equation for $F_{HK}[\rho]$ may be written as:

$$F[\rho] = T_s[\rho] + J[\rho] + E_{XC}[\rho] \tag{2.39}$$

This newly coined term is known as exchange-correlation energy, and it may be written as:

$$E_{XC}[\rho] = (T[\rho] + T_s[\rho]) + (V_{ee}[\rho] + J[\rho]) \tag{2.40}$$

Both terms in the above equation serve as correcting terms. The discrepancy among the approximate kinetic energy and the true kinetic energy is corrected by the first two components, while the latter two terms correct the difference between the real electron-electron and the classical $J[\rho]$. Consequently, it may be stated that the functional that contains all the unknown terms is exchange-correlation energy $E_{XC}[\rho]$.

By introducing the equation (2.39) into (2.25), the equation for the energy functional for a real system can take the following from:

$$E[\,\rho(\vec{r})\,] = T_s[\rho] + J[\rho] + E_{XC}[\rho] + V_{ne}[\rho]$$

$$= -\frac{1}{2}\sum_i^N \langle \varphi_i \,|\nabla^2|\, \varphi_i \rangle + \frac{1}{2}\iint \frac{\rho(\vec{r_1})\rho(\vec{r_2})}{|\vec{r_1}-\vec{r_2}|}\, d\vec{r_1} d\vec{r_2} +$$

$$+ E_{XC}[\rho] - \sum_a^M \int \frac{Z_a \rho\,(\vec{r})}{|\,R_a - \vec{r}\,|} d\vec{r} \qquad (2.41)$$

Adding the constraint into the above equation that the electron density determined by the sum of the moduli of the squared orbitals φ_i explicitly equals the ground state density of our real system of interacting electrons.

$$\rho(\vec{r}) = \sum_i^N \sum_s |\varphi_i(\vec{r}, s)|^2 = \rho_0(\vec{r}) \qquad (2.42)$$

and subsequently imposing the restriction that the orbitals φ_i must be orthonormal,

$$\int \varphi_i(\vec{r})^* \varphi_j(\vec{r}) = \delta_{ij} \qquad (2.43)$$

$$\delta_{ij} = 1 \qquad i = j$$

$$\delta_{ij} = 0 \qquad i \neq j$$

Finally, one can derive the Kohn-Sham equations:

$$\left(-\frac{1}{2}\nabla^2 + v_{eff}\right)\varphi_i = \varepsilon_i \varphi_i \qquad (2.44)$$

where, the term h_{ks} represents the Kohn-Sham one-electron Hamiltonian and is derived as:

$$h_{ks} = \left(-\frac{1}{2}\nabla^2 + v_{eff}\right) \qquad (2.45)$$

and the *effective potential* v_{eff} which is defined as:

$$v_{eff}(\vec{r}) = \int \frac{\rho(\vec{r})}{r_{12}} d\vec{r_2} + V_{XC}(\vec{r_1}) - \sum_{a}^{M} \frac{Z_a}{r_{1a}} \quad (2.46)$$

Consequently, of the exchange-correlation energy E_{XC} the sole unknown term in this last equation is the term for exchange-correlation potential V_{XC}. The functional derivative of E_{XC} with respect to the electron density defines this potential:

$$V_{XC} \equiv \frac{\partial E_{XC}}{\partial \rho} \quad (2.47)$$

It is important to note, that the Kohn-Sham method could provide the exact energy only if the exact from of the exchange-correlation energy and exchange-correlation potential were established. However, they are known. Additionally, the Kohn-Sham Eq. (2.44) must be solved continuously since the effective potential is contingent on the electron density. To determine the effective potential for this operation, we must first define a trial electron density using Eq. (2.46). Using this newly attained effective potential we may then solve the Kohn-Sham equations (2.44) and to generate the squared orbitals φ_i. Upon which, they may then be inserted into Eq. (2.46) to yield a new electron density. Until the difference among the trial and the new electron densities fulfils the specified convergence requirement the process will be repeated continuously. Upon completion, the convergent electron density may be used to determine the energy according to the Eq. (2.41).

Solely when we select an explicit version of the related potential V_{XC} and the unknown exchange-correlation functional E_{XC} does the approximation in this KS method come into effect. As a result, the distinction between DFT approaches depends on these unknown functionals.[14]

3.3.3. Exchange-Correlation Functionals

Exchange-correlation functionals frequently have a limiting behaviour (high- and low-density limit) and fit parameters to already known data. These types of functionals are commonly comprised of two sections: the correlation part E_C and exchange component E_X , analogous to conventional many-body theory.

$$E_{XC}[\rho] = E_X[\rho] + E_C[\rho] \quad (2.48)$$

John P. Perdew, using the religious allegory of *Jacob's ladder* as a reference point, presented his image of the DFT ladder that ascends from Earth (i.e., the HF world) to heaven (i.e., the highest chemical accuracy) based on these approximations (see **Figure 3.3**). [27]

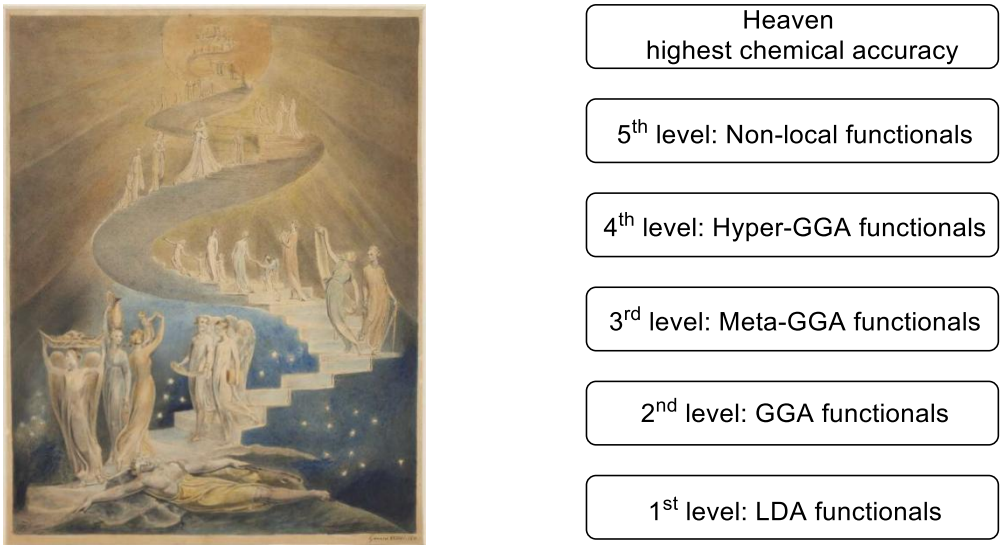

Figure 3.3.: Representation of Jacob's ladder (by William Blake on the right) and graphical representation of "Petrow's functionals ladder" (on the left). [28]

The significant advantage of the DFT, as noted by Perdew, is that we may move up or down the ladder of the functionals based on what we want to accomplish. Moving up the rungs will yield more accurate data, but the increased computational cost will be the downside.[14] Consequently, we should balance computational cost and accuracy fairly when selecting an exchange-correlation functional. It is important to note that when performing the calculations, there is not one correct answer to the question " What is the ideal functional?". The answer is singular to each case and can be determined by examining the performance of the functionals vs the experimental outcome or with high-level wave mechanics calculations.

In the following paragraphs, I will attempt to briefly outline the forms of exchange-correlation functionals that appear in Perdew's ladder and the approximations behind them.

3.3.3.1. Local Density and Local Spin Density Approximation (LDA and LSDA)

The *local density approximation* (LDA) represents the exchange-correlation functional. This approximation assumes that the density can be considered locally as a homogeneous electron gas. The term for functional E_{XC} in the LDA may be expressed as:

$$E_{XC}^{LDA}\ [\rho]\ =\ \int \int\ (\rho) d\vec{r}\ =\ E_{X}^{LDA}\ [\rho] + E_{C}^{LDA}\ [\rho] \tag{2.49}$$

The exchange functional presented in the Thomas-Fermi-Dirac method (2.34) is analogous to the exchange part in a uniform electron gas. Hence, in the LDA approximation, the exchange energy E_X is derived as:

$$E_{XC}^{LDA}\ [\rho]\ =\ -\frac{3}{4}\left(\frac{3}{\pi}\right)^{1/3} \int \rho^{4/3}\ (\vec{r}) d\vec{r} \tag{2.50}$$

There is no explicit expression for the correlation part E_{XC}^{LDA} that has been determined. Nonetheless, several authors have used highly accurate Monte Carlo numerical quantum simulations to implement complex interpolation schemes to derive analytic expressions for this term.[29] The Vosko, Wilk, and Nusair (VWN) representation is one of the most commonly used. [30]

The sum of the α and β densities is considered the total density in the LDA. It is important to note that this assumption is correct only for closed-shell systems but not for open-shell systems. When we apply the LDA to the latter instance, we get the *local spin density approximation* or LSDA. In LSDA, the term for the exchange energy can be expressed as:

$$E_{XC}^{LDA}\ [\rho]\ =\ -(2)^{1/3}\ \frac{3}{4}\left(\frac{3}{\pi}\right)^{1/3} \int \left[\rho_{\alpha}^{4/3} +\ \rho_{\beta}^{4/3}\right] d\vec{r} \tag{2.51}$$

Studies have provided evidence that the results obtained with LSDA and LDA have comparable accuracy to those achieved using the HF approach.[5] Unfortunately, we should not get too enthusiastic about these conclusions as analysing the energetic properties reveals poor overall performance of these approximations. They are

pointing to a long road ahead in developing exchange-correlation functionals before reaching the highest chemical accuracy. The introduction of the gradient of the density is the next step on Perdew's ladder, i.e., the *generalised gradient approximation* (GGA) functionals.

3.3.3.2. The Generalized Gradient Approximation (GGA)

Attempting to account for the non-homogeneity of the electron density is the most straightforward path to enhancing the LDA-based functionals. Considering that the correlation and the exchange energies depend on the electron density and its derivatives yields the first approximation, thus providing us with the basis for the *generalised gradient approximation* (GGA) functional. These functionals are also known as non-local functionals as to be differentiated from the LDA functionals. Considering them as local functionals is more pertinent because they depend solely on the density (and its derivatives) at a specific point rather than on a spatial volume as the HF exchange energy does. In GGA, the exchange-correlation functional is expressed as:

$$E_{XC}^{GGA}\ [\rho]\ =\ \int \int\ (\rho,\nabla\ \rho)d\vec{r}\ =\ E_{X}^{GGA}\ [\rho] + E_{C}^{GGA}\ [\rho] \tag{2.52}$$

In this approximation, the exchange portion is derived as:

$$E_{X}^{GGA}\ [\rho]\ =\ E_{X}^{LDA}\ [\rho]\ - \sum_{\sigma} \int F(s_{\sigma})\ \rho_{\sigma}^{4/3}(\vec{r})d\vec{r} \tag{2.53}$$

Where F represents a function of the reduced density gradient for spin σ. The term s_{σ} in eqn. 2.53 represents the local inhomogeneity parameter.

$$s_{\sigma}(\vec{r}) = \frac{|\nabla\ \rho_{\sigma}(\vec{r})|}{\rho_{\sigma}^{4/3}(\vec{r})} \tag{2.54}$$

The formulation of the first set of functionals began with the formulation of the GGA exchange functional B (or B88) by Becke.[31] These functionals are considered chemist functionals as they are based on empirical parameters whose values have been able to be reproduced experimentally. Some examples of GGA exchange

functionals that fall under this group of functionals are the modified Perdew-Wang (mPW) functional, CAM and FT97.[32–34]

On the other hand, the physicist functions are founded on principles derived from quantum mechanics. Examples of GGA exchange functionals based on the physicist functions are the P functional from Perdew, the PBE functional from Perdew, Burke, and Ernzerhof and the B86 functional by Becke. The analytical form of the GGA correlation functionals is much more complex than the exchange functionals. Hence, I will list some of the most widely utilised correlation functionals. For instance: the LYP functional from Lee, Yang and Parr, the correlation counterpart of the exchange functional *P* from Perdew (*P or P86*) and the parameter-free correlation functional by Perdew and Wang, PW91.[35–39] Theoretically, a combination of any exchange functional and all the correlations may proceed. However, only a few are presently in use.

3.3.3.3. Meta-GGA Functionals

The following rung on Perdew's ladder correlates to the meta-GGA functionals.[40] Meta-GGAs often outperform GGAs in terms of accuracy since they consider the local kinetic energy density τ (i.e., the Laplacian of the occupied orbitals). Notably, some may also include the Laplacian of the density $\nabla^2 \rho(r)$. The kinetic energy density (τ) is defined as the sum of all occupied Kohn-Sham orbitals in this type of functional:

$$\tau(\vec{r}) = \frac{1}{2}\sum_{i}^{occ} |\nabla \varphi_i(\vec{r})|^2 \qquad (2.55)$$

Compared to LDAs and GGAs, meta-GGAs can more accurately treat different chemical bonds (e.g., covalent, metallic, and weak). The meta-GGA function is defined as follows:

$$E_{XC}^{mGGA}[\rho] = \int \int (\rho, \nabla \rho, \tau) d\vec{r} \qquad (2.56)$$

Examples of this functional are the correlation functional KCIS and the exchange-correlation TPSS, VSXC and B98. [41–45]

2.3.3.4. The Adiabatic Connection: Hybrid Functionals

Another strategy that can be implemented to try and achieve a more accurate exchange-correlation functional is to use the Kohn-Sham orbitals with the exact exchange energy calculated via the HF method and to incorporate the approximate functionals solely missed by HF, i.e., the electron correlation. The functionals based on this strategy are usually known as *hybrid functionals*.[46]

$$E_{XC} = E_x^{exact} + E_C^{KC} \tag{2.57}$$

The so-called *adiabatic connection formula* (ACF) links these two components of the exchange-correlation energy.

$$E_{XC}[\rho] = \int_0^1 E_{ncl}^{\lambda}[\rho] d\lambda \tag{2.58}$$

In the above equation λ represents the *coupling strength parameter* (with values ranging from 0 to 1) and E_{ncl} term is the non-classical contribution for the electron-electron interaction for the various values of λ. At $\lambda = 0$ (the integration limit), the system becomes non-interacting system, and hence the $E_{ncl}^{\lambda=0}$ is solely comprised of exchange. Consequently, the $\lambda = 0$ (the limiting case) equates to the exact exchange. On the other side of the limiting case $\lambda = 1$, non-classical contributions come from the fully interacting system that includes correlation and exchange terms.

Implementing the LDA exchange-correlation functional $E_{ncl}^{\lambda=1}$ and assuming that E_{ncl}^{λ} is a linear function of λ yields the solution to equation 2.50. This approximation yields to what is known as the *half-and-half* (HH) combination, which was proposed by Becke [43]. The HH combination includes 50% of the LDA exchange and 50 % of the exact exchange.

$$E_{XC}^{HH} = \frac{1}{2} E_x^{\lambda=0} + \frac{1}{2} E_x^{\lambda=1} \tag{2.59}$$

BHandHLYP is one of the most commonly used variations of this combination, and it has shown to generate excellent results for radical systems.[47]

$$E_{XC}^{BHandHLYP} = \frac{1}{2} E_x^{exact} + \frac{1}{2} E_x^{LSDA} + \frac{1}{2} \Delta E_x^{B88} + \frac{1}{2} E_C^{LYP} \tag{2.60}$$

Becke produced one of the most used hybrid functionals, the *Becke 3* parameter functional, the same year as the HH combination proposal using the same scheme. [48] The exchange-correlation expression for this functional is defined as follows:

$$E_{XC}^{B3} = aE_X^{exact} + (1-a)E_X^{LSDA} + b\Delta E_X^{B88} + E_C^{LSDA} + c\Delta E_c^{PW91} \qquad (2.61)$$

Where a, b, and c represent multiple terms in the B3 functional. These parameters have the following values: a = 0.20, b = 0.72, and c = 0.81. These parameters were selected to represent multiple properties such as atomisation and ionisation energies, proton affinity and total energies as accurately as possible. Notably, the amount of exact exchange is determined by the parameter a.

Stevens et al. proposed replacing the correlation terms in this B3 functional (2.61) with the correlation functional LYP, which resulted in the creation of the well-known *B3LYP* functional.[49] Because the LYP functional includes a local portion in addition to the gradient correction, the term EX WN is introduced in this functional to eliminate this local part. This last term is equivalent to the Vosko, Wilk, and Nusair LSDA-based correlation functional.[30]

$$E_{XC}^{B3LYP} = aE_X^{exact} + (1-a)E_X^{LSDA} + b\Delta E_X^{B88} + cE_C^{LYP} + (1-a)\Delta E_c^{VWN} \qquad (2.62)$$

Since its introduction in 1994, the B3LYP functional has had remarkable success, becoming the most commonly used functional in recent years. As a result of its shortcomings, such as underestimation of energy barriers and a poor representation of non-covalent interactions (e.g., van der Waals interactions), the predominance of this functional is diminishing. [50,51] The downside of B3LYP functional, is the poor description of non-covalent interactions.

3.3.3.5. Dispersion corrections

Nonetheless, enhancing the depiction of non-covalent interactions within DFT can proceed via other alternative approaches.[51–53] Consequently, new key words and new functionals are currently being developed. Truhlar et al.'s "MXX" family of functionals stand out from these novel functionals. The first group from this set are the MOS (MO5 and MO5-2X) functionals, followed by the MO6 group functionals which consist of MO6, MO6-2X, MO6-L and M06-HF function. The third set is consistent of

the M08 functionals, which includes the M08-HX functional and last sent includes the MN15. All these functions present with different ratio of the exact exchange. Choosing the correct functional will be dependant on the atoms present and on the reaction which will be followed. Truhlar et al.'s "MXX" family of functionals fill up the gap left by the B3LYP functional as they generate better description of the non-covalent interactions. These functions are able to achieve this by means of implicit parametrization.[1,15] Nonetheless, there are multiple ways of improving these interactions. The dispersion correction (DFT-D) method, also known as Grimme's dispersion correction, is perhaps the most popular among these methods.[54] This correction is the addition of a dispersion energy factor, which is described as follows, to the Kohn-Sham energy.

$$E_{disp} = -s_6 \sum_{i=1}^{N_{at}-1} \sum_{j=i+1}^{N_{at}} \frac{C_6^{ij}}{R_{ij}^6} f_{dmp}(R_{ij}) \qquad (2.63)$$

In the Eq. 2.63, the term s_6 is a scaling factor that relies exclusively on the density functional utilised, the N_{at} term denotes the number of atoms in the system, the C term represents the dispersion coefficient for atom pair ij, the f_{dmp} is a damping function, and the interatomic distance is denoted through R_{ij} . The performance of these dispersion-corrected density functionals has significantly improved recently due to corrections to this dispersion term. [55–57]

3.3.3.6. Hyper-GGA Functionals

We reach the hyper-GGA functionals by moving up one rung on Jacob's ladder of functionals (Fig. 3). In the following paragraph, I will attempt to define the hyper-GGA term.

Various articles and books define hyper-GGA functionals as functionals that contain precise exchange. But this definition falls short because it doesn't say whether or not a functional that incorporates a portion of exact exchange (for example, hybrid functionals) qualifies as a hyper-GGA functional. On the other hand, other publications maintain that the term hyper-GGA applies to functionals that incorporate a certain amount of exact exchange. Consequently, this final definition suggests that hybrid functionals may be considered hyper-GGA functionals. It can be deduced from the

literature that this term has two distinct concepts and, as such, remains shrouded in a veil of uncertainty. Despite what one may assume, the hyper-GGA functionals do not mark the highest level on Perdew's ladder. Instead, another rung is still to be attained before reaching the peak of accuracy.

The last rung on the latter is for the fully *non-local functionals*. These functionals optimise the correlation element by assessing a part of it precisely and incorporating the exact exchange. The *interaction strength interpolation* (ISI) and the generalised *random phase approximation* (RPA) are some examples of these types of functionals.[58–61]

3.3.4. Self-Interaction Error

An additional issue concerning DFT methods is the so-called *self-interacting error*. [62]The simplest way of explaining this error is by comparing the energies obtained with the HF and the Kohn-Shan method for a one-electron system. These methods were selected as the HF method is free of self-interaction errors. Hence, we will begin with it. The equation for the electronic energy in the HF approach has not been entirely derived in this thesis. However, I will implement this expression to convey the idea of self-interaction error. Numerous general quantum chemistry books contain information on how this equation was derived.

The electronic energy of the system according to the HF is presented in the following Eq.:

$$E_{HF} = \sum_{i=1}^{N} \varepsilon_i - \frac{1}{2} \sum_{i=1}^{N} \sum_{j=1}^{N} \left(J_{ij} - K_{ij}\right) \tag{2.64}$$

Where the $J$and K are the Coulombic and exchange integrals, respectively, and ε_i is the energy of the electron i. The terms J and K are equal with opposite signs in the case of a one-electron system; hence, they can annul each other. This results in a complete cancellation of the electron's self-interaction i.

Conversely, the electronic energy in the KS method is given by:

$$E[\rho(\vec{r})] = T_S[\rho] + J[\rho] + E_{XC}[\rho] + V_{ne}[\rho] \tag{2.65}$$

With the term $J[\rho]$ Defined as:

$$J[\rho] = \frac{1}{2} \iint \frac{\rho(\overrightarrow{r_1})\rho(\overrightarrow{r_2})}{|\overrightarrow{r_1} - \overrightarrow{r_2}|} \, d\overrightarrow{r_1} \, d\overrightarrow{r_2} \tag{2.66}$$

The term $J[\rho]$ will not cancel out altogether the term E_{XC} like in the above instance, as this term also contains the density interaction itself. This lack of complete cancellation is due to the approximate expressions we must do for the unknown term E_{XC}. The *self-interaction corrected* (SIC) form of Perdew and Zunger's approximate functionals offers a solution to this issue.[63]

3.4. Basis set

Roothaan, in 1951 proposed the use of spatial basis functions to solve differential equations in the HF approximation. Hence, these equations were transformed into a set of algebraic equation that could be solved using matrix methods. An ensemble of functions that characterise the motion of electrons in space makes up a specific basis set. Choosing the right basis set is of crucial importance for calculating the mechanism since it determines the way the calculation ensues. Presently, there are multiple basis sets accessible. They were designed to enhance electron behaviour by emphasising specific properties. This thesis does not aim to provide a comprehensive discussion of these sets however, such may be found in textbooks[1-5]. Here, we will only shortly discus the two most common type of functions. The Slater-type orbitals (STOs) and Gaussian-type orbitals (GTOs).

$$\varphi^{STO} = N \, r^{n-1} e^{-\zeta r} \, Y_{lm_l} \tag{2.67}$$

and,

$$\varphi^{GTO} = N \, r^{2n-2-l} e^{-\zeta r^2} \, Y_{lm_l} \tag{2.68}$$

In the above equations (2.67 and 2.68) N represents the normalization constant, n is the natural number which emulates the *principal quantum number*, l depicts the *orbital angular quantum number*, r represents the distance between the electron and the atomic nuclei, ζ is the variational parameter of the radial function which

establishes the scope of diffusion of the function and lastly Y_{lm_l} depict the spherical functions.

Although the sole difference amongst GTOs and STOs is in the quadratic dependency with r, this difference has a far-reaching consequence in terms of the demeanour of each kind of orbital. For expanding MOs, the most useful type are the STOs. These orbitals are hydrogen-like Aos and can recreate the right electronic behaviour far away (asymptotic long-range behaviour $e^{-\zeta r}$) and near to the nucleus (r → O area). GTOs on the contrary make it easier to estimate the molecular multi-centre integrals. However, a rough estimation of a single STO necessities a linear combination of minimum three GTOs (**Figure 3.4**).

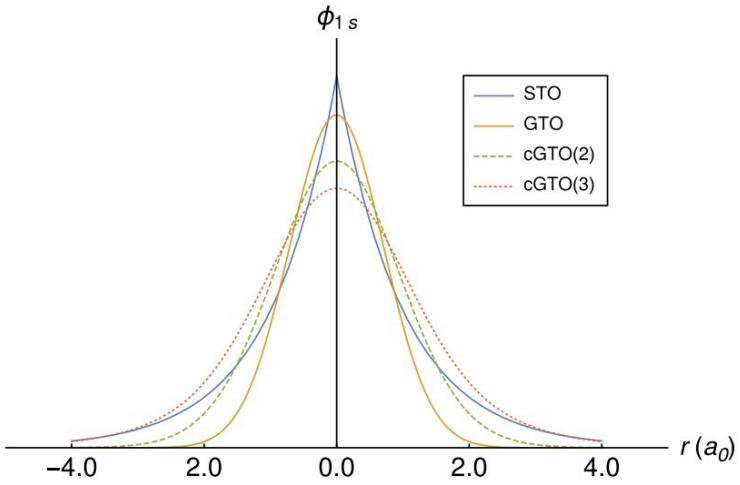

Figure 3.4.: Slater-type orbitals depicted by a linear combination of three Gaussian-type orbitals

The basis set may be classified on the number of functions implemented to characterizing each AO. For description of valence shell orbitals, more functions are commonly employed as the tend to ascribe most of the chemical reactivity. The number of functions employed to express the valence orbitals relative to the minimum biases set is expressed to the exponential factor ς . As a result, if the double functions are employed, the basis set will be referred to as double- ς. Moreover, the flexibility of the valence orbitals to account for atoms possessing loosely bound electrons (e.g. anions, metals) and the description of inhomogeneously charged atoms (e.g.

electronegative) may be introduced by the addition of small ζ exponent (diffuse functions) and by functions with higher angular momentum (polarization functions).The STO notation normally takes the initial letter of the basis set quality and adds a "P" if polarisation functions are added, so DZP signifies a double-s basis set with one polarisation function added whilst, TZ2P triple-ζ plus with two polarisation functions, and so on. In GTOs of the People-style, the first number signifies the number of primitive (Gaussian) orbitals that characterize the electrons within the inner core, and the following numbers represent the primitives of each valence orbital. Furthermore, when polarisation functions for heavy atoms are included, a single (or double) "*" is also included in the designation, whereas a single (or double) "+" will specify the addition of diffuse functions for heavy atoms. As a result, a 6-311*+ denotes six Gaussian orbitals representing each basis set function for core electrons, a triple split valence shell with three Gaussian orbitals defining each valence basis function, and diffuse functions and additional polarization on heavy elements[50,53-57].

In terms of chemical relevancy, the core electrons are less essential than valence shell electrons. The FC approximation may be implemented to reduce the computational cost of treating core electrons in systems involving elements from the third row (heavy elements) by treating the core electrons via an accurate single-atom calculations using large STOs and subsequently orthogonalizing against valence orbitals. The yielded frozen core density is then factored into the molecular computation[55,57-58].

3.5. Including the solvent effects in quantum chemistry

The preceding paragraphs aim to describe several ways to calculate the energy of the various molecules involved in the system under this thesis. The majority of biological and chemical reactions proceed in the presence of a solvent. To obtain the full image of the system, the presence of solvent must be considered as it might be imperative to the reaction outcome. The solvent effect might directly or indirectly change the outcome of the reaction. When a molecule's structure is optimised, the optimisation outcome will depend on the phase. It is important to note that the interaction between the solvent molecules and the solute will induce the solute's electronic and structural relaxation, allowing for a reciprocal polarisation and higher charge separation between the solvent molecules and the solute. In computational chemistry, two approaches are

commonly used to model solvent behaviour. The first approach for assessing solvent effects is considering a solvent shell or individual molecules around the solute. Using this method, we can obtain information about the structural impact, cavitation energy and solvation energy. In this approach, the increased number of molecules included will increase the degrees of freedom, increasing the calculation time and raising the computational cost.

Additionally, this method also presents the problem of how many and where should these additional molecules be positioned to depict the image. Methods based on Monte-Carlo and molecular dynamics can be implemented to overcome this issue. Thus, this approach is used only in specific cases in which the solvent plays an active role.

The alternative approach for modelling solvent behaviour is called the implicit method. This method is also known as the *continuum method*, as it considers the solvent molecules as a continuous medium. *The Self-Consistent Reaction Field* (SCRF)[64] is arguably the most extensively used approach of this sort, which views the solute placed in an appropriately shaped hole in the medium and the solvent as a uniform polarisable media with a dielectric constant ε. This approach is also known as the polarised continuum model (PCM).[65]

Until the solvent and solute attain self-consistency by mutual polarisation, this procedure is performed recursively with *ab initio* methods, and it is defined by the degree of perturbation exerted by the solvent on the QM Hamiltonian.

$$H^{tot}(r_s) = H^{mol}(r_s) + V^{mol+solv}(r_s) \qquad (2.69)$$

The term $V^{mol+solv}$ in the above expression includes the interaction operators needed to characterise the system response caused by switching the solute from the gas phase into a continuum medium.

On the other hand, in the PCM approach, the solvation "free energy" can be estimated as a total of different energy contributions.

$$\Delta G_{solvation} = \Delta G_{electrostatic} + \Delta G_{dispersive} + \Delta G_{repulsive} + \Delta G_{cavity} \qquad (2.70)$$

It is important to note that despite the $\Delta G_{solvation}$ term being generally considered as a Gibbs energy, in its core, it is not as the entropic terms are disregarded. In

the above equation, the term $\Delta G_{electrostatic}$ encompasses the electrostatic interaction between the solvent and the solute. The second term in the equation $\Delta G_{dispersive}$ is linked to the dispersive interactions between the solvent and the solute. Additionally, this term is favourable to the solvation. On the contrary, $\Delta G_{repulsive}$ incorporates the repulsive interaction between the solvent and solute and is always positive. Lastly, the term ΔG_{cavity} is a positive term as it correlates to the energy cost required for creating the cavity for the solute.

The SCRF model encompasses different models which depend on[12]:

- by means of which the shape and the size of the cavity are defined,
- how the dispersion contributions are calculated,
- how the charge distribution of the solvate is represented,
- how the solute is treated with *ab initio* or empirically
- how the dielectric medium is described.

Throughout this thesis, I only used the *Solute Electron Density* (SMD) model.[66] The advantage of using this model is that in its basis, it incorporates the radii and non-electrostatic factors as proposed by Truhlar and coworkers, while the solute cavity is defined as an integration of a series of overlapping spheres , centred on the atoms.

A combination of continuum and discrete approaches provides a fair balance between a comprehensive description of solvent effects and computing expense. Combining these strategies, for instance, would involve treating the outer sphere via a continuum method while explicitly considering the first solvation sphere. This method is commonly known as *discrete-continuum* method, and it was commonly utilised in this thesis to test our systems' dependency on explicit molecules.

3.6. Methodology employed in the following chapters

The DFT calculations for **Chapters 4** and **5** were done with the Gaussian16 Rev B.01 software and the hybrid density functional B3LYP. The difference in DFT methods for **Chapter 6** will be discussed at the beginning of said chapter. This functional was picked since it has been shown to produce favourable outcomes for organic

systems and non-covalent interactions. We implemented GD3BJ to take into consideration for empirical dispersion within the system.

All the atoms in the geometry optimisations were defined using the conventional 6-31G(d) basis, corresponding to BS1. All the geometries for the reactants, products, intermediates, and the transition states were optimised without any restrictions. A vibrational analysis was performed within the harmonic approximation to characterise the nature of these stationary sites. Minima were recognised more specifically by possessing an all-positive frequency set, whilst transition states by possessing one imaginary frequency. The postulated reaction pathways were double-checked by linking transition states to the respective reactants and products based on the displacement of the imaginary frequency.

Potential energies were estimated for the optimised geometries using single point calculations and the electron basis set Def2TZVP ((Valence triple-ζ) for all atoms. In our calculations, this basis was labelled as BS2. At a temperature of 298.15 K, the relative Gibbs energies were computed by combining the zero-point energy (ZPE) and the vibrational, rotational, and translational entropic contributions for all optimised configurations with BS1 and the potential energies derived with BS2.

The solvent effect in this chapter was incorporated by implementing the continuum model more concretely the SMD model for the THF solvent (ε = 7.4257). The solvent effect on this reaction was checked by repeating the first step of the postulated reaction mechanism either 2 or 4 explicit molecules of the solvent depending on the reaction in question. We were able to confirm a difference of less than 1 kcal mol^{-1} in both instances, thus no explicit molecules were used in further calculations. However, it should be noted that we used explicit molecules

The difference in the Gibbs energies in THF (ΔG) at 298 K showcased throughout this chapter were calculated via the proceeding equation:

$$\Delta G = E(BS2) + G(BS1) - E(BS1) + \Delta G^{1atm \rightarrow 1M}$$

It is worth noting that the switch from the standard gas phase (1 atm) to solution (1 M) at 298.15K was accounted for by applying a 1.9 kcal adjustment to all Gibbs values. The software CYL-view was used to create the 3D photos.

Bibliography

1. Griffiths, D. J. & Schroeter, D. F. *Introduction to quantum mechanics*. (Cambridge University Press, 2018).
2. Heisenberg, W. Über den anschaulichen Inhalt der quantentheoretischen Kinematik und Mechanik. *Z. Physik* **43,** 172–198 (1927).
3. Bitbol, M. *Schrödinger's Philosophy of Quantum Mechanics*. (Springer Netherlands, 1996).
4. Atkins, P. W. & De Paula, J. *Physical chemistry*. (W.H. Freeman, 2010).
5. Bader, R. F. W. A quantum theory of molecular structure and its applications. *Chem. Rev.* **91,** 893–928 (1991).
6. Schlegel, H. B. Exploring potential energy surfaces for chemical reactions: An overview of some practical methods. *J Comput Chem* **24,** 1514–1527 (2003).
7. Gasser, R. P. H. & Richards, W. G. *An introduction to statistical thermodynamics*. (World Scientific, 1995).
8. McQuarrie, D. A. *Statistical mechanics*. (University Science Books, 2000).
9. Zhou, H.-X. & Gilson, M. K. Theory of Free Energy and Entropy in Noncovalent Binding. *Chem. Rev.* **109,** 4092–4107 (2009).
10. Spickermann, C. in *Entropies of Condensed Phases and Complex Systems* 1–3 (Springer Berlin Heidelberg, 2011).
11. Harvey, J. *Computational chemistry*. (Oxford University Press, 2018).
12. Cramer, C. J. *Essentials of computational chemistry: theories and models*. (Wiley, 2014).
13. Wertz, D. H. Relationship between the gas-phase entropies of molecules and their entropies of solvation in water and 1-octanol. *J. Am. Chem. Soc.* **102,** 5316–5322 (1980).
14. Becke, A. D. Perspective: Fifty years of density-functional theory in chemical physics. *J. Chem. Phys.* **140,** 18A301 (2014).
15. Burke, K. Perspective on density functional theory. *The Journal of Chemical Physics* **136,** 150901 (2012).
16. Martin, R. L., Hay, P. J. & Pratt, L. R. Hydrolysis of Ferric Ion in Water and Conformational Equilibrium. *J. Phys. Chem. A* **102,** 3565–3573 (1998).
17. Poli, R. & Harvey, J. N. Spin forbidden chemical reactions of transition metal compounds. New ideas and new computational challenges. *Chem. Soc. Rev.* **32,** 1–8 (2003).
18. Pracht, P. & Bannwarth, C. Fast Screening of Minimum Energy Crossing Points with Semiempirical Tight-Binding Methods. *J. Chem. Theory Comput.* **18,** 6370–6385 (2022).
19. Harvey, J. N., Aschi, M., Schwarz, H. & Koch, W. The singlet and triplet states of phenyl cation. A hybrid approach for locating minimum energy crossing points between non-interacting potential energy surfaces. *Theoretical Chemistry Accounts: Theory, Computation, and Modeling. Theor. Chim. Acta* **99,** 95–99 (1998).
20. Cohen, A. J., Mori-Sánchez, P. & Yang, W. Challenges for Density Functional Theory. *Chem. Rev.* **112,** 289–320 (2012).
21. Hohenberg, P. & Kohn, W. Inhomogeneous Electron Gas. *Phys. Rev.* **136,** B864–B871 (1964).
22. Thomas, L. H. The calculation of atomic fields. *Math. Proc. Camb. Phil. Soc.* **23,** 542–548 (1927).
23. Lieb, E. H. & Simon, B. The Thomas-Fermi theory of atoms, molecules and solids. *Adv. Math.* **23,** 22–116 (1977).
24. Lieb, E. H. in *The Stability of Matter: From Atoms to Stars* (ed. Thirring, W.) 191–230 (Springer Berlin Heidelberg, 1991).
25. Kohn, W. & Sham, L. J. Self-Consistent Equations Including Exchange and Correlation Effects. *Phys. Rev.* **140,** A1133–A1138 (1965).

26. Geerlings, P., De Proft, F. & Langenaeker, W. Conceptual Density Functional Theory. *Chem. Rev.* **103,** 1793–1874 (2003).
27. Perdew, J. P. Jacob's ladder of density functional approximations for the exchange-correlation energy. in *AIP Conference Proceedings* **577,** 1–20 (AIP, 2001).
28. *Genesis XXVIIIc.12v*.
29. Ceperley, D. M. & Alder, B. J. Ground State of the Electron Gas by a Stochastic Method. *Phys. Rev. Lett.* **45,** 566–569 (1980).
30. Vosko, S. H., Wilk, L. & Nusair, M. Accurate spin-dependent electron liquid correlation energies for local spin density calculations: a critical analysis. *Can. J. Phys.* **58,** 1200–1211 (1980).
31. Becke, A. D. Density-functional exchange-energy approximation with correct asymptotic behavior. *Phys. Rev. A* **38,** 3098–3100 (1988).
32. Zhao, Y., Schultz, N. E. & Truhlar, D. G. Exchange-correlation functional with broad accuracy for metallic and nonmetallic compounds, kinetics, and noncovalent interactions *.J. Chem. Phys* **123,** 161103 (2005).
33. Yanai, T., Tew, D. P. & Handy, N. C. A new hybrid exchange–correlation functional using the Coulomb-attenuating method (CAM-B3LYP). *Chem. Phys. Lett.* **393,** 51–57 (2004).
34. Katriel, J., Roy, S. & Springborg, M. Nonuniversality of commonly used correlation-energy density functionals. *J. Chem. Phys.* **124,** 234111 (2006).
35. Lee, C., Yang, W. & Parr, R. G. Development of the Colle-Salvetti correlation-energy formula into a functional of the electron density. *Phys. Rev. B* **37,** 785–789 (1988).
36. JP Perdew, P Ziesche, H Eschrig. Electronic structure of solids' 91 *Akademie Verlag, Berlin* (1991).
37. Dobson, J. F., Vignale, G. & Das, M. P. *Electronic Density Functional Theory: Recent Progress and New Directions*. (Springer, 2013).
38. Perdew, J. P., Chevary, J. A., Vosko, S. H., Jackson, K. A., Pederson, M. R., Singh, D. J. & Fiolhais, C. Atoms, molecules, solids, and surfaces: Applications of the generalized gradient approximation for exchange and correlation. *Phys. Rev. B* **46,** 6671–6687 (1992).
39. Perdew, J. P., Burke, K. & Wang, Y. Generalized gradient approximation for the exchange-correlation hole of a many-electron system. *Phys. Rev. B* **54,** 16533–16539 (1996).
40. Perdew, J. P., Kurth, S., Zupan, A. & Blaha, P. Accurate Density Functional with Correct Formal Properties: A Step Beyond the Generalized Gradient Approximation. *Phys. Rev. Lett.* **82,** 2544–2547 (1999).
41. Zhao, Y., Lynch, B. J. & Truhlar, D. G. Development and Assessment of a New Hybrid Density Functional Model for Thermochemical Kinetics. *J. Phys. Chem. A* **108,** 2715–2719 (2004).
42. Tao, J., Perdew, J. P., Staroverov, V. N. & Scuseria, G. E. Climbing the Density Functional Ladder: Nonempirical Meta–Generalized Gradient Approximation Designed for Molecules and Solids. *Phys. Rev. Lett.* **91,** 146401 (2003).
43. Van Voorhis, T. & Scuseria, G. E. A novel form for the exchange-correlation energy functional. *J. Chem. Phys.* **109,** 400–410 (1998).
44. Rey, J. & Savin, A. Virtual space level shifting and correlation energies. *Int. J. Quant. Chem.* **69,** 581–590 (1998).
45. Toulouse, J., Savin, A. & Adamo, C. Validation and assessment of an accurate approach to the correlation problem in density functional theory: The Kriger–Chen–Iafrate–Savin model. *J. Chem. Phys.* **117,** 10465–10473 (2002).
46. Jones, R. O. Density functional theory: Its origins, rise to prominence, and future. *Rev. Mod. Phys.* **87,** 897–923 (2015).

47. Rimola, A., Rodríguez-Santiago, L. & Sodupe, M. Cation−π Interactions and Oxidative Effects on Cu^{+} and Cu^{2+} Binding to Phe, Tyr, Trp, and His Amino Acids in the Gas Phase. Insights from First-Principles Calculations. *J. Phys. Chem. B* **110,** 24189–24199 (2006).
48. Becke, A. D. Density-functional thermochemistry. III. The role of exact exchange. *J. Chem. Phys.* **98,** 5648–5652 (1993).
49. Stephens, P. J., Devlin, F. J., Chabalowski, C. F. & Frisch, M. J. Ab Initio Calculation of Vibrational Absorption and Circular Dichroism Spectra Using Density Functional Force Fields. *J. Phys. Chem.* **98,** 11623–11627 (1994).
50. Zhao, Y. & Truhlar, D. G. Density Functionals with Broad Applicability in Chemistry. *Acc. Chem. Res.* **41,** 157–167 (2008).
51. Sun, Y. Y., Kim, Y.-H., Lee, K. & Zhang, S. B. Accurate and efficient calculation of van der Waals interactions within density functional theory by local atomic potential approach. *J. Chem. Phys* **129,** 154102 (2008).
52. Von Lilienfeld, O. A., Tavernelli, I., Rothlisberger, U. & Sebastiani, D. Optimization of Effective Atom Centered Potentials for London Dispersion Forces in Density Functional Theory. *Phys. Rev. Lett.* **93,** (2004).
53. Sato, T., Tsuneda, T.Hirao, K. Van der Waals interactions studied by density functional theory. *Mol. Phys.* **103,** 1151–1164 (2005).
54. Grimme, S. Accurate description of van der Waals complexes by density functional theory including empirical corrections. *J Comput Chem* **25,** 1463–1473 (2004).
55. Grimme, S., Ehrlich, S. & Goerigk, L. Effect of the damping function in dispersion corrected density functional theory. *J Comput Chem* **32,** 1456–1465 (2011).
56. Grimme, S. Semiempirical GGA-type density functional constructed with a long-range dispersion correction. *J Comput Chem* **27,** 1787–1799 (2006).
57. Grimme, S., Antony, J., Ehrlich, S. & Krieg, H. A consistent and accurate *ab initio* parametrization of density functional dispersion correction (DFT-D) for the 94 elements H-Pu. *J. Chem. Phys.* **132,** 154104 (2010).
58. Furche, F. Molecular tests of the random phase approximation to the exchange-correlation energy functional. *Phys. Rev. B* **64,** 195120 (2001).
59. Langreth, D. C. & Perdew, J. P. Theory of nonuniform electronic systems. I. Analysis of the gradient approximation and a generalization that works. *Phys. Rev. B* **21,** 5469–5493 (1980).
60. Seidl, M., Perdew, J. P. & Kurth, S. Simulation of All-Order Density-Functional Perturbation Theory, Using the Second Order and the Strong-Correlation Limit. *Phys. Rev. Lett.* **84,** 5070–5073 (2000).
61. Yan, Z., Perdew, J. P. & Kurth, S. Density functional for short-range correlation: Accuracy of the random-phase approximation for isoelectronic energy changes. *Phys. Rev. B* **61,** 16430–16439 (2000).
62. Bao, J. L., Gagliardi, L. & Truhlar, D. G. Self-Interaction Error in Density Functional Theory: An Appraisal. *J. Phys. Chem. Lett.* **9,** 2353–2358 (2018).
63. Perdew, J. P. & Zunger, A. Self-interaction correction to density-functional approximations for many-electron systems. *Phys. Rev. B* **23,** 5048–5079 (1981).
64. Tomasi, J. & Persico, M. Molecular Interactions in Solution: An Overview of Methods Based on Continuous Distributions of the Solvent. *Chem. Rev.* **94,** 2027–2094 (1994).
65. Miertuš, S., Scrocco, E. & Tomasi, J. Electrostatic interaction of a solute with a continuum. A direct utilizaion of AB initio molecular potentials for the prevision of solvent effects. *Chem. Phys.* **55,** 117–129 (1981).

66. Marenich, A. V., Cramer, C. J. & Truhlar, D. G. Universal Solvation Model Based on Solute Electron Density and on a Continuum Model of the Solvent Defined by the Bulk Dielectric Constant and Atomic Surface Tensions. *J. Phys. Chem. B* **113,** 6378–6396 (2009).

Chapter 4: Alkali metal-mediated Pudovik reaction

This chapter is based on a manuscript that has been published: I. Bozhinovska, ; G. Ujaque; M. Westerhause; A.Lledós; Understanding alkali-metal driven hydrophosphorylation: mechanism and challenges in the Pudovik reaction, Catal. Sci. Technol., 2025, 15, 3888–3905.

Unless otherwise stated, I carried out all computational calculations, data analysis, discussions, and writing up of the conclusions on my own, with assistance from my supervisors.

4.1. Introduction

The combined computational and experimental study presented in this chapter aims to elucidate the reaction mechanism involved in the Pudovik reaction catalysed by alkali-metal based catalysts.[1] This research topic was initially introduced in **Chapter 1: Introduction**. Inspired by an experimental study conducted by Westerhausen and colleagues, our research endeavours to propose a plausible reaction mechanism and to determine the influence of the alkali cation and the nature of the P-bound group on the outcome of the Pudovik reaction.[2] To achieve this, we conducted a variety of additional experiments and employed Density Functional Theory (DFT) calculations. The original experimental results are summarized in **Section 4.1.1**, with detailed data provided in **Tables 4.1** and **4.2.** In this study, they suggest that the nature of the cation is pivotal in determining the outcome of the reaction, and they assert that the specific R substituent present on the di(organyl)phosphinites also influences the reaction outcome.

The nature of the active species plays a crucial role in the catalytic outcome.[3,4] Specifically, the choice of alkali cation exerts a significant influence on the activity of the active species. While much research has been dedicated to elucidating the reaction pathways for transition metal-based catalysts in the Pudovik reaction, the scientific community has yet to establish a definitive mechanism for the majority of alkali-catalysed reactions, including the one described here. [3,5–10] Thus far, for Pudovik reaction diverse catalysts have been examined as per example: K-HMDS (HMDS = hexamethyldisilazane), Al_2O_3/KOH, rhodium(I), nickel and bases in general. Notably, the formation of observed products and their by-products in the presence of air may be attributed to radical mechanisms. [11–18] Whilst writing this chapter Westerhausen *et al.* proposed, from labelling experiments and DFT calculations, a mechanism for the reaction of trimethylsilyl (TMS) acetylene with potassium di(aryl)phosphinite, prepared by metallation of a secondary phosphineoxide with potassium hexamethyldisilazanide at room temperature.[11] This work does differentiate from ours as the TMS group, which is prominently featured in their mechanism, is an easy leaving group, that has a tendency to not react in a similar manner to the aryl and alkyl groups studies in this thesis.

Our objectives in this thesis were to utilize computational approaches to investigate the plausibility of the suggested mechanism for alkali metal-mediated Pudovik reactions.[2] Additionally, we aimed to analyse alternative pathways and various factors that might influence the outcome of these reactions. Furthermore, we focused on assessing how variations in the tested alkynes might impact the stereo- and regio-selective outcomes through DFT calculations.

In this chapter, our primary focus was on conducting DFT calculations to elucidate the mechanism according to the published experimental data.[2] We firstly analysed the formation and deactivation of the active species. Afterwards, we delved into examining the modes of interaction between the active species and phenylacetylene. Following this, we proceeded to analyse the proposed reaction mechanism involving alkali cations (Li, Na, and K) and various di(organyl)phosphineoxides (organyl = Mes, Ph, OEt, and Cy).

4.1.1. Experimental Section

As previously mentioned, all the experiments for this particular part were performed in the research group of Prof. Westerhausen at Friedrich-Schiller-Universität and published in the paper “Scope and Limitations of the s-Block Metal-Mediated Pudovik Reaction”.[2] The reactions (**Scheme 4.1**) between di(organyl)phosphineoxides and phenylacetylene with 5% alkali metal based bis(trimethylsilyl)amides (M-HMDS) as catalysts were carried out at room temperature in THF.

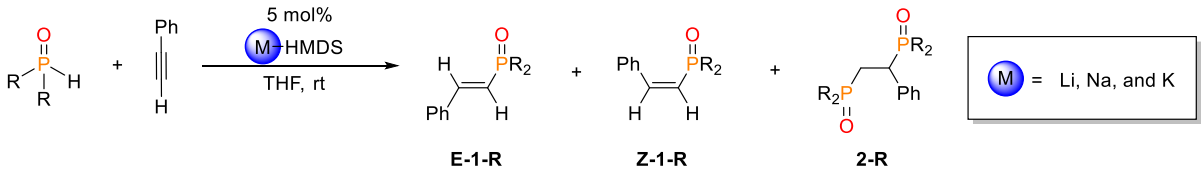

Scheme 4.1: Alkali metal-mediated hydrophosphorylation of phenylacetylene with di(organyl)phosphineoxides (R = Mes, Ph, OEt and Cy) *via* M-HMDS (M = Li, Na, and K) depicting the possible products.

The Pudovik reaction exhibited a notable dependency on both the P-bound substituent and the nature of the s-block metal. Notably, regardless of the P-bound

group and the alkali meal utilised the yielded product possessed anti-Markovnikov regioselectivity. The influence of alkali metals from the utilized alkali metal bis(trimethylsilyl)amide complexes is summarized in **Table 4.1**, while the impact of the P-bound substituent is detailed in **Table 4.2.** Consequently, varying ratios of products and different conversion rates were observed depending on the alkali metal utilised in the experiment and the P-bound substituent. It is important to note that the conversion into products was assessed in the initial study by monitoring the decline of the phosphineoxide using ^{31}P NMR spectrum integration, and the product ratio was calculated accordingly.

Comparing the three alkali cations in the case of P-bound mesityl group, the following conclusions can be drawn: The smaller metal-based catalyst (Li-HMDS) was not able to mediate the reaction within 1h. However, after 27 hours a conversion of 8% was detected with 5/1 ratio for E/Z isomers. In contrast, catalysts based on heavier alkali metals such as Na and K were able to mediate the reaction within 1h with 31% and 95% conversion rate respectively. This resulted in the formation of E and Z isomers in 3/1 ratio for both mediated reactions. Interestingly, the ratio for the potassium mediated reaction only slightly changed from 3/1 to 5/1 for E/Z upon 27 hours. However, in the case of sodium-catalysed hydrophosphorylation, a notable change was observed. After approximately one day, the resonance of the **Z-1-Mes** disappeared nearly completely, resulting in a yield of 7.5% of **2-Mes** and a 92.5% E/Z ratio, equivalent to a 31/1 ratio of E/Z isomers. In the initially study they proposed that this behaviour indicates that the **Z-1-Mes** is a kinetically favoured product of the reaction with lower stability, whilst the **E-1-Mes** is the thermodynamically favoured product with a significantly increased stability. The change in the E/Z ratio it has also been ascribed in the this study to a greater steric strain in the **Z-1-Mes** compared to the **E-1-Mes**.[2] They suggest that consequently, the double hydrophosphorylation step is likely to primarily occur on the **Z-1-Mes** compound to reduce steric strain, thereby producing the less hindered 2-Mes and lowering the concentration of **Z-1-Mes**.

Table 4.1.: Dependency of the Pudovik reaction (addition of dimesitylphosphineoxide across phenylacetylene) on the alkali metal of the utilised bis(trimethylsilyl)amide catalyst.

Entry	Metal	After 1h		After 27 h	
		Conv. [%]	E/Z	Conv. [%]	E/Z
1	Li	0	-	>8	5/1
2	Na	31	3/1	>99	31/1[a]
3	K	93	3/1	>99	5/1

[a] The quantity of **Z-1-Mes** is reduced because of a preferred second Na-mediated hydrophosphorylation that yields **2-Mes**.

After discussing the influence of the alkali cation on the hydrophosphorylation reaction across phenylacetylene, let's now delve into the influence of the P-bound group in the potassium mediated reaction. In the instance of dimesitylphosphineoxide the hydrophosphorylation generated only phenylethenyl-dimesitylphosphineoxide (styryl-di(mesityl)phosphineoxide or **1-Mes** (**entry 1** from **Table 4.2**) of *E*/*Z*-ratio of 83/17. When one mesityl substituent was substituted with a phenyl, the reaction rate decreased, leading to a drop in conversion from 93% to 76% after 1 hour (**entry 2**, **Table 4.2)**, with no observed formation of the Z isomer. Additionally, double-hydrophosphorylated phenylacetylene **2-Ar** was detected as the major product upon 27h in this case. Substitution of all mesityl P–bound substituents with phenyl fast-tracks the second hydrophosphorylation up to the point that **1-Ph** products were observed with less than 1% conversion whilst, **2-Ph** product was observed with almost 99% conversion regardless of the incomplete conversion (**entry 3**). Under these circumstances, potassium-mediated hydrophosphorylation of phenylacetylene *via* alkyl (**entry 4**) and alkoxide P - bound substituents (**entry 5**) is inhibited.

Table 4.2.: Dependency of the hydrophosphorylation across phenylacetylene on the P-bound group of the di(organyl)phosphineoxide, using K-HMDS as catalyst.

Entry	P-bound group (R)	After 1h			After 22 h		
		Conv. [%]	1-Ar (E/Z)	2-Ar	Conv. [%]	1-Ar (E/Z)	2-Ar
1	Mes	93	100 (83/17)	0	>99	100 (83/17)	0
2	Mes/Ph	76	36 (100/0)	64	>99	16 (100/0)	84
3	Ph	14	<1	>99	36	<1	>99
4	Cy	0	/	/	0	/	/
5	OEt	0	/	/	0	/	/

It should be noted that the experimental results were summarized initially as they were conducted first and published. Therefore, the experimental and computational studies were not conducted simultaneously. In the next sections, we will discuss the theoretical findings conducted in this study in conjunction with the experimental results.

4.1.2. Computational Section

As a result of the varying outcomes in reactions, which are influenced by the choice of alkali cation and the specific P-bound group, we decided to perform a theoretical exploration to understand the factors governing these reactions.

4.1.2.1. Proposed mechanism for the Pudovik reaction

To elucidate the experimental results, we started the Density Functional Theory (DFT) investigations with the proposed mechanism outlined in the initial study.[2] The postulated reaction mechanism on which the computational study is based is depicted in **Scheme 4.2** Metallation of di(organyl)phosphineoxide by M-HMDS of the alkali metals would be the initial step, i.e. the formation of the active species, the alkali metal diorganyl phosphinites (M-OPR_2). The ensuing step is a nucleophilic attack from the phosphorous atom of M-OPR_2 (active species) across the C≡C functional group, with the following step being protonation of this intermediate with a proton coming from an

additional molecule of R_2-P(O)H. This step regenerates M-OPR_2 and produces *E*/*Z*-mixtures of mono-phosphorylated **1-R**. Experimentally, this addition yields only anti-Markovnikov product, thus regioselectivity is decided in this first step. The experimental finding reveals that a second phosphinite will be added to the newly formed hydrocarbon moiety as it is still highly reactive yielding bis-phosphorylated compounds, only in the instance in which the C=C double bond may be activated again. It is known fact that the activation of C=C double bond necessitates more energy.[19] The addition of the second moiety will be dependent on the P-bound substituent on the phosphineoxide and on the alkali cation present in the active species. The following and last step is another protonation step generating **2-R**. It has been established experimentally that bis-phosphorylated **2-R** will precipitate from the reaction mixture.[2] Consequently, it will not impede the equilibrium by interconverting back to **1-R**. M-$OPAr_2$ molecules formed as side products in the protonation steps can be used again in the following catalytic cycle.

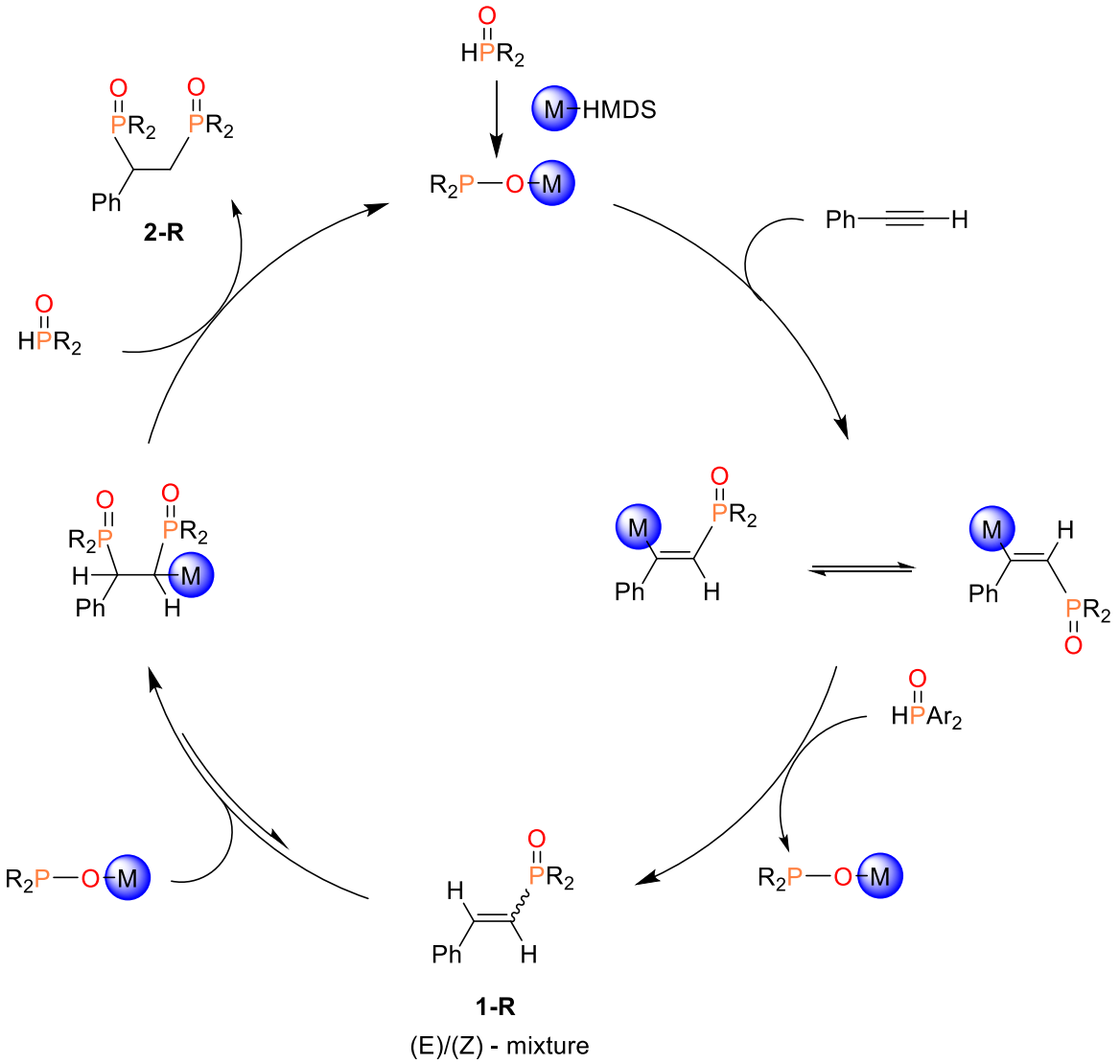

Scheme 4.2: Proposed mechanism for the formation of the **1-R** and the subsequent 2,3-bisphosphorylated compounds adapted from ref.2.

Prior to delving into the exploration of the mechanism, we first investigated the prototropic tautomerism inherent in phosphinylidene compounds to clarify the nature of the active species. Following this preliminary exploration will allow as to assess the thermodynamic feasibility for formation of the alkali metal phosphinites M-OPR$_2$, which serve as the active species.

4.1.2.2. Prototropic tautomerism within phosphinylidene compounds

Phosphinylidene compounds tend to exist in two species: P(V) and P(III).[20] The so-called P(V) form $1A_1$ /$1A_2$ is almost invariably the most stable species although in case of strong electron acceptors the less stable P(III) form B may become the more stable species (**Scheme 4.3**).[20,21] A recent experimental and computational study by Montchamp *et al.* on this tautomerism indicated that the direct P,O-proton transfer would proceed through a strained three-membered ring, *via* unaffordable reaction barrier.[22] This tautomerism requires catalysis by a proton shuttle, such as a water molecule to ensue. The gas-phase calculation for the diphenylphosphineoxide favoured the P(V) P-H form by 6.8 kcal mol^{-1} with an energy barrier of 30.8 kcal mol^{-1} which was computed assuming catalysis by a single H_2O molecule. We also computed Gibbs energy difference between both isomers as 10.2 kcal mol^{-1} in THF also in favour of the P(V) tautomer. Hence, it can be concluded that the predominant species in our solution will be the A_1/A_2 configuration with absence of B configuration. Consequently, all further calculations will be conducted with the A configuration of the Ar_2-P(O)H reagent.

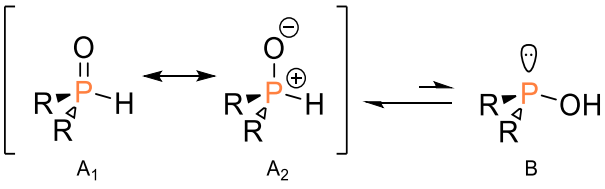

Scheme 4.3: Prototropic tautomerism within phosphinylidene compounds.

4.1.2.3. Formation and deactivation of active species

Alkali metal diorganylphosphinites (M-OPR_2) are the active species in the Pudovik reaction. As per the published study, the alkali metal diarylphosphinites M-OPR_2 were prepared in situ by metallation of R_2-P(O)H with the hexamethyldisilazane complexes of the alkali metals. Overall, the formation of the metal-phosphinites (active species) from the corresponding M-HMDS catalysts and R_2-P(O)H can be described

by **reaction 1.** However, speciation and solvation of M-HMDS and M-OPR_2 species in solution is a major issue.

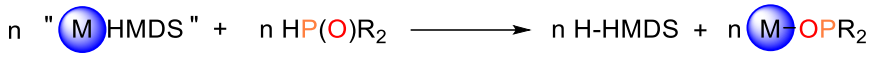

(1)

For these calculations we also took into consideration the aggregation states of M-HMDS in THF. Alkali cation hexamethyldisilazane reagents display a complex relationship of solvation and aggregation. A variety of M-HMDS aggregates have been characterized in solid state by X-ray diffraction analysis, both unsolvated and solvated by several solvent molecules. Unsolvated Li-HMDS is known to be a trimer in the solid state, although disolvated dimers and solvent coordinate monomers have been also structurally characterized.[23,24] Solid state structure of Na-HMDS is also a trimer, while X-ray structures of solvated homoleptic K-HMDS aggregates are dimeric.[25,26] Solution structures are highly solvent dependent. In THF solvent, Li-HMDS has been described as a dimer-monomer mixture [27] Two recent papers have analysed aggregation and solvation in Na- and K-hexamethyldisilazide in a number of solvents.[25,26] These thorough studies showed a dominance of disolvated dimers in monofunctional solvents of intermediate donicity, as THF. For this reason, and for the sake of comparison between the three alkali-cations, we have considered disolvated dimeric M-HMDS structures to compute the thermodynamics of the formation of M-OPR_2 species in THF solution (see below **Scheme 4.4**). [26,28–30] Although a crystal structure of K-HMDS showed only bis-THF solvated dimer, tetrasolvated dimers have been proposed in THF solution and for potassium we have also considered the tetrasolvated dimer as initial state of K-HMDS.[25,30] We have verified that steric constraint hampers the stabilization of such dimers for the Na- and Li-HMDS**. Figure 4.1** displays the optimised structures in THF of M-HMDS reagents.

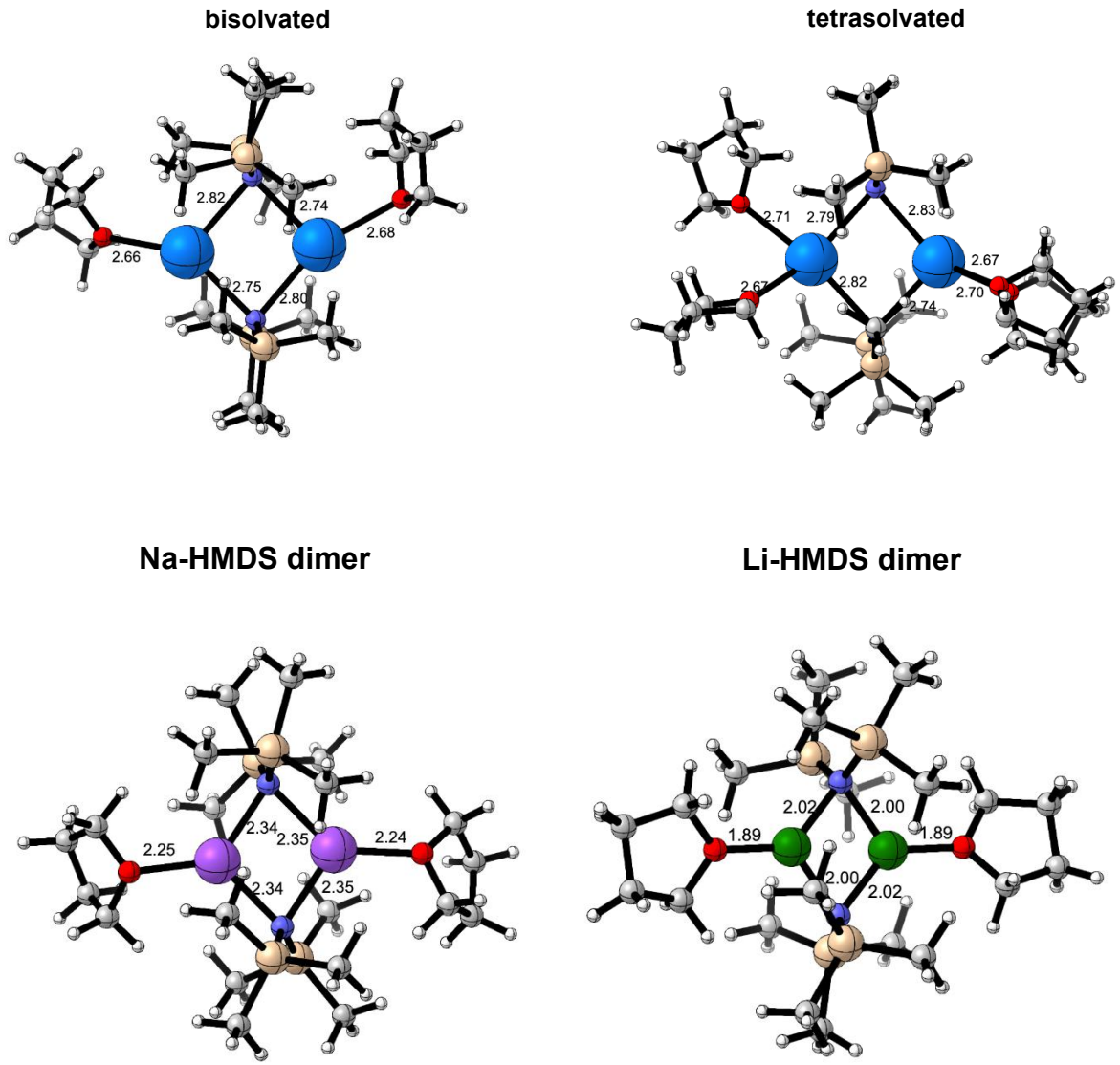

Figure 4.1.: Optimised structures in THF solution of M-HMDS reagents considered in the computational study. The distances presented are given in Å.

To get a deeper insight into the formation of the active species we have analysed the two steps that yield M-OPR$_2$ from M-HMDS and R$_2$P(O)H: i) the disaggregation of the disolvated dimeric M-HMDS (step 1), and ii) deprotonation of the phosphineoxide by monomeric M-N(SiMe$_3$)$_2$ (step 2) (see **Scheme 4.4**).

For the step 1, we calculated ΔG_R values of 18.8, 22.3, and 16.6 kcal mol^{-1} for the disaggregation of disolvated K, Na, and Li M-HMDS dimers, respectively. For potassium, starting from the tetrasolvated dimer, the computed ΔG_R is 17.1 kcal mol^{-1}.

Additionally, a value of 15 kcal mol^{-1} for the non-solvated dimer at 195 K has been recently reported.

Regarding step 1, we have computed ΔG_R of 18.8, 22.3 and 16.6 kcal mol^{-1}, respectively, for the disaggregationof K, Na and Li disolvated M-HMDS dimers. For potassium, taking as starting structure the tetrasolvated dimer the computed ΔG_R is 17.1 kcal mol^{-1}. For the non-solvated dimer a computed value of 15 kcal mol^{-1} at 195 K has been recently reported.[25] With these values ΔG_R disaggregationseems to be thermodynamically hindered. Experimentally, dimers are found at low solvent concentrations, but at elevated THF concentrations dimer-to-monomer disaggregationhappens. [24,25]

The previous ΔG_R arise from a description of the monomeric species as monosolvated adducts, that would be the situation at very low concentrations of solvent.

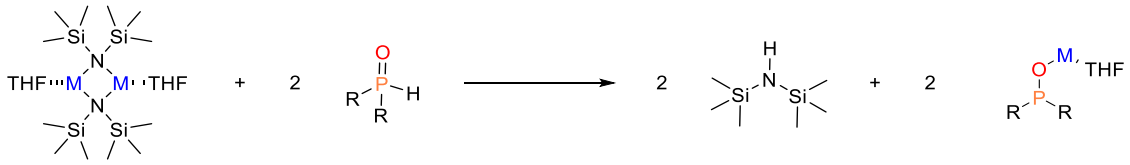

Step 1

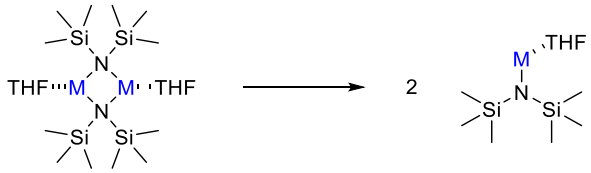

Step 2

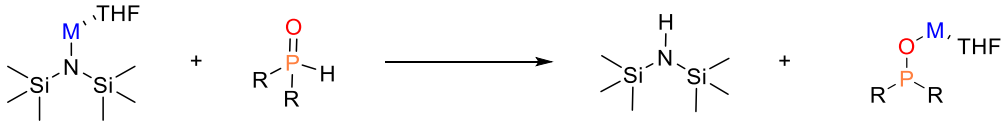

Scheme 4.4: General scheme for the two steps involved in the generation of active species M-OPR_2 (M = Li, Na and K; R = Mes; For M = K and R = Mes, Ph, OEt, and Cy).

At higher solvent concentration tetrasolvated $(THF)_4$-M-HMDS monomers have been proposed to be the most abundant species in solution. Describing the

disaggregationstep as in **Scheme 4.5** very different ΔG_R values of -18.3 kcal mol^{-1} (K, disolvated dimer), -1,5 kcal mol^{-1} (K, tetrasolvated dimer), -12.8 kcal mol^{-1} (Na) and 1.0 kcal mol^{-1} (Li) are obtained. Thus, solvation of monomers is the driving force displacing the reaction toward deaggregation. In these calculations we have employed a cluster model of $(THF)_4$ for disolvated dimers and $(THF)_6$ for tetrasolvated K-dimer) to describe the solvent molecules that will coordinate to the monomer. We have already showed that this model gives reliable values for solvent coordination processes.[31] **Figure 4.2** depicts the optimised structures of the M-HMDS monomers.

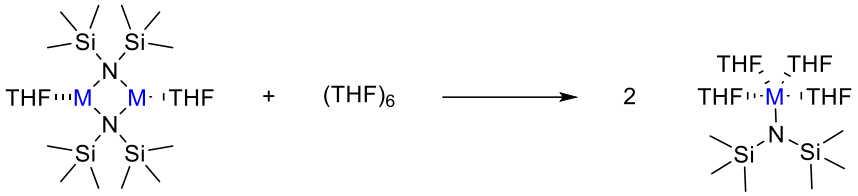

Scheme 4.5: Disaggregation of M-HMDS disolvated dimers to yield tetrasolvated monomers.

Taking into account the stabilization of the deaggregated monomer by tetrasolvation, breaking of the M-HMDs dimer is easy for potassium and sodium bis(trimethylsilyl) amides. However, for Li-HMDS disaggregation is much less favourable and the concentration of monomer in solution should be much smaller. This could be one reason for the lower efficiency of Li-HMDS in the Pudovik reaction (see **Table 4.1**).

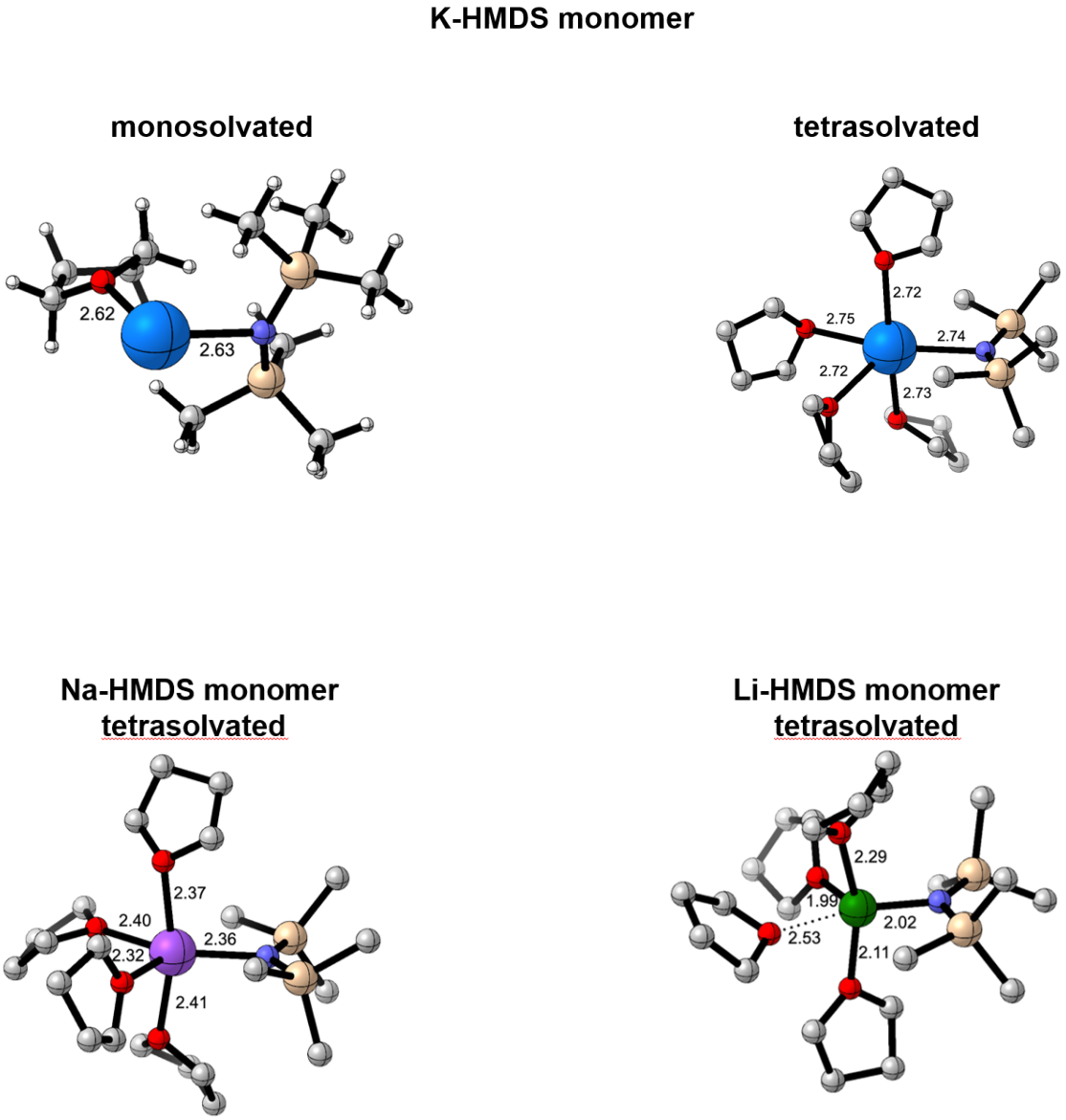

Figure 4.2.: Optimised structures in THF solution of M-HMDS monomers considered in the computational study. For K-HMDS mono- and tetrasolvated species are compared. C-H hydrogen atoms are omitted in tetrasolvated species for clarity reasons. The distances are given in Å.

In the second step of the reaction (**Scheme 4.4**), we also investigated how different P-bound groups affect the formation of the active species for M = K. We considered both monosolvated $(THF)_1$ and tetrasolvated $(THF)_4$ species. The results summarized in **Table 4.3** indicate that the impact of cation solvation on this proton transfer

reaction is significantly less pronounced compared to its effect on the disaggregation step.

Table 4.3.: Gibbs reaction (ΔG_R) and activation ($\Delta G^{\ddagger}$) energies (kcal mol^{-1}) for the proton transfer step (**step 2**, **Scheme 4.4**) of the generation of active species M-OPR$_2$ at the B3LYP-D3/def2-TZVP/SMD(THF)//B3LYP-D3BJ/6-31G(d,p)/SMD(THF) level of theory.

Entry	Metal	P-bound group (R)	ΔG_R		$\Delta G^{\ddagger}$
			$(THF)_1$[a]	$(THF)_4$[b]	
1	Li	Mes	-5.7	*-19.7*	16.6 *(17.3)*[b]
2	Na	Mes	-8.0	*-9.9*	11.7
3	K	Mes	-8.1	*-9.2*	11.2 *(9.5)*[b]
4	K	Mes/Ph	-8.1	*-9.3*	12.0
5	K	Ph	-11.7	*-13.1*	7.1
6	K	Cy	8.6	*7.8*	13.0
7	K	OEt	-15.3	*-13.6*	6.4

[a] Monosolvated species.

[b] Tetrasolvated species (numbers in italics).

Except for the M = Li case with a mesityl P-bound group (see **Table 4.3**, **entry 1**), the ΔG_R values for monosolvated and tetrasolvated species are comparable. Therefore, to simplify the calculations, we computed the Gibbs energy profiles and located all structures (intermediates and transition states) for the P-to-N proton transfer (**Scheme 4.6**) using monosolvated species. To ensure the accuracy of this simplification, we also computed the energy profile for the tetrasolvated species when M = Li and K cases, mesityl P-bound group (**Table 4.3**, **entries 1** and **3** respectively). The barriers ($\Delta G^{\ddagger}$) for both mono- and tetrasolvated species were found to be similar. The optimized structures for the M = K; R = Mes pathway are shown in **Figure 4.3**.

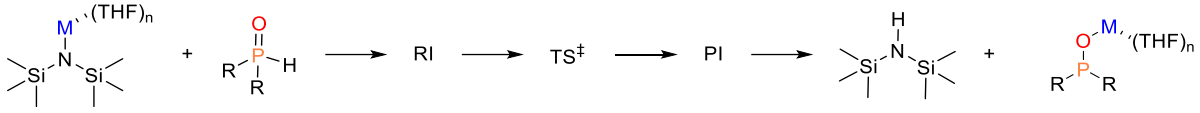

Scheme 4.6: General scheme for the proton transfer step in the formation of alkali metal diorganylohosphinites (M-OPR$_2$).

Coordinating the alkali metal to the oxygen atom of phosphineoxide in the initial intermediate **RI** places the P-H proton in the vicinity of the N-centre where it will be transferred (**Figure 4.3**).

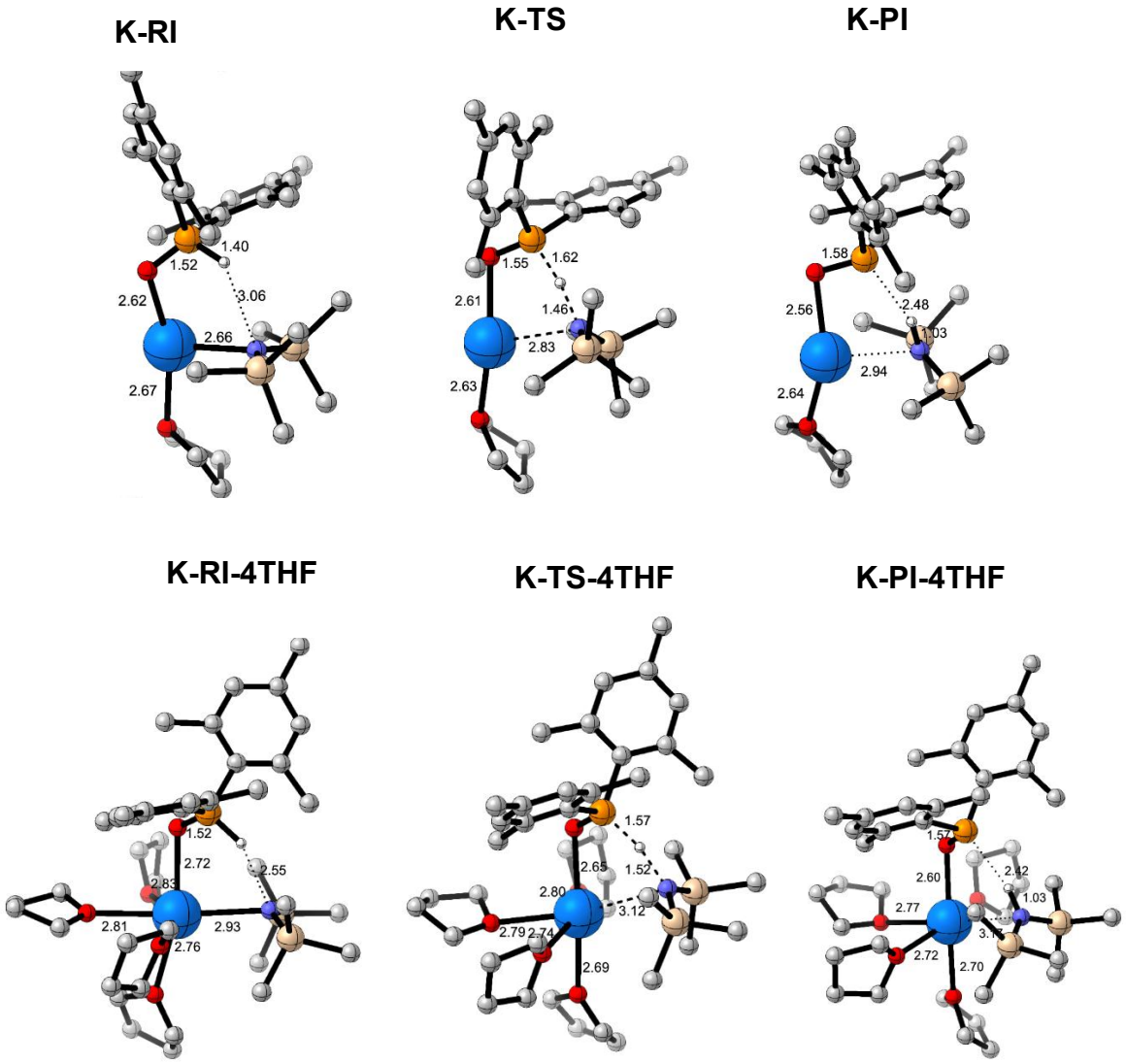

Figure 4.3.: Optimized structures of intermediates (**RI** and **PI**) and transition state (**TS**) in the proton transfer step for the generation of K-OPMes$_2$ with monosolvated (top) and tetrasolvated (bottom) structures. Certain hydrogen atoms are omitted for clarity reasons. The distances presented are given in Å.

Figure 4.4. A depicts the Gibbs energy profile for the three alkali cations (M = Li, Na, and K; with R = Mes) and **Figure 4.4.B** the influence of the P-substituent (M = K; R = Mes, Mes/Ph, Ph, Cy and OEt). For the three cations when the P-bound group is mesityl (R = Mes), the reaction is exergonic and proceeds with low energy barriers. However, the barrier for M = lithium is notably higher (16.6 kcal mol^{-1}) compared to sodium and potassium, which exhibit similar values (11.7 and 11.2 kcal mol^{-1}, respectively).

The reaction exhibits a strong dependency on the P-bound group of the phosphineoxide. Notably, with R = Cy, the process is highly unfavourable ($\Delta \mathbf{G_R}$ = 7.8 kcal mol^{-1}), indicating an inefficient stabilization of the resulting alkyl phosphinite. The unfeasibility of formation of K-$OPCy_2$ appears as the main reason for the inhibited of hydrophosphorylation with $Cy_2P(O)H$ (**Table 4.2**). Conversely, the reaction is highly exergonic with $(OEt)_2P(O)H$, although hydrophosphorylation does not proceed in this case either, suggesting an alternative reason for the lack of reactivity in this case.

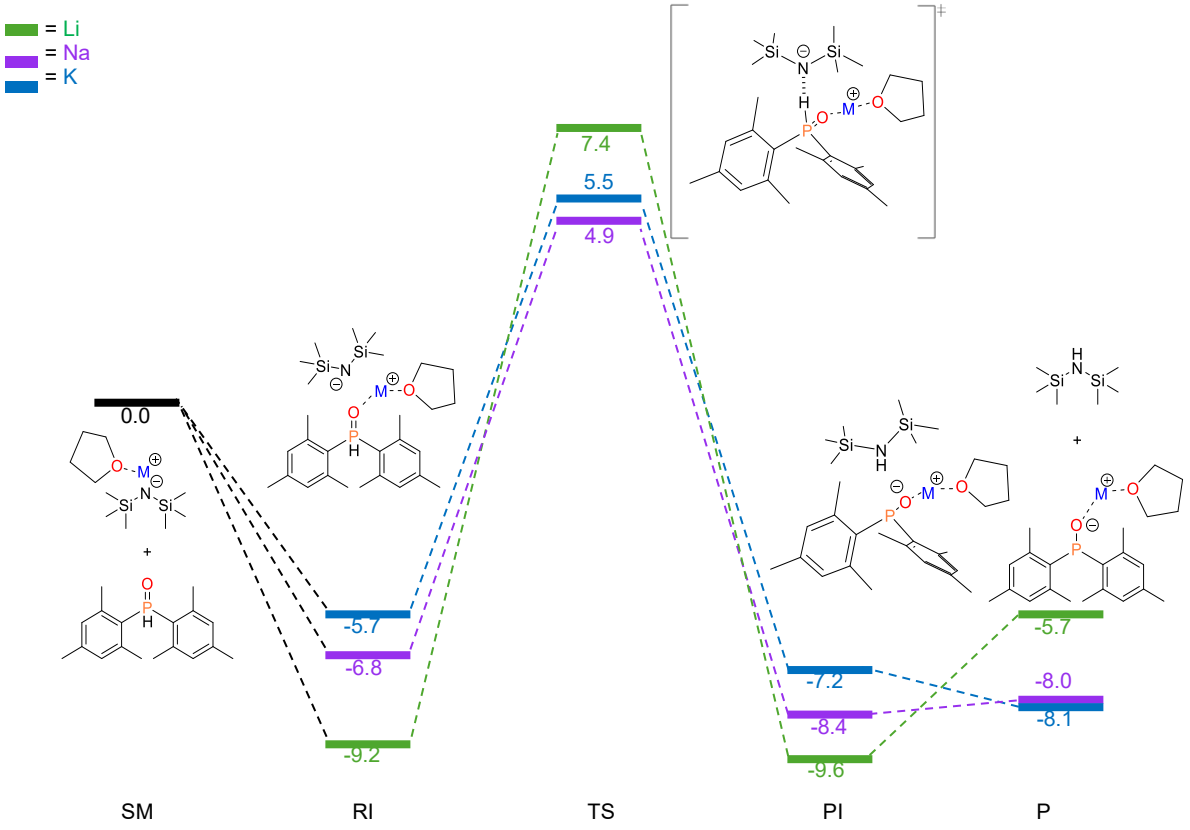

Figure 4.4.A.: Gibbs energy profile in THF (ΔG_{THF} kcal mol^{-1}) at 298 K for the proton transfer step for the generation of M-OPR$_2$ active species considering monosolvated structures at the B3LYP-D3/def2-TZVP/SMD(THF)//B3LYP-D3BJ/6-31G(d,p)/SMD(THF) level of theory (R = Mes, M = Li (green), Na (purple), K(blue); the ..... line between the metal cation and the oxygen atom signifies the interaction between them; the TS is marked as ‡).

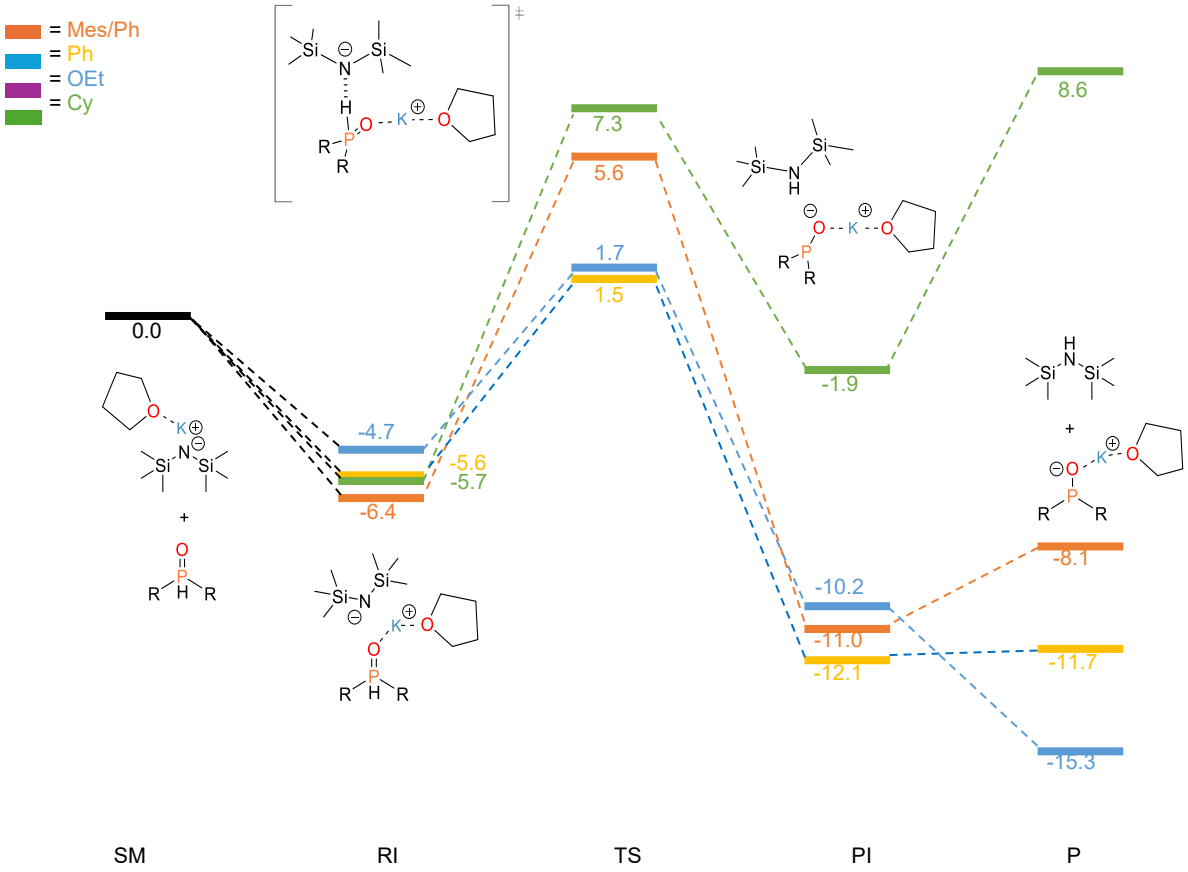

Figure 4.4.B.: Gibbs energy profile in THF (ΔG_{THF} kcal mol^{-1}) at 298 K for the proton transfer step for the generation of M-OPR$_2$ active species considering monosolvated structures at the B3LYP-D3/def2-TZVP/SMD(THF)//B3LYP-D3BJ/6-31G(d,p)/SMD(THF) level of theory (M = K, Mes/Ph (orange), Ph (blue), Cy (green), OEt (purple); the ..... line between the metal cation and the oxygen atom signifies the interaction between them; the TS is marked as ⋯⋯.). (SM = starting materials, RI = reaction intermediate, TS = transition stat, PI = product intermediate, P = product).

Until now we have analysed the formation of alkali metal phosphinites that will be the catalyst of the Pudovik reaction. However, the concentration of these active species in solution can be considerably decreased by two main side-reactions, dimerisation and dismutation, that are deactivating processes (**Scheme 4.7**).

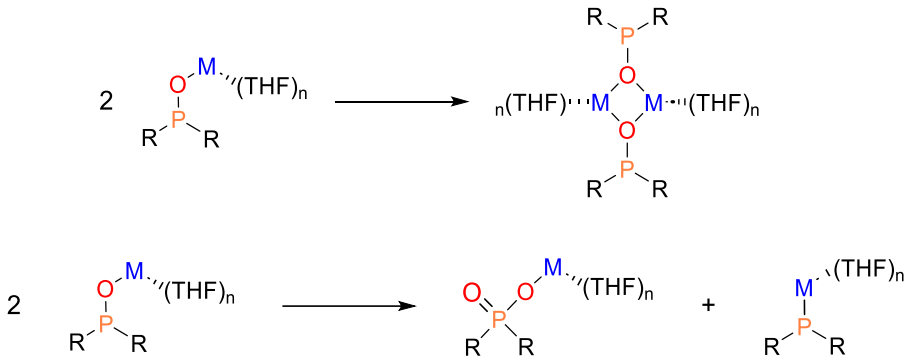

Scheme 4.7: Deactivation processes of alkali metal diorganylphosphinites M-OPR$_2$: dimerisation (top) and dismutation (bottom).

Crystal structures of alkali metal diarylphosphinites exhibit aggregation. Tetranuclear lithium and potassium diarylphosphinites with central M_4O_4 cages have been characterized.[32,33] However, the coordination chemistry of alkali metal diarylphosphinites is still not well understood. A recent study from Prof. Westerhausen's group reported the metalation of dimesitylphosphineoxide with n-butyllithium, sodium, and potassium HMDS in THF, resulting in the alkali metal dimesitylphosphinites M-OPMes$_2$.[34] The dinuclear complex [(THF)$_3$(Li-O-PMes$_2$)$_2$] was crystallized from the lithium reagent, while tetranuclear compounds of the type [(THF)M-O-PMes$_2$]$_4$ with central heterocubane cages were obtained from Na- and K-HMDS. In the potassium reaction, substituting methyl groups in the phenyl ring with bulkier triisopropyl groups yields the dimeric [(THF)$_4$(K-O-PMes$_2$)$_2$], with two THF ligands coordinated to each potassium center.[34]

We have computationally studied the dimerisation of alkali metal diarylphosphinites. We found that the reduced steric pressure from the P-substituents, compared to the bistrimethylsilyl groups of HMDS, permits the coordination of two THF molecules to each cation, resulting in a tetrasolvated dimer (**Scheme 4.8**).

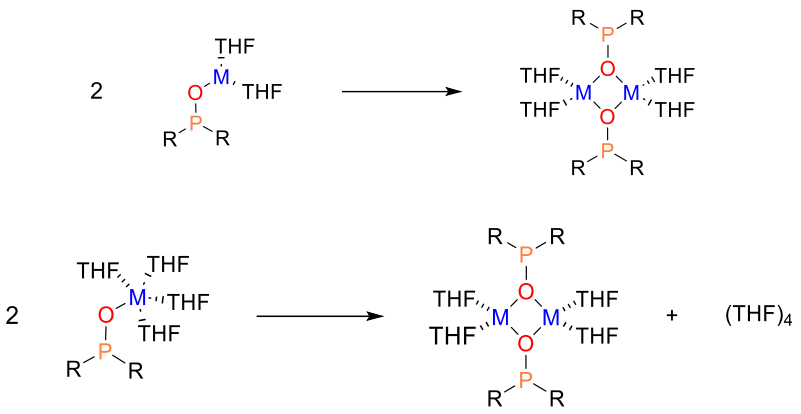

Scheme 4.8: Dimerisation process of M-OPR$_2$ phosphinites considering disolvalted (top) or tetrasolvated (bottom) monomers.

As for the M-HMDS case, we have taken into account the solvation state of the monomer by computing the reaction with both the disolvated and tetrasolvated species. **Figure 4.5** displays the optimised structures of dimesitylphospinite.

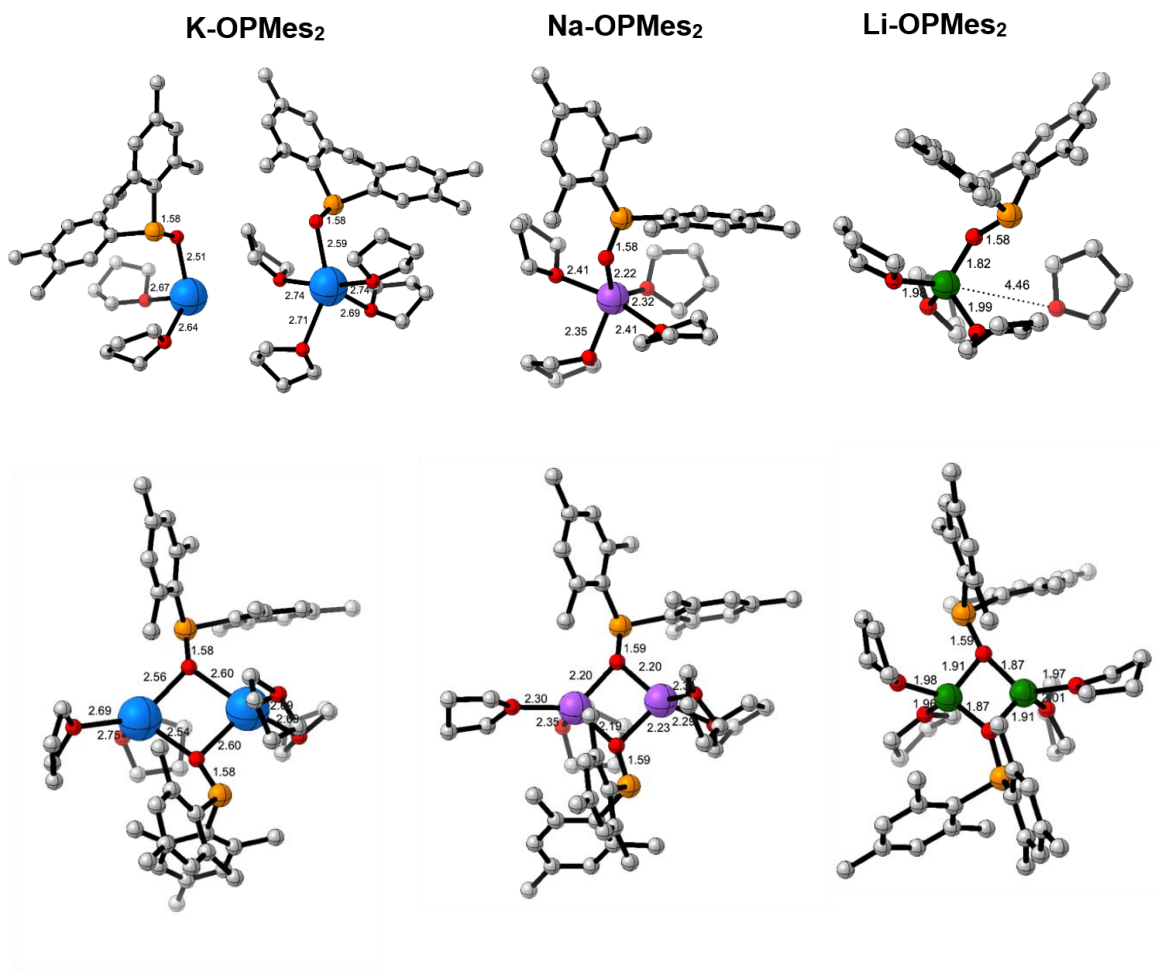

Figure 4.5.: Optimised structures of monomeric (top) and dimeric (bottom) alkali metal dimesityl phosphinites. For K-monomer di- and tetrasolvated species are compared. Certain hydrogen atoms are omitted for clarity reasons. The distances presented are given in Å.

Table 4.4 contains the computed Gibbs reaction energies for the dimerisation reactions depicted in **Scheme 4.8**. As observed for the disaggregation of dimeric M-HMDS (**Scheme 4.5**) the solvation state of the monomer has a major influence on the thermodynamics of the reaction. Values obtained with tetrasolvated monomers give a more realistic description of the situation in pure THF solvent. For potassium, the reaction is at equilibrium with a notable presence of monomeric active species. In contrast, for sodium and lithium, the reaction is displaced toward the dimer side, substantially decreasing the concentration of the active species in the THF solution.

Table 4.4.: Gibbs reaction energies (ΔG_R, kcal mol^{-1}) for the dimerisation of M-OPR$_2$ phosphinites at the B3LYP-D3/def2-TZVP/SMD(THF)//B3LYP-D3BJ/6-31G(d,p)/SMD(THF) level of theory (**Scheme 4.8**).

Entry	Metal	P-bound group (R)	ΔG_R	
			$(THF)_2$[a]	$(THF)_4$[b]
1	Li	Mes	-18.7	*-3.8*
2	Na	Mes	-21.1	*-4.4*
3	K	Mes	-21.0	*-0.7*
4	K	Mes/Ph	-19.7	*-1.7*
5	K	Ph	-25.1	*-0.2*
6	K	OEt	-20.4	*-3.4*

[a] Bisolvated species.

[b] Tetrasolvated species (numbers in italics).

It is known that some alkali metal phosphinites M-OPR$_2$, as Li-OPMes$_2$, dismutate into phosphinate (M(O$_2$PMes$_2$)) and phosphanide (M-PR$_2$) (**Scheme 4.7**, bottom).[35] Homologous potassium diphenylphosphinite dismutate as well.[36] Enhancing steric requirements of the P-bound substituents makes more difficult the disproportionation reaction. Thus, we also assessed the thermodynamics of the dismutation considering tetrasolvated species (**Scheme 4.9**). ΔG_R of the dismutation reaction are gathered in **Table 4.5**.

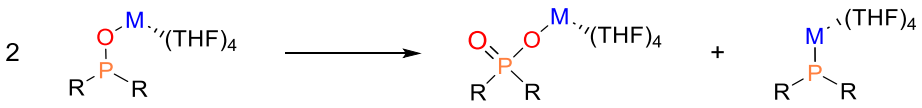

Scheme 4.9: Dismutation process of M-OPR$_2$ phosphinites considering tetrasolvated species.

The results highlight that dismutation is thermodynamically favoured for the three alkali metal cations, with the trend K > Na > Li. Regarding P-substituents with K, very similar values are obtained with Mes, Mes/Ph, and Ph. Contrarily, disproportionation seems to be unfavourable with R = OEt. As dismutation implies approaching to

solvated M-OPR_2 phosphinites, it is clear that steric effects will play a major role in the kinetics of the reaction.

Table 4.5.: Gibbs reaction energies (ΔG_R, kcal mol^{-1}) for the dismutation of M-OPR_2 phosphinites to phosphinates ($M(O_2PMes_2)$) and phosphanides ($M\text{-}PR_2$) at the B3LYP-D3/def2-TZVP/SMD(THF)//B3LYP-D3BJ/6-31G(d,p)/SMD(THF) level of theory (**Scheme 4.9**).

Entry	Metal	P-bound group (R)	ΔG_R
1	Li	Mes	-5.7
2	Na	Mes	-13.4
3	K	Mes	-19.3
4	K	Mes/Ph	-17.2
5	K	Ph	-20.0
6	K	OEt	17.1

We have located the transition state for the dismutation of disolvated K-$OPPh_2$ (**Figure 4.6**). In this TS the interaction of the oxygen atom that is being transferred between the two phosphorous with two potassium cations is decreasing its electronic density, thus facilitating its approach to phosphorous. The computed barrier is rather high, the TS is 32.8 kcal mol^{-1} above the two separated $(THF)_2$-K-$OPPh_2$, making this process as it is unfeasible at the reaction conditions. There appears that the phosphineoxide present in the reaction medium plays a role as a Brönsted acid decreasing the barrier.

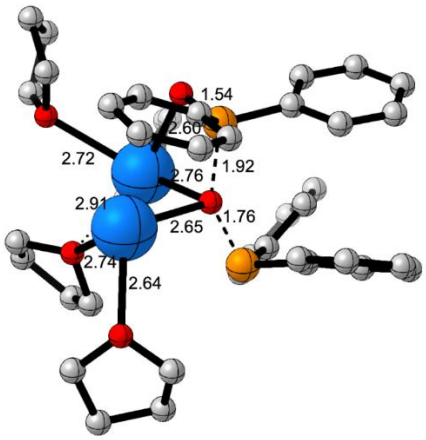

Figure 4.6.: Transition state for the dismutation of disolvated K-$OPPh_2$ to diphenylphosphinate and diphenylphosphamide. Certain hydrogen atoms are omitted for clarity reasons. The distances presented are given in Å.

Speciation and solvation issues make very difficult the computational simulation of the formation and deactivation of the alkali metal phosphinite active species in the Pudovik reaction in THF solution. To get more accurate results would require performing DFT-based molecular dynamics simulations, as done for Schlenk equilibrium of Grignard reagents, that are out of the scope of this work.[37] Moreover, dimerisation and dismutation reactions involve two alkali metal phosphinite molecules and will be influenced by concentration effects, not taken into account in the calculations. However, static DFT calculations can give useful hints on the behaviour of these systems in solution, provided that a careful description of solvation by means of introducing in the computed system explicit THF molecules is done. Our analysis was confined to a small number of species; additional species may possibly be present in solution. Nevertheless, our study points out that the concentration of active species in solution should be very dependent on both the alkali metal cation and the P-bound groups. In our study potassium alkali metal cation combined with bulky mesityl groups in phosphorous that hinder aggregation and dismutation phosphinite appears as the best combination to afford high concentration of active species in solution.

4.1.2.4. Nucleophilicity of alkali metal phosphinites

As mentioned earlier, s-block metal catalysts facilitate the formation of metal phosphinites (M-OPR$_2$), which serve as nucleophilic intermediates. These intermediates undergo addition reactions with unsaturated substrates, resulting in the formation of P–C bonds.[38] As nucleophiles, they are characterized by a high-lying HOMO. This HOMO arises from the lone pair on phosphorous, interacting in an antibonding manner with the p orbital of oxygen. **Figure 4.7** illustrates this HOMO for K-OPMes$_2$

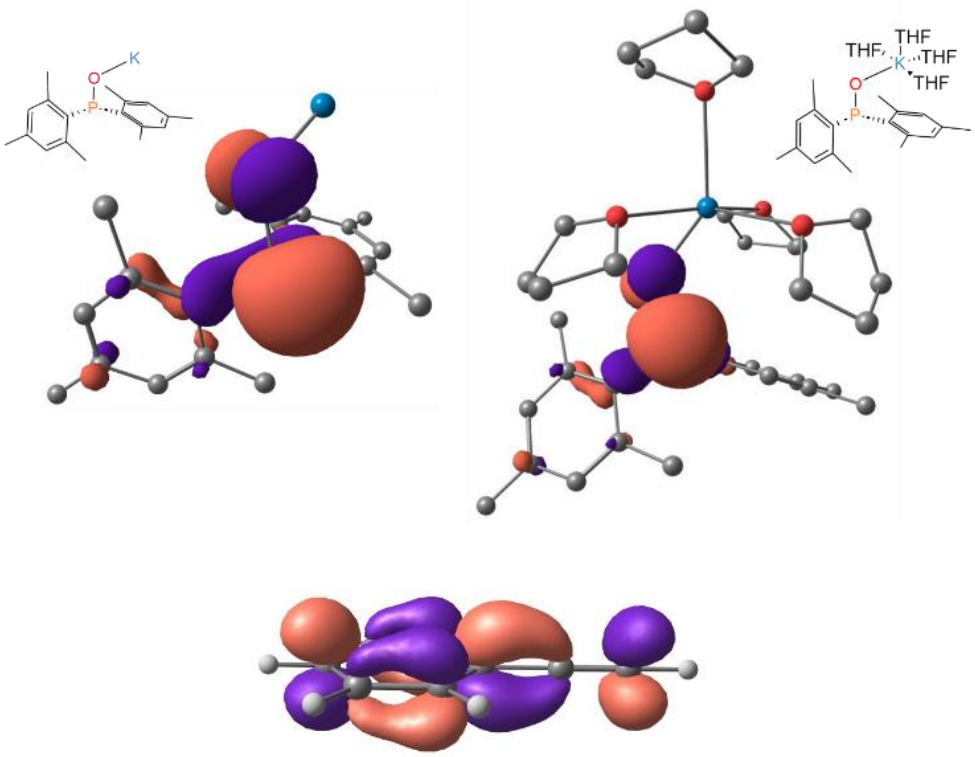

Figure 4.7.: Top: Calculated HOMO of K-OPMes$_2$ without explicit THF molecules solvating the cation (left) and with four THF solvent molecules (right). **Bottom**: LUMO of phenylacetylene.

To assess the relative nucleophilicity of the species involved in the nucleophilic addition, as well as the impact of solvation on this property, we calculated the empirical global nucleophilicity index (*N*) for all the species. This index is derived from the HOMO energies obtained using the Kohn-Sham approach and is defined as:

$$N = \varepsilon_{HOMO}(Nu) - \varepsilon_{HOMO}\ (TCE)$$

,where tetracyanoethylene (TCE) serves as the reference due to its highly negative ε_{HOMO}, ensuring positive N values.[39] According to this model, organic molecules with N≥3.0eV are considered strong nucleophiles, while those exceeding this threshold are classified as supernucleophiles.[40]

Table 4.6.: Energy of HOMO Molecular Orbital, Nucleophilicity Index and Natural Atomic Charge at the alkali metal of alkali metal phosphinites at the B3LYP-D3/def2-TZVP/SMD(THF)//B3LYP-D3BJ/6-31G(d,p)/SMD(THF) level of theory.

Entry	metal phosphinites (M-OPR_2)	No explicit THF			$(THF)_4$		
		HOMO Energy (eV)	*N* (eV)[a]	M charge[b]	HOMO Energy (eV)	*N* (eV)[a]	M charge[b]
1	$[OPMes_2]^-$	-3.26	5.38	/	/	/	/
2	K-$OPMes_2$	-4.15	4.49	0.97	-4.09	4.55	0.92
3	Na-$OPMes_2$	-4.32	4.32	0.96	-4.12	4.52	0.89
4	Li-$OPMes_2$	-4.55	4.09	0.95	-4.29	4.35	0.89
5	H-$OPMes_2$	-5.53	3.11	0.52[d]	/	/	/
6	K-OPPhMes	-4.26	4.38	0.96	-4.09	4.55	0.92
7	K-$OPPh_2$	-4.45	4.19	0.95	-4.32	4.32	0.91
8	K-$OPCy_2$	-3.97	4.67	0.95	-3.84	4.80	0.90
9	K-$OPOEt_2$	-5.19	3.45	0.94	-4.97	3.67	0.88

[a] Relative nucleophilicity index, taking tetracyanoethylene (TCE), which is the expected least nucleophilic neutral species, as a reference: $N = \varepsilon_{HOMO}(Nu) - \varepsilon_{HOMO}\,(TCE)$. In THF $\varepsilon_{HOMO}\,(TCE) = -8.64\,eV$.

[b] Natural Atomic Charge at the alkali metal.

[c] H instead of M.

The *N* values in **Table 4.6** clearly show that deprotonation of phosphineoxide significantly enhances the nucleophilicity of P-nucleophiles. The N value rises from 3.11 in dimesityl phosphineoxide to over 4 in alkali metal phosphinites, classifying them as supernucleophiles. The effect of the cation is minimal but follows the order K

> Na > Li. Phosphorous substituents have a more pronounced effect on nucleophilicity, with a notable decrease when R = OEt. Adding four explicit THF molecules to solvate the cation has a negligible effect on N, slightly increasing it. NPA atomic charges on the metal indicate a primarily ionic interaction between the metal and the oxygen atom in the phosphinite.

4.1.2.5. Modes of interaction of the metal cation with the π-systems

Hitherto it is known that alkali metal cations tend to interact with varying degrees with different aromatic systems through what is known as "cation-π interaction". [41] There are multiple factors which will have influence on the cation-π interaction, such as charge transfer and donor-acceptor effects, induced dipoles in the aryl ring and in the triple C≡C bond, and the also the notion that sp^2-hybridized carbon is more electro negative than a hydrogen.[42–44] Thus, prior to continuing with the exploration on the reactions mechanisms we investigated the modes of interactions the metal cation from the active species (M-OPMes_2) would have with the π-systems of the phenylacetylene. In this instance, the cation may establish two types of interaction: i) π-interaction with C≡C triple bond or ii) π-interaction with an aryl moiety (see **Scheme 4.10**).

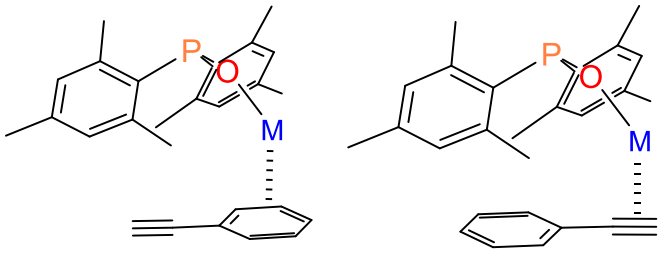

Scheme 4.10: Possible modes of interaction between the alkali cation in the M-OP-Mes_2 and phenylacetylene. The interaction amongst the alkali cation and the π-systems is presented by (⋯⋯) line in the scheme.

Three points must be stressed out from the calculations; One is that the metal cation π-interactions have a very weak nature. Taking the most stable structures ΔG of -0.8 (K), -1.6 (Na), and -2.9 (Li) kcal mol^{-1} have been computed for these interactions. The most stable confirmations for the three alkali cations are depicted in **Figure 4.8**). As it may be seen, all of the interactions are slightly favourable. These values

correlate to a weak M-π binding energy in a highly dynamic system, where the presence of the metal cation should have minimal effect on π system. The second point concerns the orientation of the metal cation with regards to π-systems in their most stable conformations. Its notable that potassium cation preferably coordinates with the aryl-system rather than the triple bond C≡C π-system. On the contrary lithium cation will preferentially coordinate to the π -system of the C≡C triple bond rather than the aryl-system, with sodium cation preferable coordination falling somewhere in the middle (**Figure 4.8**).

Our findings are in accordance with the calculations from Pardiue *et al.* on carbon–hydrogen bond deprotonation by alkali metal superbases.[45] Additionally, upon recreating the conformations with additional P-bound groups (P–Ph) we are able to determine that the inductive effect from groups will not modify the coordinating mode of the alkali cation. A more direct comparison cannot be made with the results from Robertson *et al.*[46] as in our case we have a triple bond present; however, the deformation of the phenyl ring is also noted in our findings. The transfer of the alkali metal away from the triple moiety and towards the aromatic π system causes a deformation of the ring due to the delocalization of the negative charge on $C_{internal}$ into the aryl ring. These types of deformation have been studied eloquently and comprehensively by Harder and coworkers. [47–49]

Our findings regarding metal effects in the cation-π interaction did match with the findings of Schleyer on the conformational “floppiness” of the metal cations.[42,46,50] Our most stable structures calculated for each metal nicely reproduce previously reported X-ray structures by Robertson *et al.*[51] The solvated metal cation progressively shifts from the lateral 'carbanionic' carbon to the aromatic π system as the alkali metal's size rises, facilitating the complex to remain monomeric in our theoretical structures and in the X-ray structures. This “floppiness” of the metal cations presented the biggest challenge in the search of TS as significant change in the positioning induced small changes in energy values, however this aspect will be discussed more into detail latter on.

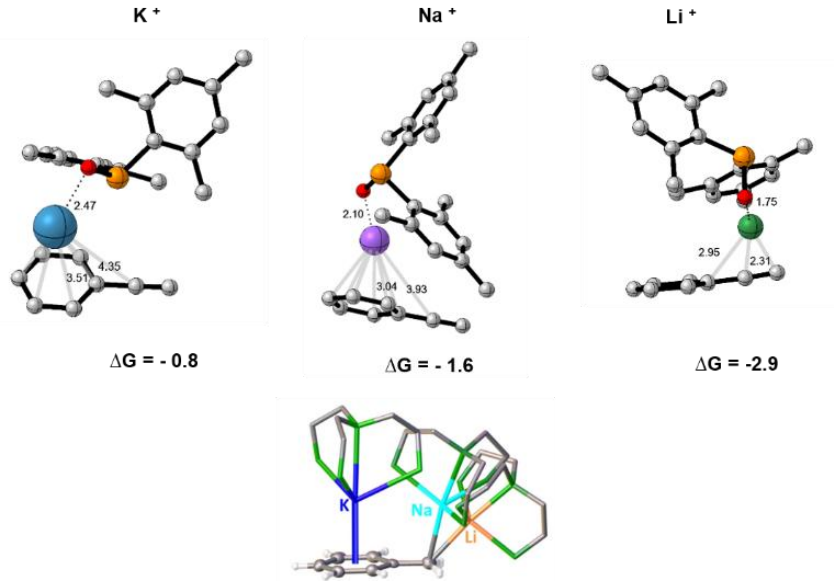

Figure 4.8.: Top: most stable conformations computed for phenylacetylene·M-OP-Mes_2 (M = Li^+ (green), Na^+ (purple), and K^+ (blue)) adducts. **Bottom**: X-ray structures of $PhCH_2M{\cdot}Me_6TREN$ (M = Li, Na, and K) complexes.[48] *ΔG binding in kcal mol^{-1}. Certain H atoms are omitted for clarity reasons. The distances are given in Å.

Having determined the Gibbs energy of formation for the active species and the mode of interactions of the active species with the phenylacetylene we now move on and begin with the exploration of the proposed reaction mechanism.

4.1.2.6. The effect of the metal cation

Experimentally, it was observed that alkali complexes (M-HMDS; M = Li, Na, and K) can mediate the Pudovik reaction with increased catalytic reactivity for larger congeners (see **Table 4.1**; **Section 4.1.1**). As a result, we decided to embark on theoretical investigations into the reaction mechanism, aiming to explore whether varying the cation would induce changes in the mechanism. All subsequent calculations pertaining to the influence of the metal cation on the overall reaction mechanism were performed with a P-bound mesityl substituent.

4.1.2.6.1. Potassium mediated Pudovik reaction (P-bound Mesityl subsituent)

As expressed above, experiments showcased that the potassium mediated reaction of phenylacetylene with dimesitylphosphineoxide at r.t. had the highest conversion rate upon 1h with conversion of 93% (see **Table 4.1**; **entry 3**), thus we will commence analysing the estimated energy pathways with this reaction. In **Section 4.1.2.3.** we discussed the issues related with the formation and deactivation of the active species and now we assume it is present in the reaction medium. Before calculating the reaction mechanism for yielded products, we analysed the thermodynamic *via*bility of the monohydrophosphorylated products (E and *Z* isomer; **E/Z-1-R**) and the *via*bility of the bishydrophosphorylated product (**2-R**), according to **reaction 2**:

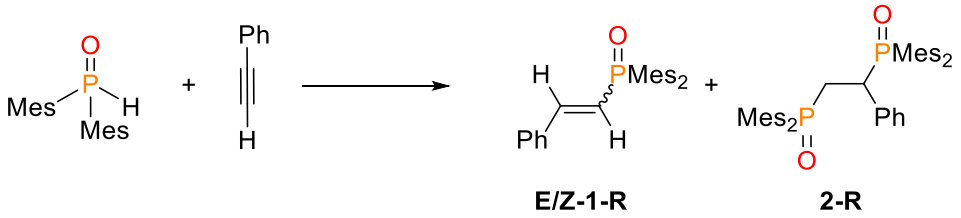

(2)

We estimated that the reactions for formation of *Z*,*E-isomer*s and the bis-product to be exergonic, with a ΔG of -20.8, -25.6 and -20.4 kcal mol^{-1} respectively. Terminal alkynes are acidic, hence side reaction because of acid-bas (protonation-deprotonation) equilibria with the active species might follow **reaction 3**.

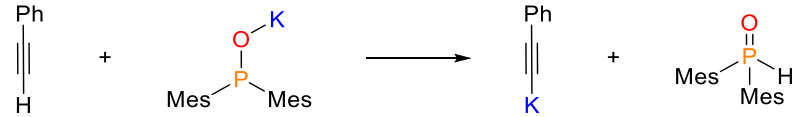

(3)

According to the theoretical estimations this side reaction can be discarded due to a ΔG = 15. 8 kcal mol^{-1}.

4.1.2.6.1.1. Where is the Regioselectivity Defined?

As stated above, potassium metal-mediated reaction of phenylacetylene with dimesitylphopshine oxide at room temperature had the highest conversion of 93% upon 1h (see **Table 4.1**, **entry 3**). Hydrophosphorylation reaction across the $C \equiv C$ bond of terminal alkyne may yield two products: Markovnikov and anti-Markovnikov depending on the carbon atom onto which the nucleophilic attack proceeds.[4,49] As presented in **Section 4.1.1.**, experimental findings show formation of only the latter product. Hence, with the aim to provide a better understanding of stereoisomeric yield, we decided to try and unravel why there is no formation of Markovnikov product in the experimental findings. We decided to compute the pathway leading to the Markovnikov product and compare it to the pathway leading to the anti-Markovnikov product. The comparison was solely done for the nucleophilic attack and the generated intermediate from this step, no calculations were conducted for the subsequent protonation steps. The Gibbs energy profile comparing both steps is depicted in **Figure 4.9**, whilst the optimized structures for the transition states are illustrated in **Figure 4.10**.

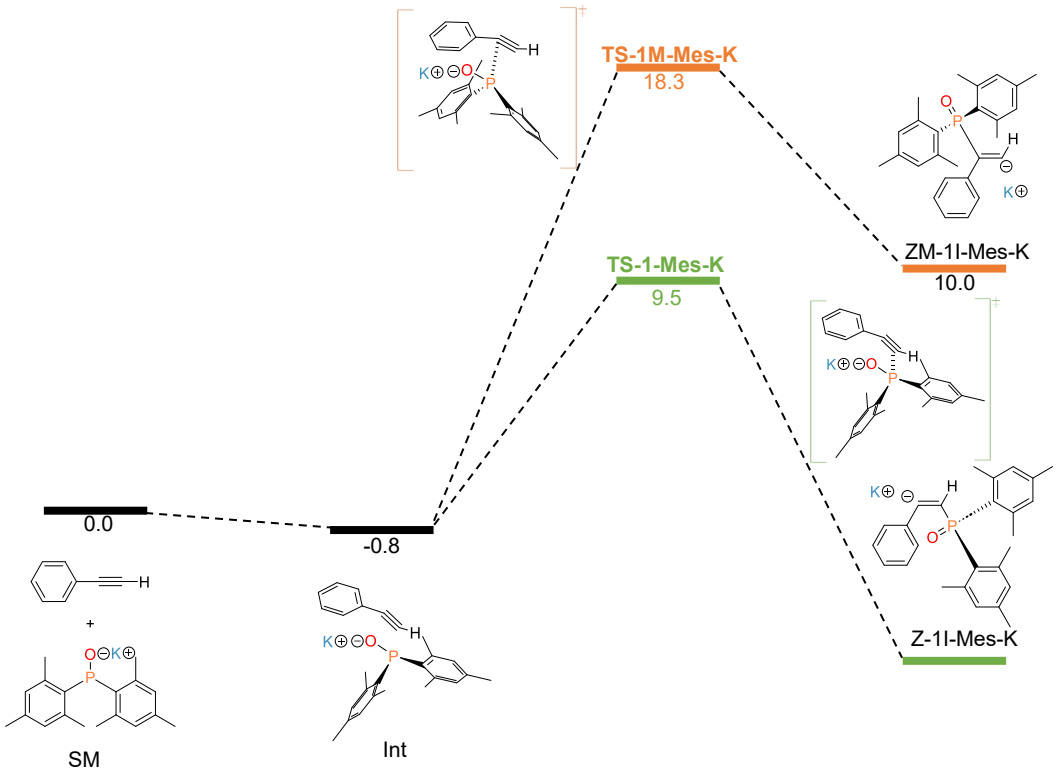

Figure 4.9.: Computed Gibbs energy profile in THF (ΔG_{THF} kcal mol^{-1}) at 298 K for the two nucleophilic attacks leading to formation of anti-Markovnikov intermediate (**TS-1-Mes-K**; green) and the formation of the Markovnikov intermediate (**TS-1M-Mes-K**; orange) in the case of potassium metal-mediated Pudovik reaction at the B3LYP-D3/def2-TZVP/SMD(THF)//B3LYP-D3BJ/6-31G(d,p)/SMD(THF) level of theory (SM = starting materials, Int = initial intermediate).

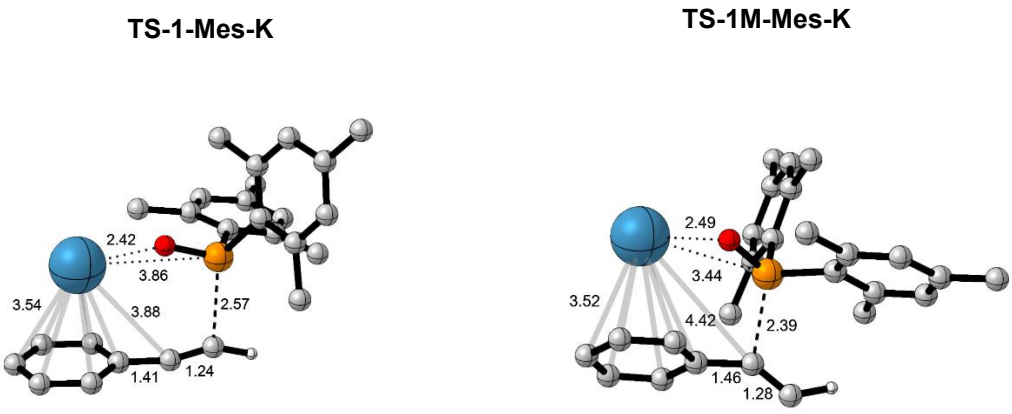

Figure 4.10.: Optimised structures for the transition states for Markovnikov (right) vs anti-Markovnikov (left) additions. Certain hydrogen atoms are omitted for clarity reasons. The distances presented are given in Å.

Comparing the barriers for both additions, the nucleophilic attack for the formation of Markovnikov intermediate (**TS-1M-Mes-K**, 19.1 kcal mol^{-1}) has a higher transition state than that of the anti-Markovnikov transition (**TS-1-Mes-K**, 10.3 kcal mol^{-1}). Another noteworthy difference between these two steps is the different stability of the intermediates. According to the estimated calculations the anti-Markovnikov intermediate has a relative energy of –6.2 kcal mol^{-1}, whilst the Markovnikov intermediate lies 10.0 kcal mol^{-1} above separated reactants. The anti-Markovnikov intermediate is simultaneously the thermodynamic and kinetic favored intermediate. The reason is that the phenyl group is a π-withdrawing group, thus, making the hydrogen atom-bonded carbon more electrophilic and promoting the site for nucleophilic attack. In the **TS-1M-Mes-K** the alkali cation will predominantly interact with the phenyl moiety whilst in the **TS-1-Mes-K** the potassium will interact with both the phenyl moiety and the $C_{Internal}$ (**Figure 4.10**). We also performed the same testing with potassium diphenyl phosphinite and got similar results with **TS-1-Ph-K** having a barrier of 10.6 kcal mol^{-1} and **TS-1M-Ph-K** having a barrier of 18.3 kcal mol^{-1}.

Accordingly, it may be concluded, that the formation of the anti-Markovnikov product will be favoured by the electronic effect. Ergo, DFT calculations agree with the experimental findings and give us a possible explanation of why the Markovnikov product is not formed.

4.1.2.6.1.2. Formation of *Z-isomer*

Having determined theoretically the preference for the formation of the anti-Markovnikov intermediate in the previous section, we set our next focus on calculating the reaction mechanism for the *Z-isomer* (the isomer formed with the smaller yield; see **Table 4.1**; **entry 3**) whilst, applying the above postulated mechanism (see **Scheme 4.2**), with the aim to attain and provide a better understanding of the stereo-isomeric yield. The theoretical investigations for this reaction rendered the reaction profile illustrated in **Figure 4.11**. **Figure 4.12** contains optimized structures for the two transition states involved in the formation of *Z*-dimesityl(styryl)phosphineoxide.

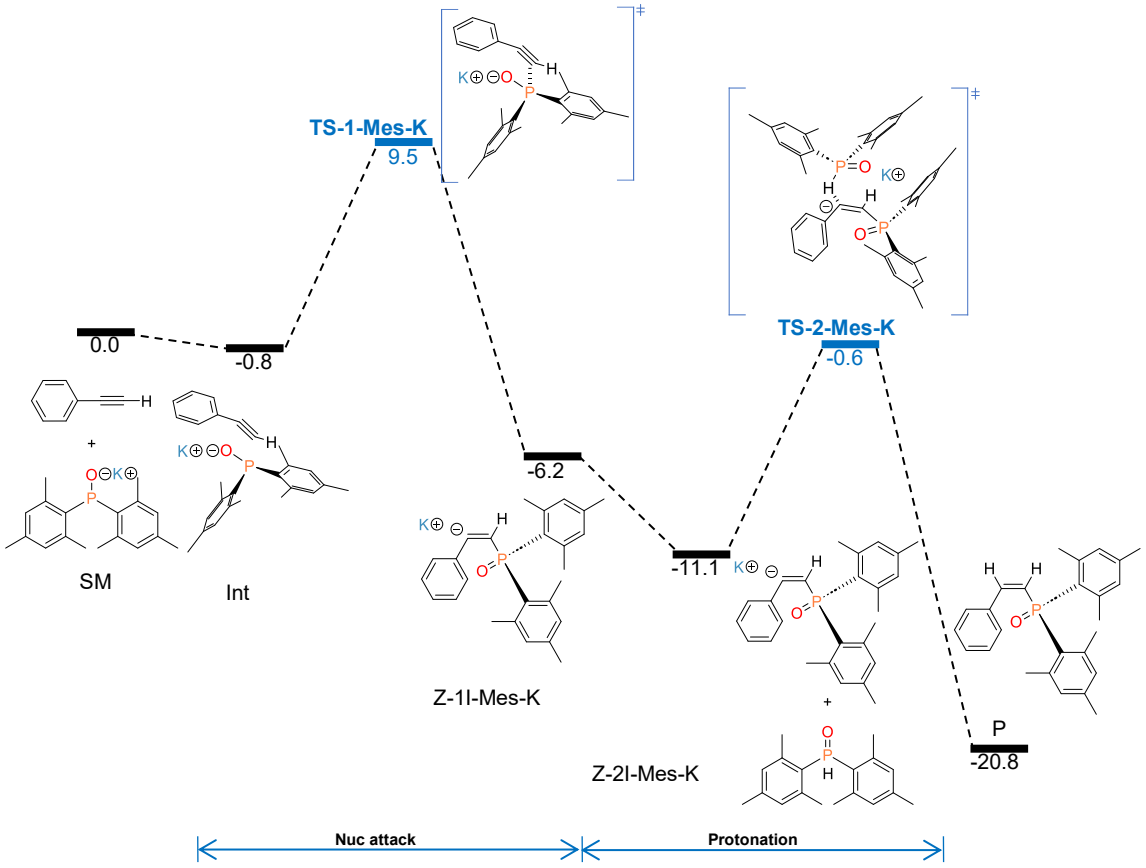

Figure 4.11.: Computed Gibbs energy profiles in THF (ΔG_{THF} in kcal mol^{-1}) at 298 K for potassium-mediated hydrophosphorylation of phenylacetylene for the formation of *Z-isomer* with di(mesityl)phosphineoxide, using K-HMDS as catalyst at the B3LYP-D3/def2-TZVP/SMD(THF)//B3LYP-D3BJ/6-31G(d,p)/SMD(THF) level of theory.

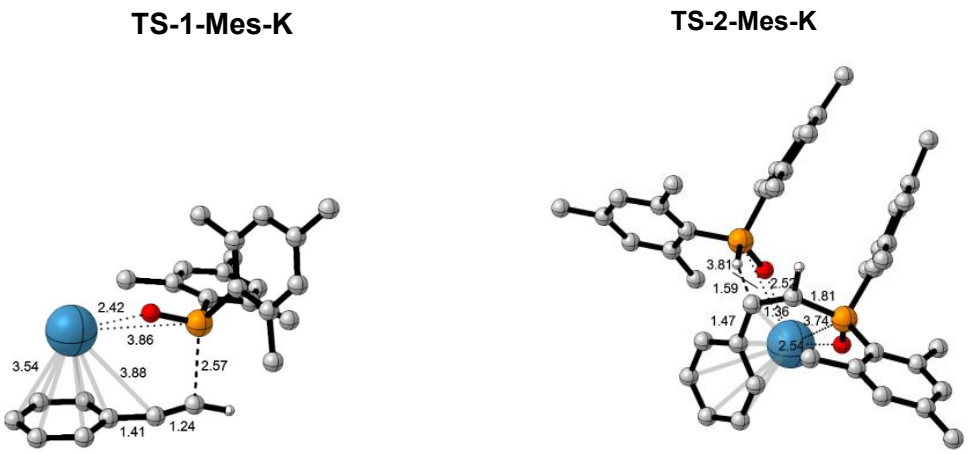

Figure 4.12.: Selected optimised structures for both transition states involved in the potassium metal-mediated Pudovik reaction for formation of *Z*-dimesityl(styryl)phosphineoxide. H atoms are omitted for clarity reasons. The distances presented are given in Å.

The hypothesised reaction mechanism (**Scheme 4.2**) calls for the formation of mono-hydrophosphorylated alkenes to proceed *via* two steps. The first step is the nucleophilic attack to the $C_{terminal}$[1] of C≡C triple bond of phenylacetylene by the potassium-activated P-nucleophile. In principle, this addition can result in two stereoisomeric vinyl intermediates depending on the whether the phenyl substituent is positioned cis or trans to the di(phenyl)phosphineoxide. However, before the attack a concomitant interaction is necessary. In this instance we estimated this interaction to be favourable with -0.8 kcal mol^{-1} (see **Section 4.1.2.4.**). We were able to locate **TS-1-Mes-K** with an energy barrier of 10.3 kcal mol^{-1} which generates the **Z-1I-Mes-K** intermediate at -6.2 kcal mol^{-1} below separated reactants. In this TS the potassium cation will interact with the π-aryl system at 3.18 Å[2] (see **Figure 4.12**). The second step leading to formation of mono-hydrophosphorylated alkenes is a protonation step. In the case of Mes_2-P(O)H as the protonating agent we were able to find two distinct feasible routes depending on the interaction of the potassium cation with the oxygen atoms present in the other molecules. Since the route with potassium bounded to as many oxygens as possible presented with the lowest energy barrier, only this route

[1] Under $C_{terminal}$ we mean the C atom the furthest from the phenyl group.
[2] This distance is measured from a dummy atom in the centre of the phenyl ring to the cation. From now on whenever mentioned distance between a cation and phenyl ring, the meaning will remain the same.

will be described herein. We estimated an energy barrier for this step (**TS-2-Mes-K**) of 11.7 kcal mol^{-1}.

Moreover, we also tested H-HMDS as a proton donor molecule. H-HMDS will be formed as a side product upon the formation of active species M-OPMes$_2$, thus it may be incorporated later in the cycle. The Gibbs energy profiles comparing both transition states for both pathways (H-HMDS; **TS-2H-Mes-K** vs Mes$_2$-P(O)H; **TS-2-Mes-K**) is illustrated in **Figure 4.13**. The optimised structure for the transition states for the protonation step for formation of *Z-isomer* are depicted in **Figure 4.14.** As it may be seen from **Figure 4.14,** we attempted to keep the same orientation for both TS, as to allow for a better comparison. Protonation with Mes$_2$-P(O)H happens with a lower barrier (10.5 kcal mol^{-1}) than with H-HMDS (15. 8 kcal mol^{-1}).

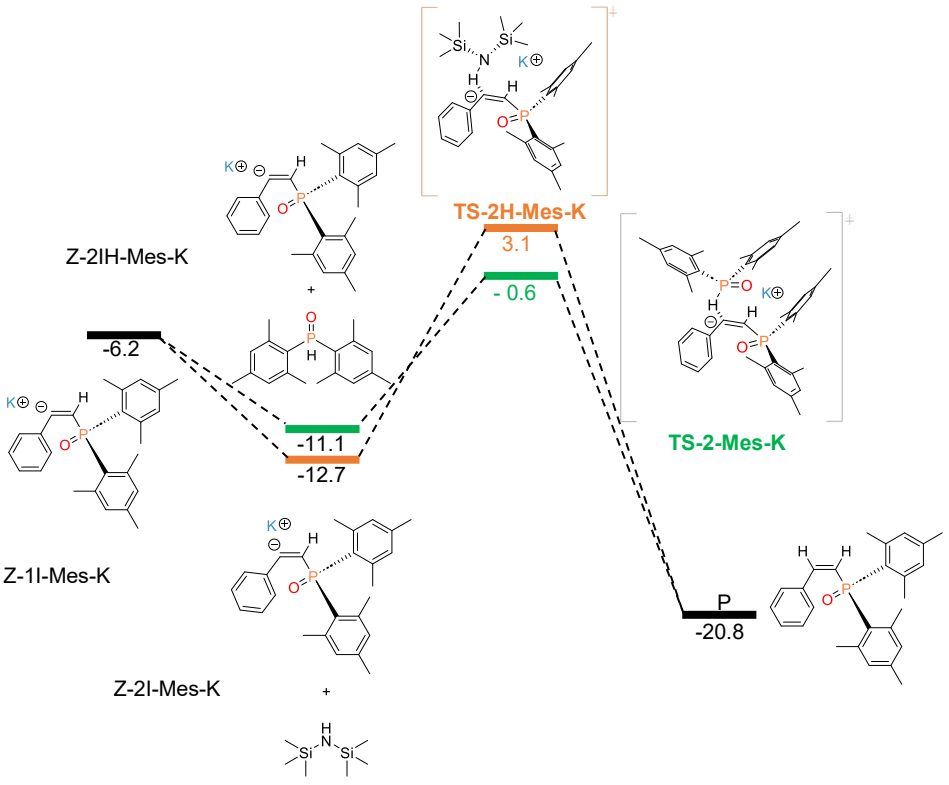

Figure 4.13.: Computed Gibbs energy diagram comparing H-HMDS (orange) vs Mes$_2$-P(O)H (green) as possible proton donors for the proton step in potassium metal-mediated Pudovik reaction which yields the *Z*-dimesityl(styryl)phosphineoxide at the B3LYP-D3/def2-TZVP/SMD(THF)//B3LYP-D3BJ/6-31G(d,p)/SMD(THF) level of theory.

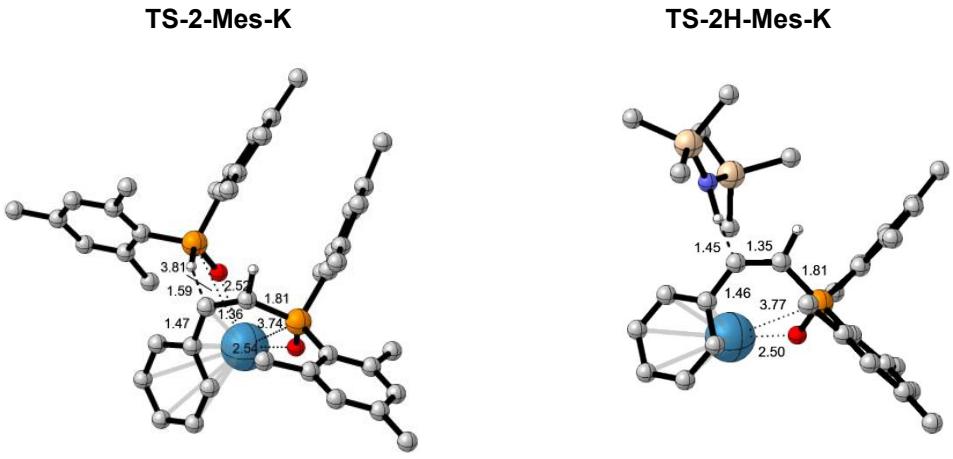

Figure 4.14.: Selected optimised structures for both transition states involved in the protonation step (H-HMDS; **TS-2H-Mes-K** vs Mes_2-P(O)H; **TS-2-Mes-K**) for potassium metal-mediated Pudovik reaction for formation of *Z*-dimesityl(styryl)phosphineoxide. Certain H atoms are omitted for clarity reasons. The distances presented are given in Å.

Interestingly, based on the calculations for this mechanism, we cannot definitively determine which step is the rate-determining step (RDS) as the energy barriers are too close in value (10.3 and 10.5 kcal mol^{-1} for the first and second steps, respectively). It should be noted that overall, the formation of Z-dimesityl(styryl)phosphineoxide is exergonic -20.8 kcal mol^{-1}.

Up to this point, we have considered the cation in its unsolvated form, modelling the THF solvent as a continuum medium with a dielectric constant of ε = 7.43 (SMD model), without including any explicit THF molecules in the system. To evaluate the validity of this approach, we computed the Gibbs energy profile for the addition leading to the Z isomer, where potassium is solvated by one and two explicit THF molecules. Since the cation interacts with both the π system and the oxygen atom of the phosphinite, coordinating two THF molecules to the potassium cation provides a more accurate representation of its first coordination sphere. **Figure 4.15** compares the transition states for nucleophilic addition (**TS-1-Mes-K**) and protonation (**TS-2-Mes-K**) with 0, 1, and 2 THF molecules explicitly coordinated to K.

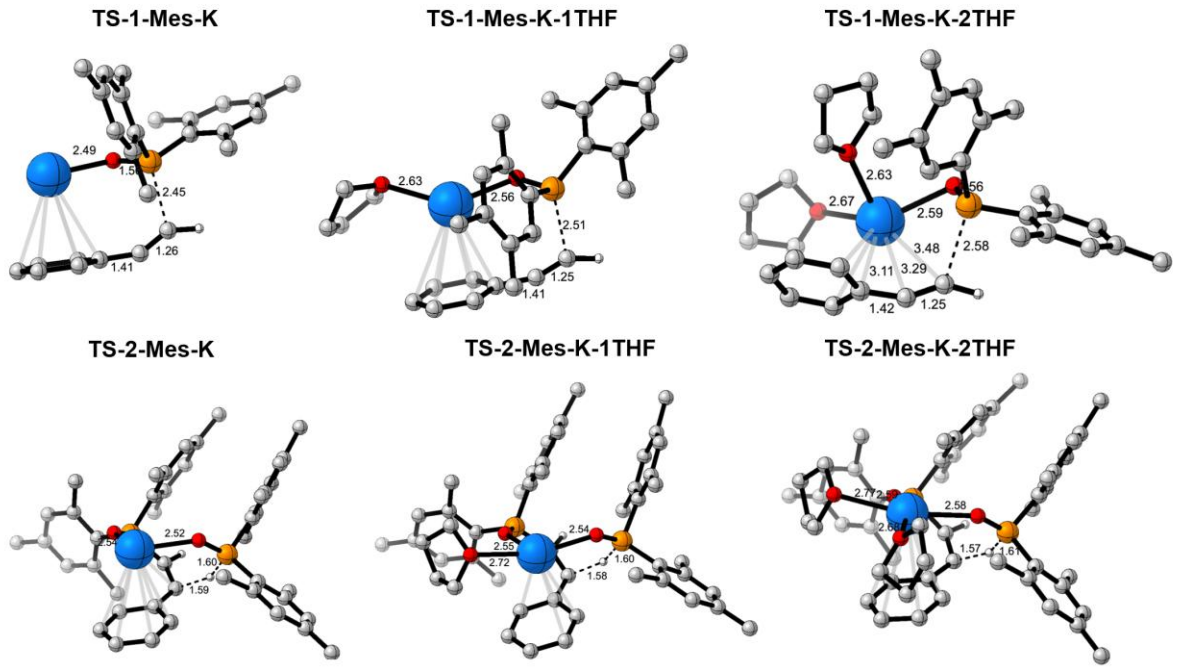

Figure 4.15.: Selected optimised structures for transition states for the nucleophilic addition (**TS-1-Mes-K**) and the protonation (**TS-2-Mes-K**) with 0, 1 and 2 explicit THF molecules coordinated to K. Certain H atoms are omitted for clarity reasons. The distances presented are given in Å.

In **Table 4.7** the Gibbs energy barriers ($\Delta G^{\ddagger}$) for both steps with 0, 1, and 2 explicit THF molecules are compared.

Table 4.7.: Gibbs activation energies ($\Delta \mathbf{G}^{\ddagger}$, kcal mol^{-1}) for the two steps involved in the formation of the Z isomer with a different number of explicit solvent molecules $(THF)_n$ at the B3LYP-D3/def2-TZVP/SMD(THF)//B3LYP-D3BJ/6-31G(d,p)/SMD(THF) level of theory.

Entry	$(THF)_n$	Nuc attack	Protonation
1	n = 0	10.3	10.5
2	n = 1	12.0	10.0
3	n = 2	11.2	9.7

Results in **Table 4.7** showcase a minor influence of coordinating THF molecules to the potassium cation. For this reason, the complications introduced in the optimisations by the THF molecules and the big number of calculations to be performed, from now the model employed in the calculations collected in this chapter does not include explicit THF molecules.

After estimating the Gibbs energy profile for the formation of the *Z-isomer*, we will now proceed to discuss the Gibbs energy profile for the formation of the *E-isomer*.

4.1.2.6.1.3. Formation of *E-isomer*

After theoretically proposing the reaction mechanism for the formation of the *Z-isomer*, our next step was to propose a reaction mechanism for the formation of the *E-isomer*. The Gibbs energy diagram affording the *E-isomer* is depicted in **Figure 4.16**, whilst **Figure 4.17** contains the optimised structures for the TS that constitute the mechanism for formation of *E-isomer*.

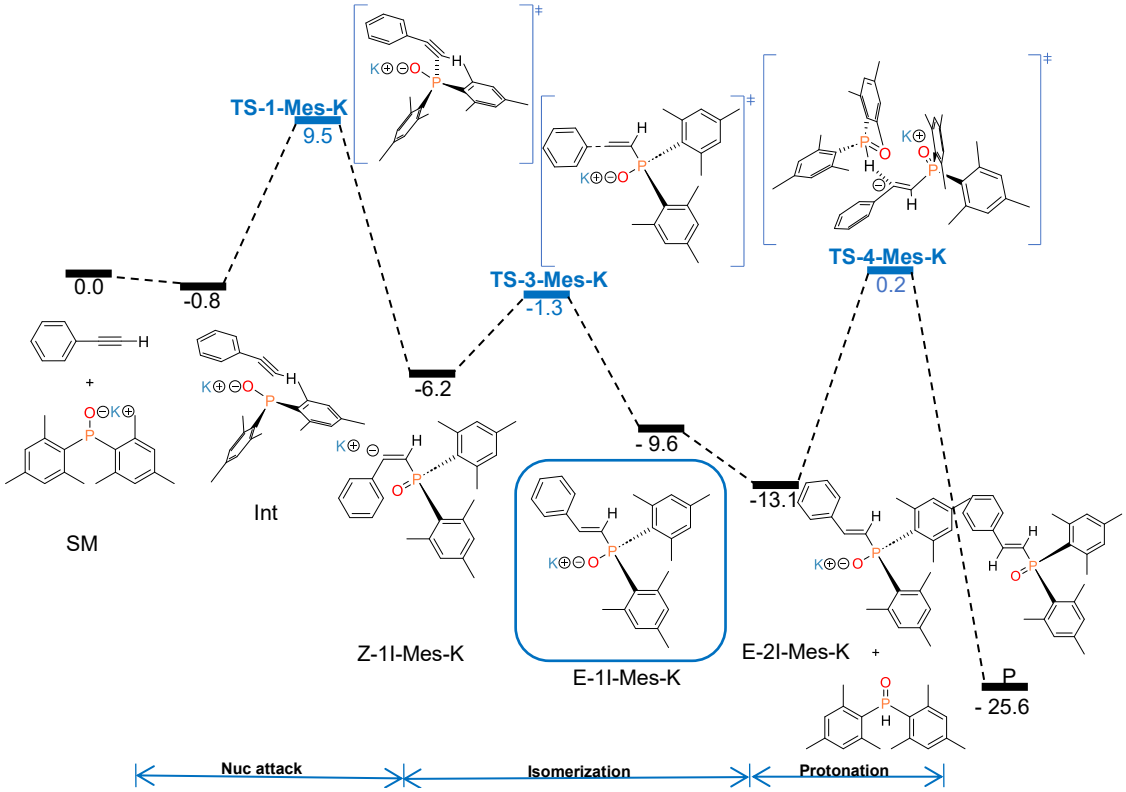

Figure 4.16.: Computed Gibbs energy profile in THF (ΔG_{THF} kcal mol^{-1}) at 298 K for potassium-mediated hydrophosphorylation of phenylacetylene for the formation of E-dimesityl(styryl)phosphineoxide with di(mesityl)phosphineoxide, using K-HMDS as catalyst at the B3LYP-D3/def2-TZVP/SMD(THF)//B3LYP-D3BJ/6-31G(d,p)/SMD(THF) level of theory. (SM = starting materials, Int = initial intermediate. P = product)

TS-1-Mes-K

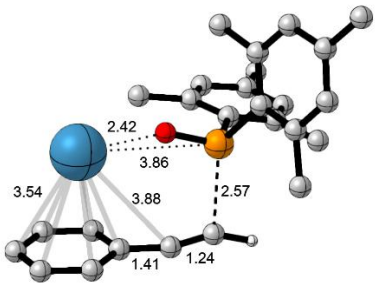

TS-3-Mes-K

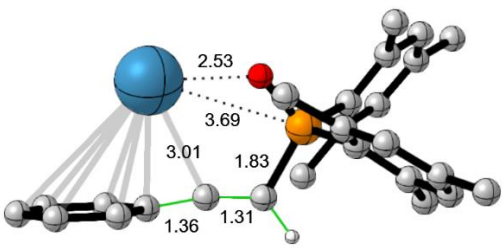

TS-4-Mes-K

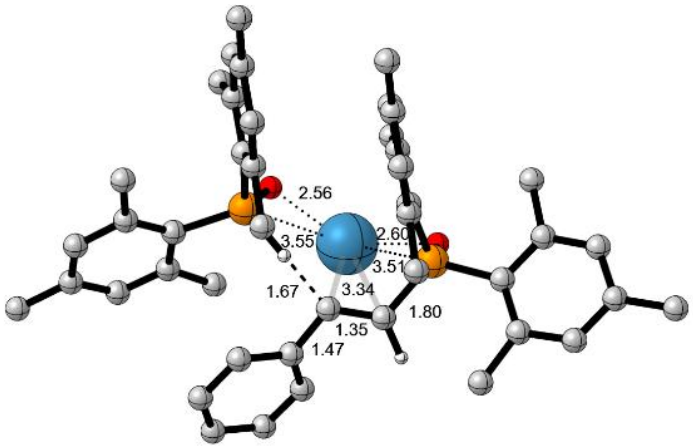

Figure 4.17.: Selected optimised structures for the transition states involved in the potassium metal-mediated mechanism for formation of E-dimesityl(styryl)phosphineoxide. In the image for **TS-3-Mes-K** we have marked (green lines) the dihedral angle which marks the rotation around the double bond that facilitates the isomerization step. Certain H atoms are omitted for clarity reasons. The distances presented are given in Å.

Numerous attempts were conducted to attain the direct nucleophilic attack for formation of the **E-1I-Mes-K** intermediate. However, all of them proved to be futile. Interestingly, the same preference for the Z isomer was found in the study of the Na-HMDS mediated enolization of ketone.[50] Thermal study on the E/Z isomerization of Mes_2-P(O)–C(Me)═C(H)Ph conducted by Westerhausen *et al.* showcased that at slightly elevated temperature (80°C) a rotation around the $C = C$ double bond is feasible with an estimated low barrier of 14.1 kcal mol^{-1}.[15] Thus, this gave us an idea to sought after a transition state that is an isomerization step which would yield a **E-1I-Mes-K** starting from **Z-1I-Mes-K** intermediate. We proposed this isomerization step to ensue before the protonation step, as in that instance the energy of isomerization will be lower.

We were able to locate the transition state for this step (**TS-3-Mes-K**) and as such it corresponds to bending of the $C_{terminal}$-$C_{internal}$-C_{Ph}[3] angle (see **Figure 4.17**). The change proceeding in the coordination of the potassium cation along the isomerization is remarkable. In **Z-1I-Mes-K** intermediate the cation is interacting with π system of

[3] By C_{Ph}, we refer to the carbon atom that is bonded to phenyl moiety and the $C_{internal}$, , whilst under $C_{internal}$ we mean the C atom that is attached to $C_{terminal}$ and C_{Ph}.

the aryl whilst in **E-1I-Mes-K** intermediate the cation is σ coordinating to the $C_{internal}$) (see **Figure 4.18**). According to the profile this isomerization occurs with a barrier of only 4.9 kcal mol^{-1}, low enough to be easily surpassed at the temperature at which the reaction happens. This transformation is additionally assisted by thermodynamics as **E-1I-Mes-K** is found at -9.9 kcal mol^{-1} in the Gibbs energy profile, whilst intermediate **Z-1I-Mes-K** is placed at -6.2 kcal mol^{-1}.

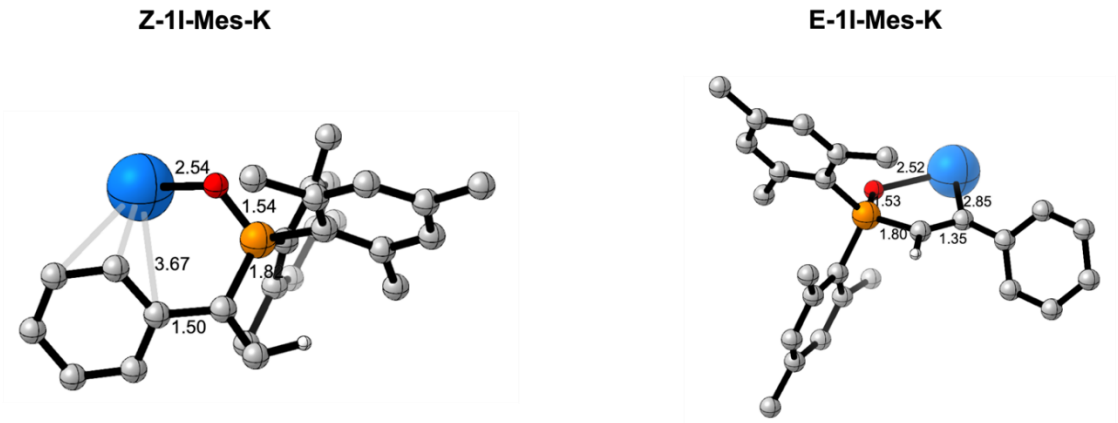

Figure 4.18.: Comparison of the intermediates preceding the protonation step for the formation of *Z*- (**Z-1I-Mes-K**) and *E-isomer*s. Certain H atoms are omitted for clarity reasons. The distances presented are given in Å.

In the final step, **E-1I-Mes** intermediate is protonated by an additional molecule of $Mes_2P(O)H$ through transition state **TS-4-Mes-K** (crossing a barrier of 12.9 kcal mol^{-1}), generating the final product (at - 25.6 kcal mol^{-1}) and as the side product the active species. In the same manner as in the proton step yielding *Z-isomer*, the potassium cation will preferably bind to both oxygen atoms present as to go through reaction pathways with the lowest energy barrier.

After analysing the Gibbs energy profiles for the formation of both Z and E isomers, we can draw several conclusions. The ***E-isomer*** (-25.6 kcal mol^{-1}) shows greater thermodynamic stability than the ***Z-isomer*** (-20.8 kcal mol^{-1}) ergo, the outcome of this reaction is governed by the thermodynamics.

4.1.2.6.1.4. Formation of bishydrophosphorylated alkanes and cyclization

Based on experimental evidence, it's observed that in this scenario, the reaction with $Mes_2P(O)H$ doesn't progress to form bishydrophosphorylated alkanes but instead halts at mono-hydrophosphorylated alkenes. This differs from cases where there are smaller P-bound substituents (refer to **Table 4.2**; **entries 2** and **3**). The second nucleophilic attack will proceed at $C_{internal}$. For the double addition to occur, the newly formed alkene moiety must also be capable of activation to allow for the addition of another phosphineoxide, ultimately leading to bishydrophosphorylated compounds. It is important to highlight that in one side **Z-1P-Mes** is less stable than **E-1P-Mes**, and in the other side, there is more room for a second addition in **Z-1P-Mes** than in **E-1P-Mes** (**Figure 4.19**).

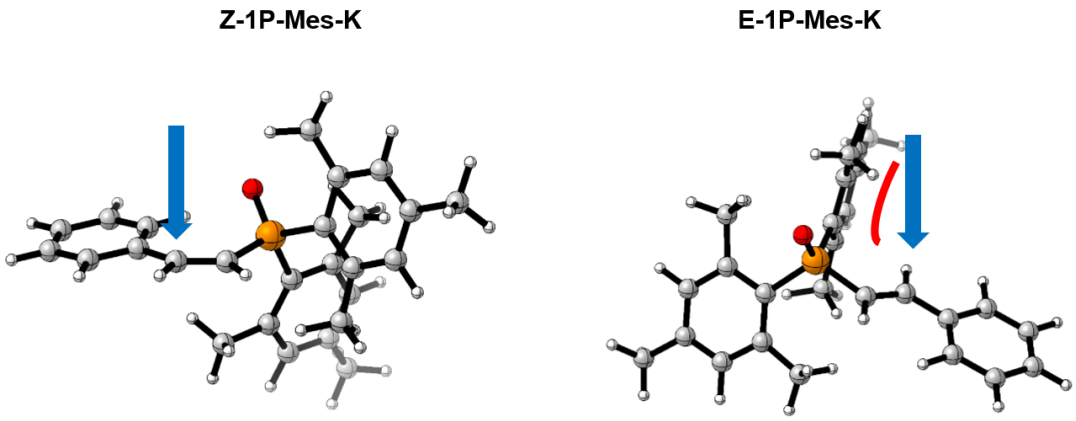

Figure 4.19.: Accessibility for a second addition in *Z*- and *E*- mono-hydrophosphorylated alkenes.

Consequently, the second hydrophosphorylation would expect to preferentially occur at **Z-1P-Mes**, as experimentally happens in case of phenyl P-bound groups. We have computed the second addition starting from **Z-1P-Mes**. The mechanistic steps for the second addition closely mirror those of the first addition, as depicted in **Scheme 4.2**. The Gibbs energy diagram affording the bishydrophosphorylated alkane is depicted in **Figure 4.20.** The optimised structures for the transition states involved in the formation of bishydrophosphorylated alkane are presented in the **Figure 4.21**.

The second nucleophilic attack will proceed at $C_{internal}$ and displays a higher energy barrier than for the 2nd nucleophilic attack (16.2 vs 11.8 kcal mol^{-1}; **Figure 4.20.** and **4.11.**). This increase in the energy barrier is most likely brought by reduced electron density in alkanes in comparison to alkynes. Additionally, this step is endergonic with the formed intermediated (**DA-1I-Mes-K**) at -19.2 kcal mol^{-1}. The energy barrier for the protonation step is even higher than that of the nucleophilic attack (**TS-2-Mes-DA**; $\Delta \mathbf{G}^{\ddagger}$ = 26.6 kcal mol^{-1}), making the second addition unfeasible for the dimesityl phosphineoxide.

Based on the DFT results, it can be concluded that the inhibition of bishydrophosphorylated alkane formation in this case may be attributed to two main factors: i) increased energy barriers for the 2nd nucleophilic attack and the 2nd protonation step, and ii) lower thermodynamic stability of the doubly phosphorylated product (-20.4 kcal mol^{-1}) compared with the monophosphorylated ones (Z: -20.8; E: -25.6 kcal mol^{-1}) . These findings are consistent with the experimental results as this product was not observed (see **Table 4.2**; **entry 1**).

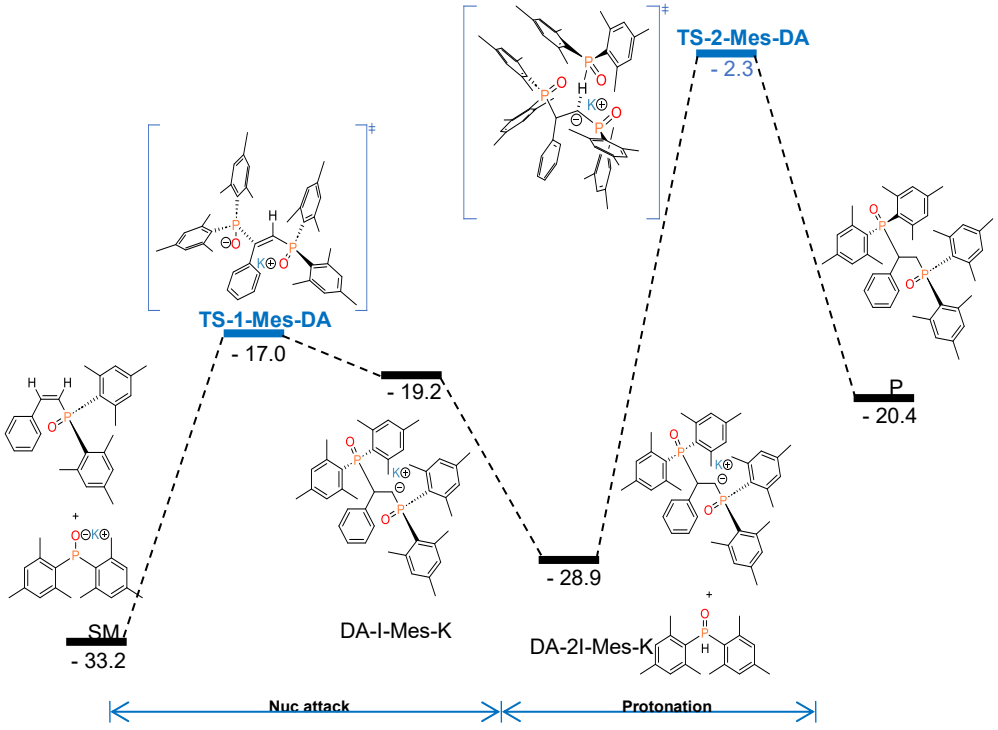

Figure 4.20.: Computed Gibbs energy profile in THF (ΔG_{THF} kcal mol^{-1}) at 298 K for potassium-mediated bishydrophosphorylation of phenylacetylene with di(mesityl)phosphineoxide, using K-HMDS as catalyst at the B3LYP-D3/def2-TZVP/SMD(THF)//B3LYP-D3BJ/6-31G(d,p)/SMD(THF) level of theory.

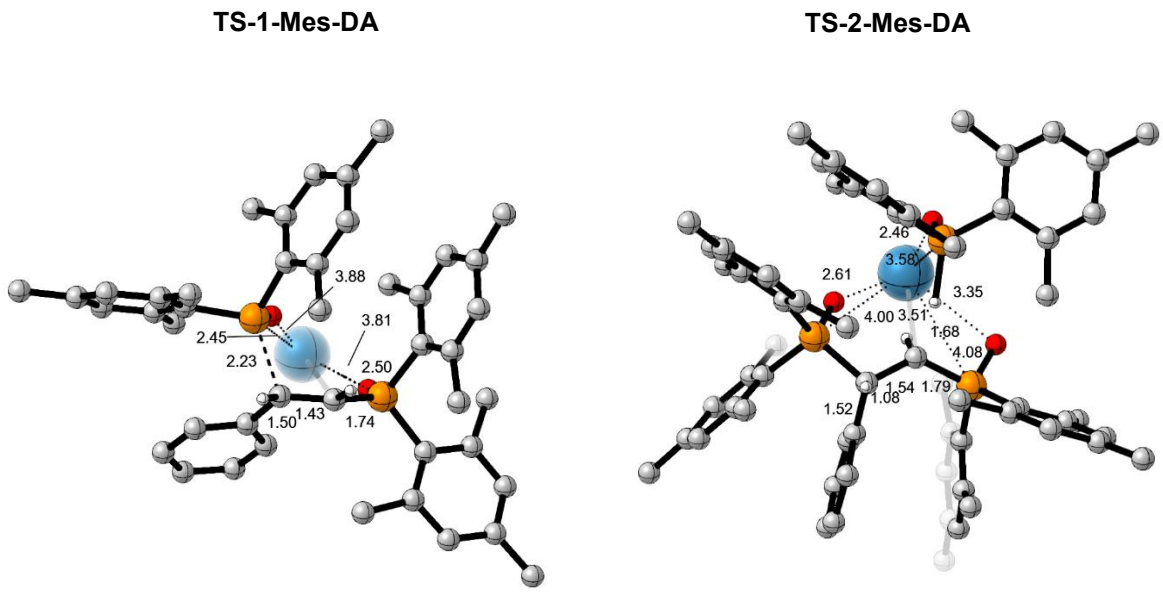

Figure 4.21.: Optimised structures for the transition states involved in the potassium-mediated hydrophosphorylation of phenylacetylene for formation of bishydrophosphorylated alkanes from Z-dimesityl(styryl)phosphineoxide. Certain H atoms are omitted for clarity reasons. The distances presented are given in Å.

Experimentally, only very low concentrations of the double-hydrophosphorylation product have been observed.[2] Calculations show that the rather high barrier computed for the second P-addition makes highly disadvantageous the addition of a second $Mes_2P(O)H$ onto the alkenyl moiety formed in the first addition. On the contrary, experiments showed the formation of 2-benzyl-1-mesityl-5,7-dimethyl-2,3-dihydrophosphindole 1-oxide. It has been proposed that this product comes from a cyclization reaction resulting from the deprotonation of *ortho*-methyl group of a mesityl substituent in the *Z*-product of the first addition, followed by cyclization triggered by an intramolecular nucleophilic attack at the alkenyl substituent of this carbanion. The final product should be formed by protonation with $H\text{-}N(SiMe_3)_2$.[2]

We have computationally assessed the proposed mechanism. **Figure 4.22** displays the computed Gibbs energy profile for the cyclization, and **Figure 4.23** illustrates the transition states of the process.

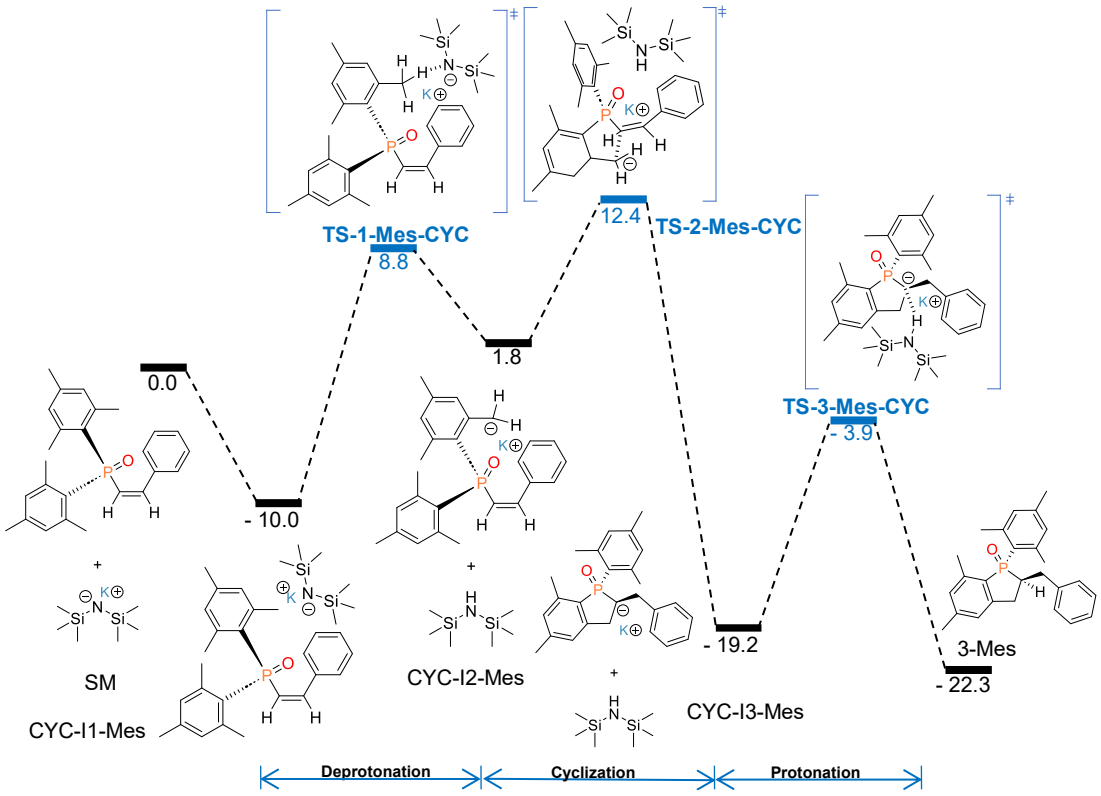

Figure 4.22.: Computed Gibbs energy profile in THF (ΔG_{THF} kcal mol^{-1}) at 298 K for the potassium-mediated cyclization process of **Z-1P-Mes** yielding 2-benzyl-1-mesityl-5,7-dimethyl-2,3-dihydrophosphindole 1-oxide (**3-Mes**), at the B3LYP-D3/def2-TZVP/SMD(THF)//B3LYP-D3BJ/6-31G(d,p)/SMD(THF) level of theory.

The formation of the phosphindole 1-oxide product (**3-Mes**) comprises three steps. Initially, there is a strong interaction between the oxygen of **Z-1P-Mes** and the potassium of K-HMDS. This interaction approaches the nitrogen center of K-HMDS to a C-H bond of an *ortho*-methyl group of the mesityl substituent and allows its easy deprotonation, that requires a barrier of only 18.8 kcal mol^{-1} (**TS-1-Mes-CYC**, **Figure 4.21.**). This is the first step of the reaction. The second step is the cyclization, in which the carbanion formed by the deprotonation attacks the alkenyl carbon bonded to phosphorous, closing the cycle. This second step has a barrier of 10.6 kcal mol^{-1} (**TS-2-Mes-CYC**, **Figure 4.23**). Finally, protonation at the benzylic carbon atom by H-HMDS yields the phosphindole 1-oxide product **3-Mes** after crossing a barrier of 15.3 kcal mol^{-1} (**TS-3-Mes-CYC**, **Figure 4.23**) and regenerates the catalytic species K-HMDS. The cyclization product is found 22.3 kcal mol^{-1} below **Z-1P-Mes-K**, proving that there is a strong thermodynamic driving force favoring cyclization. The cyclic **3-Mes** product is 1.9 kcal mol^{-1} more stable than the double-added product.

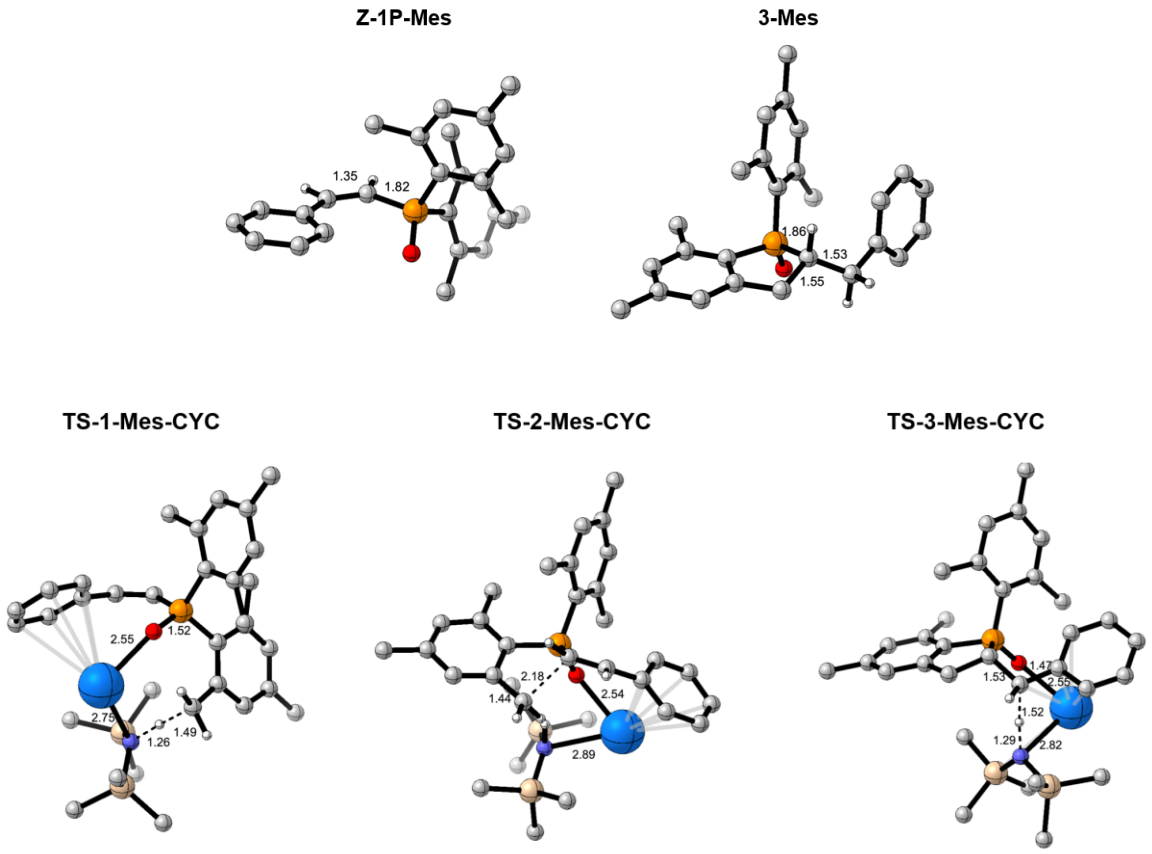

Figure 4.23.: Selected structures along the formation of phosphindole 1-oxide (**3-Mes**) by cyclization the *Z-isomer* formed in the first P-addition (**Z-1P-Mes)**. Top: reactant and product; bottom: transition states. Certain H atoms are omitted for clarity reasons. The distances presented are given in Å.

4.1.2.6.2. Sodium mediated Pudovik reaction (P-bound Mesityl substituent)

With the reaction mechanism for potassium-mediated hydrophosphorylation of phenylacetylene to mono- and bishydrophosphorylated products analysed, we can now turn our attention to investigating sodium-mediated hydrophosphorylation of phenylacetylene to monohydrophosphorylated products. Experimentally, the reaction exhibited a 31% conversion within 1 hour, with a ratio of 3/1 for E/Z isomers. After 27 hours, the conversion rate increased to over 99%, and the ratio of E/Z isomers shifted to 31/1 (see **Table 4.1**; **entry 2**). The quantity of **Z-1-Mes** product decreases due to a preferred second Na-mediated hydrophosphorylation, leading to the formation of 2-Mes.

4.1.2.6.2.1. Formation of *Z-isomer*

The addition of di(mesityl)phosphineoxide onto phenylacetylene resulting in monohydrophosphorylated products when the catalyst is Na-HMDS was investigated using an analogous mechanism as the one proposed in the case of K-HMDS. **Figure 4.24** depicts the Gibbs energy profile to produce *Z-isomer*. Selected optimised structure for the discussed TSs are illustrated in **Figure 4.25**.

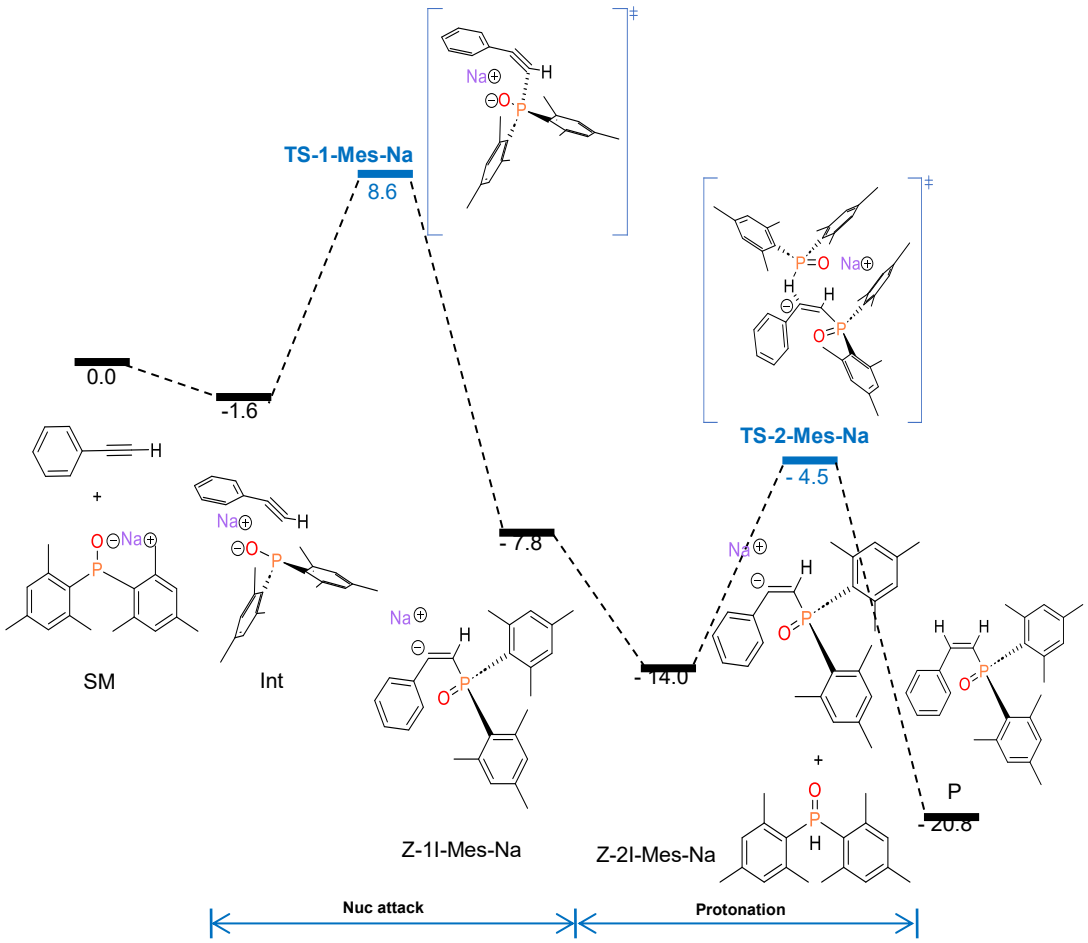

Figure 4.24.: Computed Gibbs energy profile in THF (ΔG_{THF} kcal mol^{-1}) at 298 K for sodium-mediated Pudovik reaction generating *Z*-dimesityl(styryl)phosphineoxide at the B3LYP-D3/def2-TZVP/SMD(THF)//B3LYP-D3BJ/6-31G(d,p)/SMD(THF) level of theory.

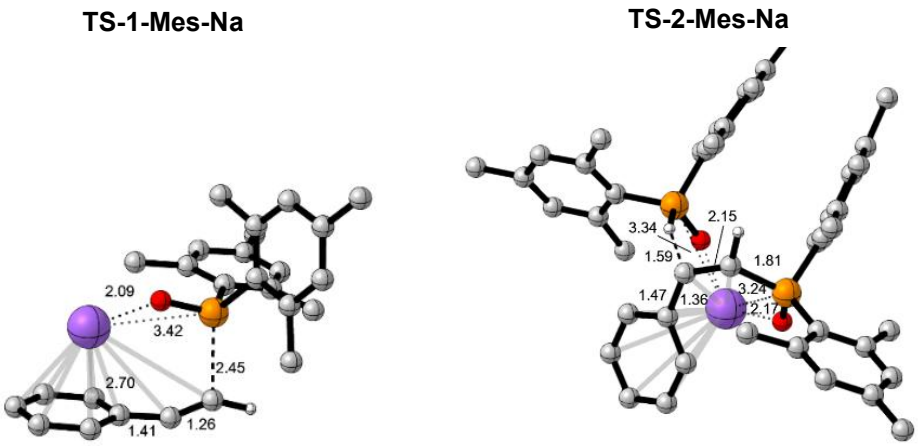

Figure 4.25.: Selected optimised structures for the transition states involved in the mechanism of sodium metal-mediated Pudovik reaction for formation of *Z*-dimesityl(styryl)phosphineoxide. Certain H atoms are omitted for clarity reasons. The distances presented are given in Å.

This mechanism starts with a slightly favourable concomitant interaction of -1.6 kcal mol^{-1}, for further discussion see **Section 4.1.2.5.** Then the nucleophilic attack happens (**TS-1-Mes-Na**) with an energy barrier of 10.2 kcal mol^{-1}. The intermediate produced by **TS-1-Mes-Na** is **Z-1I-Mes-Na**, which lays at -7.8 kcal mol^{-1} below the separated reactants (phenylacetylene + Na-$OPMes_2$). The protonation step, which follows the formation of the pro-*Z-isomer*, is helped by an extra Mes_2-P(O)H molecule. The protonation step progresses through the transition state (**TS-2-Mes-Na**) and necessitates an energy barrier of 9.5 kcal mol^{-1} and yields the *Z-isomer*.

Overall, it can be concluded that the formation of *Z-isomer* can proceed easily under the reaction conditions. This finding is in accordance with the experimental data (see **Table 4.1**, **entry 3**).

4.1.2.6.2.2. Formation of *E-isomer*

The reaction mechanism for the creation of this isomer will be analogous to the one for the potassium-mediated formation of *E-isomer*. **Figure 4.26** depicts the Gibbs energy profile derived to produce the *E-isomer*. **Figure 4.27** shows the optimised geometries for the transition states involved in the mechanism.

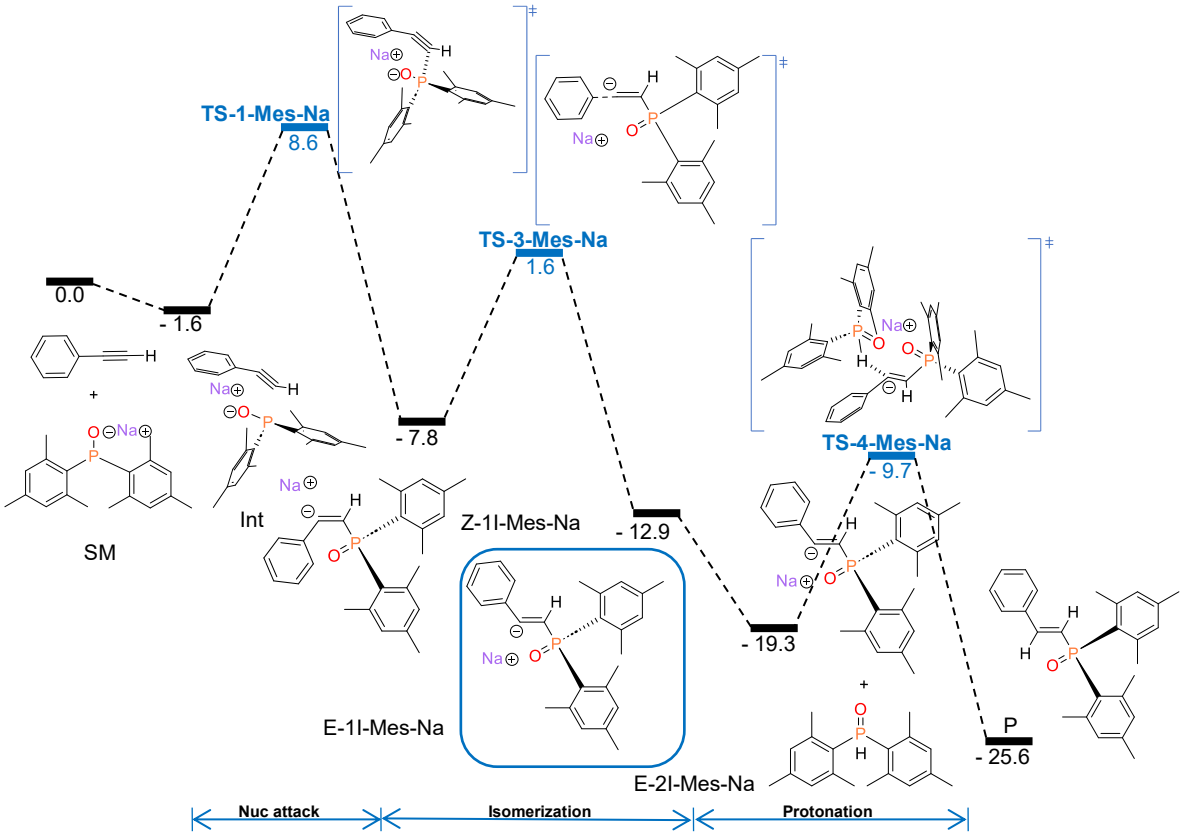

Figure 4.26.: Computed Gibbs energy profile in THF (ΔG_{THF} kcal mol^{-1}) at 298 K for sodium-mediated Pudovik reaction generating E-dimesityl(styryl)phosphineoxide at the B3LYP-D3/def2-TZVP/SMD(THF)//B3LYP-D3BJ/6-31G(d,p)/SMD(THF) level of theory.

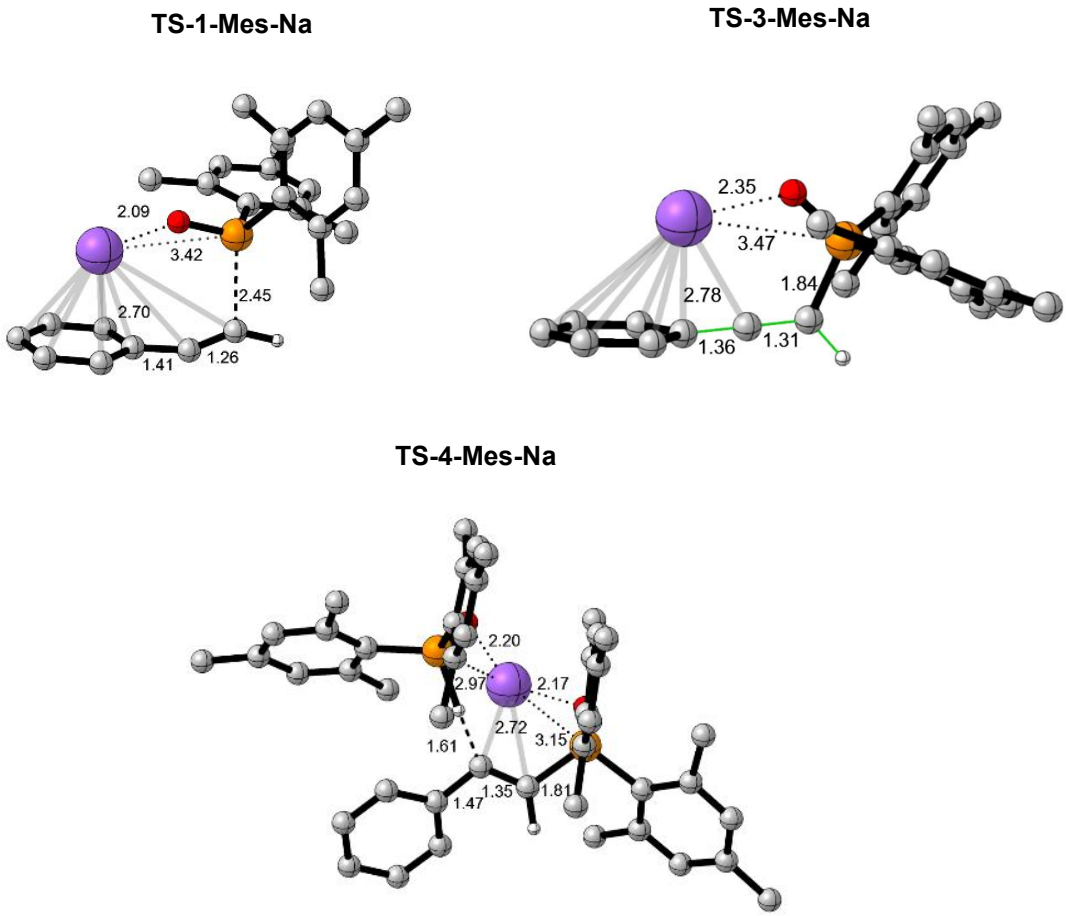

Figure 4.27.: Selected optimised structures for the transition states involved in the sodium metal-mediated mechanism for formation of E-dimesityl(styryl)phosphane. In the image for **TS-3-Mes-Na** we have marked the dihedral angle which marks the rotation around the double bond that facilitates the isomerization step. Certain H atoms are omitted for clarity reasons. The distances presented are given in Å.

The reaction pathway will be akin up to the creation of the **Z-1I-Mes-Na**. Following this, the **Z-1I-Mes-Na** will proceed through an isomerization step (**TS-3-Mes-Na**; 9.4 kcal mol^{-1}) to generate the **E-1I-Mes-Na** intermediate (-12.9 kcal mol^{-1}). As a result, we can argue that this step is thermodynamically favoured. This step is accomplished in the same manner as in potassium-mediated reaction. The final step is the protonation step **TS-4-Mes-Na** and this step will proceed with an energy barrier of 9.6 kcal mol^{-1}.

Upon analysing the Gibbs energy profiles for sodium-metal-mediated formation of both Z and E isomers, we can draw the same conclusions as for potassium-metal-mediated formation of Z and E isomers. Hence, we deduced from the DFT results that the key difference lies in the step for formation of the active species i.e., the reduced rate of conversion may be attributed to a minor concentration of the active species in the reaction medium.

4.1.2.5.3. Lithium mediated Pudovik reaction (P-bound Mesityl substituent)

With the reaction mechanism for sodium- and potassium-mediated hydrophosphorylation of phenylacetylene established, we can now turn our attention to investigating lithium-mediated hydrophosphorylation of phenylacetylene to mono-hydrophosphorylated products. Experimentally, this reaction showed no conversion upon 1h. However, after 27h, the conversion rate changed to 8% with 5/1 ratio for E/Z isomers (see **Table 4.1**; **entry 1**).

4.1.2.6.3.1. Formation of *Z-isomer*

The same postulated reaction mechanism was followed as in the potassium (K-HMDS) and sodium (Na-HMDS) mediated reactions. The Gibbs energy profile for lithium metal-mediated formation of *Z-isomer* is depicted in **Figure 4.28**. The optimized geometries for the transition states discussed in this mechanism are depicted in **Figure 4.29**.

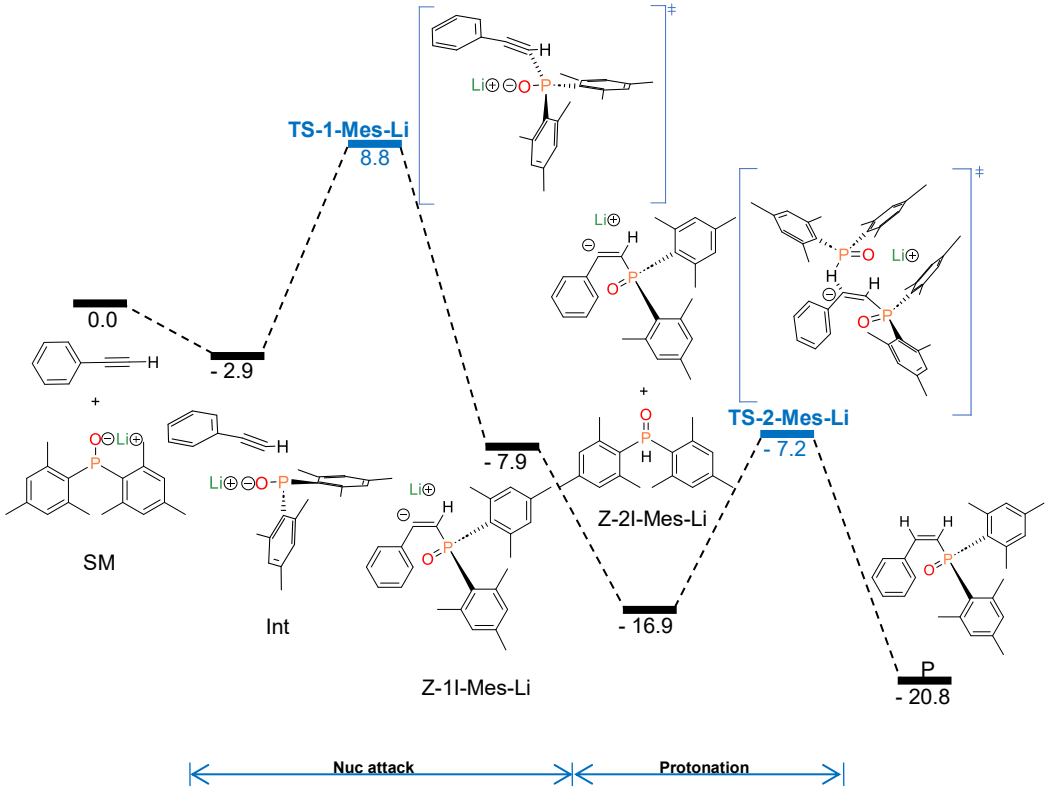

Figure 4.28.: Computed Gibbs energy profile in THF (ΔG_{THF} kcal mol^{-1}) at 298 K for lithium metal-mediated Pudovik reaction generating *Z*-dimesityl(styryl)phosphineoxide at the B3LYP-D3/def2-TZVP/SMD(THF)//B3LYP-D3BJ/6-31G(d,p)/SMD(THF) level of theory.

For the reaction to being we would need a concomitant interaction amongst the lithium atom and the aryl π-system. We were able to calculate that this interaction would lay at -2.9 kcal mol^{-1} below separated reactants (see **Section 4.1.2.4**), thus the initial interaction is favourable. The mechanism officially begins with a nucleophilic attack from the Li-OPMes$_2$ onto the C$_{Ph}$ from phenylacetylene (**TS-1-Mes-Li**) with an energy barrier of 11.7 kcal mol^{-1}. The yielded intermediate from **TS-1-Mes-Li** is **Z-1I-Mes-Li** which lies at -7.9 kcal mol^{-1} below the separated reactants (**1 + Li-OPMes$_2$**). The ensuing step for the formation of the *Z-isomer* is the protonation step which will be aided by an additional Mes$_2$-P(O)H molecule. The protonation proceeds through the transition state (**TS-2-Mes-Li**) with energy barrier of 9.7 kcal mol^{-1} and affords the *Z-isomer* at -20.8 kcal mol^{-1} below separated reactants.

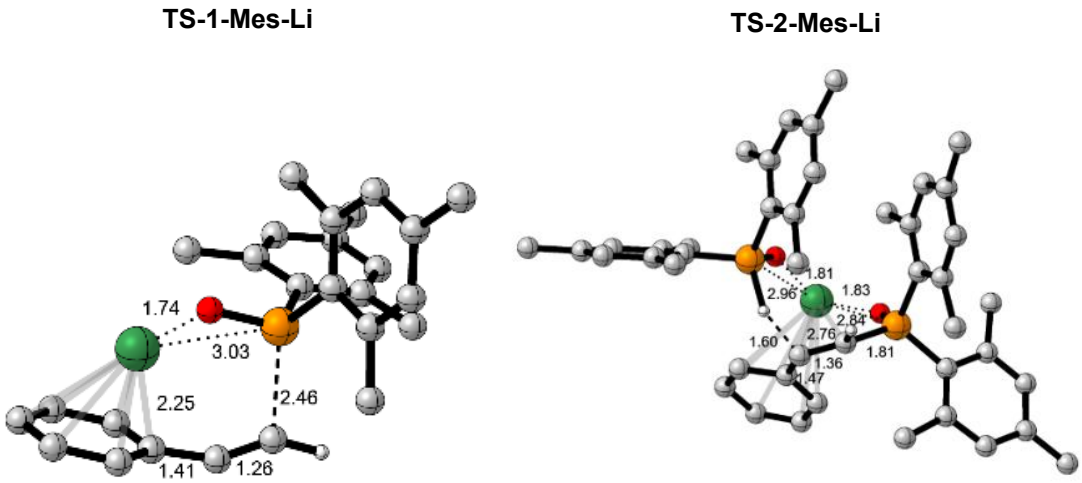

Figure 4.29.: Optimised structures for the transition states involved in the lithium metal -mediated mechanism for formation of *Z*-dimesityl(styryl)phosphineoxide. Certain H atoms are omitted for clarity reasons. The distances presented are given in Å.

Overall, the estimated energy barriers for lithium metal-mediated Pudovik reaction suggest that the formation of the *Z-isomer* should proceed without any hindrance. Therefore, the lack of reaction progress is likely not due to the mechanism itself but rather to another underlying cause, primarily the formation of the active species as established in **Section 4.1.2.3**.

4.1.2.6.3.2. Formation of *E-isomer*

As per the experimental results, the formation of the *E-isomer* occurred with a ratio of 5/1, albeit with the lowest conversion rate of 8% after 27 hours. The reaction mechanism for the formation of this isomer will follow analogous steps to those observed in the case of potassium mediated Pudovik reaction. **Figure 4.30** showcases the Gibbs energy profile obtained for the formation of *E-isomer*. The optimized geometries for the transition states involved in the mechanism are presented in **Figure 4.31**.

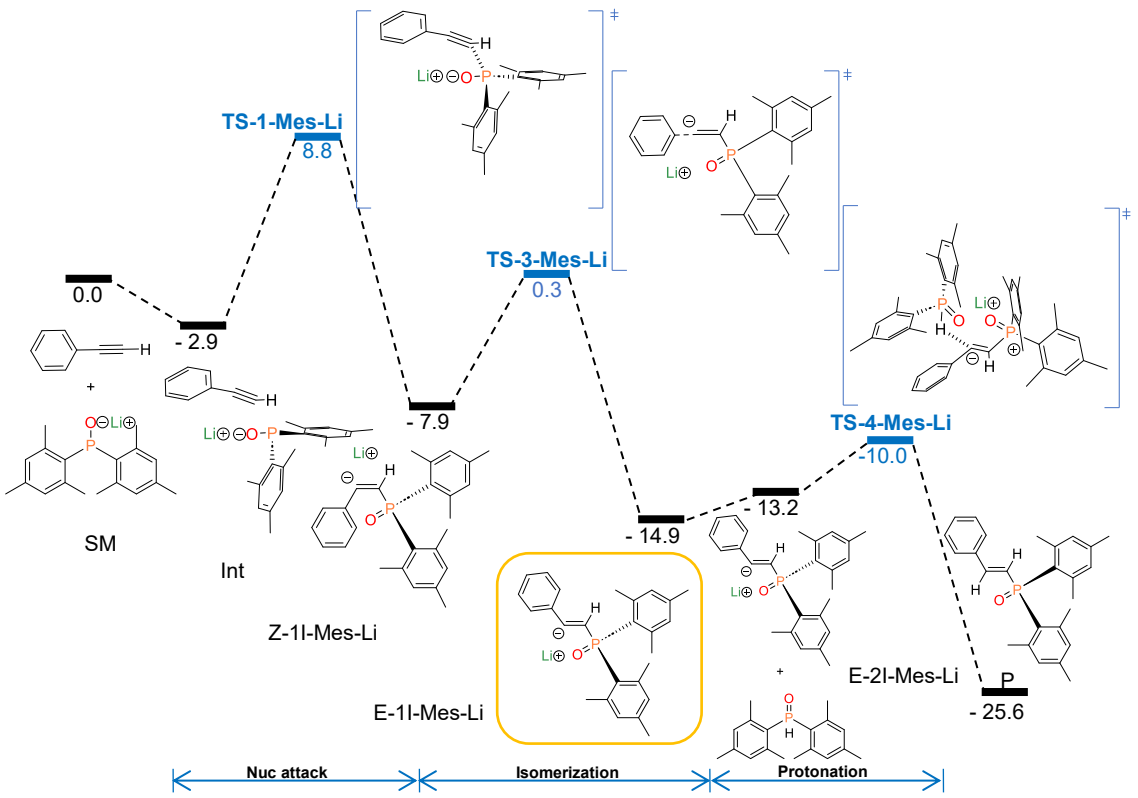

Figure 4.30.: Computed Gibbs energy profile in THF (ΔG_{THF} kcal mol^{-1}) at 298 K for lithium-mediated hydrophosphorylation of phenylacetylene for the formation of *E*-dimesityl(styryl)phosphineoxide with di(mesityl)phosphineoxide, using Li-HMDS as catalyst at the B3LYP-D3/def2-TZVP/SMD(THF)//B3LYP-D3BJ/6-31G(d,p)/SMD(THF) level of theory.

The reaction mechanism up to the formation of the **Z-1I-Mes-Li** will be identical. Upon this the **Z-1I-Mes-Li** will undergo an isomerization step **TS-3-Mes-Li** (8.2 kcal mol^{-1}) which would yield the **E-1I-Mes-Li** intermediate (-16.9 kcal mol^{-1}). Thus, it can be concluded that this step is thermodynamically driven. This step takes place essentially through bending of the $C_{terminal}$-$C_{internal}$-C_{Ph} angle and involves simultaneous change in coordination of the lithium cation, from interacting with π system of the aryl in **Z-1I-Mes-Li** to be σ coordinated to $C_{internal}$ in the lithium-vinyl intermediate **E-1I-Mes-Li** (**Figure 4.31**).

TS-1-Mes-Li

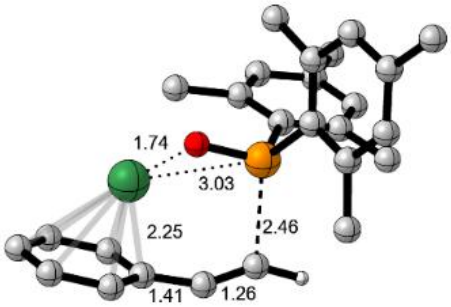

TS-3-Mes-Li

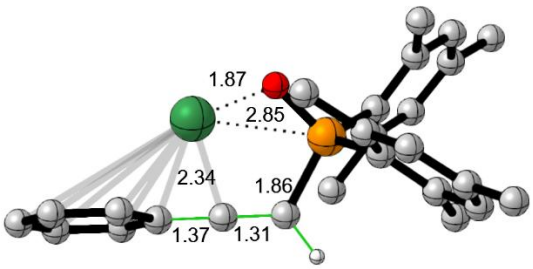

TS-4-Mes-Li

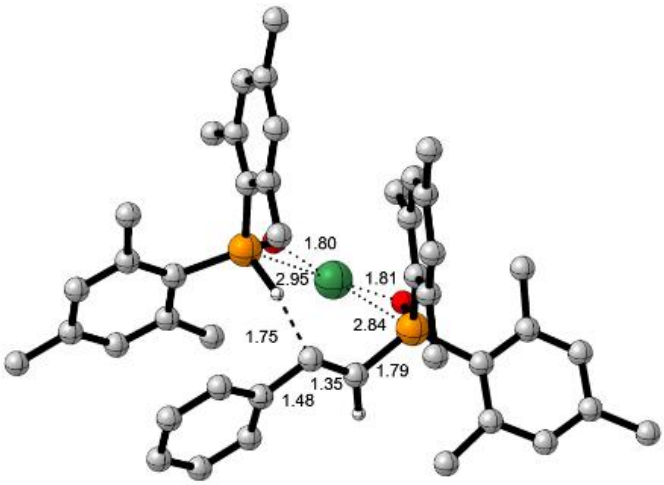

Figure 4.31.: Optimised structures for the transition states involved lithium-mediated hydrophosphorylation of phenylacetylene for the formation of *E*-dimesityl(styryl)phosphineoxide with di(mesityl)phosphineoxide, using Li-HMDS as catalyst. In the image for **TS-3-Mes-Li** we have marked the dihedral angle which marks the rotation around the double bond that facilitates the isomerization step. Certain H atoms are omitted for clarity reasons. The distances presented are in Å.

After analysing the Gibbs energy profiles for potassium-, sodium-, and lithium-metal-mediated Pudovik reaction, it is evident that the formation of both E and Z isomers can proceed without hindrance in all cases. However, the only notable difference observed throughout the calculations lies in the energy required for the formation of the active species. This indicates that while the alkali cations may appear to be spectators, they play a significant role in the reaction mechanism. Therefore, it is inaccurate

to consider alkali cations as freely interchangeable, as there are differences in the steps and intermediates depending on the identity of the alkali cation.

4.1.2.6.4. Role of the cation in the Pudovik reaction (P-bound Mesityl substituent)

To check the effect of the alkali metal on the overall process we investigated the addition step with M = H, that means retaining the hydrogen atom in the phosphineoxide. It is important to note that the P(III) tautomer is consistently less stable, regardless of the P-bound group. The Gibbs energy profile for this addition involving a P-bound mesityl group is depicted in **Figure 4.32** whilst, the optimized structure of the transition state may be found in **Figure 4.33**.

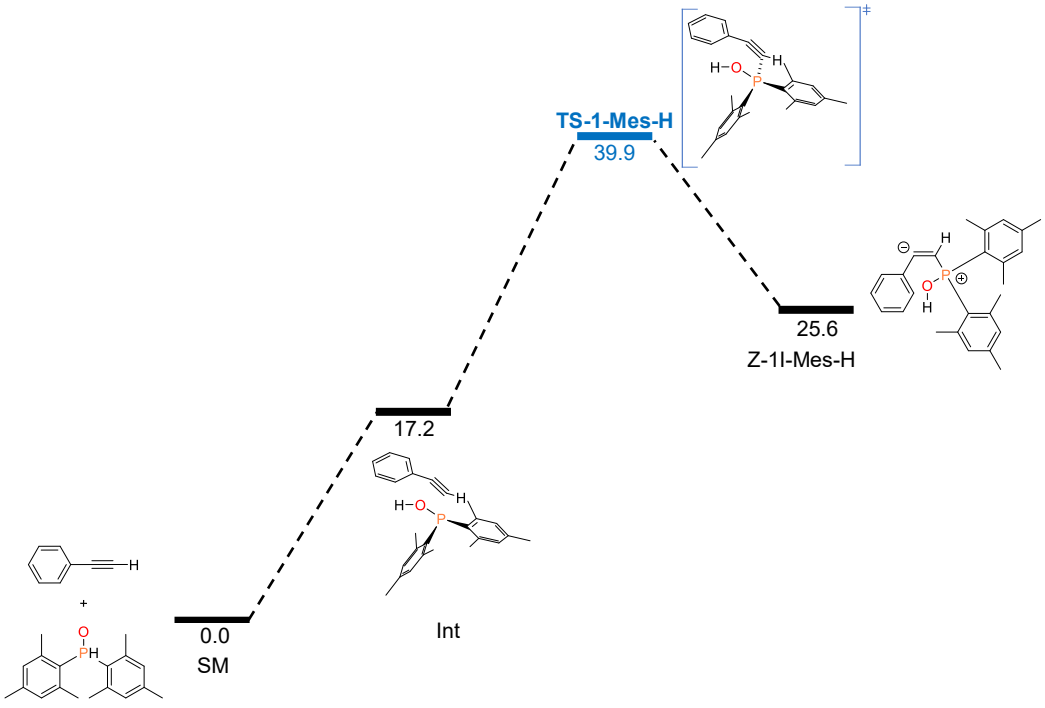

Figure 4.32.: Computed Gibbs energy profile in THF (ΔG_{THF} kcal mol^{-1}) at 298 K for the formation of pro-*Z-isomer* with Mes_2-P(O)H at a B3LYP-D3/def2-TZVP/SMD(THF)//B3LYP-D3BJ/6-31G(d,p)/SMD(THF) level of theory.

TS-1-Mes-H

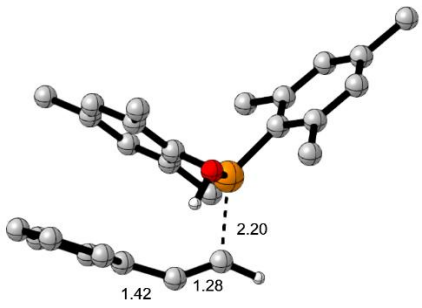

Figure 4.33.: Optimised structures for the transition states involved in for the formation of pro-*Z-isomer* with M = H. Certain H atoms are omitted for clarity reasons. The distances presented are given in Å.

Replacing the alkali cation with a proton result in the loss of the cation-π interaction, leading to unstable initial adduct with positive Gibbs energy values. Additionally, the Gibbs energy of activation for the nucleophilic attack increases more than twofold compared to when the K ion is present in the catalyst, rising from $\Delta\mathbf{G}^{\ddagger}$= 10.3 kcal mol^{-1}(K) to $\Delta\mathbf{G}^{\ddagger}$= 22.7 kcal mol^{-1}(H). Furthermore, the overall Δ_rG value becomes positive for the reaction in which the metal is replaced by a proton, indicating a less thermodynamically stable product (25.6 kcal mol^{-1}). In contrast, when M = K, the overall Δ_rG value is negative, suggesting a thermodynamically plausible reaction (-6.2 kcal mol^{-1}). Moreover, this matches our experimental findings as when the catalyst is omitted the reaction doesn't ensue.

The results in this section, as well as in the previous ones, demonstrate that alkali cations play a role not only in reducing the reaction barriers and increasing the stability of intermediates but also in facilitating the formation of the active species.

4.1.2.7. The effect of the P-bound group

In the following section we will discuss the influence of the P-bound group on the overall outcome of the reaction. In this section we will discuss the cases when we have Ph, cyclohexyl and OEt as P-bound groups. The following discussion pertains to potassium mediated reactions. The discussion regarding the formation of E/Z isomers

when the P-bound groups consist of both Ph and Mes simultaneously is omitted, as there was no significant difference observed compared to when Mes was the sole P-bound group.

4.1.2.7.1. P-bound group phenyl substituent

As a reminder, experimentally this reaction proceeds with conversion of 14% upon 1h of which <1% formation of **1-R** (E/Z) and >99% formation of **2-R** (see **Table 4.2**; **entry 3**).

4.1.2.7.1.1. Formation of *Z-isomer*

The 1st nucleophilic attack for the formation for the Z isomer proceeds *via* anti-Markovnikov addition (**TS-1-Ph-K**; 11.4 kcal mol^{-1}), yielding intermediate **Z-1I-Ph-K** (-7.6 kcal mol^{-1}). In this TS the potassium cation interacts with the π-aryl system at a distance of 3.16 Å, so this interaction takes place at a shorter distance than for **TS-1-Mes-K**.[4] Hence, it may be deduced that increased interaction of the cation with the π-aryl system does not always lead to lower energy barrier. The ensuing step is the protonation step (**TS-2-Ph-K**; 9.5 kcal mol^{-1}) which leads to the formation of ***Z-isomer*** (-29.2 kcal mol^{-1}). **Figure 4.34** showcases the estimated Gibbs energy barrier for the formation of the Z isomer, whilst **Figure 4.35** depicts selected amended structures.

[44] Reminder: The distance is estimated by inserting a dummy atom within the phenyl ring and calculating the distance from the dummy atom to the alkali cation.

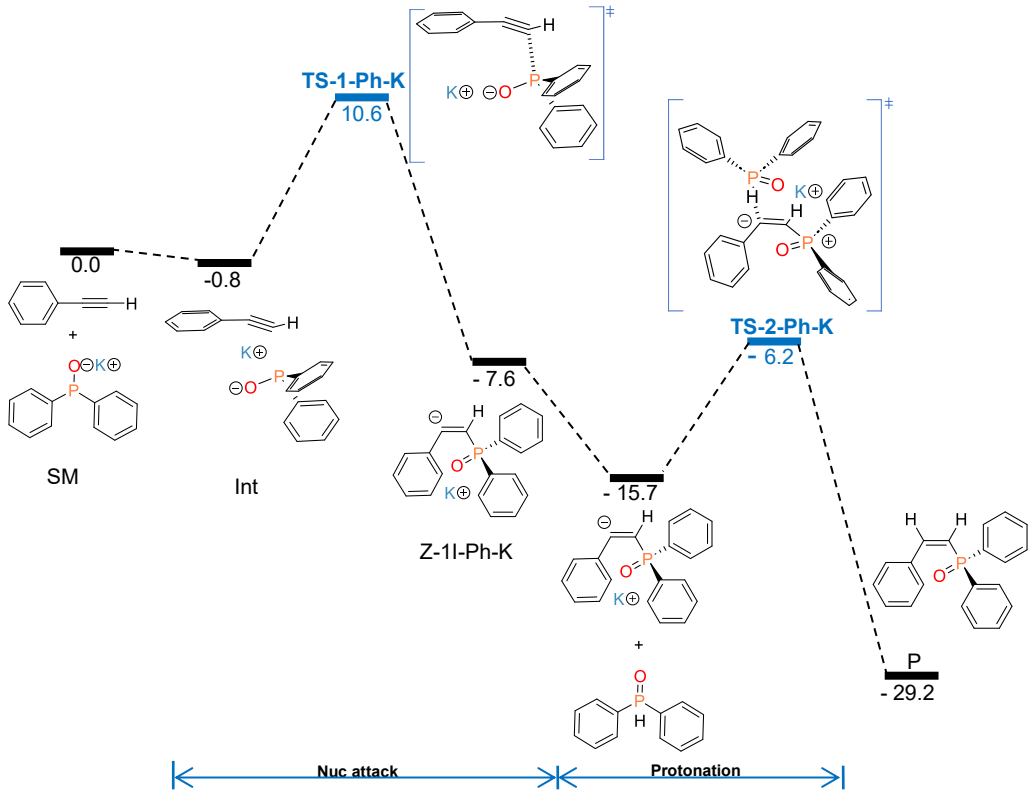

Figure 4.34.: Computed Gibbs energy profile in THF (ΔG_{THF} kcal mol^{-1}) at 298 K for potassium-mediated hydrophosphorylation of phenylacetylene for the formation of *Z*-diphenyl(styryl)phosphineoxide with di(phenyl)phosphineoxide, using K-HMDS as catalyst at the B3LYP-D3/def2-TZVP/SMD(THF)//B3LYP-D3BJ/6-31G(d,p)/SMD(THF) level of theory.

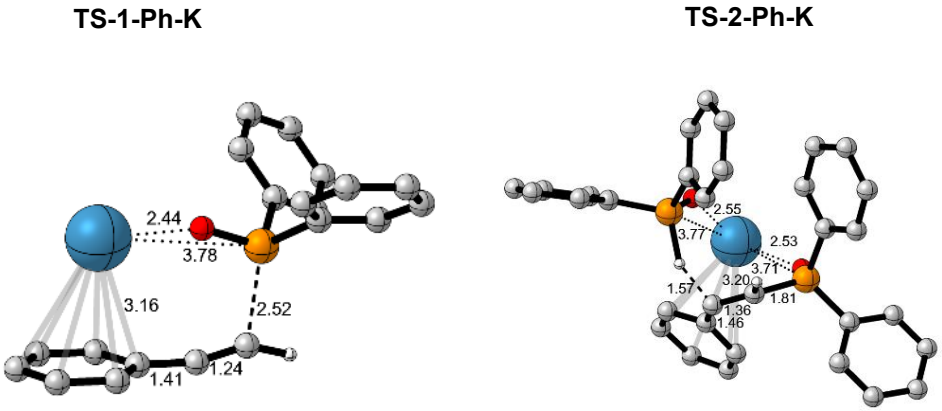

Figure 4.35.: Selected optimised structures for the transition states involved in the potassium metal-mediated mechanism for formation of *Z*--diphenyl(styryl)phosphineoxide. Certain H atoms are omitted for clarity reasons. The distances presented are given in Å.

From the Gibbs energy profile for the formation of the *Z-isomer* we can see that there are not steps which hinder this reaction. Following the pattern from P-bound mesityl group in this case too we cannot say which step is the RDS, as the difference between the two steps is less than 2 kcal mol^{-1}.

4.1.2.7.1.2. Formation of *E-isomer*

In this instance we were also able to detect only direct formation of the intermediate with the pro-Z configuration (**Z-1I-Ph-K**). **Figure 4.36** shows the calculated Gibbs energy barrier for the creation of the E isomer, on the other hand, **Figure 4.37** depicts the optimized structures for the corresponding transition states.

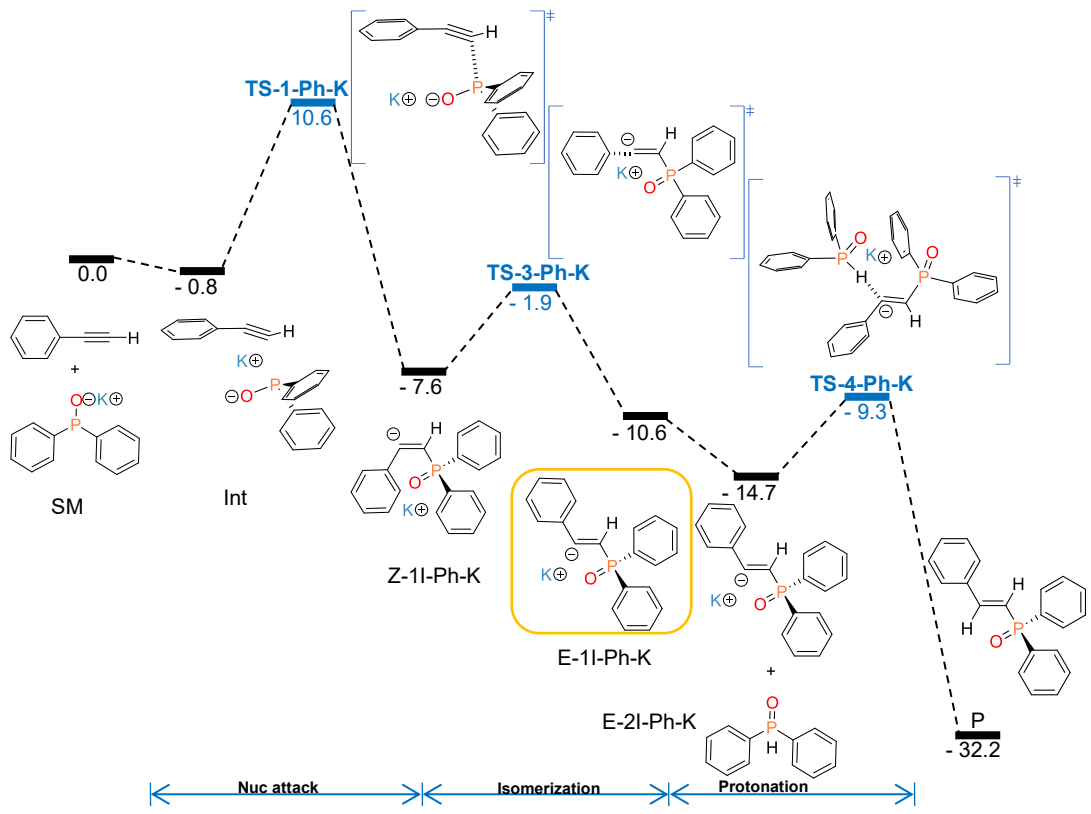

Figure 4.36.: Computed Gibbs energy profile in THF (ΔG_{THF} kcal mol^{-1}) at 298 K for the potassium-mediated hydrophosphorylation of phenylacetylene for the formation of *E*-diphenyl(styryl)phosphineoxide with di(phenyl)phosphineoxide, using K-HMDS as catalyst at the B3LYP-D3/def2-TZVP/SMD(THF)//B3LYP-D3BJ/6-31G(d,p)/SMD(THF) level of theory.

Hence, having determined the 1st nucleophilic attack the ensuing step of isomerization **TS-3-Ph-K** was estimated to proceed with a barrier of 5.7 kcal mol^{-1}. The distinguished change in the coordination of the potassium cation along the isomerisation, from interacting with the π system of the aryl in **Z-1I-Ph-K** to be σ coordinated to $C_{internal}$ in the potassium-vinyl intermediate **E-1I-Ph-K** as in the mesityl case (**Figure 4.16**) was also observed. Comparatively the **E-1I-Ph-K** (-10.6 kcal mol^{-1}) intermediate is more thermodynamically favoured over **Z-1I-Ph-K** (- 7.6 kcal mol^{-1}) intermediate.

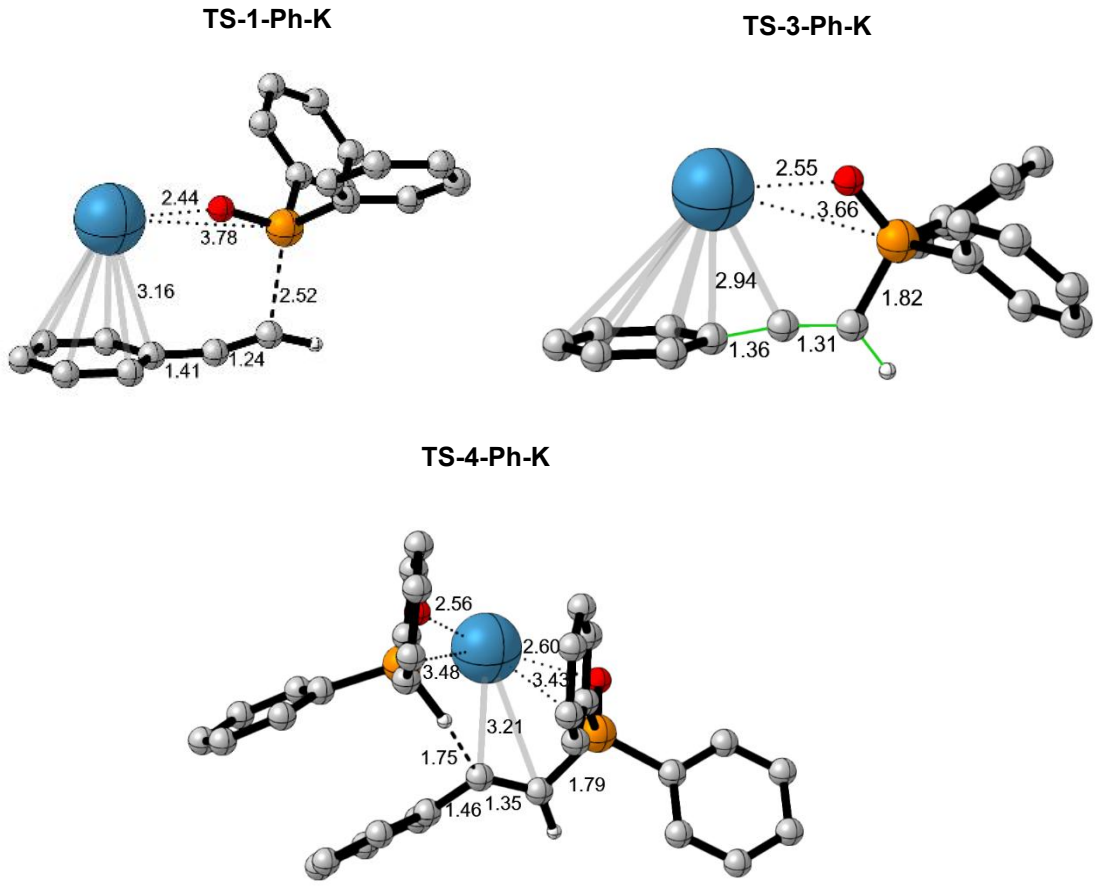

Figure 4.37.: Selected optimised structures for the transition states involved in the potassium-mediated hydrophosphorylation of phenylacetylene for formation of *E*- diphenyl(styryl)phosphineoxide with di(mesityl)phosphineoxide, using K-HMDS as catalyst. In the image for TS-3-Ph-K we have marked (green line) the dihedral angle which marks the rotation around the double bond that facilitates the isomerization step. Certain H atoms are omitted for clarity reasons. The distances presented are given in Å.

The successive protonation step will follow with a low energy barrier of (5.4 kcal mol^{-1}) and will lead to formation of the *E-isomer* of the alkenyl diphenylphosphineoxide

(ΔG = -32.2 kcal mol^{-1}). It may be concluded that overall, the formation of *E-isomer* is overall exergonic (-32.2 kcal mol^{-1}) and it is governed by thermodynamics (***Z-isomer***; -29.2 kcal mol^{-1}). The results in this section mirror the results for the formation of the E and Z isomer when P-bound groups is mesityl.

4.1.2.7.1.3. Formation of bisphosphorylated product

When the P-bound group is phenyl, the formation of the double hydrophosphorylation product takes place and is preferred over the formation of the monophosphorylated product (see **Table 4.2**; **entry 3**).[4] The newly formed alkene moiety is reactive enough to add another phosphinite leading to bishydrophosphorylated compounds. Just like the first hydrophosphorylation, the second one will proceed in two steps: nucleophilic attack and a protonation step. We have followed the second addition from both *Z*- and *E-isomer*s, showing very similar feature. The Gibbs energy profile for the formation of the bisphosphorilated alkane product from the *Z*-alkenyl diphenyl phosphineoxide is displayed in **Figure 4.38**. The optimized structure for the TSs for the formation of the bis-phosphorylated product are illustrated in **Figure 4.39**.

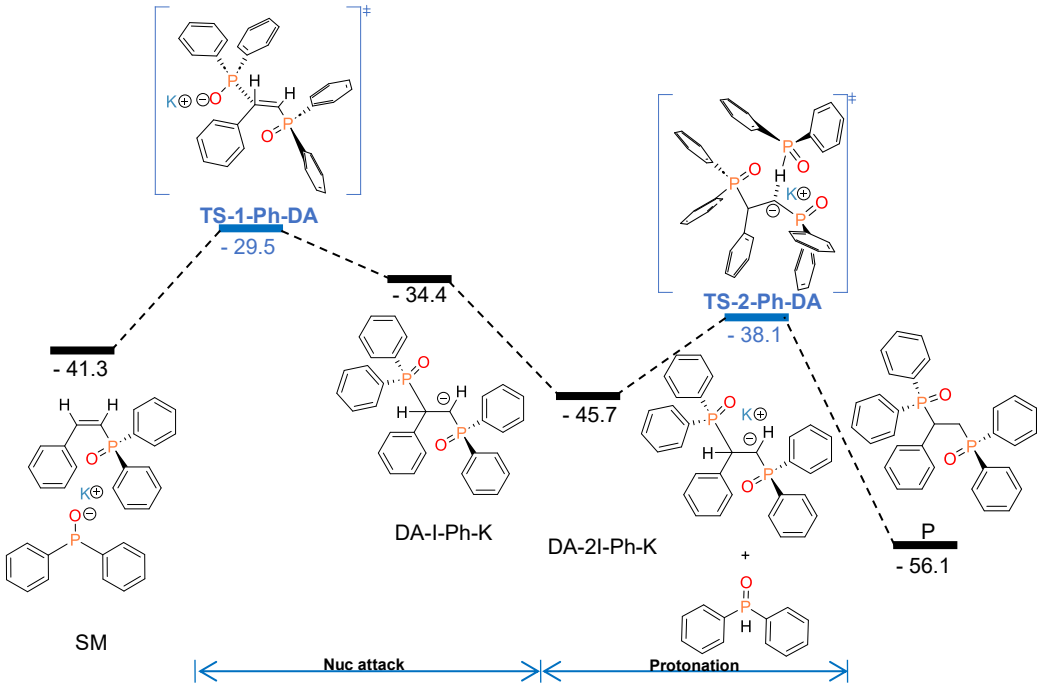

Figure 4.38.: Computed Gibbs energy profile in THF (ΔG_{THF} kcal mol^{-1}) at 298 K for potassium-mediated bishydrophosphorylation of phenylacetylene for the formation of

bishydrophosphorylated product with di(phenyl)phosphineoxide, using K-HMDS as catalyst from *Z*-diphenyl(styryl)phosphineoxide at the B3LYP-D3/def2-TZVP/SMD(THF)//B3LYP-D3BJ/6-31G(d,p)/SMD(THF) level of theory.

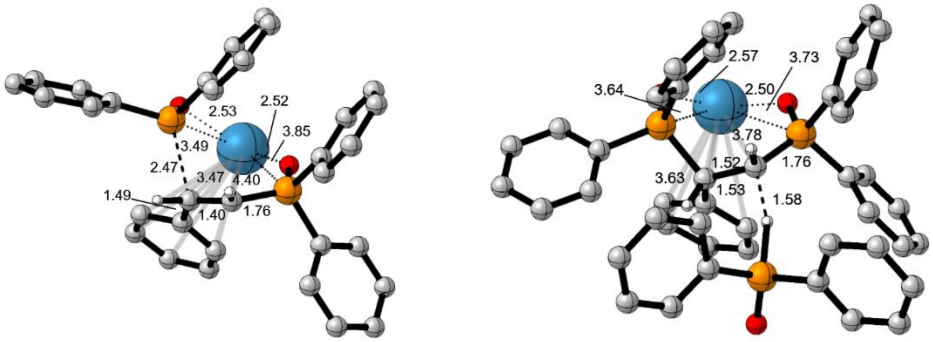

Figure 4.39.: Selected optimised structures for the transition states involved in potassium metal-mediated bishydrophosphorylation of phenylacetylene for the formation of bis-phosphorylated product with di(phenyl)phosphineoxide, using K-HMDS as catalyst. Certain H atoms are omitted for clarity reasons. The distances presented are given in Å.

The nucleophilic addition step of the second phosphorylation, when compared to that of the first phosphorylation, shows an insignificant difference in barrier heights (see **Figures 4.34** vs **4.38**). However, it is lower than that for the second addition to the mesityl system (16.2 kcal mol^{-1}, **Figure 20**). The protonation barrier for **TS-2-Ph-K** (7.6 kcal mol^{-1}) is also much lower than that for the mesityl substituted phosphineoxide (26.6 kcal mol^{-1}). The final product is very stable (-56.1 kcal mol^{-1}) showing a strong thermodynamic driving force for the process. Overall, these theoretical findings justify the experimental observance of a >99% conversion of the bishydrophosphorylation product with the diphenyl phosphineoxide (**Table 4.2**, **entry 3**).

4.1.2.7.2. P-bound group cyclohexyl substituent

According to the experimental results the reaction when P-bound group are cyclohexyl is inhibited (see **Table 4.2**; **entry 4**). Our study on the formation of the catalytic active species gives evidence that K-$OP(Cy)_2$ can be hardly formed under

reaction conditions (see **Section 4.1.2.3.**) However, for comparative purposes we also computed the energy pathway for this reaction.

Our investigations afforded the energy reaction profile for the Z isomer which is depicted in **Figure 4.40**. The optimized structures for the TSs implicated in this mechanism are shown in **Figure 4.41**.

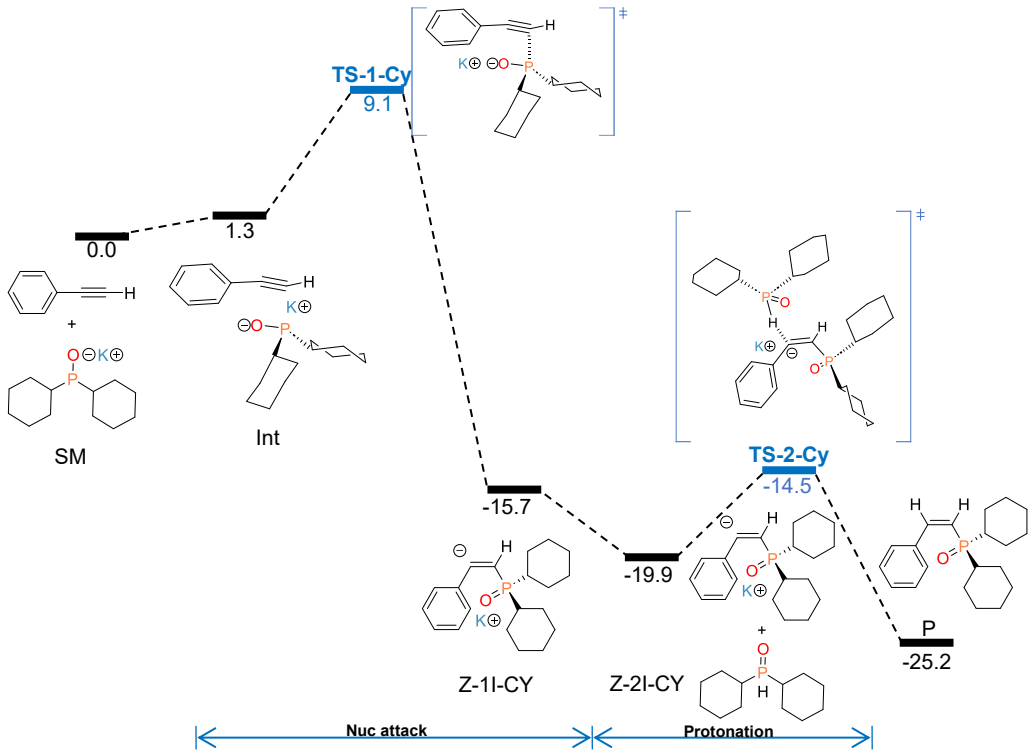

Figure 4.40.: Computed Gibbs energy profile in THF (ΔG_{THF} kcal mol^{-1}) at 298 K for potassium-mediated hydrophosphorylation of phenylacetylene for the formation of *Z*-dicyclohexyl(styryl)phosphineoxide with di(cyclohexyl)phosphineoxide, using K-HMDS as catalyst at the B3LYP-D3/def2-TZVP/SMD(THF)//B3LYP-D3BJ/6-31G(d,p)/SMD(THF) level of theory.

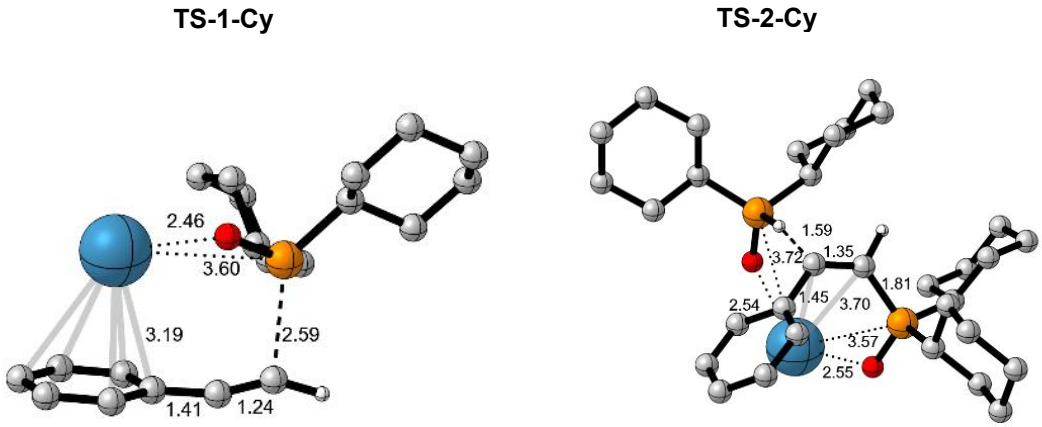

Figure 4.41.: Optimised structures for the transition states involved in the potassium-mediated hydrophosphorylation of phenylacetylene for the for formation of *Z*- dicyclohexyl(styryl)phosphineoxide with di(cyclohexyl)phosphineoxide, using K-HMDS as catalyst. Certain H atoms are omitted for clarity reasons. The distances presented are given in Å.

As already established, the first step of the reaction mechanism is the nucleophilic attack (**TS-1-Cy**) and it affords the intermediate **Z-1I-CY** (- 15.2 kcal mol^{-1}) with an energy barrier of 9.1 kcal mol^{-1}. Upon generation of **Z-1I-CY**, the protonation takes place with a relative energy barrier of 5.4 kcal mol^{-1} (**TS-2-Cy**) resulting in the final product (-25.2 kcal mol^{-1}).

In the estimated energy pathway, the highest energy barrier corresponds to the nucleophilic attack *via* **TS-1-Cy**. Since both computed barriers are low and have similar values to when the P-bound group is Ph and the reaction proceeds, the prevailing factor for why this reaction to be suppressed might only be attributed to the formation of the active species.

4.1.2.7.3. P-bound group ethoxy substituent

In the case of P-bound alkoxy groups the potassium-mediated hydrophosphorylation of phenylacetylene is also suppressed (see **Table 4.2**; **entry 5**). However, the initial study of the formation and deactivation of active species (see **Section 4.1.2.3**) does not show noticeable differences whit cases in which the reaction happens. Moreover, K-$OP(Cy)_2$ seems to be stable toward dismutation. Therefore, this is not likely to be the cause for the suppressed reaction. Here, we will solely address the formation of the *Z-isomer*. The reaction with the PCy_2 phosphineoxide involves the same steps as

the other di(aryl) potassium-mediated hydrophosphorylation of phenylacetylene. The most noteworthy difference amongst these mechanisms is the interaction between potassium cation and the additional oxygen atoms. The Gibbs energy profile for this mechanism is presented in **Figure 4.42**, whilst the optimized geometries for the transition states involved in this mechanism are presented in **Figure 4.43**.

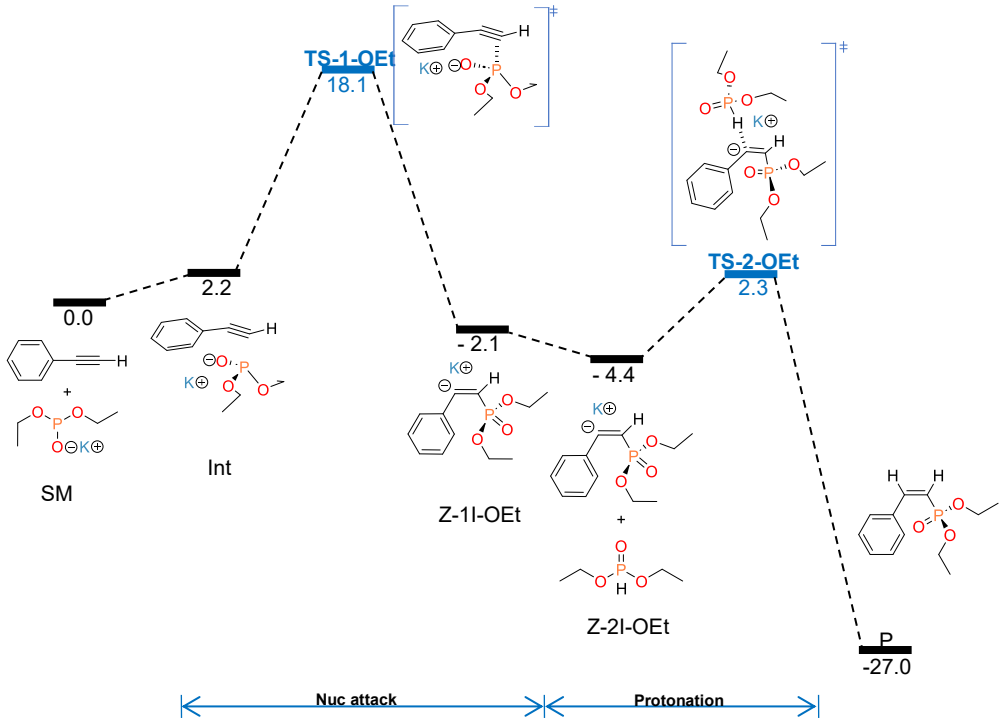

Figure 4.42.: Computed Gibbs energy profile in THF (ΔG_{THF} kcal mol^{-1}) at 298 K for potassium-mediated hydrophosphorylation of phenylacetylene for the formation of *Z*-diethoxy(styryl)phosphineoxide with di(ethoxy)phosphineoxide, using K-HMDS as catalyst at the B3LYP-D3/def2-TZVP/SMD(THF)//B3LYP-D3BJ/6-31G(d,p)/SMD (THF) level of theory.

TS-1-OEt **TS-2-OEt**

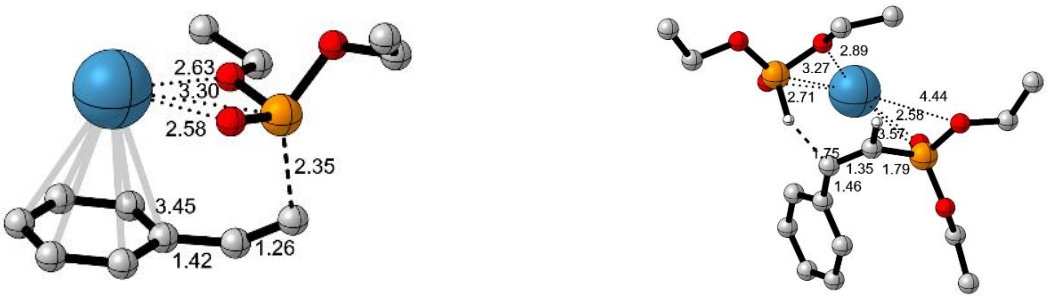

Figure 4.43.: Optimised structures for the transition states associated with the potassium -mediated hydrophosphorylation of phenylacetylene for the formation of *Z*-diethoxy(styryl)phosphineoxide with di(ethoxy)phosphineoxide, using K-HMDS as catalyst. Certain H atoms are omitted for clarity reasons. The distances presented are given in Å.

The nucleophilic attack (**TS-1-OEt**) results in the intermediate **Z-1I-OEt** (-2.1 kcal mol^{-1}) with an energy barrier of 15.9 kcal mol^{-1}. Once **Z-1I-OEt** is formed, an additional molecule of OEt_2-P(O)H will protonate it with an energy barrier of only 6.7 kcal mol^{-1} (**TS-2-OEt)** generating the product (-27.0 kcal mol^{-1}).

Overall, it can be concluded that the reaction is exergonic (-27.0 kcal mol^{-1}), with the nucleophilic attack being the rate-determining step for this mechanism. The energy barrier for **TS-1-OEt** is 7.8 kcal mol-1 higher than the one estimated for **TS-1-Mes**, indicating that in terms of reaction rates, this reaction should be several orders of magnitude slower. The higher barrier for the nucleophilic attack, related to the lower nucleophilicity of the p-centre surrounded by oxygen atoms, might be the reason for the non-observance of reaction in this case.

4.2. Conclusion

The goal of this chapter was to elucidate the key factors influencing the stereo- and regio-selectivity in catalytic P-C bond formation across unsaturated substrates and to clarify the role of alkali metal ions in the reaction mechanism. More concretely, this work aimed on clarifying the reaction mechanism for the alkali metal-mediated Pudovik reaction i.e., the addition of secondary phosphineoxides across phenylacetylene *via* alkali metal hexamethyldidilazides (M-HMDS; M = Li, Na and K). Based on the previous experimental results (see **Table 4.1** and **4.2**), it was deduced that the metal cations play a crucial role as the conversion showed dependence on the softness and the radius of the metal ions, regardless of the P-bounded group in the P(V) compounds for this addition. Overall, the lighter s-block metal congener Li-HMDS was not able to mediate any of the reactions, whilst the congeners of the heavier alkali metal bis(trimethylsilyl)amides M-HMDS (M = K and Na) effectively promoted hydrophosphorylation across phenylacetylene.

The active species can be generated by deprotonation of dimesityl phosphineoxide by alkali metal hexamethyldisilazanides (M-HMDS). However, the formation of the active species may be affected by deactivation processes, such as aggregation and dismutation, which can reduce the concentration of catalytically active species in the reaction medium that can dilute the concentration of the catalytically active species in the reaction medium. The thermodynamic feasibility of the formation of the active species (metal-phosphinite catalyst, M-OPR_2) from the corresponding M-HMDS catalysts and R_2-P(O)H displayed a strong dependence on the P-bound groups and moreover varied strongly depending on the alkali cation (see **Tables 4.3, 4.4** and **4.5**). Our calculations indicated that alkali metal dimesitylphosphinites (M-$OPMes_2$, where M = Li, Na, and K) are sufficiently nucleophilic to serve as active species in the formation of P–C bonds during the addition reaction. Notably, the influence of the alkali metal cation on the addition process is minimal, resulting in only slight variations in the nucleophilicity of the phosphinite.

We also determined that the interaction of the alkali cation from the active species with the π-systems is contingent on the alkali cation, with the lithium cation preferably interacting with the C≡C bond, whilst potassium predominantly interacting with the π-system from the phenyl ring, the interaction of sodium was on the middle of the π system.

Experimentally, for alkali mediated Pudovik reaction, all of the reactions proceeded to yield the anti-Markovnikov product regardless if the reaction proceeded to E/Z isomer. Implementing DFT methods we were able to determine that this outcome arises from the lower activation energy and its thermodynamic preference. The Anti-Markovnikov regioselectivity is governed by the π-withdrawing nature of the phenyl group, which enhances the electrophilicity of the terminal carbon, thereby facilitating the nucleophilic attack. More interestingly, the results derived from this study revealed that the kinetically preferred product is the Z whilst the thermodynamically preferred is the E isomer for this section. We reached a limitation in our studies as we were not able to find a nucleophilic attack directly yielding pro-E intermediate, thus, we proposed an isomerization step from pro-Z intermediate to explain the observed stereoselectivity in the reaction.

The estimated energy profiles indicated that the reaction pathways could proceed under the reaction conditions and without significant variations related to the alkali metal. To furthermore assess the influence of the metal cation over the reaction barriers, substituting the metal ion with a hydrogen atom (effectively a proton). his substitution revealed that replacing the alkali cation with a proton effectively doubles the barrier for the nucleophilic attack (**Table 4.8**; **entry 1**), demonstrating that using the alkali cation is essential for the reaction to occur. However, the energy barriers did not exhibit significant differences based on the type of alkali cation (see **Table 4.8**). Interestingly, the DFT results reflected the same trend observed experimentally regarding the ability of the alkali metals to catalyse the Pudovik reaction in relation to chemical hardness M^+ (M = Li, Na, and K).

Table 4.8.: Computed Gibbs energy barriers in THF ($\Delta \mathbf{G}^{\ddagger}$ kcal mol^{-1}) at 298 K for the two steps of Pudovik reaction (addition of dimesitylphosphineoxide across phenylacetylene) depending on the alkali metal of the utilised bis(trimethylsilyl)amide catalyst (M-HMDS; M = Li, Na and K) at the B3LYP-D3/def2-TZVP/SMD(THF)//B3LYP-D3BJ/6-31G(d,p)/SMD(THF) level of theory.

Entry	Metal	***Z-isomer*** ($\Delta \mathbf{G}^{\ddagger}$)		***E-isomer*** ($\Delta \mathbf{G}^{\ddagger}$)		
		Nuc attack	Protonation	Nuc attack	Isomerization	Protonation
1	H	22.7	/	/	/	/
2	Li	11.7	9.7	11.7	8.2	3.2
3	Na	10.2	9.5	10.2	9.4	9.6
4	K	10.3	10.5	10.3	4.9	12.9

The inhibition of the lithium mediated Pudovik reaction might be attributed to a reduced concentration of the active species in the reaction medium, arising from a less favourable disaggregation of the Li-HMDS dimer (ΔG = 1.0 kcal mol^{-1}), a highest barrier for the P- to N- proton transfer step (see **Table 4.3**) and a higher tendency to dimerisation (see **Table 4.4**). It may be concluded that the identity of the alkali cations does play a significant role in the formation of the active species but, not in the Pudovik reaction itself. Indeed, the no-reaction with $Cy_2P(O)H$ can be attributed to the no-formation of the K-$OPCy_2$ active species. As it may be seen from **Table 4.8** there is no discernible difference between the energy steps yielding *Z* vs *E-isomer*, with the exception of protonation step for formation of *E*-somer for lithium mediated reaction. Additionally, we were able to determine that H-HMDS can function as an additional protonating agent within the reaction mixture, and in certain cases, it might even be the preferred choice in certain situations.

The energy barriers also showed dependence amongst the different P–bound substituents (see **Table 4.9**). The influence on the P-bound substituent is the most pronounced when comparing the energy barrier for the nucleophilic step between P-bound group Mes and OEt. In this case we see almost doubling of the energy necessary for this step to proceed. Moreover, for P-bound OEt group we can say that the hindering step is indeed the nucleophilic attack, as the energy of formation of the active species is exergonic -14.0 kcal mol^{-1}. However, as the energy barriers for both steps

for the case of R = Cy are similar to those for R-Mes and R-Ph, the limitation of this reaction may be ascribed to the unfavourable thermodynamics for the of the active species ($\Delta \mathbf{G_R}$ = 7.8 kcal mol^{-1}).

Table 4.9.: Computed Gibbs energy barriers in THF ($\Delta \mathbf{G}^{\ddagger}$ kcal mol^{-1}) at 298 K for the two steps of hydrophosphorylation across phenylacetylene depending on the P-bound group of the di(organyl)phosphineoxide, using K-HMDS as catalyst at the B3LYP-D3/def2-TZVP/SMD(THF)//B3LYP-D3BJ/6-31G(d,p)/SMD(THF) level of theory.

Entry	**P-bound group**	***Z-isomer*** ($\Delta \mathbf{G}^{\ddagger}$)	
		Nuc attack	Protonation
1	Mes	10.3	10.5
2	Ph	11.4	9.5
3	Cy	9.1	5.4
4	OEt	18.1	6.7

We also investigated the formation of the bishydrophosphorylated product for R = Mes and R = Ph. Our results indicate that in the case of R = Ph, the second addition proceeds with low energy barriers, making it feasible under the reaction conditions. Additionally, thermodynamic analysis supports this second addition, as the bishydrophosphorylated product is more stable than the monohydrophosphorylated products. In contrast, for the bulkier mesityl groups (R = Mes), the barriers are significantly higher, especially during the protonation step, with the *E-isomer* being the thermodynamically favored product. Moreover, the cyclization of the *Z*-alkene product leads to the formation of a phosphindole 1-oxide product, which has a lower energy barrier than the second addition. These results underscore the critical role of steric effects and thermodynamic stability in shaping the reactivity and product distribution in these catalytic processes.

In the protonation steps with R_2-P(O)H and the 2nd nucleophilic attack for double addition we discovered that the alkali cation will prefer to be bounded with as many

oxygen atoms as possible from the neighbouring molecules. This proved to be intrinsic as it also had lowering effect on the barrier for the protonation steps specifically

Therefore, we confirmed theoretically that these cations are not only “spectator” species, but they rather play a significant role in the outcome of these conversions in each step of the reaction. Theoretical results also indicate that generation of the active species is crucial for the activity shown by the metal. Moreover, we were able to provide evidence that the formation of the active species is dependent on the P-bound group on the phosphineoxide and on the alkali cation.

In conclusion, this study highlights the significant gaps in computational research concerning s-block metal-promoted reaction mechanisms compared to transition metal processes. It is particularly important as it provides a deeper understanding of the behavior of alkali cations, revealing the complexities of using “floppy” alkali cations and mapping out the associated reaction pathways. The findings emphasize the potential of alkali metal-based catalysts for future catalytic applications, particularly in the formation of stereo- and regio-selective P–C bonds.

Additionally, the research underscores that a fundamental understanding of these reaction mechanisms is highly advantageous for developing non-toxic and readily available catalysts for future homogeneous catalytic reactions. Expanding upon these concepts may lead to intriguing applications in hydrogenation, hydrosilylation, hydroamination processes, and beyond. Furthermore, while detailed quantitative insights typically require extensive DFT-based molecular dynamics simulations, our results demonstrate that static DFT calculations with a cluster-continuum solvent model can effectively yield valuable insights and reveal essential trends in the behaviour of these systems, paving the way for further exploration in s-block metal catalysis.

Bibliography

1. Dillon, K. B., Mathey, F. & Nixon, J. F. *Phosphorus, the carbon copy: from organophosphorus to phospha-organic chemistry*. (Wiley, 2001).
2. Fener, B. E., Schüler, P., Ueberschaar, N., Bellstedt, P., Görls, H., Krieck, S. & Westerhausen, M. Scope and Limitations of the s-Block Metal-Mediated Pudovik Reaction. *Chem. Eur. J.* **26,** 7235–7243 (2020).
3. Ananikov, V. P., Khemchyan, L. L., Beletskaya, I. P. & Starikova, Z. A. Acid-Free Nickel Catalyst for Stereo- and Regioselective Hydrophosphorylation of Alkynes: Synthetic Procedure and Combined Experimental and Theoretical Mechanistic Study. *Adv Synth Catal* **352,** 2979–2992 (2010).
4. Banerjee, I., Harinath, A. & Panda, T. K. Alkali Metal Catalysed Double Hydrophosphorylation of Nitriles and Alkynes. *Eur J Inorg Chem* **2019,** 2224–2230 (2019).
5. Fortunato, L., Moglie, Y., Dorn, V. & Radivoy, G. Hydrophosphorylation of aliphatic alkynes catalyzed by CuNPs/ZnO for the synthesis of vinyl phosphonates. A DFT study on the reaction mechanism. *RSC Adv.* **7,** 18707–18713 (2017).
6. Ananikov, V. P. & Beletskaya, I. P. Alkyne Insertion into the M-P and M□H Bonds (M=Pd, Ni, Pt, and Rh): A Theoretical Mechanistic Study of the C-P and C-H Bond-Formation Steps. *Chem. Asian J.* **6,** 1423–1430 (2011).
7. Liu, L. L., Wu, Y., Wang, Z., Zhu, J. & Zhao, Y. Mechanistic Insight into the Copper-Catalyzed Phosphorylation of Terminal Alkynes: A Combined Theoretical and Experimental Study. *J. Org. Chem.* **79,** 6816–6822 (2014).
8. Li, J., Gao, Z., Guo, Y., Liu, H., Zhao, P., Bi, X., Shi, E. & Xiao, J. Copper-catalyzed stereo- and regioselective hydrophosphorylation of terminal alkynes: scope and mechanistic study. *RSC Adv.* **12,** 18889–18896 (2022).
9. Chen, T., Zhao, C.-Q. & Han, L.-B. Hydrophosphorylation of Alkynes Catalyzed by Palladium: Generality and Mechanism. *J. Am. Chem. Soc.* **140,** 3139–3155 (2018).
10. Alonso, F., Beletskaya, I. P. & Yus, M. Transition-Metal-Catalyzed Addition of Heteroatom−Hydrogen Bonds to Alkynes. *Chem. Rev.* **104,** 3079–3160 (2004).
11. Fener, B. E., Schüler, P., Pröhl, F. E., Görls, H., Liebing, P. & Westerhausen, M. s-Block Metal Base-Catalyzed Synthesis of Sterically Encumbered Derivatives of Ethane-1,2-diyl-bis(diphenylphosphineoxide) (dppeO $_2$). *Organometallics* (2024).
12. Semenzin, D., Etemad-Moghadam, G., Albouy, D., Diallo, O. & Koenig, M. Dual Radical/Polar Pudovik Reaction: Application Field of New Activation Methods. *J. Org. Chem.* **62,** 2414–2422 (1997).
13. Zagidullin, A. A., Sakhapov, I. F., Miluykov, V. A. & Yakhvarov, D. G. Nickel Complexes in C–P Bond Formation. *Molecules* **26,** 5283 (2021).
14. Zhang, J.-S., Zhang, J.-Q., Chen, T. & Han, L.-B. t-BuOK-mediated reductive addition of P(O)–H compounds to terminal alkynes forming β-arylphosphine oxides. *Org. Biomol. Chem.* **15,** 5462–5467 (2017).
15. Härling, S. M., Fener, B. E., Krieck, S., Görls, H. & Westerhausen, M. Potassium Dimesitylphosphinite Catalyzed Intermolecular Hydrophosphorylation of Alkynes. *Organometallics* **37,** 4380–4386 (2018).
16. Saga, Y., Han, D., Kawaguchi, S., Ogawa, A. & Han, L.-B. A salt-free synthesis of 1,2-bisphosphorylethanes via an efficient PMe3-catalyzed addition of >P(O)H to vinylphosphoryl compounds. *Tetrahedron Lett.* **56,** 5303–5305 (2015).
17. Yoshimura, A., Saga, Y., Sato, Y., Ogawa, A., Chen, T. & Han, L.-B. An efficient base-catalyzed double addition of H-phosphine oxides to alkynes. *Tetrahedron Lett.* **57,** 3382–3384 (2016).

18. Platten, A. W. J., Borys, A. M. & Hevia, E. Hydrophosphinylation of Styrenes Catalysed by Well-Defined s-Block Bimetallics. *ChemCatChem* **14,** (2022).
19. Sciortino, G., Muñoz-López, S., Lledós, A. & Ujaque, G. Comparative Mechanistic Study on the [Au(NHC)] $^{+}$ -Catalyzed Hydration of Alkynes, Alkenes, and Allenes. *Organometallics* **39,** 3469–3479 (2020).
20. Guthrie, J. P. Tautomerization equilibria for phosphorous acid and its ethyl esters, free energies of formation of phosphorous and phosphonic acids and their ethyl esters, and p K_a values for ionization of the P—H bond in phosphonic acid and phosphonic esters. *Can. J. Chem.* **57,** 236–239 (1979).
21. Vincze, D., Ábrányi-Balogh, P., Bagi, P. & Keglevich, G. A Mechanistic Study on the Tautomerism of H-Phosphonates, H-Phosphinates and Secondary Phosphine Oxides. *Molecules* **24,** 3859 (2019).
22. Janesko, B. G., Fisher, H. C., Bridle, M. J. & Montchamp, J.-L. P(═O)H to P–OH Tautomerism: A Theoretical and Experimental Study. *J. Org. Chem.* **80,** 10025–10032 (2015).
23. Mootz, D., Zinnius, A. & Böttcher, B. Assoziation im festen Zustand von Bis(trimethylsilyl)amidolithium und Methyltrimethylsilanolatoberyllium. *Angewandte Chemie* **81,** 398–399 (1969).
24. Henderson, K. W., Dorigo, A. E., Liu, Q.-Y. & Williard, P. G. Effect of Polydentate Donor Molecules on Lithium Hexamethyldisilazide Aggregation: An X-ray Crystallographic and a Combination Semiempirical PM3/Single Point *ab Initio* Theoretical Study. *J. Am. Chem. Soc.* **119,** 11855–11863 (1997).
25. Spivey, J. A. & Collum, D. B. Potassium Hexamethyldisilazide (KHMDS): Solvent-Dependent Solution Structures. *J. Am. Chem. Soc.* **146,** 17827–17837 (2024).
26. Woltornist, R. A. & Collum, D. B. Aggregation and Solvation of Sodium Hexamethyldisilazide: Across the Solvent Spectrum. *J. Org. Chem.* **86,** 2406–2422 (2021).
27. Lucht, B. L. & Collum, D. B. Lithium Hexamethyldisilazide: A View of Lithium Ion Solvation through a Glass-Bottom Boat. *Acc. Chem. Res.* **32,** 1035–1042 (1999).
28. Ojeda-Amador, A. I., Martínez-Martínez, A. J., Kennedy, A. R. & O'Hara, C. T. Structural Studies of Cesium, Lithium/Cesium, and Sodium/Cesium Bis(trimethylsilyl)amide (HMDS) Complexes. *Inorg. Chem.* **55,** 5719–5728 (2016).
29. Mulvey, R. E. & Robertson, S. D. Synthetically Important Alkali-Metal Utility Amides: Lithium, Sodium, and Potassium Hexamethyldisilazides, Diisopropylamides, and Tetramethylpiperidides. *Angew Chem Int Ed* **52,** 11470–11487 (2013).
30. Ojeda-Amador, A. I., Martínez-Martínez, A. J., Robertson, G. M., Robertson, S. D., Kennedy, A. R. & O'Hara, C. T. Exploring the solid state and solution structural chemistry of the utility amide potassium hexamethyldisilazide (KHMDS). *Dalton Trans.* **46,** 6392–6403 (2017).
31. Del Pozo, J., Pérez-Iglesias, M., Álvarez, R., Lledós, A., Casares, J. A. & Espinet, P. Speciation of $ZnMe_2$, ZnMeCl, and $ZnCl_2$ in Tetrahydrofuran (THF), and Its Influence on Mechanism Calculations of Catalytic Processes. *ACS Catal.* **7,** 3575–3583 (2017).
32. Härling, S. M., Görls, H., Krieck, S. & Westerhausen, M. Potassium-Mediated Hydrophosphorylation of Heterocumulenes with DiarylphosphineOxide and Sulfide. *Inorg. Chem.* **55,** 10741–10750 (2016).
33. Berthold, C., Thomas-Hargreaves, L. R., Ivlev, S. I. & Buchner, M. R. An approach towards the synthesis of lithium and beryllium diphenylphosphinites. *Zeitschrift für Naturforschung B* **76,** 651–658 (2021).
34. Fener, B. E.; Schüler, P.; Liebing, P.; Görls, H.; Westerhausen. M. Syntheses and Structures of Dimesitylphosphinite Complexes of the Alkali Metals as well as their Catalytic Activity in Hydro-phosphorylation Reactions. *Submitted*

35. Beswick, M. A., Cromhout, N. L., Harmer, C. N., Palmer, J. S., Raithby, P. R., Steiner, A., Verhorevoort, K. L. & Wright, D. S. Metal selection of ligand functionality in $[(mes)_2P(\cdots O)_2Li\cdot_2thf]_2$ and $[\{(Me_3Si)_2N\}Cd\{(mes)_2P\cdots O\}_2Li\cdot_2thf]$ (mes = $C_6H_2Me_3$-2,4,6). *Chem. Commun.* 583–584 (1997).
36. Härling, S. M., Krieck, S., Görls, H. & Westerhausen, M. Influence of 18-Crown-6 Ether Coordination on the Catalytic Activity of Potassium and Calcium Diarylphosphinites in Hydrophosphorylation Reactions. *Inorg. Chem.* **56,** 9255–9263 (2017).
37. Peltzer, R. M., Eisenstein, O., Nova, A. & Cascella, M. How Solvent Dynamics Controls the Schlenk Equilibrium of Grignard Reagents: A Computational Study of CH_3MgCl in Tetrahydrofuran. *J. Phys. Chem. B* **121,** 4226–4237 (2017).
38. Wang, Z.-Y., Guo, Q., Xu, S. & Wang, K.-K. Nucleophilic H-Phosphites, H-Phosphinates, and H-Phosphine Oxides in Organic Reactions. *Synthesis* **53,** 3683–3698 (2021).
39. Jaramillo, P., Domingo, L. R., Chamorro, E. & Pérez, P. A further exploration of a nucleophilicity index based on the gas-phase ionization potentials. *J. Mol. Struct. THEOCHEM* **865,** 68–72 (2008).
40. Ríos-Gutiérrez, M., Saz Sousa, A. & Domingo, L. R. Electrophilicity and nucleophilicity scales at different DFT computational levels. *J of Physical Organic Chem* **36,** e4503 (2023).
41. Dougherty, D. A. The Cation–π Interaction. *Acc. Chem. Res.* **46,** 885–893 (2013).
42. Rae, A., Byrne, K. M., Brown, S. A., Kennedy, A. R., Krämer, T., Mulvey, R. E. & Robertson, S. D. Sigma/pi Bonding Preferences of Solvated Alkali-Metal Cations to Ditopic Arylmethyl Anions. *Chem. Eur. J.* **28,** (2022).
43. Kim, D., Hu, S., Tarakeshwar, P., Kim, K. S. & Lisy, J. M. Cation−π Interactions: A Theoretical Investigation of the Interaction of Metallic and Organic Cations with Alkenes, Arenes, and Heteroarenes. *J. Phys. Chem. A* **107,** 1228–1238 (2003).
44. Mecozzi, S., West, A. P. & Dougherty, D. A. Cation−π Interactions in Simple Aromatics: Electrostatics Provide a Predictive Tool. *J. Am. Chem. Soc.* **118,** 2307–2308 (1996).
45. Pardue, D. B., Gustafson, S. J., Periana, R. A., Ess, D. H. & Cundari, T. R. Computational study of carbon–hydrogen bond deprotonation by alkali metal superbases. *Comput. Theor. Chem.* **1019,** 85–93 (2013).
46. Davidson, M. G., Garcia-Vivo, D., Kennedy, A. R., Mulvey, R. E. & Robertson, S. D. Exploiting σ/π Coordination Isomerism to Prepare Homologous Organoalkali Metal (Li, Na, K) Monomers with Identical Ligand Sets. *Chem. Eur. J.* **17,** 3364–3369 (2011).
47. Feil, F. & Harder, S. *α* , *α* -Bis(trimethylsilyl)-Substituted Benzyl Complexes of Potassium and Calcium. *Organometallics* **19,** 5010–5015 (2000).
48. Feil, F. & Harder, S. Benzyl Complexes of the Heavier Alkaline-Earth Metals: The First Crystal Structure of a Dibenzylstrontium Complex. *Organometallics* **20,** 4616–4622 (2001).
49. Harder, S., Ruspic, C., Bhriain, N. N., Berkermann, F. & Schürmann, M. Benzyl Complexes of Lanthanide(II) and Lanthanide(III) Metals: Trends and Comparisons. *Z. Naturforsch. B* **63,** 267–274 (2008).
50. Gorrell, I. B. Chapter 2. Alkali and alkaline earth metals. *Annu. Rep. Prog. Chem., Sect. A* **91,** 3 (1994).
51. Armstrong, D. R., Davidson, M. G., Garcia-Vivo, D., Kennedy, A. R., Mulvey, R. E. & Robertson, S. D. Monomerizing Alkali-Metal 3,5-Dimethylbenzyl Salts with Tris(*N* , *N* -dimethyl-2-aminoethyl)amine (Me_6 TREN): Structural and Bonding Implications. *Inorg. Chem.* **52,** 12023–12032 (2013).
52. Togni, A. & Grützmacher, H. *Catalytic heterofunctionalization: from hydroanimation to hydrozirconation*. (Wiley-VCH, 2001).

53. Woltornist, R. A. & Collum, D. B. Ketone Enolization with Sodium Hexamethyldisilazide: Solvent- and Substrate-Dependent *E* – *Z* Selectivity and Affiliated Mechanisms. *J. Am. Chem. Soc.* **143,** 17452–17464 (2021).

Chapter 5: Alkali metal-mediated hydrophosphination of butadiyne

The results in the ensuing chapter are from combined experimental/computational study on the hydrophosphination of diphenylbutadiyne mediated by alkali-based catalysts. The article for this chapter is currently under preparation in the hopes to be published soon. Unless otherwise noted, all experimental data, computational calculations, data analysis, discussion, and writing up of the results were done by myself, with some help from my supervisors.

5.1. Introduction

In recent years, great number of new synthetic procedures have been discovered to be catalysed by alkali metal-based catalysts, amongst which is hydrophosphination.[1–5] Alkali-metal-mediated catalytic reactions in general are more cost effective and environmentally benign than most transition metal catalysed reactions.[6–9] Additionally, the outcome of the reaction may be tuned by the choice of the metal (Lewis acidity, size, hardness), and by the solvent used (basicity, donor strength, denticity, bulkiness). Thus far, the primary research on the hydrophosphination of alkynes has been conducted on the essential alkali metals sodium and potassium used as catalysts.[10,11] Nonetheless, from a mechanistic point of view they are deceitfully insidious to comprehend in comparison to more common transition metal based catalysed reactions as they are redox-inert and do not allow for oxidative addition and reductive elimination steps to ensue.

Hydrophosphination may be used to create new C-P bonds by addition of phosphanes across unsaturated bonds. This reaction might yield alkenylated (**1**) or alkylated (**2**) phosphanes and/or phosphole products (see **Scheme 5.1**). The summary of diverse catalyst systems that have been explored experimentally were discussed in depth in the Introduction chapter and may be found in reviews.[3,12–14] It should be noted that the products range will differ depending on the atmosphere (e.g., presence of air or inert atmosphere), as in some conditions radical processes my occur.

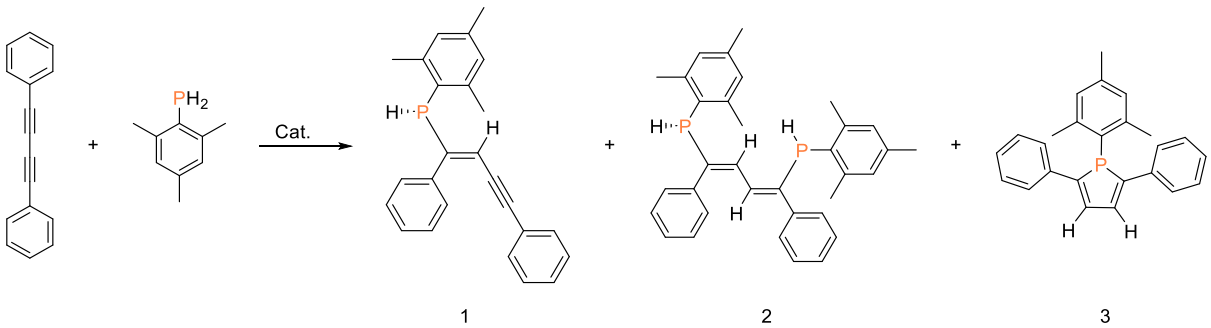

Scheme 5.1: Hydrophosphination of diphenylbutadiyne yielding alkenylated (**1**), alkylated (**2**) phosphanes and phosphole **(3)**.

This chapter combines computational and experimental research aimed to shed insight on the reaction mechanism involved in the hydrophosphination of butadiynes catalysed by M-HMDS of the alkali metals (M = Li, Na, and K; M-HMDS = metal bis(trimethylsilyl)amides). The mechanism of hydrophosphination reaction yielding 1H-2,5-phospholes is a topic that has not been significantly explored *via* DFT methods. Hitherto, DFT studies have been conducted on elucidating the relationship amongst the structure and the properties, the aromatic character of the phosphole and its Diels-Alder reactivity.[13,15–18] However, computational studies depicting the actual formation for the phosphole are more than scarce and remain a grey area that needs to be investigated. In fact, the first proposed in silico mechanism for transition metal free route to phospholes featuring an exocyclic alkene unit was reported recently by Roesler *et al.*[18–20] In their system they use a lithium phosphanide anion (PhP(TMS)Li) and diphenylbutadiyne with dimethoxyethane (DME) as solvent. Intriguingly, in this study they proposed a "bare" anionic system for the investigation of the reaction mechanism. Therein, the authors concluded that the presence of the alkali metal cation is not strictly necessary, and additionally may induce separated ion pairs in their case due to the type of the solvent utilised. In their proposed mechanism the first step is a nucleophilic attack onto C_1[5] of the 1,4-diphenylbutadiyne. Following this, they propose a silyl migration, where the weaker P-Si bond is cleaved in favour of forming a more stable C-Si bond, succeeded by an isomerization step. The intermediate with the correct configuration for subsequent cyclization step will be generated in this step. A subsequent step of nucleophilic attack onto C_4, yields the 5-membered ring. Finally, the process concludes with protonation. However, despite the outcome of these works, the role the metal cation plays in the catalytic process remains undetermined as the studies conducted by Roesler *et al.* were limited solely to one alkali cation (lithium). The changes of the reaction mechanism that are brought on by simply changing one alkali cation with another and thus vital understanding of the mechanism aren't fully explored. The role the alkali cations play in the reaction mechanism, are over all controversial, because the existing research on incorporating alkali cations as explicit

[5] By C_1 or $C_{Internal}$ we mean the C atom closest to the phenyl substituent from the one of C≡C triple bonds present in the butadiyne; C_2 is the C atom closest to the C_1, whilst C_3 is the C atom from the adjacent C≡C triple bond closest to C_2 , lastly, C_4 is the other C atom connected to the other phenyl substituent present in the diyne system whilst, simultaneously connected to C_3.

cations has recognized that there is limitation to precision in DFT calculation on the result because of their “floppiness”.[21]

Hence, this research topic was prompted for the search of more efficient catalyst for the formation of phospholes (one-pot synthesis at room temperature) and to obtain a better understanding of the reaction mechanism for the formation of phospholes. In the view of this image, we decided to conduct a combined experimental and computational study to gain deeper understanding of the reaction for alkali-mediated hydrophosphination of butadiyne using M-HMDS as catalysts. We decided to conduct this study on the basis of the previously successful hydrophosphorylation of butadiyne using M-HMDS as catalysts.[22] Additionally, alkali-based hexamethyldisilazanides haven’t yet been explored as possible catalysts for the formation of phospholes. Nonetheless, similar alkali bases have been proven to be very successful in the process of hydrophosphination of butadiyne.[5,23] Alkali based hexamethyldisilazanides are great examples for cheap and environmentally benign catalysts based on group 1 metals. We decided to explore experimentally and computationally three different alkali base catalysts (M-HMDS; M = Li, Na, and K) to investigate the influence that the nature of the cation plays on the overall reaction outcome.

More precisely, the purpose of this study was to determine both experimentally and computationally the general model for alkali-mediated addition of phosphanes across diynes. With this in mind, we experimentally analysed alkali hexamethyldisilazanides to determine the effect of the nature the alkali metal has over the reaction’s outcome, and we computed the Gibbs energy profiles for those reactions using DFT methods.

The results obtained will be presented in the two following subsections: i) experimental results on alkali-mediated formation of P-aryl-2,5-diphenyl-phosphole and ii) computational results, which contains mechanistic studies. Each of these two main subsections will be split into multiple subsections.

5.2. Experimental results:

In this section we will focus on presenting our experimental results and on their scientific discussion for the reactivity study on discovering the most successful alkali

metal-based catalyst for addition of primary phosphanes across diphenylbutadiyne *via* hexamethyldisilazanides.

5.2.1. Influence of the metal on hydrophosphination

To produce reliable studies, freshly prepared alkali metal mesityl phosphanides were utilized and the following protocol was implemented. The alkali metal phosphanides M−P(H)Mes were generated in situ *via* metalizing $MesPH_2$ with the alkali hexamethyldisilazanides (M-HMDS; M = Li, Na, and K), resulting in the analogous metal phosphanides. The ^{31}P NMR spectroscopy was used to confirm qualitative conversion. Mesityl phosphine ($MesPH_2$; $C_9H_{13}P$) and 5 mol % of the amide were mixed at room temperature in 5 mL of THF in a Schlenk flask, followed by addition of a stoichiometric quantity of the 1,4-diphenylbutadiyne. The aliquot was protolyzed upon one hour using a couple of drops of methanol. The formed product was analysed *via* ^{31}P NMR spectroscopy. The general scheme for the reaction is depicted in **Scheme 5.2**.

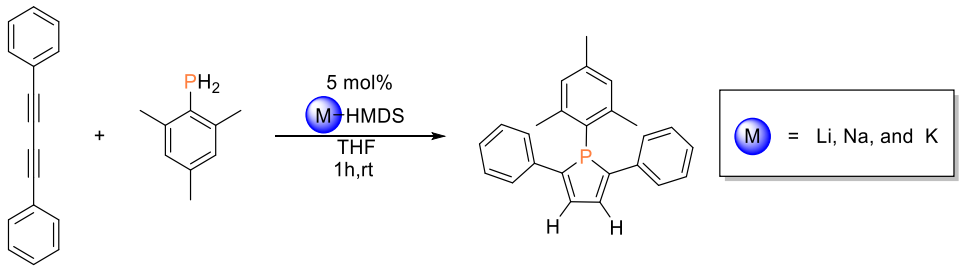

Scheme 5.2: Alkali-mediated hydrophosphination of diphenylbutadiyne with mesitylphosphane, using M-HMDS (M = Li, Na, and K) as catalysts at room temperature yielding P-mesityl-2,5-diphenyl-phosphole.

The outcome of the experimental results is summarised in **Table 5.1**. In less than an hour 1-mesityl-2,5-diphenyl-1H-phosphole formed quantitatively at room temperature. From this data, it was deducted that the hydrophosphination proceeds regio and stereo-selectively to generate 1H-phosphole. This process could not be mediated by the catalysts based on smaller congeners, such as Li-HMDS (**entry 1**). However,

fast conversion was detected for the complexes of the heavier metals' sodium and potassium (see **Table 5.1**; **entry 2** and **3**). Surprisingly, in the case of Li-HMDS also the addition of 18-crown-6 could not increase of the rate of conversion.[6] The formation of the double-addition product is most likely impeded as no additional products were observed. However, later we will explore computationally why this reaction might be inhibited (see **Section 5.3.4.3.**). The conversion rate was determined *via* ^{31}P NMR spectroscopy after one hour, which remained unchanged even after 24 h. Under these reaction conditions no other products were formed, thus indicating that the generated phosphole is the thermodynamic product of the reaction. ^{31}P NMR spectroscopic monitoring at 162 MHz of the alkali-mediated hydrophosphination of 1.4-diphenylbutadiyne with mesitylphosphineoxide is illustrated in **Figure 5.1**.

Table 5.1.: Dependency of the hydrophosphination (addition of mesityl phosphineacross diphenylbutadiyne) on the alkali metal of the tested bis(trimethylsilyl)amide catalysts.

Entry	Metal	Conversion after 1h (%)
1	Li	/
2	Na	63
3	K	>99

[66] The solution mixture was refluxed for 24h at 75 °C, and upon completion of the 24h ^{31}P NMR was checked, as there was no activity we decided to add another 5mol% of the pre-catalyst, reflux it again, however, despite repeating the procedure 5 times no change in the conversion was detected.

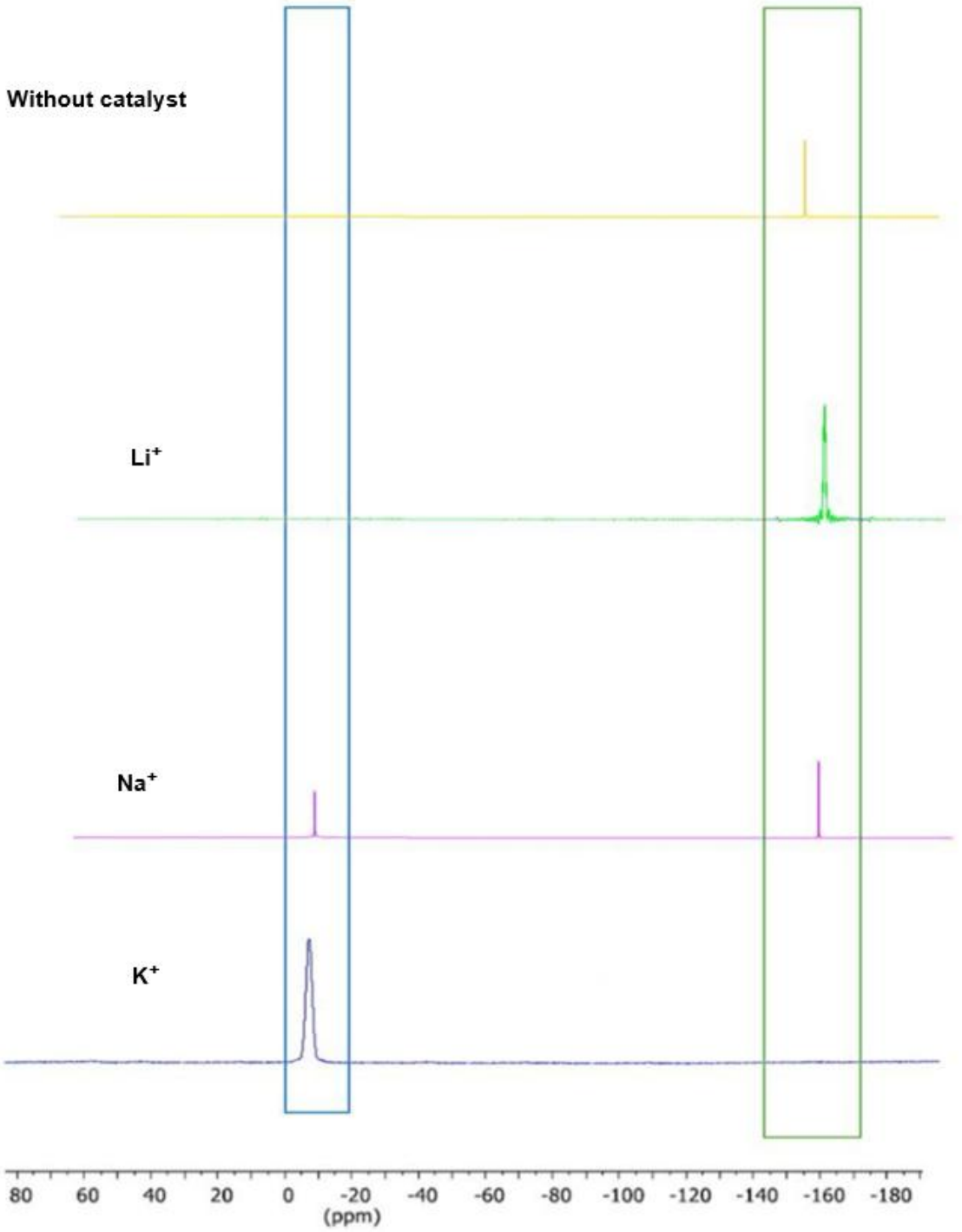

Figure 5.1.: ^{31}P NMR spectroscopic monitoring at 162 MHz of the alkali-mediated hydrophosphination of 1,4-diphenylbutadiyne with mesityl phosphine at room temperature yielding 1-mesityl-2,5-diphenylphosphole.

Hence, the nature of the alkali cation plays a significant role in the conversion rate and subsequently in the reaction mechanism. Thus, alkali cations cannot be considered as freely interchangeable and as spectators in the reaction.

5.2.2. NMR data of 1-mesityl-2,5-diphenyl phosphole

The NMR data confirms the structure of 1-mesityl-2,5-diphenyl-1H-phosphole, with clear distinctions between the aromatic and aliphatic regions. The numbering scheme of 1-mesityl-2,5-diphenyl-2,3-dihydro phosphole may be found in **Figure 5.2** below.

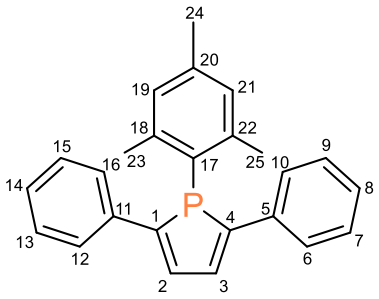

Figure 5.2.: Numbering scheme of 1-mesityl-2,5-diphenyl-2,3-dihydro phosphole

The ^{31}P spectrum (162 MHz, [D8] THF) depicts one singlet at δ = - 7.55 ppm. The ^{1}H NMR (400 MHz, [D_8] THF) of 1-mesityl-2,5-diphenyl-1H-phosphole shows a multiplet at δ = 7.21-7.08 ppm (6H) and another at δ = 7.07-7.00 ppm (4H), corresponding to the aromatic protons of the phenyl groups. A broad singlet at δ = 6.89 ppm (2H) is assigned to the *meta* protons of the mesityl ring, while another singlet at δ = 6.54 ppm (2H) corresponds to the protons at the potions C_2 and C_5 of the phosphole ring. The mesityl methyl groups produce singlets at δ = 1.87 ppm (3H, *para*-CH_3) and δ = 2.42 ppm (6H, *ortho*-CH_3).

The $^{13}C\{^{1}H\}$ (101 MHz, [D_8] THF) NMR spectrum shows peaks for the quaternary carbons of the mesityl ring at δ = 138.6 ppm (C20) and δ = 137.7 ppm (C17). Additional quaternary aromatic carbons are observed at δ = 136.6 ppm (C4), 135.9 ppm (C14), and 134.8 ppm (C12). The phenyl ring carbons resonate at δ = 130.3 ppm

(C15), 129.9 ppm (C10), 129.7 ppm (C11), and 128.6 ppm (C13). The phosphole ring methylene carbons C2 and C3 may be found at δ = 110.1 ppm. The methyl carbons of the mesityl substituent are observed at δ = 23.3 ppm (C24, para-CH_3) and δ = 19.2 ppm (C23/C25, ortho-CH_3). These data support the assigned structure of the compound 3 and confirm the successful formation of 3 (see **Scheme 5.2**)..[14,24,25]

A)

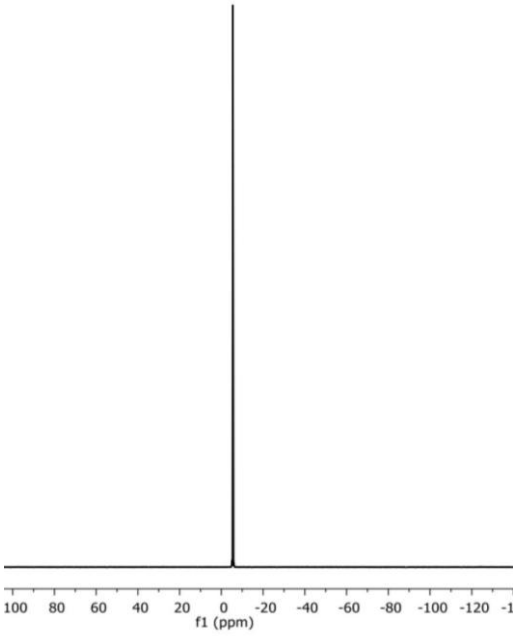

B)

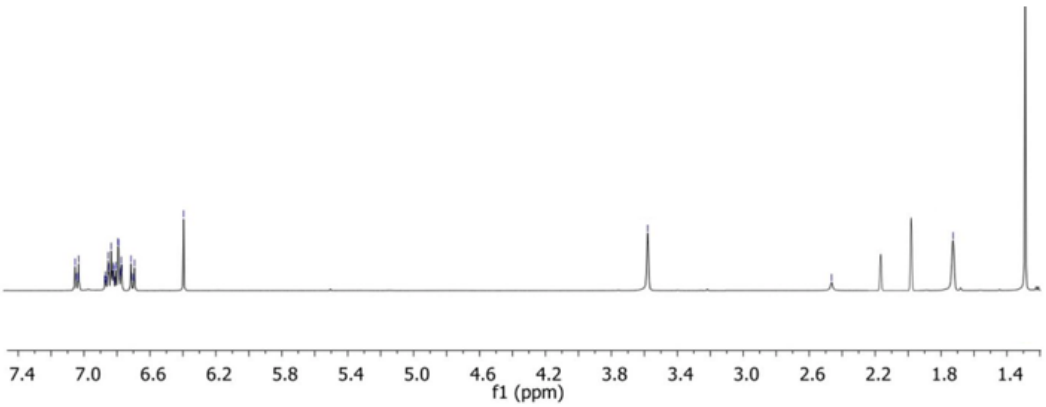

C)

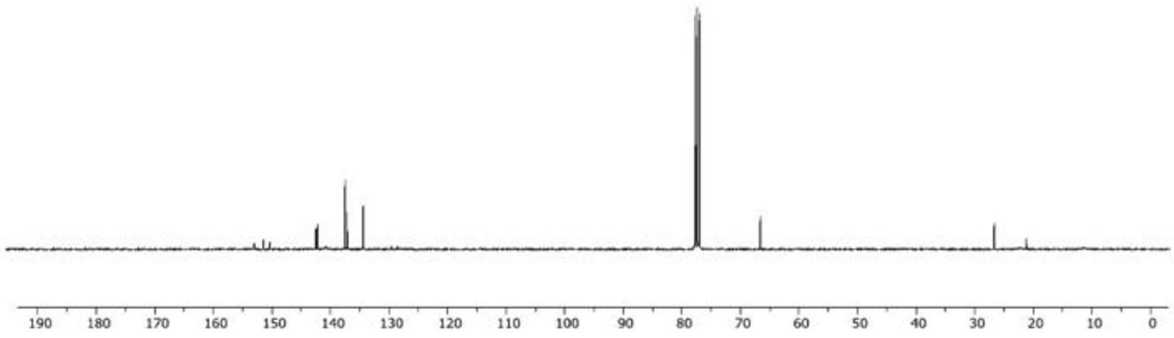

Figure 5.3.: A) ^{31}P {H} NMR **B)** ^{1}H NMR and **C)** ^{13}C {H} NMR spectra monitored at 162, 101, and 400 MHz, respectively, for 1-mesityl-2,5-diphenylphosphole in [D_8]-THF at room temperature.

Time-dependent ^{31}P NMR spectrum (162 MHz, 297 K, d_8-THF) conducted at -80°C under the same conditions as initially, except temperature, by a fellow lab member Benjamin Fener provides essential insights into the precursors yielding 1-mesityl-2,5-diphenyl-phosphole and it is depicted in **Figure 5.4**. The spectrum indicates the formation of about 5% secondary phosphanes, with resonances at δ = -78 ppm and -90 ppm, suggesting the presence of two possible *E*/*Z-isomer*s. This data supports a mechanism involving a nucleophilic attack on position C1, followed by protonation as the initial two steps for the formation of the phosphole (see **Section 5.3.1** below). The reaction time significantly impacts the formation and stability of intermediates. Notably, no expected phosphole product was observed. Additionally, a peak at δ = -160.07 ppm corresponds to mesityl phosphane, while a signal at 10.16 ppm relates to dimesityl phosphineoxide, $Mes_2P(O)$, likely present in the starting material. Thus, providing us with some guidance for the starting point when proposing the reaction mechanism for the formation of 1-mesityl-2,5-diphenyl-2,3-dihydro-phosphole.

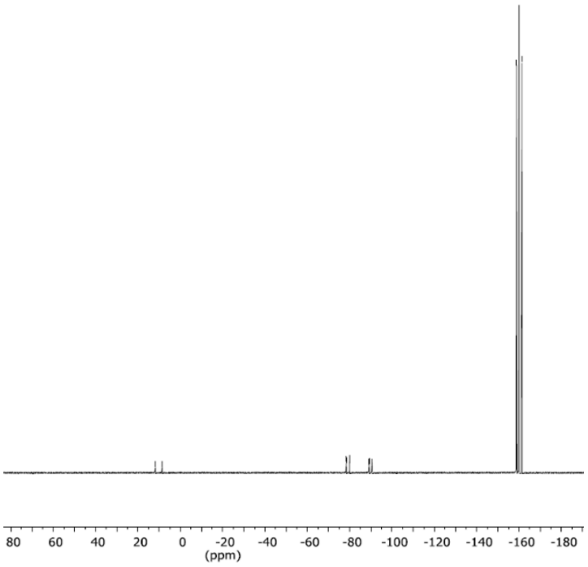

Figure 5.4.: ^{31}P NMR spectra monitored at 162 MHz of the formation of 1-mesityl-2,5-diphenylphosphole in $CDCl_3$ at room temperature.

5.2.3. Crystal structure of 1-mesityl-2,5-diphenyl-1H-phosphole

We were able to successfully obtain single crystals of 1-mesityl-2,5-diphenylphosphole. In this section we will discuss the crystal structure of the newly formed 1H-phosphole. The molecular structure and numbering scheme of 1-mesityl-2,5-diphenylphosphole are illustrated in **Figure 5.5**. The newly formed phosphole crystalized in the monoclinic space group $P\,2_1/c$. Consequently, due to the steric crowding induced by the presence of mesityl substituent, the P-bound aryl substituent has nearly a perpendicular orientation to the phosphole ring and the substituents in the 2 and 5 positions. Hence, the torsion angle amongst C1-P1-C17-C22 is 133.17°. Because the phosphorous atom has a pyramidal environment, the lone pair will have a poor overlap with the endocyclic dienic system (see **Figure 5.5**), resulting in a significant drop in delocalization within the system and subsequently the aromaticity. However, it should be noted that the aryl rings of the butadiyne unit do not take up a coplanar orientation, as the phenyl ring attached onto carbon C1 is slightly puckered. This conformation prevents further delocalization, thus putting in question the aromaticity of this compound, in accordance with computational and experimental papers.[18,25–28] The heterocyclic core P1-C1-C2-C3-C4 is planar. The average bond length between the endocyclic C1-C2

and C3-C4 atoms is 1.366 Å, which is in the range for C=C double bonds. The bond length between C2-C3 is 1.437(2) Å and this distance is only slightly smaller than a single bond between sp^2 hybridized carbon atoms. The two exocyclic bonds C1-C11 and C_4-C_5 have a mean distance of 1.468 Å putting these bonds within the range of single bonds. The value of 1.47 Å is an expected single bond between sp^2 hybridized C atoms, the value of 1.44 Å is slightly smaller. Therefore, we have delocalization within the cis-arranged endocyclic butadiene system. Interestingly, the endocyclic P-C bond lengths are 1.796 and 1.802 Å with a longer bond being exocyclic P1-C17 with 1.829(2) Å. The bond lengths in compound **3** (1-mesityl-2,5-diphenylphosphole) are similar to those in comparable compounds. The reported bond length for P-C_{phenyl} in 1,2,5-triphenylphosphole is 1.822 Å, whilst the average bond length of P-C (sp^2) single bond in $Ph_3P{=}CH_2$ is 1.823 Å.[29–31] The bond angle C1-P1-C17 being nearly tetrahedral at 109.75(7)° is very close to the ideal tetrahedral angle of 109.28°, indicating minimal strain and an energetically favourable arrangement.[32,33] The slightly wider angle of C_4-P1-C17 at 112.08(7)° represents a small de*via*tion from this ideal geometry, yet it still falls within the expected range for such molecular structures. When compared to analogous angles in 1-mesityl-2,5-diphenyl-1H-phosphole, which are narrower (104.4° and 106.2°), the observed widening is consistent with the idea that adjusting bond angles involves less energetic cost than stretching bonds. [30] This is because widening an angle primarily affects the spatial distribution of electron clouds, which is energetically less demanding than stretching a bond, which requires overcoming the significant electrostatic forces that maintain the bond length.[34] Overall, the structural characteristics observed in the compound are typical of such phosphole derivatives, where minor variations in bond lengths and angles are dictated by the balance between bond strength and electron cloud distribution.

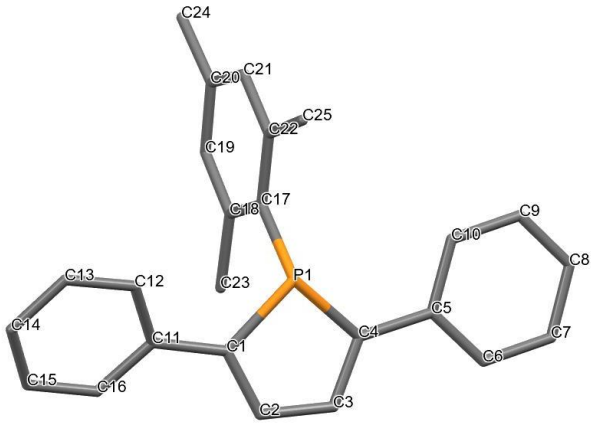

Figure 5.5.: Molecular structure and numbering scheme of 1-mesityl-2,5-diphenyl-2,3-dihydro-1H-phosphole (compound **3**). H atoms are omitted for clarity reasons.

Selected bond lengths (Å): P1-C1 1.7964(17), P1-C4 1.8024(16), P1-C17 1.8291(16), C1-C2 1.363(2), C1-C11 1.467(2), C2-C3 1.437(2), C3-C4 1.369(2), C4-C5 1.470(2). Selected bond angles (°): C1-P1-C4 92.31(8), C1-P1-C17 109.75(7), C4-P1-C17 112.08(7), C2-C1-P1 108.08(12), C2-C1-C11 126.86(15), C11-C1-P1 124.46(12), C1-C2-C3 115.10(15), C4-C3-C2 115.11(15), C3-C4-P1 107.58(12), C3-C4-C5 127.04(15), C5-C4-P1 124.51(12), C6-C5-C4 121.86(15), C10-C5-C4 120.53(14), C12-C11-C1 121.23(15), C16-C11-C1 120.74(15), C18-C17-P1 124.04(12), C22-C17-P1 116.21(12).

Having experimentally explored the influence of the alkali cation on the outcome of the hydrophosphination reaction and the NMR and XRD data of the newly formed phosphole, we will now move onto the computational section of this Chapter.

5.3. Computational results

In this section, we will show our computational findings and their scientific significance for the reactivity study on determining the most successful alkane-based catalyst for the addition of primary phosphanes across diphenylbutadiyne *via*

hexamethyldisilazanides. We will begin this section by proposing a mechanism for the formation of the phosphole; then we will go into exploring the proposed mechanism for each of the alkali cations individually and we will finish this section with the discussion about double hydrophosphination.

5.3.1. The proposed reaction mechanism for formation of 2,5-substituted phospholes

The project aimed to conduct a comparative analysis of the reaction mechanism catalysed by different alkali cations (M-HMDS; M = Li, Na, and K). Additionally, it sought to understand why only the formation of phosphole was observed experimentally. To achieve these goals, the reaction mechanism for the alkali metal-mediated addition of mesitylphosphineacross diphenylbutadiyne was analysed using computational methods. This analysis involved investigating how the different alkali cations influence each step leading to the formation of the phosphole individually and exploring the factors that drive the selective formation of phosphole.

Since from our experimental testing the reaction has shown dependence on the cation present in the system, we propose a reaction mechanism in which the alkali cation is explicitly present. It should be noted that calculations were also conducted without the presence of the cation just as “bare” anionic reaction to determine to which extent the cation has influence on the system (this is discussed in **Section 5.3.4.4**). The proposed mechanism is depicted in **Scheme 5.3**, where **M** signifies the alkali metal and the cationic site.

We propose the initial step to be the metalation of mesitylphosphineby M-HMDS (M = Li, Na, and K), thus generating the active species (i.e., alkali mesitylphosphanides) necessary for the cycle to begin. This step will be discussed separately from the rest of the cycles (see **Section 5.3.2.**). The ensuing step would be the nucleophilic attack by alkali mesitylphosphanides (M-P(H)Ar) onto the C_1[7] from one of the C≡C triple bonds present in the diyne, thereby forming the first P-C bond. It should

[7] By C_1 or $C_{Internal}$ we mean the C atom closest to the phenyl substituent from the one of C≡C triple bonds present in the butadiyne; C_2 is the C atom closest to the C_1, whilst C_3 is the C atom from the adjacent C≡C triple bond closest to C_2 , lastly, C_4 is the other C atom connected to the other phenyl substituent present in the diyne system whilst, simultaneously connected to C_3.

be noted that the formation of pro-Z intermediate will be favoured. This intermediate possesses the configuration necessary for the 2nd nucleophilic attack onto the adjacent triple bond unit, yielding a 5-membered ring. Following the nucleophilic attack, we propose a protonation step to ensue. For this step we suggest two possible routes i) protonation by an additional molecule of mesitylphosphine($MesPH_2$) or ii) protonation by an H-HMDS molecule. This step would generate a *Z-isomer* and depending on the protonation route it might generate a molecule of active species M−P(H)Mes or M-HMDS (catalyst). Both molecules may be used in the following step i.e., deprotonation of the proton present on the phosphorous atom. Hence, this step may also proceed *via* two pathways. In this step either H-HMDS or $MesPH_2$ will be reformed depending on the pathway taken. The next step is the cyclization, for which we propose an intramolecular nucleophilic attack from the phosphorous atom onto the adjacent triple bond unit to yield a 5-membered ring i.e., nucleophilic attack onto C_4. The final step, which will generate the phosphole may be obtained by the same two routes as the previous protonation step and it would regenerate the same molecules (active species or M-HMDS). It's noteworthy to mention that experimentally only formation of phosphole was observed. However, computationally we also explored the possibility of double hydrophophination on C_1 - C_4 and C_2 - C_4.

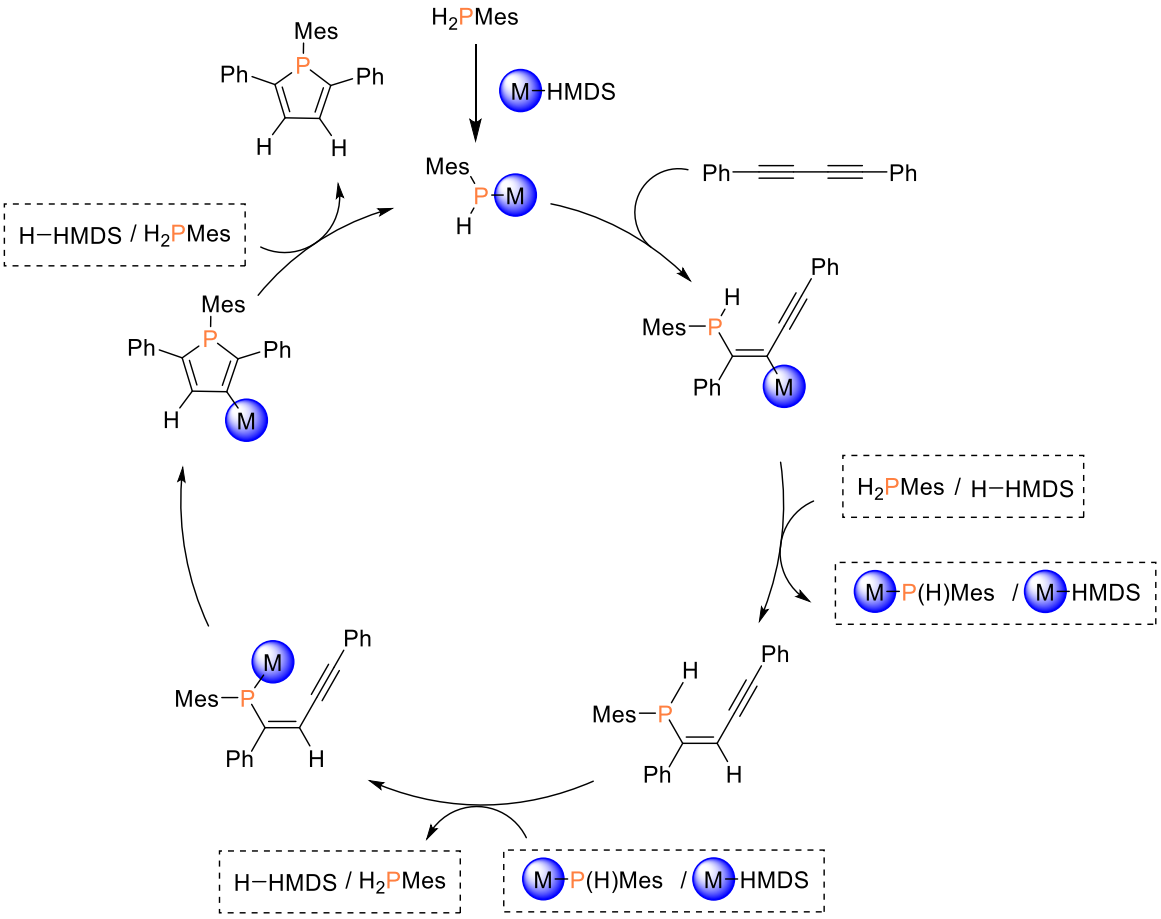

Scheme 5.3: Mechanistic proposal for formation of phosphole resulting from alkali-mediated hydrophosphination.

5.3.2. Formation and deactivation of the alkali metal mesitylphosphanide active species

Mesitylphosphanide anion is the nucleophile in the alkali mediated hydrophosphination of diphenylbutadiyne. These M-P(H)Mes active species were prepared in situ by metalation of mesitylphosphine($MesPH_2$) with the hexamethyldisilazanides of the alkali metals (M-HMDS) following **reaction 1**.

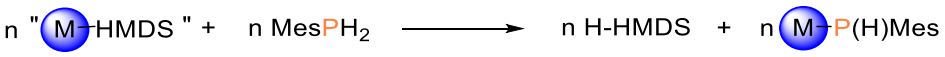

(1)

As we did for the parent alkali metal phosphinites in **Chapter 4** (Section **4.1.2.3**), the exploration of the reaction mechanism started by determining the feasibility of the formation of the alkali metal phosphanide active species, as well as their possible deactivation modes.

Assuming a dimeric nature of M-HMDS (M = Li, Na, and K) in THF solutions,[35–37] reaction (1) involves two steps. The first one is the deaggregation of M-HMDS dimers to generate M-HMDS monomers. This step was already discussed in Section **4.1.2.3** of **Chapter 4**. The second step is the proton transfer of a $MesPH_2$ proton from the phosphorous atom to the nitrogen centre of the M-HMDS monomers (**Scheme 5.4**). This step also happens for the generation of alkali metal phosphinites (**Chapter 4**, **Scheme 4.6**).

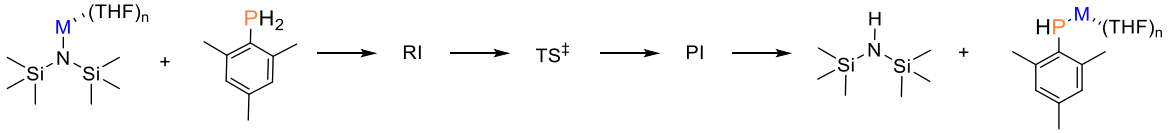

Scheme 5.4: General scheme for the proton transfer step in the formation of alkali metal mesitylphosphanides (M-P(H)Mes).

Based on the findings in **Chapter 4** concerning the impact of cation solvation on this reaction, we have primarily studied the reaction using monosolvated cations to save computational time. However, we have also conducted some verification with tetrasolvated species for comparison **Table 5.2** collects Gibbs reaction ($\Delta \mathbf{G_R}$) and activation ($\Delta \mathbf{G}^{\ddagger}$) energies for the proton transfer step. The optimized structures for the M = K pathway are depicted in **Figure 5.4.**

Table 5.2.: Gibbs reaction (ΔG_R) and activation ($\Delta G^{\ddagger}$) energies (kcal mol^{-1}) for the proton transfer step (**Scheme 5.4**) of the generation of active species M-MesPH.

Entry	Metal	ΔG_R		
		$(THF)_1$[a]	$(THF)_4$[b]	$\Delta G^{\ddagger}$
1	K	-4.3	*-5.6*	8.7
2	Na	-3.8	*-5.8*	7.8
3	Li	3.8	*-7.1*	15.2

[a] Monosolvated species.

[b] Tetrasolvated species (numbers in italics).

In mesitylphosphanes oxygen-alkali cation interactions that guide the reaction for phosphineoxides are not possible. A cation-π interaction with the phenyl ring of the mesityl substituent allows approaching $MesPH_2$ to M-HMDS in the initial **M-RI** intermediates (**Figure 5.6**). From them an easy P- to N- proton transfer takes place, although the barriers show dependence with the cation, as displayed in **Figure 5.6**. The lowest one is with potassium (8.7 kcal mol^{-1}) and the highest one with lithium (15.2 kcal mol^{-1}).

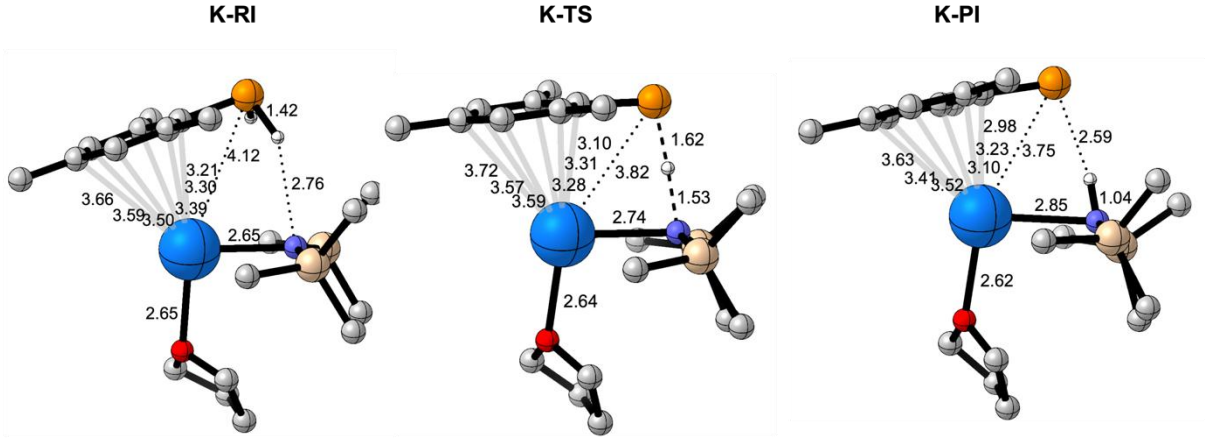

Figure 5.6.: Optimized structures of intermediates (**RI** and **PI**) and transition state (**TS**) in the proton transfer step for the generation of K-P(H)Mes with monosolvated structures. C-H hydrogen atoms are omitted for clarity reasons. The distances are given in Å.

Figure 5.7 depicts the Gibbs energy profile for the generation of the active species M-P(H)Mes for the three alkali cations (M = Li, Na, and K). Apart for formation of Li-P(H)Mes (see **Table 2**, **entry 3**), the ΔG values for both monosolvated and tetrasolvated species are comparable, though tetrasolvation consistently results in a more exergonic process.

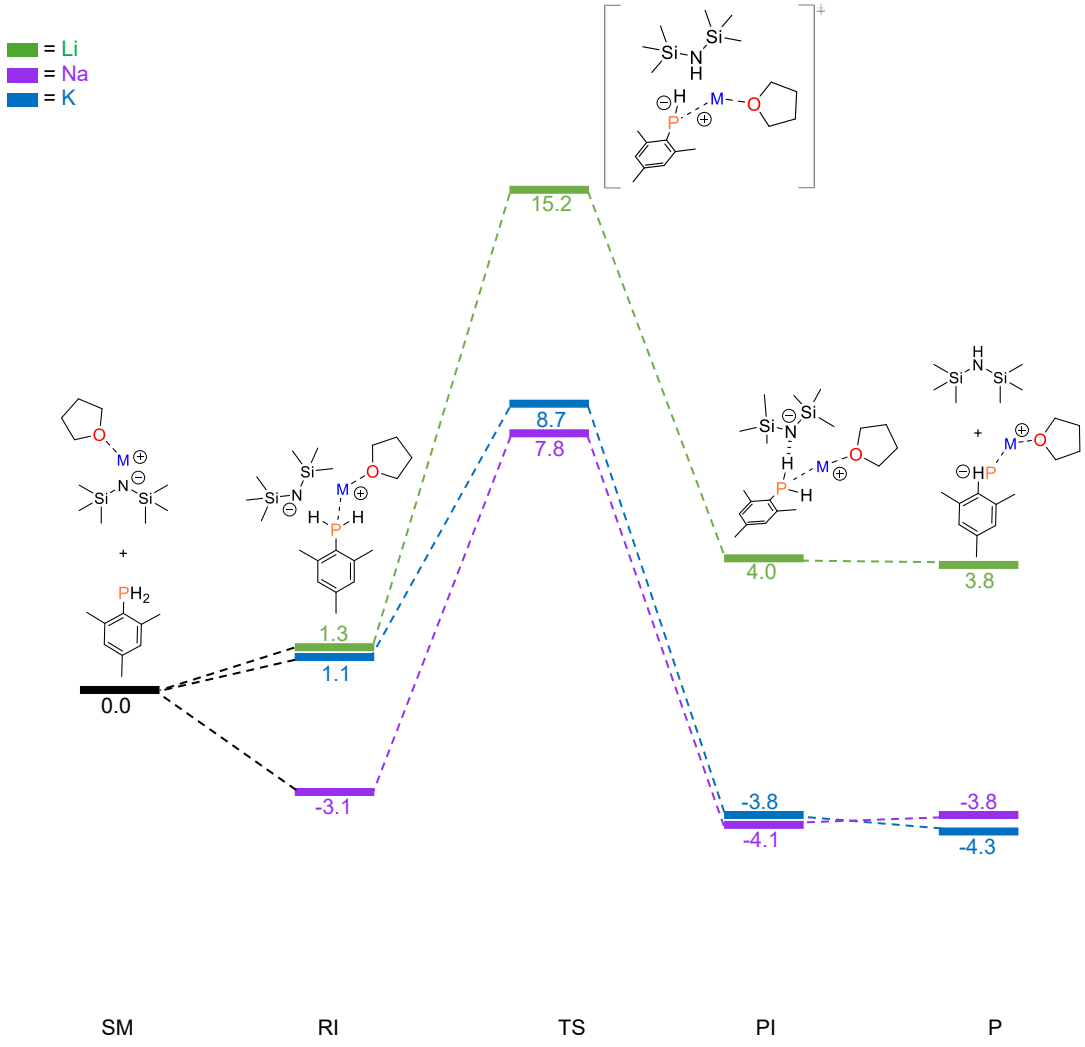

Figure 5.7.: Gibbs energy profile in THF (ΔG_{THF} kcal mol^{-1}) at 298 K for the proton transfer step for the generation of M-P(H)Mes active species (M = Li, Na, and K) considering monosolvated structures at a B3LYP-D3/def2-TZVP/SMD(THF)//B3LYP-D3BJ/6-31G(d,p)/SMD(THF) level of theory; the ····· line between the metal cation and the oxygen atom signifies the interaction between them; the TS is marked as ····· .).

The M-P(H)Mes active species in solution can be described as contact ion pairs with a phosphanide anion and a solvated cation. The absence of an oxygen centre,

as in phosphinites, avoids coordination of the cation. The ion pair character is increased when increasing the number of solvent molecules solvating the cation, the ions moving away in the tetrasolvated structures (**Figure 5.8**).

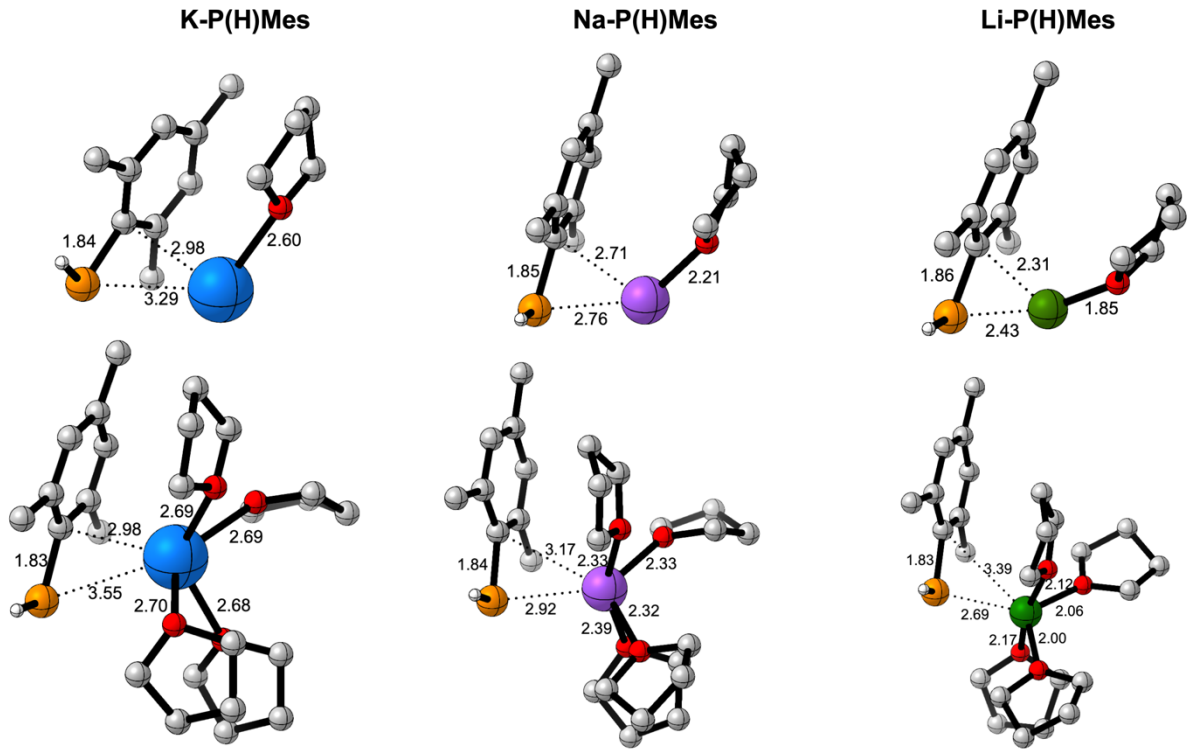

Figure 5.8.: Optimized structures of monosolvated (top) and tetrasolvated (bottom) M-P(H)Mes active species. C-H hydrogen atoms are omitted for clarity reasons. The distances are given in Å.

Alkali metal phosphanides can aggregate and they can adopt a wide variety of structural motif in the solid state, including dimers, trimers, tetramers and higher aggregates. The oligomeric nature of alkali metal phosphanides can be preserved in solution, thus decreasing the concentration of the monomeric active species. [38–41] Dimeric structures with a Li_2P_2 rhombus-shaped core and each lithium cation solvated with two THF molecules have been proposed for [(Dipp)(Mes)P]Li in THF solution. [41] Less sterically hindered diarylphosphanide complexes such as $Ph_2PLi(THF)_n$ favour dimeric, or higher oligomeric structures. [38] On the contrary, a monomeric structure is preferred for $[(Dipp)_2P]Na(THF)_{1.5}$ at low temperatures.[41]

We have performed calculations to estimate the feasibility of the dimerisation process for M-P(H)Mes active species. Similarly to what we did in **Chapter 4** for alkali metal phosphinites, we have computed the thermodynamics of the dimerisation reaction assuming tetrasolvated monomers and disolvated dimers (**Scheme 5.5**). **Figure 5.9** depicts the bisolvated dimeric species in THF.

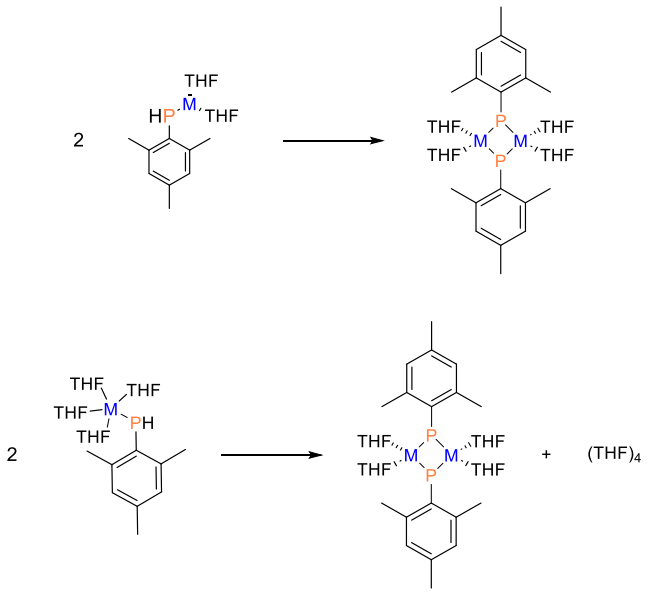

Scheme 5.5.: Dimerisation process of M-P(H)Mes phosphanides considering tetrasolvated (bottom) monomers.

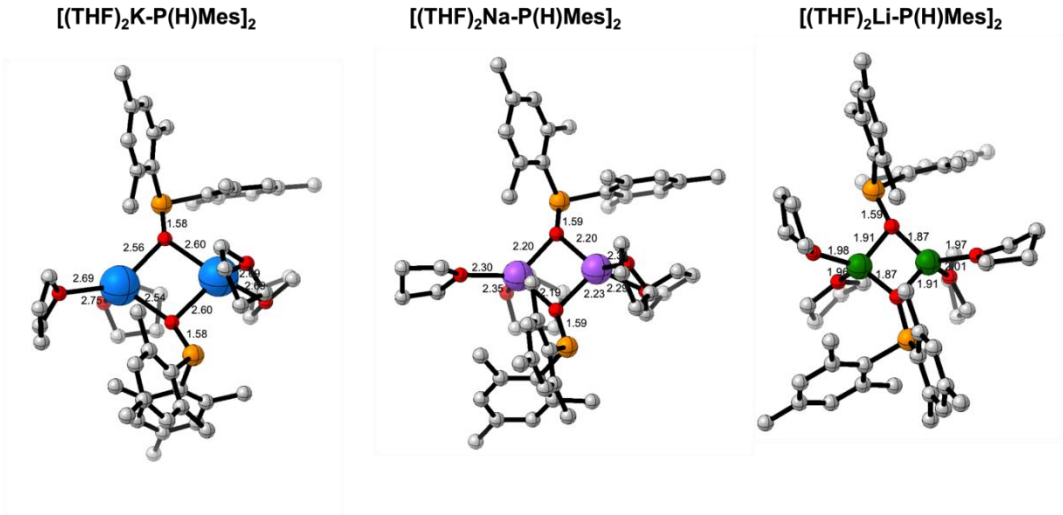

Figure 5.9.: Optimized structures for the dimeric species of $(THF)_2$M-P(H)Mes. Certain H atoms are omitted for clarity reasons. Distances are shown in Å.

Table 5.3 collects the computed Gibss reaction energies for the dimerisation reactions depicted in **Scheme 5.5**. Dimerisation of alkali metal phosphanides is less favoured than that of the parent phosphinites (**Table 4.4**, **Chapter 4**). For comparative reasons we have computed the same ΔG_R assuming monosolvated monomers. The results in both cases are very different. With monosolvated monomers the reaction is highly exergonic for all the cations. On the contrary, with tetrasolvated monomers, a situation more akin to the actual system in solution, the reaction is clearly endergonic for potassium and sodium. For lithium it is also endergonic, but with a significant presence of dimeric species.

Table 5.3.: Gibbs reaction energies (ΔG_R, kcal mol^{-1}) for the dimerisation of M-P(H)Mes phosphanides (**Scheme 5.5**).

		ΔG_R	
Entry	**Metal**	**$(THF)_1$[a]**	**$(THF)_4$[b]**
1	K	-13.4	*8.4*
2	Na	-15.5.	*8.4*
3	Li	-16.9	*2.7*

[a] Monosolvated species.

[b] Tetrasolvated species (numbers in italics).

As outlined in **Chapter 4**, the computational analysis of active species formation and deactivation reveals the complexity of these processes, primarily due to speciation and solvation challenges. This underscores the need for accurately modelling the solvent environment to achieve reliable quantitative results. Our calculations indicate that lithium phosphanide exhibits the highest formation barrier and the least endergonic dimerisation reaction. These findings suggest a lower concentration of the lithium active species in solution.

5.3.3. Modes of interaction of the metal cation with the π-systems

Following the formation of the active species, it is anticipated that the metal cation from these species (M-P(H)Mes) will interact with the π-systems (C≡C triple bonds and/or the phenyl substituents) in the 1,4-diphenylbutadiyne for the reaction to ensue.

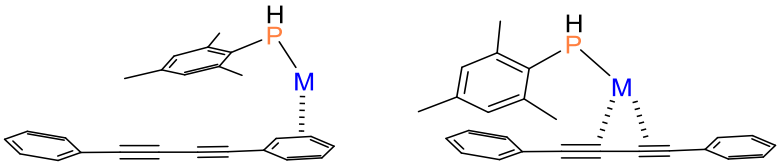

Scheme 5.6: Possible π-interaction modes between alkali mesitylphosphanide and diphenylbutadiyne

Prior to commencing with the calculations for exploring the reaction mechanism, the interaction of the metal cation with both systems was investigated for the three alkali metals (M = Li, Na, and K). **Scheme 5.6** displays the most common interaction modes found for the three metal cations. Several conformations were explored for the interaction between the active species and the diphenylbutadiyne. The most stable conformations for each of the alkali metals are shown in **Figure 5.10**., together with the computed binding energy (Δ*G*).

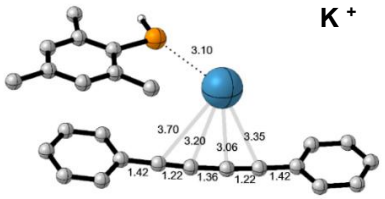

K +

ΔG = - 3.4

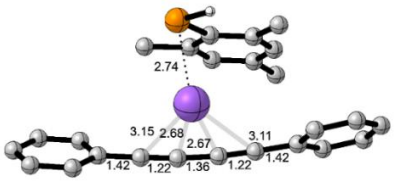

Na +

ΔG = - 2.2

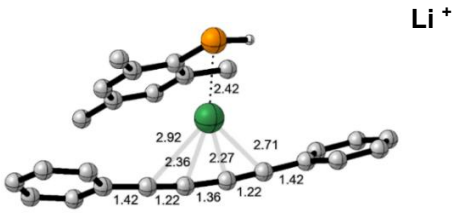

ΔG = - 3.4

Figure 5.10.: Most stable conformations computed for interaction of 1,4-diphenyl-butadiyne with alkali mesitylphosphanide (M-P(H)Mes); (M = Li (green), Na (purple), K(blue)). The binding energy ΔG was calculated in kcal mol^{-1}. The C-bound H atoms are omitted. The distances presented are given in Å.

From these calculations two points should be highlighted: i) the very weak nature of these metal cation-π interactions. Considering the most stable configurations for interaction for the three metals the estimated ΔG values were within the range from –3.4 (K) to -2.2 (Na) kcal·mol^{-1} (**Figure 5.10**). These values show a weak M – π binding in a highly dynamic system in which the presence of the metal ion should have minimal effect on the π system. ii) The second point pertains to the positioning of the metal cation regarding π-systems in the most stable structures generated for the three alkali metals. Interestingly, all three alkali cations will preferably interact with the double C≡C triple bond π-system. The coordination of the alkali metal will be of the type η^4. These findings showcase identical pattern to the findings regarding the alkaliphosphinites and their interaction with diphenylbutadiyne, which has been discussed in **Chapter 4** and hitherto, have been confirmed for other π-systems, interacting with alkali cations.[42,43] Hence, it can be concluded that the preferred mode of interaction of the alkali cation is independent of the mode of coordination of the phosphorous atom present in the system, but its contingent on the size of the cation.

5.3.4. Mechanism for formation of 1-mesityl-2,5-diphenyl-1H-phosphole

5.3.4.1. Potassium-mediated reaction

We will begin this discussion about the alkali catalysed formation of phosphole with the potassium-mediated reaction. This reaction has the highest conversion rate (>99%). Thus, with the aim of generating a better understanding of the reaction of formation of phosphole, we shift our attention on determining the most likely reaction pathway using DFT methods. The Gibbs energy profile calculated for the most likely reaction pathway is illustrated in **Figure 5.11**, whilst the optimized transition state structures associated with the mechanism with the lowest energy barriers are depicted in **Figure 5.12**.

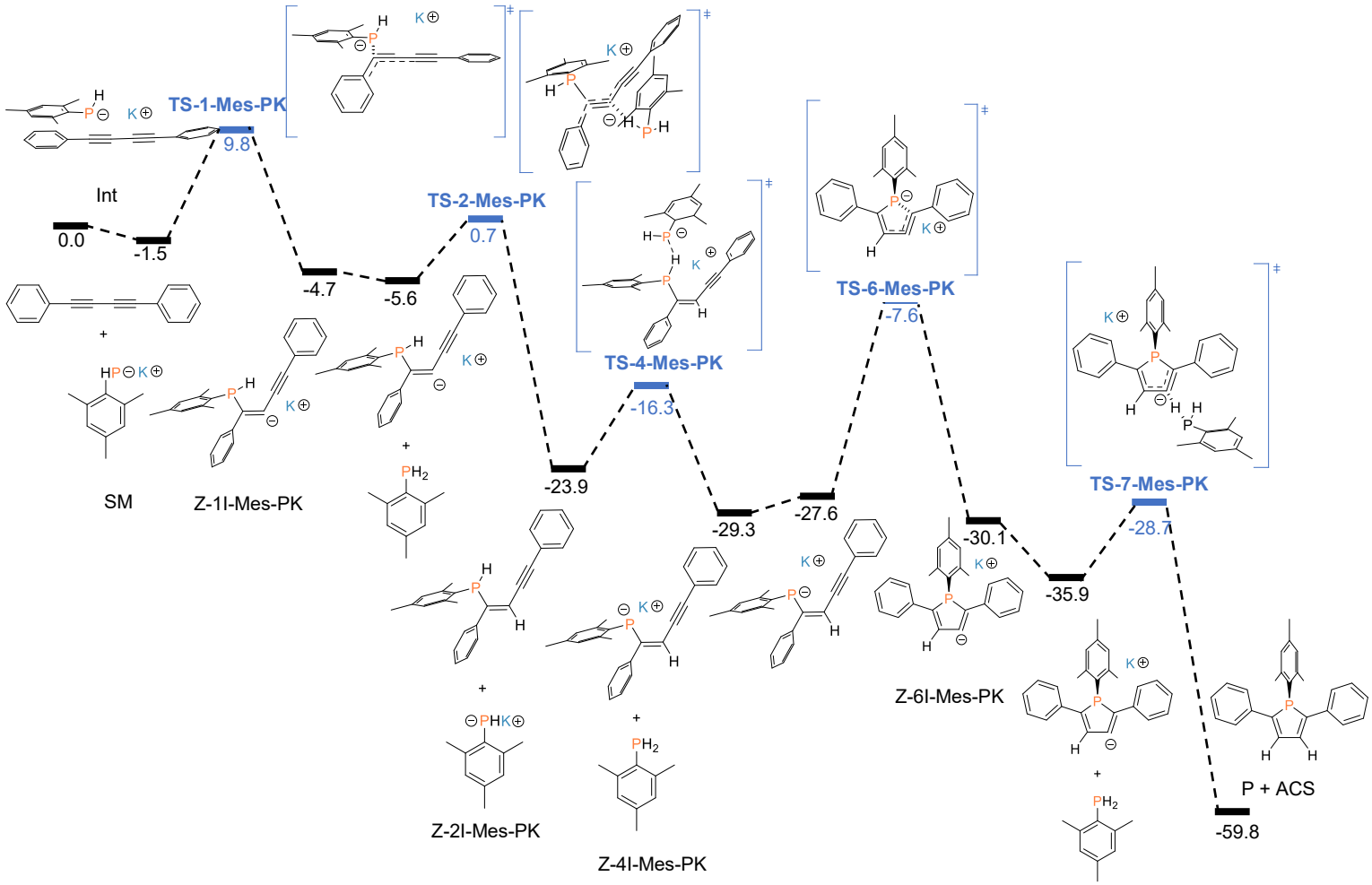

Figure 5.11.: Computed Gibbs energy profile in THF (ΔG_{THF} kcal mol^{-1}) at 298 K for potassium-mediated hydrophosphination of diphenylbutadiyne for the formation of phosphole, using K-HMDS as catalyst at a B3LYP/Def2TZVP level of theory.

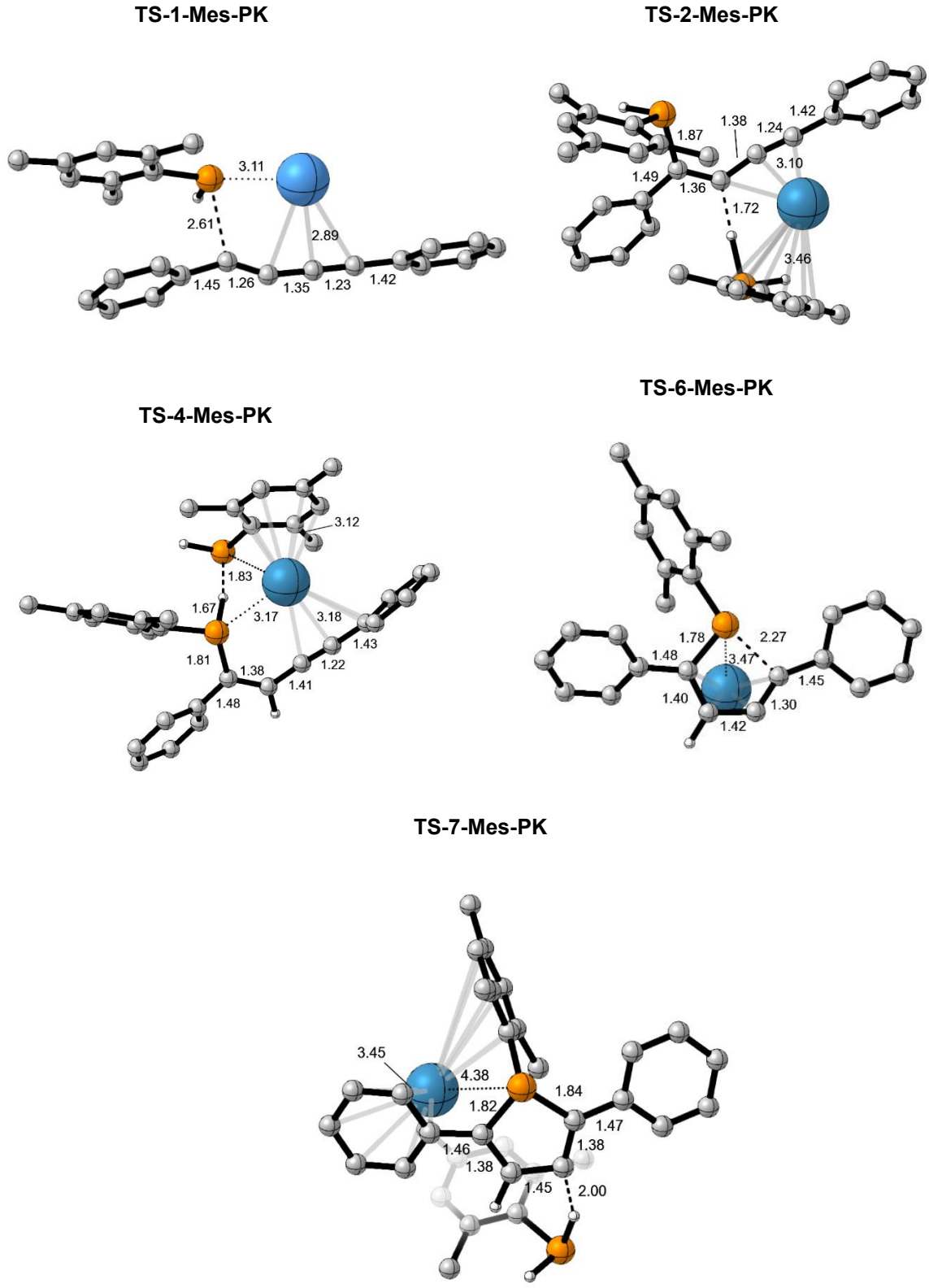

Figure 5.12.: Optimized structures for the lowest transition states for the potassium-mediated formation of phosphole. Certain H atoms are omitted for clarity reasons. Distances are shown in Å.

This mechanism will begin upon initial formation of the M-P(H)Mes (metal phosphanide/active species) as illustrated in **Scheme 5.3**. The formation of active species has been discussed previously in **Section 5.3.2.** For the reaction to proceed, a concomitant interaction is necessary between the 1,4-diphenylbutadiyne and alkali mesitylphosphanide. We estimated the most favourable interaction to lay at -3.4 kcal mol^{-1} bellow separated reactants. Hence, the initial interaction is marginally favoured. Indeed, the mechanism will begin with a nucleophilic attack from the alkali mesitylphosphanide onto C_1 from diphenylbutadiyne (**TS-1-Mes-PK**), with an energy barrier of 13.2 kcal mol^{-1}. Looking at **Figure 5.12** for **TS-1-Mes-PK** we can notice that the potassium cation has a weak interaction with the phosphorous atoms (3.11 Å), but a stronger interaction with C-C conjugated system (2.89 Å). Moreover, we can also see a slightly displaced staggered stacking between the phenyl and the mesityl moieties. The intermediate which is formed from this nucleophilic attack is **Z-1I-Mes-PK** and it may be found at -4.7 kcal mol^{-1} below separated reactants (DPBD + K-P(H)Mes). It should be noted that we also explored that addition of metal phosphanide across C_2 and this step presented with an energy barrier of 19.6 kcal mol^{-1}, which is 6.4 kcal mol^{-1} higher than that in C_1 and it yielded a thermodynamically less stable intermediate (**P-1-MesA-PK**) at -0.4 kcal $^{-1}$. Hence, it may be concluded that the addition across C_1 is both kinetically and thermodynamically favoured over addition onto C_2. The Gibbs energy diagram comparing both nucleophilic attacks (**TS-1-Mes-PK** and **TS-1-MesA-PK**) and the respective optimized structure for **TS-1-MesA-PK** (Part B) may be found in **Figure 5.13, A** and **B**, respectively. As this energy barrier was estimated to be higher than the energy barrier necessary for the nucleophilic attack proceeding on C_1, we excluded the computational calculations for the 2,3-two folded addition.

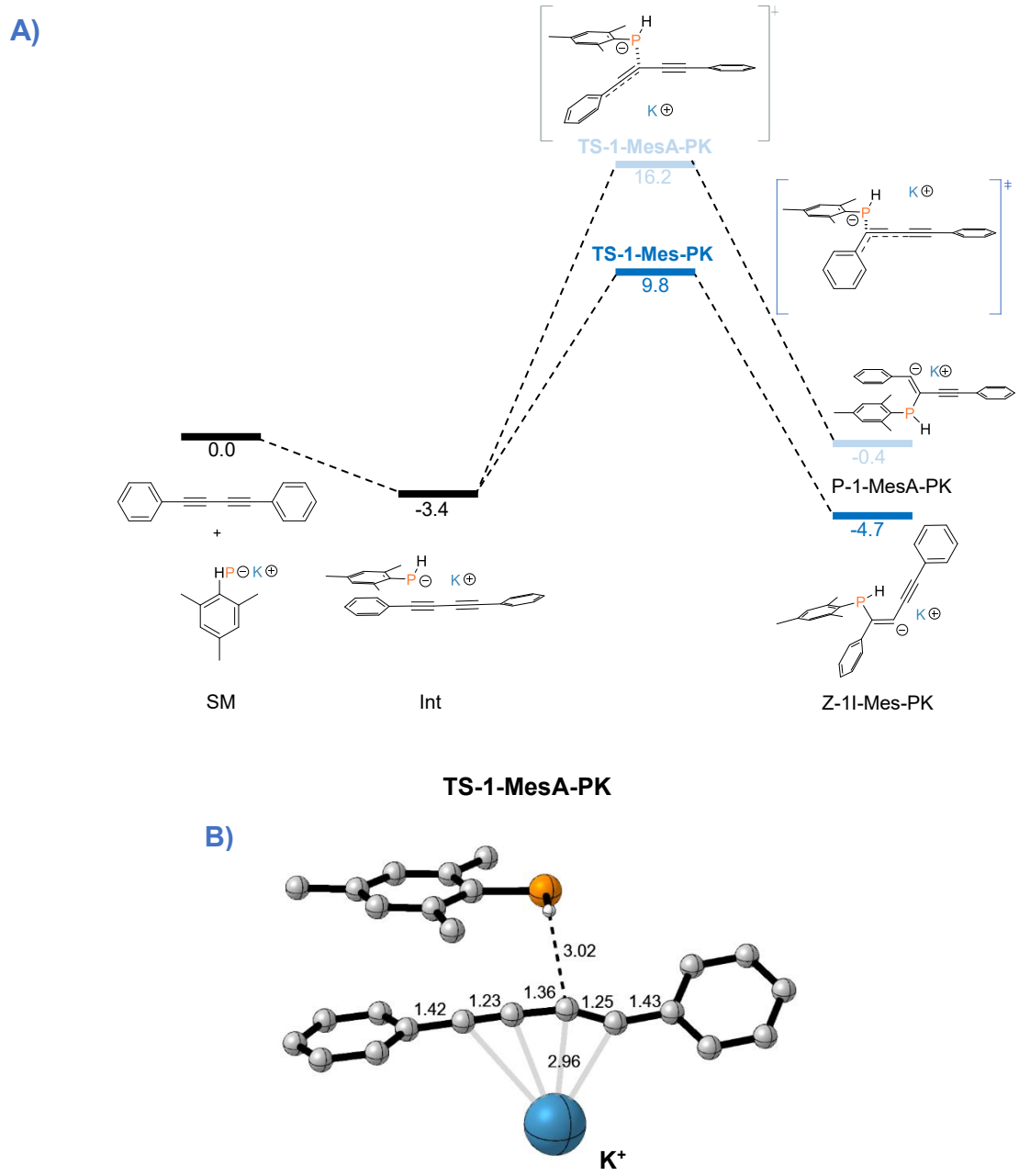

Figure 5.13.: A) Gibbs energy profile in THF (ΔG_{THF} kcal mol^{-1}) at 298K for 1st nucleophilic attack C1 (blue pathway) vs C2 (pink pathway) by potassium phosphanide onto 1,4-diphenylbutadiyne at the B3LYP-D3/def2-TZVP/SMD(THF)//B3LYP-D3BJ/6-31G(d,p)/SMD(THF) level of theory and B) Optimized structure for transition state for 1st nucleophilic attack onto C2 atom. Certain H atoms are omitted for clarity reasons. Distances are shown in Å.

The intermediate **Z-1I-Mes-PK** from **TS-1-Mes-PK** possesses the correct conformation to proceed subsequently with ring closure. Hence, no need for isomerization is required. The potassium cation in this intermediate predominantly interacts with the

diyne system. In addition, we also determined the thermodynamic stability of **Z-1I-Mes-PK** (-4.7 kcal $^{-1}$ kcal mol^{-1}) and **E-1I-Mes-PK** (-1.5 kcal mol^{-1}). Therefore, we can say that besides possessing the correct configuration suited to undergo ring closure, the intermediate **Z-1I-Mes-PK** is also thermodynamically more stable than **E-1I-Mes-PK** intermediate. We were also able to exclude isomerization as a step to proceed from **Z-1I-Mes-PK** into **E-1I-Mes-PK** as we estimated an energy barrier of 17.8 kcal mol^{-1}.

Initially we proposed that the protonation step would induce simultaneously a subsequent metalation step i.e., reactivation of the phosphorous atom for the cyclization step. However, despite numerous attempts, we were not able to attain a step which would induce a protonation and simultaneous metalation at the phosphorous atom. Consequently, we concluded that the most probable pathway for this step is a stepwise protonation and then consecutive deprotonation/metalation. Ergo as proposed in **Scheme 5.3**, we tested both $MesPH_2$ and H-HMDS as proton donors for the proceeding protonation step. The molecule of H-HMDS is formed as a side product upon the formation of the active species, thus they are also available as Brønsted acids. Before confirming that the pronation proceeds *via* a route of $MesPH_2$ or H-HMDS as proton donor, we also considered the possibility of intramolecular protonation (i.e., transfer of the H atom attached to the phosphorous atom onto C_2). Nonetheless, we were able to exclude this possibility, as the yielded intermediate in the previous step does not bear the necessary configuration for interaction between the P and the C_2 atom. The Gibbs energy profile depicting the two possible calculated modes for the protonation step ($MesPH_2$ or H-HMDS) are presented in **Part A** of **Figure 5.14,** whilst **Part B** illustrates the TS in which the H-HMDS is the proton donor.

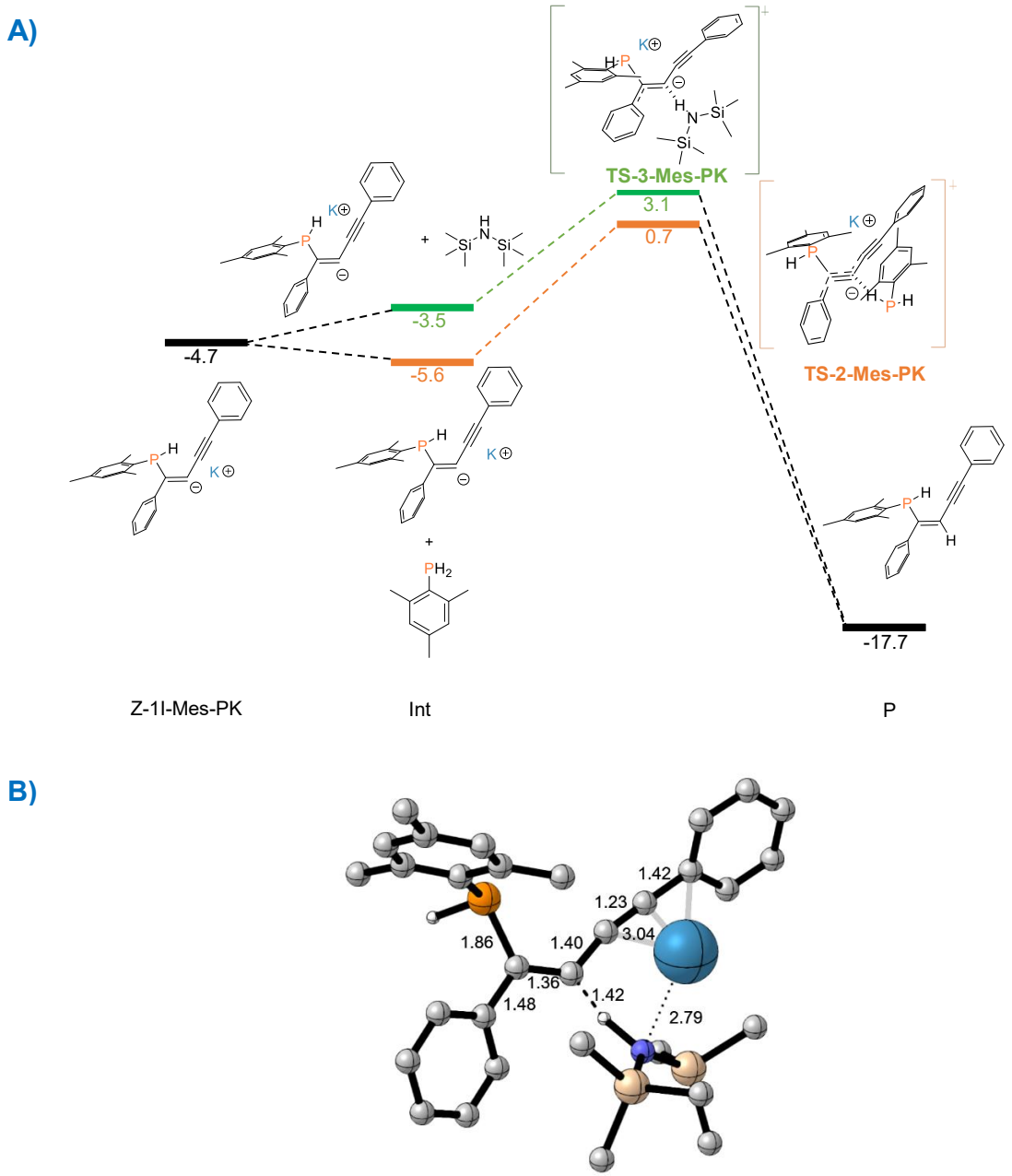

Figure 5.14.: **A)** Computed Gibbs energy profile of possible modes for 1st protonation step in THF (ΔG_{THF} kcal mol^{-1}) at 298 K for potassium-mediated hydrophosphination of diphenylbutadiyne for the formation of phosphole, using K-HMDS as catalyst at the B3LYP-D3/def2-TZVP/SMD(THF)//B3LYP-D3BJ/6-31G(d,p)/SMD(THF) level of theory. The pathway through $MesPH_2$ (**TS-2-Mes-PK**) and H-HMDS (**TS-3-Mes-PK**) are depicted with orange and green, respectively. **B)** Optimized structure for the protonation step in the potassium-mediated formation of phosphole when H-HMDS is the proton donor. Certain H atoms are omitted for clarity reasons. Distances are shown in Å.

As illustrated in **Figure 5.14**, we attempted to keep the same configuration of the proton donor molecules, regardless of which molecule we used as donor conductive, to provide better comparison with the analogous step provided in **Figure 5.12.** From **Figure 5.14**, we can see that the protonation step with the smallest energy barrier is with $MesPH_2$ as a Brønsted acid (**TS-2-Ph-K** of 6.3 kcal mol^{-1}) with a marginal distinction to H-HMDS as a proton donor (**TS-3-Ph-K** of 6.6 kcal mol^{-1}). Consequently, we concluded that the protonation step most probably will proceed *via* both pathways for this step. As it may be noted from **Figure 5.12** and **5.14** the potassium cation in this step will preferably interact with the C-C conjugated system regardless of the molecule which is used as a donor. In these two TSs, the coordination of the potassium cation with phosphorous atom proceeds at a larger distance. Concurrently, with the formation of the **Z-2I-Mes-PK**, M-HMDS or M-P(H)Mes will be formed depending on the pathway of formation.

For the following step we propose deprotonation of the phosphorous atom (cf. **Scheme 5.3**). This step is necessary as the cyclization may not proceed if the phosphorous atom is still protonated. The two molecules (M-P(H)Mes and M-HMDS) generated in the previous step may be involved in this step. The Gibbs energy profile depicting the two possible calculated modes for the deprotonation step ($MesPH_2$ or H-HMDS) is presented in **Part A** of **Figure 5.15,** whilst **Part B** illustrates the TS in which the H-HMDS is the proton donor.

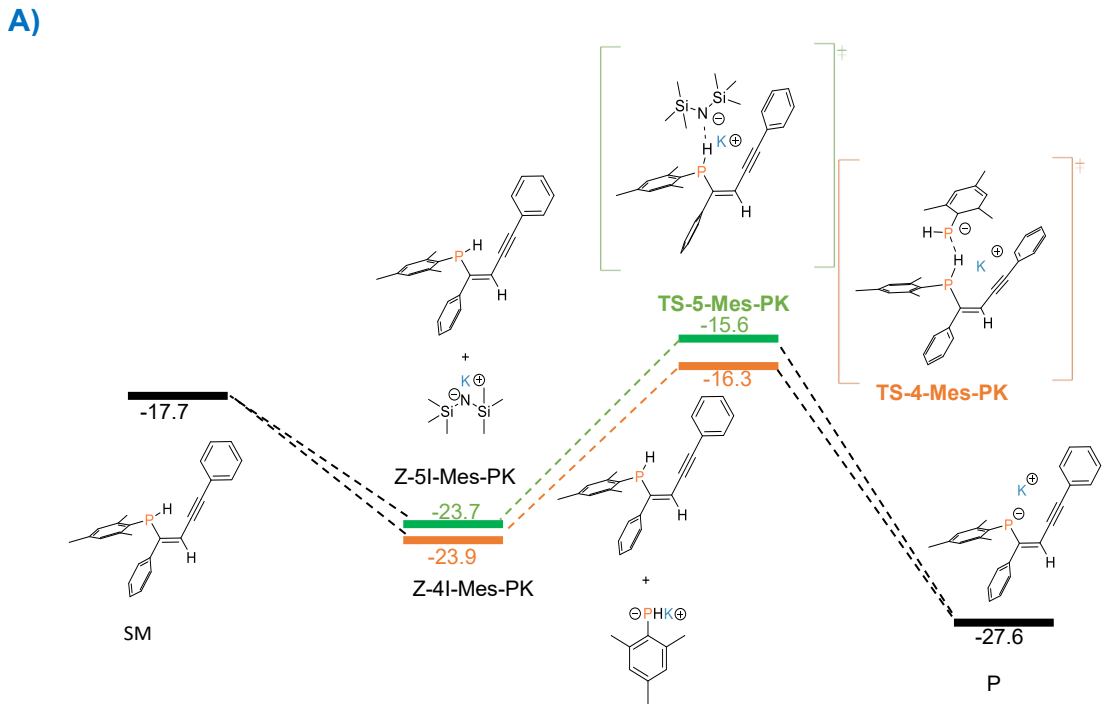

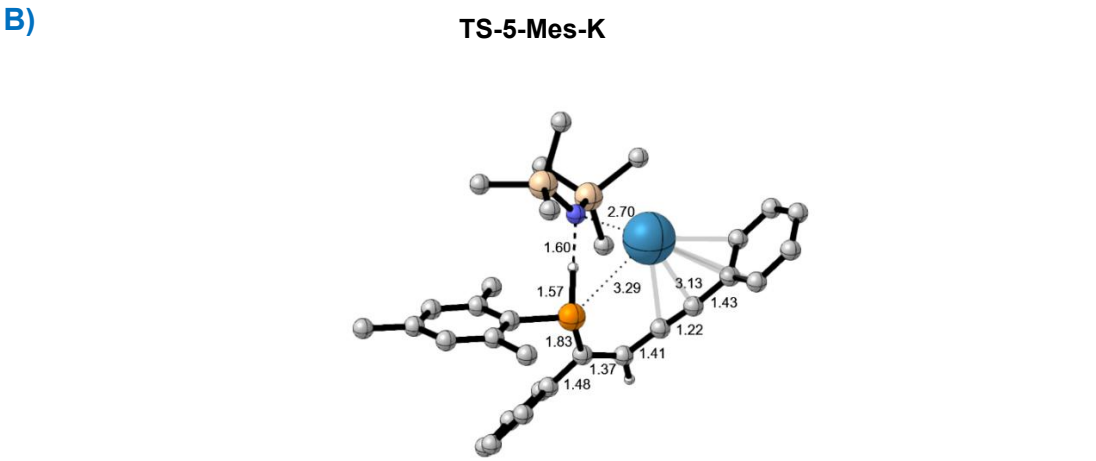

Figure 5.15.*:* **A)** Computed Gibbs energy profile of possible modes for the P-H deprotonation step in THF (ΔG_{THF} kcal mol^{-1}) at 298 K for potassium-mediated hydrophosphination of diphenylbutadiyne for the formation of phosphole, using K-HMDS as catalyst at the B3LYP-D3/def2-TZVP/SMD(THF)//B3LYP-D3BJ/6-31G(d,p)/SMD(THF) level of theory. The pathway through $MesPH_2$ (**TS-2-Mes-PK**) and H-HMDS (**TS-3-Mes-PK**) are depicted with orange and green, respectively. **B)** Optimized structure for the deprotonation transition states for potassium-mediated formation of phosphole when H-HMDS is the proton acceptor. Certain H atoms are omitted for clarity reasons. Distances are shown in Å.

As shown in **Figures 5.12** and **5.15**, we assumed that the proton acceptor molecules will be positioned in similar arrangement regardless of which molecule we used as Brønsted base. Additionally, we can see that the change of the proton acceptor molecules does not induce any significant change in the interaction between the potassium cation and the diyne moiety. Also, the interaction remains with very weak character. Analogously to the preceding step the deprotonation with M-P(H)Mes has a lower energy barrier (**TS-4-Mes-PK**; 7.6 kcal mol^{-1}) than with M-HMDS (**TS-5-Mes-PK**; 8.1 kcal mol^{-1}). In the generated intermediate **Z-4I-Mes-PK,** the potassium cation is between the phosphorous atom and the triple bond. This unique positioning may be one of the factors governing the "activation" of the triple bond to undergo a subsequent nucleophilic attack and yield a 5-membered ring. In this step subsequently of the deprotonation we will regenerate either a $MesPH_2$ or H-HMDS molecule, depending on the taken TS pathway. Notably, there are no π - π interactions in this step nor in the previous between the mesityl moiety of the phosphanide and the phenyl substituents of the diyne. In both steps, protonation and deprotonation, the potassium cation will likewise interact with a weak interaction with the mesityl moiety.

Before continuing with the discussion on the ensuing steps, it should be mentioned that according to the theoretical results for the 1st protonation step and subsequent deprotonation step, we cannot say with certainty which is the protonating agent: H-HMDS or $MesPh_2$. This is due to the energy barriers being so close in energetic value. Hence, it may be deduced that most likely in the reaction mixture, we have a mixture of both protonating/deprotonating agents, simultaneously executing their roles.

Having obtained the prerequisite conformation in the previous step and having "activated" the second triple bond present we may proceed to the last step in our proposed mechanism i.e. the ring closing step. For the cyclization step **TS-6-Mes-PK** we estimated an energy barrier of 21.7 kcal mol^{-1}. The generated intermediate **Z-6I-Mes-PK** is found at -30.1 kcal mol^{-1} beneath isolated reactants. Remarkably, in this step too, the main interaction of the potassium cation is with the C-C conjugated system. This weak interaction most likely aids in lowering the energy barrier for the cyclization step, nonetheless later we will discuss more into detail the role the alkali cation plays in the overall mechanism (see **Section 5.3.4.4.**).

For the last protonation step, we explored the possibility of protonation by the two possible proton donor molecules generated in the previous step ($MesPH_2$ or H-HMDS; see **Figure 5.12**, **Part A**). Following the trend from the first protonation step, the energy barrier for $MesPH_2$ was marginally lower (**TS-7-Mes-PK**, 7.2 kcal mol^{-1}), than when the protonation step proceeds with H-HMDS as donor (**TS-8-Mes-PK**, 8.1 kcal mol^{-1}). These findings are akin to the data for the first protonation step. As the energy barriers are similar for both proton donor molecules in the reaction's mixture this step can proceed *via* both routes. Interestingly, in **TS-7-Mes-PK** the potassium cation interacts with three aryl rings: the phenyl ring from the diyne moiety, the P_{bound} mesityl moiety and the mesityl moiety from the $MesPH_2$ donor molecule. In **TS-8-Mes-PK** the interaction of the cation is solely with the phosphole, the cation is not in the vicinity of the H-HMDS donor. The optimized structures for **TS-7-Mes-PK** and **TS-8-Mes-PK** are illustrated in **Figure 5.12 and 5.16 Part B**, respectively.

A)

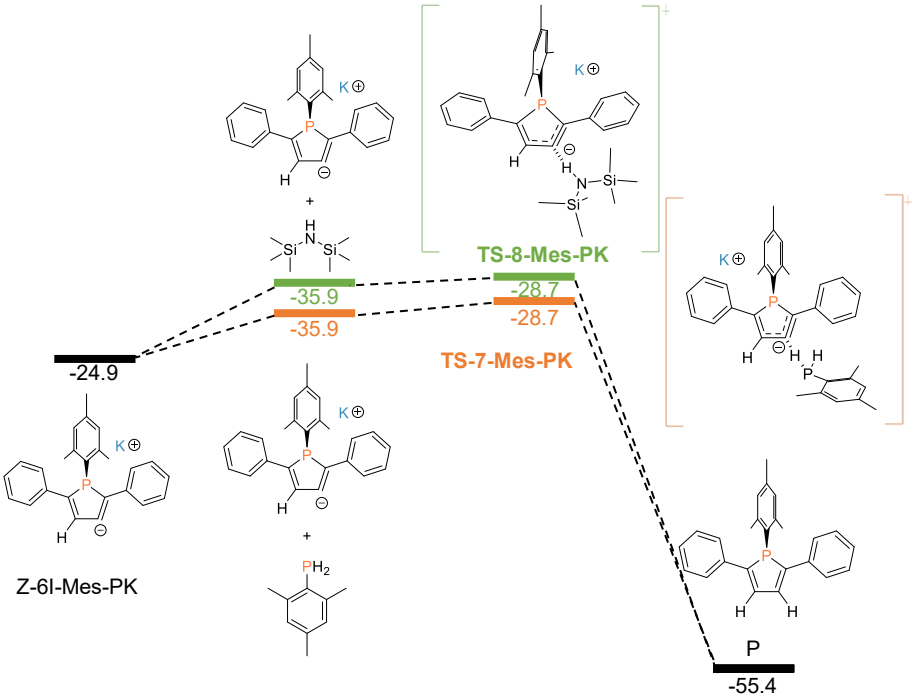

B)

TS-8-Mes-K

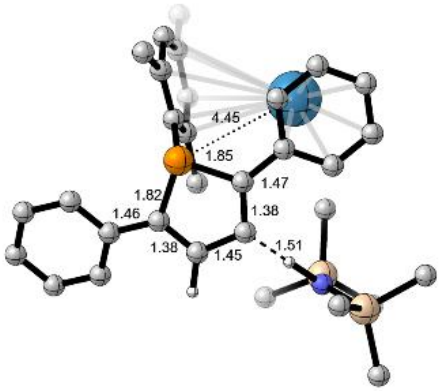

Figure 5.16.: A) Gibbs energy profile in THF (ΔG_{THF} kcal mol^{-1}) at 298K for 2nd protonation step at the B3LYP-D3/def2-TZVP/SMD(THF)//B3LYP-D3BJ/6-31G(d,p)/SMD(THF) level of theory for potassium metal-mediated hydrophopshination. The pathways though **TS-7-Mes-PK** and **TS-8-Mes-PK** are depicted with orange and green, respectively. **B)** Optimized structure for transition state for 2nd protonation step for H-HMDS as proton donor. Certain H atoms are omitted for clarity reasons. Distances are shown in Å.

We can summarize the results as follows: the reaction is exergonic by -55.4 kcal mol^{-1}, with the highest relative energy barrier within the reaction mechanism corresponding to the cyclization step having an energy barrier of 21.7 kcal mol^{-1}. All the estimated energy barriers could be surmounted under the reaction's conditions. Hence, the computational results are indeed in agreement thus far with the experimental results for potassium-mediated formation of phosphole.

Before proceeding to the discussion of the computed reactions for sodium and lithium, it should be noted that the limitation to this study is that this mechanism has only been computed but not confirmed *via* kinetic NMR studies.

5.3.4.2. Sodium-mediated reaction

The potential energy hypersurface of this reaction has been thoroughly investigated to shed light on the decreasing reaction rates observed for harder alkali metals for this reaction. Analogous to the mechanism calculated for potassium-mediated formation of phosphole, the sodium catalysed reaction of mesitylphosphinewith diphenylbutadiyne yielding 1-mesityl-2,5-diphenyl-1H-phosphole was computed. Details on the formation of the active species may be found in **Section 5.3.2**. The Gibbs energy profile generated for the reaction n is depicted in **Figure 5.17**. **Figure 5.18** depicts the optimised transition state structures associated with the mechanism.

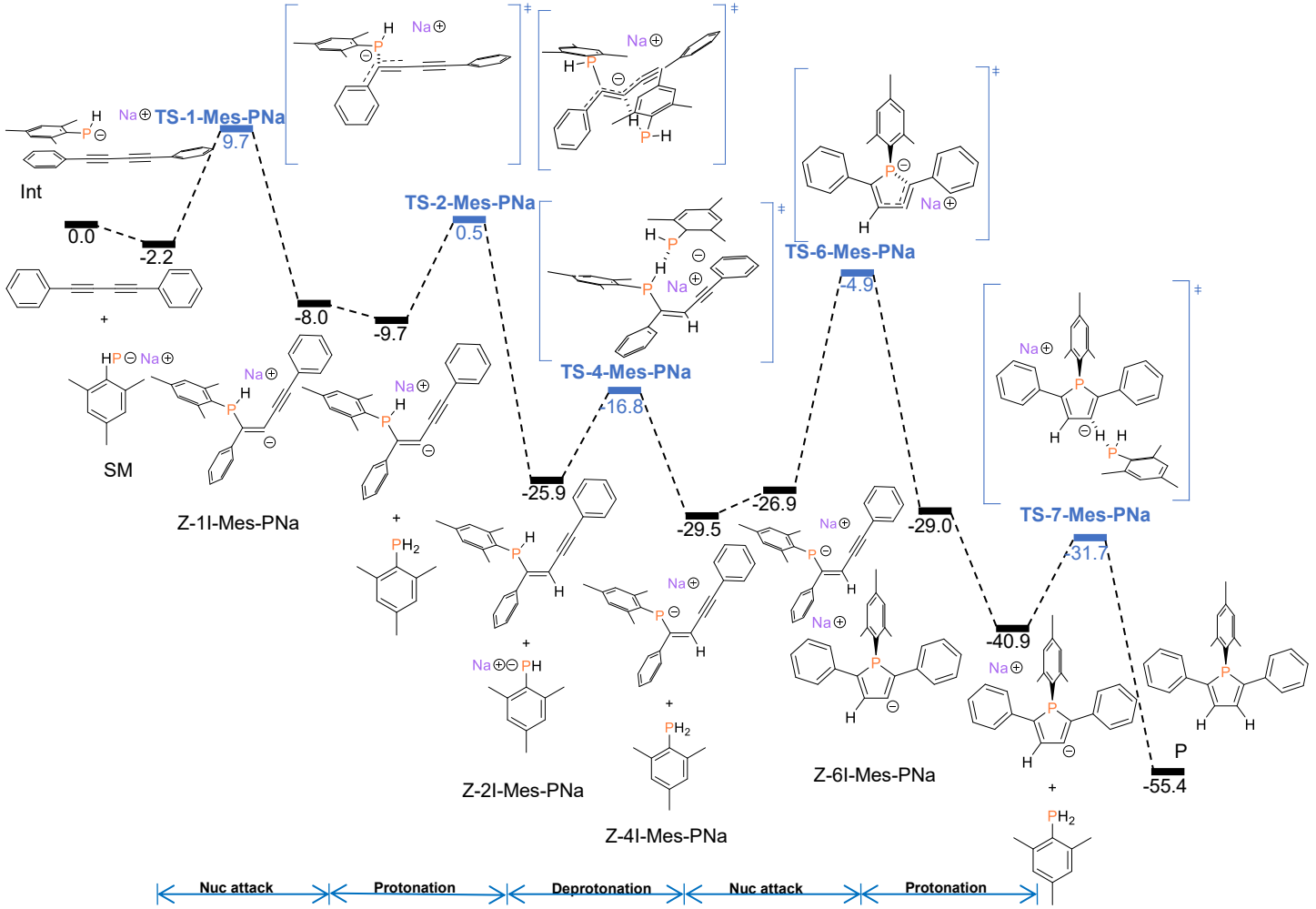

Figure 5.17.: Computed Gibbs energy profile in THF (ΔG_{THF}/kcal mol^{-1}) at 298 K for sodium-mediated hydrophosphination of diphenylbutadiyne for the formation of phosphole, using Na-HMDS as catalyst at the B3LYP-D3/def2-TZVP/SMD(THF)//B3LYP-D3BJ/6-31G(d,p)/SMD(THF) level of theory.

TS-1-Mes-PNa

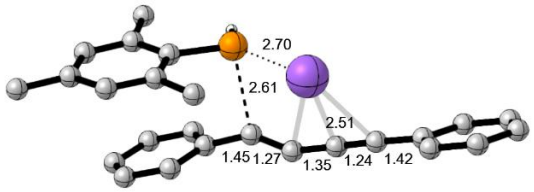

TS-2-Mes-PNa

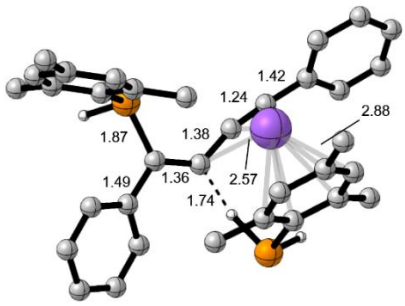

TS-4-Mes-PNa

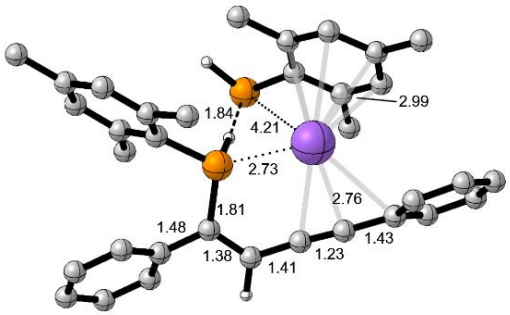

TS-6-Mes-PNa

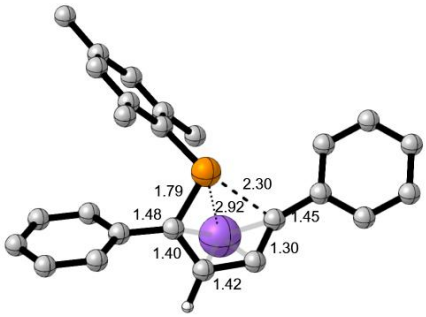

TS-7-Ph-Na

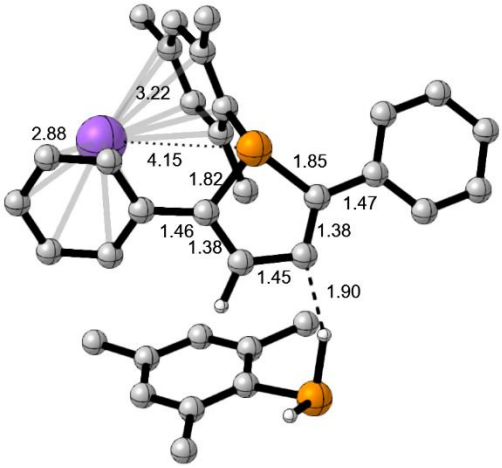

Figure 5.18.: Optimized structures for the lowest transition states involved in the sodium-mediated formation of phosphole. Certain H atoms are omitted for clarity reasons. Distances are shown in Å.

Correspondingly to the formerly estimated pathway, this mechanism begins with the nucleophilic attack (**TS-1-Mes-PNa**) of sodium mesitylphosphanide to C_1 of the diphenylbutadiyne with an energy barrier of 11.9 kcal mol^{-1}. The intermediate resulting from this first step is **Z-1I-Mes-PNa** with a Gibbs energy of -8.0 kcal mol^{-1} below separated reactants. Comparing **Figure 5.12** with **Figure 5.18** we can see that sodium cation prefers to interact at a shorter distance with the phosphorous anion (and the C-C conjugated system), than the potassium cation in this akin TS (**TS-1-Mes-PK**), (2.70 Å vs 3.11Å and 2.51 Å vs 2.89Å, correspondingly). The change of the cation will not induce change in the generated intermediate upon the nucleophilic attack in the sense of the steoreochemistry.

For this mechanism we also proceeded with determining the ensuing step: protonation with both $MesPH_2$ (**TS-2-Mes-PNa**) and H-HMDS (**TS-3-Mes-PNa**) as proton donors. For the former TS we estimated an energy barrier of 10.2 kcal mol^{-1}, whilst for the later TS we estimated an energy barrier of 10.9 kcal mol^{-1}. The increase in the energy barriers compared to potassium mediated reaction may be attributed to the stronger interaction of the sodium cation with the phosphorous anion and the C-C conjugated system, as the conformations in which the transition states proceeds are remarkably akin (see **Figure 5.12** and **5.18**).

In the same manner as for potassium we estimated the energy barriers for the deprotonation with both molecules: $MesPH_2$ (**TS-4-Mes-PNa**; 9.1 kcal mol^{-1}) and H-HMDS (**TS-5-Mes-PNa**; 10.3 kcal mol^{-1}). Regardless of the change in nature of the cation, the TS (**TS-4-Mes-PNa**) is akin to the **TS-5-Mes-PK** conformationally. In comparison to the potassium cation in **TS-4-Mes-PK** the sodium cation in **TS-4-Mes-PNa** interacts at a shorter distance with the diyne system (2.76 Å vs 3.16 Å) and with the mesityl moiety (2.99 Å vs 3.12 Å). The interaction of the alkali cation with the two phosphorous atoms will also proceed at a shorter distance: 2.73 Å vs 3.17 Å for M-P_{bound}[8] and 4.21 Å vs 4.39 Å for M-$P_{acceptor}$[9]. All these changes in distances may be attributed to the size difference amongst the two alkali cations.

The second to last step; ring closing **TS-6-Mes-PNa** for the formation of the phosphole has an energy barrier of 24.6 kcal mol^{-1}. The generated intermediate **E-6I-**

[8] By P_{bound} we mean the P atom connected to C_1 *via* the first nucleophilic attack.
[9] By $P_{acceptor}$ we mean the P atom from to M-(H)PMes (the acceptor molecule).

Mes-PNa is found at 29.0 kcal mol^{-1} beneath isolated reactants. This energy barrier is only slightly larger when compared to the analogous step in **TS-6-Mes-PK** (21.7 kcal mol^{-1}). Nonetheless, this energy barrier can be surmounted under the reaction conditions in which the reaction proceeds.

The final step, which generates 1-mesityl-2,5-diphenyl-1H-phosphole was determined to proceed with an energy barrier of 9.2 and 9.7 kcal mol^{-1} for $MesPH_2$ (**TS-7-Mes-PNa**) and H-HMDS respectively. Contrary to the last step, the change of the cation in this TS induces a notable change at which the TS proceeds (**TS-7-Mes-PNa** vs **TS-7-Mes-PK**; 1.90 Å vs 2.0 Å). The difference between these TSs may be attributable to the change of interaction of the alkali cations with the aryl moieties.

To summarise, the reaction mechanism has the highest energy barrier (24.6 kcal mol^{-1}) for the cyclization step, making it the rate determining step. As it may be seen from **Figure 5.17**, with the exception of the energy barrier for the 1^{st} nucleophilic attack the rest of the estimated energy barriers are indeed slightly elevated compared to the akin estimated energy barriers for potassium-mediated reactions (**Figure 5.11**). The findings demonstrate the limitations of why sodium-mediated hydrophosphination proceeds with a lower conversion rate, comparatively to the potassium mediated reaction. Hence it may be concluded that the computational calculations thus far, do indeed match the experimental results.

5.3.4.3. Lithium-mediated reaction

In contrast to the above findings for potassium and sodium, lithium mesitylphosphanide presented no tendency to react with diphenylbutadiyne under these reaction conditions, according to the experimental findings. With the reaction pathways established for both potassium and sodium-catalysed reaction, we next computed the corresponding Gibbs energy profile for lithium-mediated formation of phosphole (following the proposed mechanism in **Scheme 5.3**). The calculated Gibbs energy profile is illustrated in **Figure 5.19**, whilst the optimized structures for the transition states involved in the mechanism are depicted in **Figure 5.20**. Details on the formation of the active species may be found in **Section 5.3.2**.

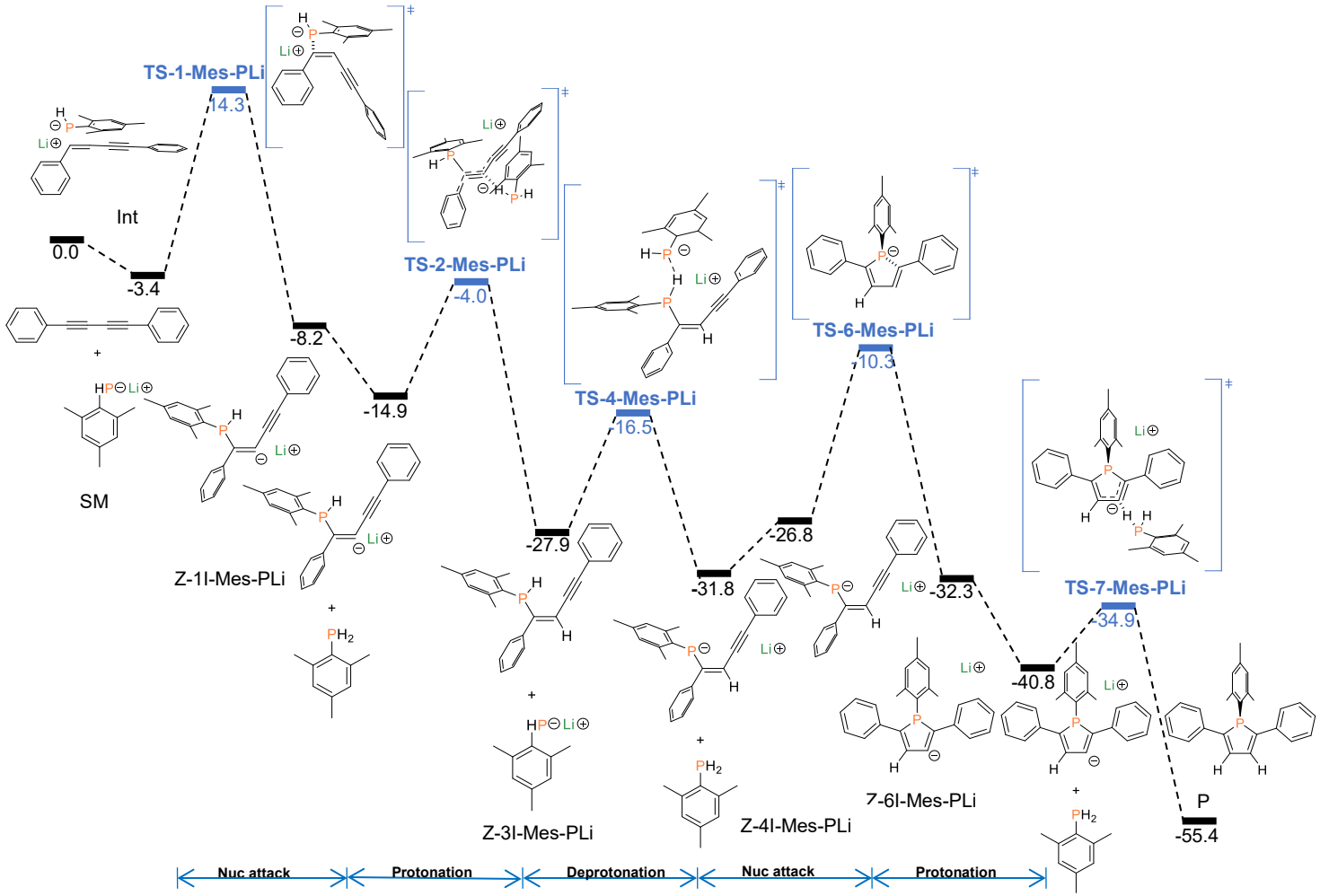

Figure 5.19.: Computed Gibbs energy profile in THF (ΔG_{THF}/kcal mol^{-1}) at 298 K for lithium-mediated hydrophosphination of diphenylbutadiyne for the formation of phosphole, using Li-HMDS as catalyst at the B3LYP-D3/def2-TZVP/SMD(THF)//B3LYP-D3BJ/6-31G(d,p)/SMD(THF) level of theory.

TS-1-Mes-PLi

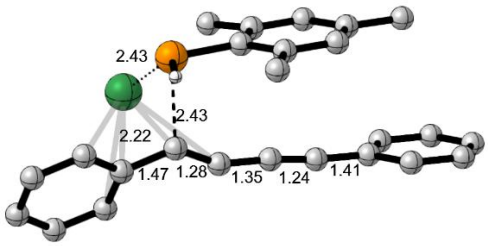

TS-2-Mes-PLi

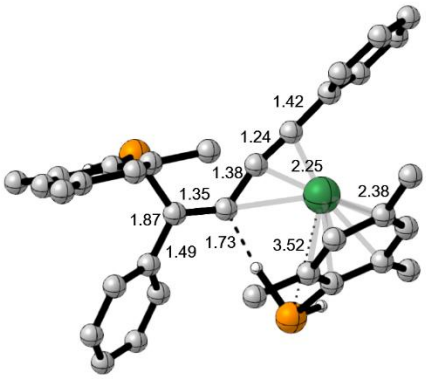

TS-4-Mes-PLi

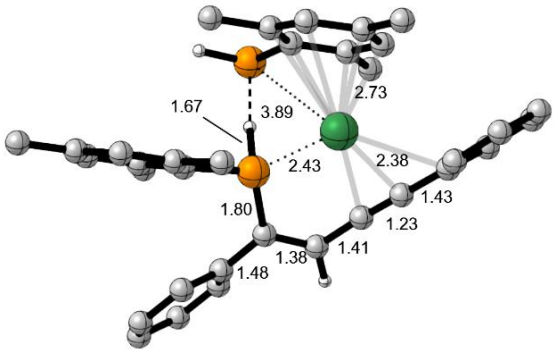

TS-6-Mes-PLi

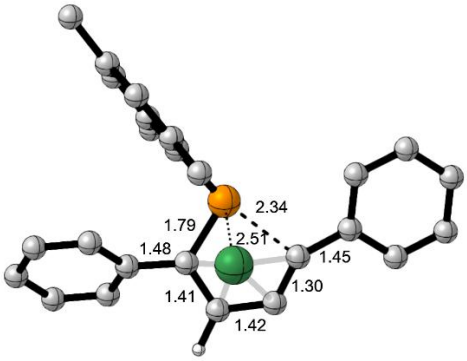

TS-7-Mes-Li

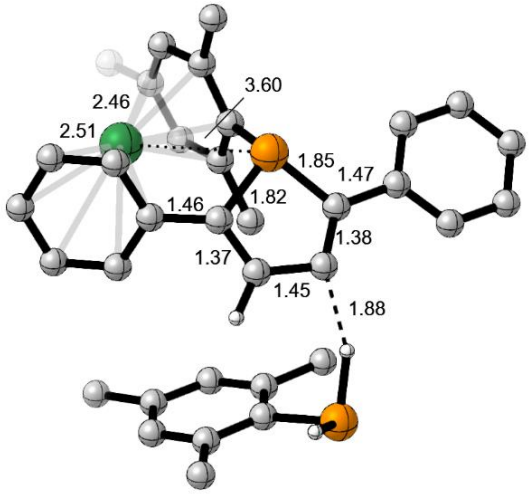

Figure 5.20.: Optimized structures for the lowest transition states involved in the lithium-mediated formation of phosphole. Certain H atoms are omitted for clarity reasons. Distances are shown in Å.

The nucleophilic attack by lithium mesitylphosphanide on diphenylbutadiyne proceeds *via* **TS-1-Mes-PLi** (17.7 kcal mol^{-1}) and provides a route for the formation of **Z-1I-Mes-PNa.** However, there is an imperative difference between the configuration of this transition state and the transition states **TS-1-Mes-PNa** and **TS-1-Mes-PK**. Comparatively in the **TS-1-Mes-PNa** and **TS-1-Mes-PK** (see **Figures 5.18** and **5.12, respectively**), the mesityl moiety preferably interacts in a staggered stacking way with the aryl substituent, whereas in the **TS-1-Mes-PLi** (see **Figure 5.20**) the mesityl moiety will rather interact with the C-C conjugated system. Ergo, the lithium cation will interact more strongly with the aryl system than with the C-C conjugated system. This significant change in bonding interaction could be due to the lithium cation being the smallest cation out of tested alkali cations, thus interacting much more strongly with both the phosphinemoiety and the diyne. Attempts were made to locate a transition state with a similar conformation to the **TS-1-Mes-PNa** and **TS-1-Mes-PK**. However, every time we attempted to locate another transition state, we discovered a transition state with a conformation analogous to the one of the **TS-1-Mes-PLi**. The **Z-1I-Mes-PLi** intermediate has the correct configuration to proceed with the ring closure later in the catalytic cycle, regardless of the different configuration in which the **TS-1-Mes-PLi** progresses. Upon the nucleophilic attack, the following step in the proposed catalytic cycle is the protonation step, which generates the intermediate **Z-2I-Mes-PLi** and M-P(H)Mes or M-HMDS depending on the route. We estimated an energy barrier of 10.9 kcal mol^{-1} in the case of proton donor being $MesPH_2$ **(TS-2-Mes-PLi**), whilst in the case of proton donor being H-HMDS we estimated a barrier of 12.9 kcal mol^{-1}. Conformationally, these two located transition states are analogous to the other TSs, previously determined. The distance between the lithium cation and the phosphinemoiety or the C-C conjugated is shorter than for the comparative step for sodium and potassium cation (3.10 Å (K) vs 2.57 Å (Na) vs 2.25 Å (Li) and 3.46(Na) Å vs 2.88 Å(Na) vs 2.28 Å(Li) respectively), however, the distance between the lithium cation and the P_{donor} remained the same as in **TS-2-Mes-PNa**. Notably, as the cation size decreased, the energy barrier for the 1st protonation step increased. This increase in energy barrier may be attributed to the increased interaction of the cation with the π-systems.

For the subsequent step of deprotonation, we estimated an energy barrier of 11.4 kcal mol^{-1} in the instance of M-P(H)Mes (**TS-4-Mes-PLi**) and 12.2 kcal mol^{-1} for M-HMDS as deprotonating agents. In line with the previous steps, this step also

necessitates a greater energy barrier to be surmounted for the lithium cation in comparison to the larger congeners regardless of the deprotonating agent. It is interesting to note that both **TS-4-Mes-PLi** and **TS-5-Mes-PLi** follow the same trend as for the previous step i.e. the lithium cation interacts at a shorter distance with both the mesityl moieties and the C-C conjugated system, compared to the sodium and potassium cations. Evaluating more specifically the distances in **TS-4-Mes-PLi** vs. **TS-4-Mes-PK** (see **Figure 5.20** and **5.12**), we can see that the distance of the potassium cation with the mesityl moiety is at 3.12 Å, while with the C-C conjugated system it is at 3.18 Å, whereas the lithium cation will interact with the mesityl moiety at 2.73 Å and with the C-C conjugated system at 2.38 Å. However, the intermediate **Z-4I-Mes-PLi** may be found at -26.8 kcal mol^{-1} and as such it is the most thermodynamically similar value to **Z-4I-Mes-PNa** (-26.9 kcal mol^{-1}). The intermediate **Z-4I-Mes-PK** (-27.6 kcal mol^{-1}) remains the most thermodynamically stable amongst these intermediates.

The intermediate **Z-4I-Mes-PLi** will then proceed with the second nucleophilic attack i.e., cyclization step (**TS-6-Mes-PLi)** with an energy barrier of 21.5 kcal mol^{-1}. The coordination of the lithium atom follows the same manner as in the akin TSs for the other alkali-mediated reactions, but the shorter distance between the cation and the C-C conjugated system is present in this TS, too. Interestingly, in this case the cyclization step will proceed with the smallest energy barrier among the three alkali cations. The generated intermediate **Z-6I-Mes-PLi** (-32.3 kcal mol^{-1}), is the most thermodynamically stable between the akin intermediates **Z-6I-Mes-PNa** (-29.0 kcal mol^{-1}), and **Z-6I-Mes-PK** (-30.1 kcal mol^{-1}). Hence, it may be deduced that the identity of the alkali cation does play a role in the thermodynamic stability of the intermediates, and not just in the TS.

The formation of the final product from the intermediate **Z-6I-Mes-PLi** in this case was also estimated considering two pathways: a) $MesPH_2$ and b) H-HMDS as proton donor molecules. Our computational findings showed that the energy barrier necessary for the final protonation step to proceed *via* the first pathway is 5.9 kcal mol^{-1}(**TS-7-Mes-PLi**), whilst, *via* the second pathway is 6.9 kcal mol^{-1}.

In summary, the results thus far indicate that some energy barriers for lithium are indeed higher than those for sodium and potassium in the hydrophosphination of diphenylbutadiyne to yield phosphole. However, the rate-determining step (RDS) of

cyclization (21.5 kcal/mol) is similar to that of the potassium system (21.7 kcal/mol) and lower than that for sodium (24.6 kcal/mol). This suggests that the unsuitability of Li-HMDS as a catalyst may not be due to the reaction itself but rather to the generation of active species, which might be insufficient to initiate the reaction. Given the current understanding from this section and **Section 5.3.2**, the reason for the inhibition of this reaction remains unclear. Further theoretical and experimental investigations are needed to uncover the underlying cause. The results discussed thus far demonstrate the crucial role the correct choice of the alkali cation in the catalyst plays for the overall outcome of the reaction.

5.3.4.4. Reaction without alkali metal cation

For the sake of comparison, the reaction mechanism without the presence of alkali cation was also evaluated. Moreover, as mentioned previously, Roesler *et al.* also proposed a reaction mechanism for the formation of phosphole *via* a “bare” anionic system.[19] Our experimental and computational results presented thus far demonstrate that this is not necessarily true, quite the opposite. We propose that the alkali cation does play a crucial role in the reaction mechanism. Even though we did not replicate the previously reported proposed mechanism in terms of the proposed steps, we investigated the proposal of “bare” anionic system i.e., omitting the cation and seeing how that will influence the reaction mechanism. This scenario could occur in a highly polar solvent where the alkali cation/phosphanide ion pair dissociates. However, this is unlikely in THF (ε = 7.4), where such dissociation is minimal.[44–46] Notably, the effect the solvent has over the outcome of the reaction is explored experimentally in the original study conducted by Westerhausen *et al.*[22] The estimated Gibbs energy profile for the “bare” anionic mechanism is depicted in **Figure 5.21**, whilst still keeping the same steps from **Scheme 5.3**. The optimized structures for transition states for formation of phosphole *via* a “bare” anionic pathway are depicted in **Figure 5.22**.

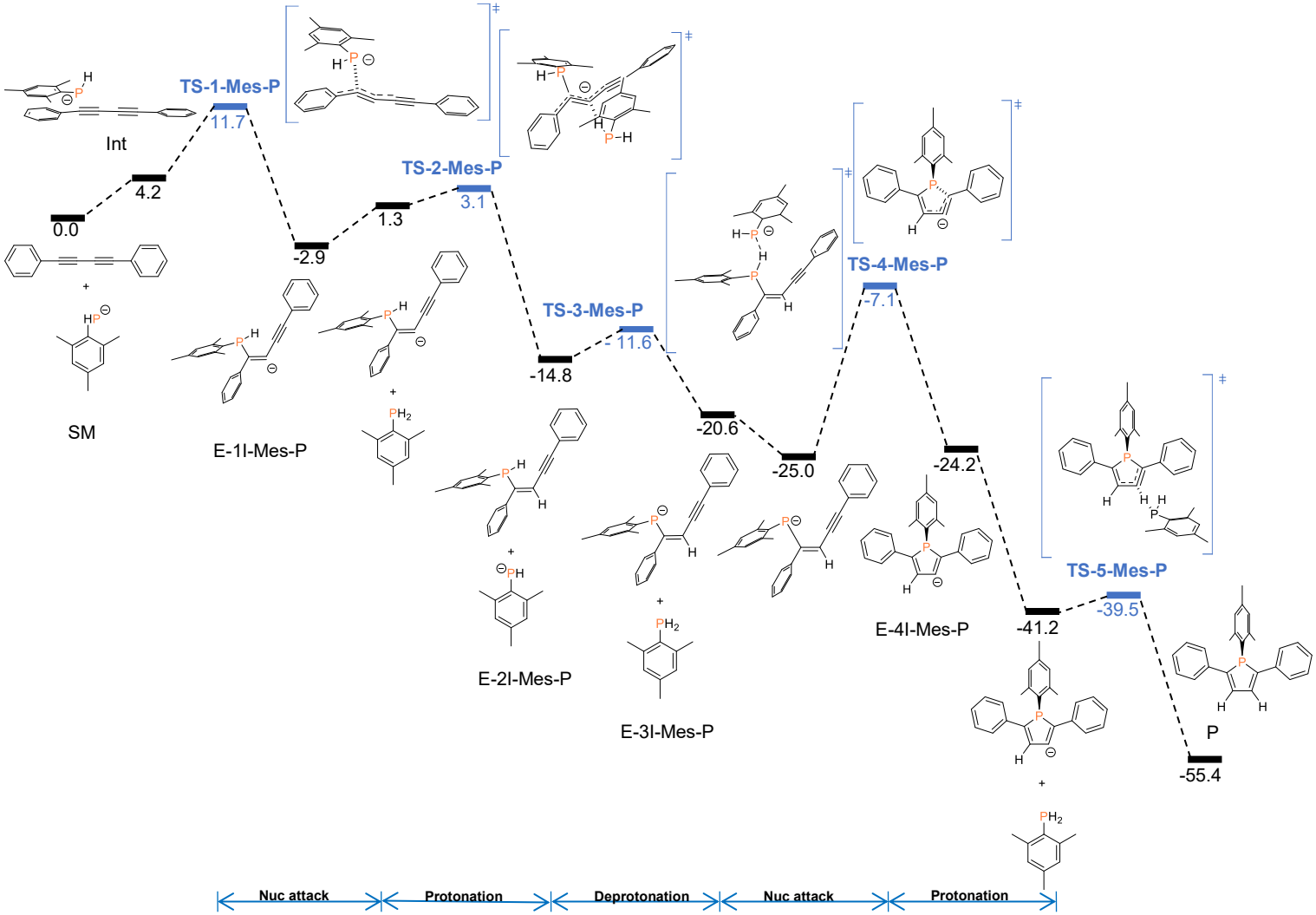

Figure 5.21.: Computed Gibbs energy profile in THF (ΔG_{THF} kcal mol^{-1}) at 298 K for formation of phosphole via an "bare" anionic pathway at the B3LYP-D3/def2-TZVP/SMD(THF)//B3LYP-D3BJ/6-31G(d,p)/SMD(THF) level of theory.

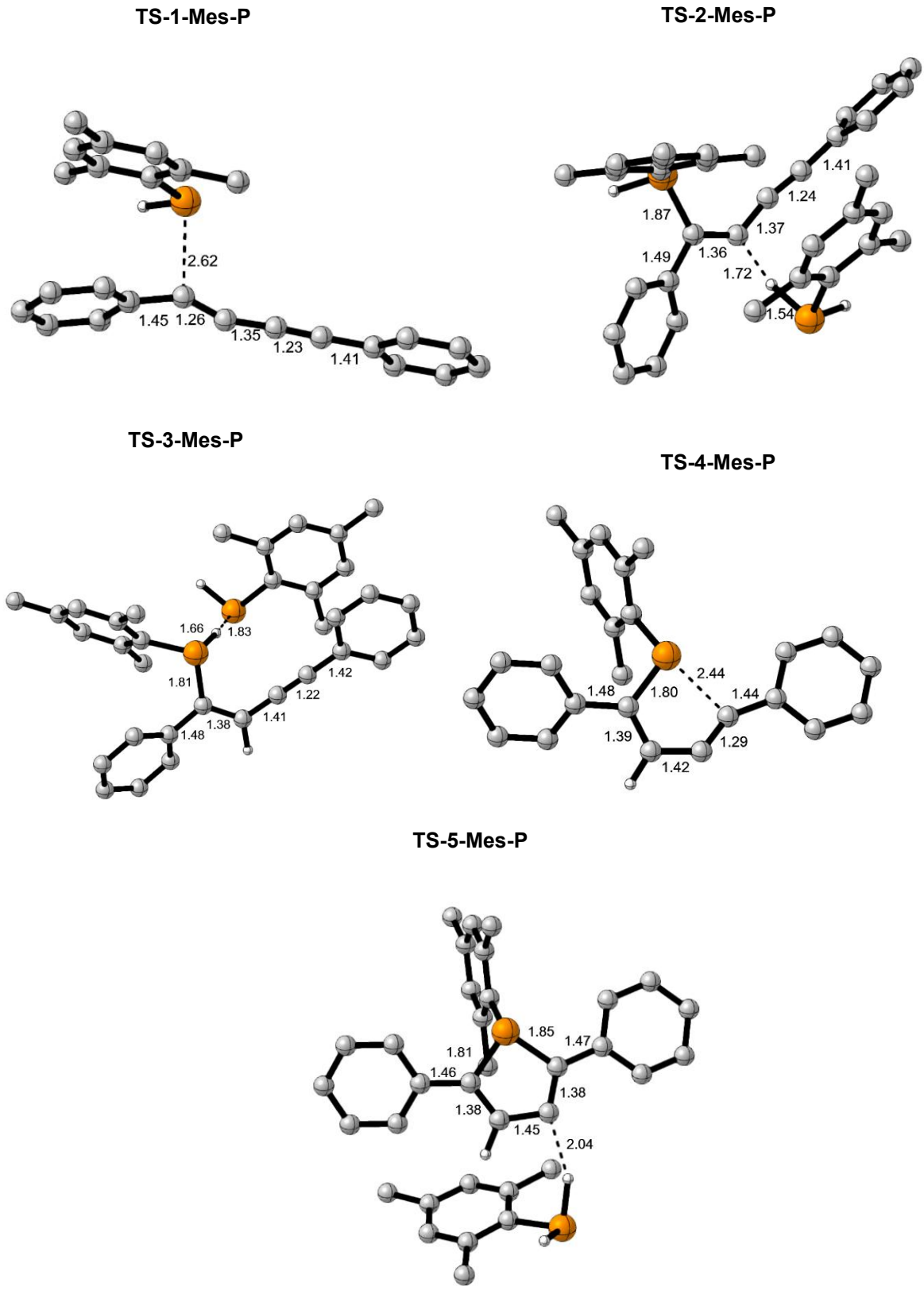

Figure 5.22.: Optimized structures for the lowest transition states for formation of phosphole *via* a “bare” anionic pathway. Certain H atoms are omitted for clarity reasons. Distances are shown in Å.

As it can be deduced from **Figure 5.21** the estimated profile following a “bare” anionic pathway does not differentiate significantly from the estimated reaction pathways which incorporate explicitly the alkali cations.

Our findings showed that the nucleophilic attack TS-1-Mes-P has an energy barrier of 11.7 kcal mol^{-1}. The TS will proceed in akin manner to the 1st nucleophilic attacks in which either the potassium or sodium cation is present. However, the concomitant interaction in this case is the most thermodynamically disfavoured and it may be found at 4.2 kcal mol^{-1} above the reactants. Before continuing with the discussion, it should be mentioned that we solely estimated the two protonation steps and the deprotonation step with $MesPH_2$ and M-P(H)Mes, respectively. However, the introduction in this instance of an additional molecule of $MesPH_2$ caused an increase in energy for the intermediates from -2.9 kcal mol-1(**Z-1I-Mes-P**) to 1.3 kcal mol-1(**Z-1I-Mes-P** + MesPH2). This increase energy is opposite from what we have seen when we incorporate the cation into the mechanism. The protonation step was estimated to proceed with an energy barrier of 6.0 kcal mol-1 (**TS-2-Mes-P**). Following the last step, the deprotonation step will also proceed with the small energy barrier (**TS-3-Mes-P**; 3.2 kcal mol^{-1}), when there is no explicit cation present. Interestingly, all the generat-ed intermediates thus far in this mechanism are less thermodynamically stable than the analogous intermediates with incorporated explicit cations. We noted that the cy-clization step in this instance necessitates an energy barrier of 17.9 kcal mol^{-1}(**TS-4-Mes-P**). Compared to the other three cyclization steps, this step has a lower energy barrier than the similar steps involving alkali cations. Therefore, we concluded that although the cyclization step is the rate-determining step (RDS), the influence of the cation in this step might be limiting. The last protonation step proceeds with an energy barrier of 1.7 kcal mol-1 (**TS-5-Mes-P**). Notably, this is the smallest energy barrier found for this mechanism.

Our comparative study points out that the main influence of the alkali cation is in stabilizing reaction intermediates, but it has a minor effect in the barrier of the RD cyclization step, in any case slightly raising its energy. The “non-cation” situation would correspond to a highly polar solvent, in which alkali cation/phosphanide ion pairs split. However, this is not expected to occur in a low polar medium as THF, in which the presence of these contact ion pairs seems to be undeniable, and, as it is, cations should be included in the computed system.

5.1.4.5. Potassium-mediated bishydrophosphination

In addition to estimating the Gibbs energy barrier for the formation of phosphole we estimated the Gibbs energy barrier for the formation of the 1,4-bishydrophosphination product as this is one of the possible by-products of this reaction. As depicted in **Section 5.3.4.1**, the energy barrier for the addition of metalated mesitylphosphanide onto C_2 of diphenylbutadiyne is higher by 6.4 kcal mol^{-1} than onto C_1. Hence, the 2,3- and 2,4-twofold possible additions were excluded from further exploration. We decided to conduct these additional calculations as this type of additions have been observed for calcium-mediated hydrophosphination of butadiynes with $HPPh_2$.[5] Notably, experimentally these additions as mentioned before, were not observed in our reactions.

The pathway by which the 1,4-bisphosphination product is generated shares the first two steps with the mechanism for the formation of phosphole i.e., 1st nucleophilic attack onto C_1, followed by a protonation step yielding the mono- hydrophosphination product. These two steps are followed by another nucleophilic attack with an additional molecule of M-P(H)Mes onto C_4 and finalized through another protonation step on C_3 atom. The Gibbs energy profile for formation of 1,4-bishydrophosphination product catalysed *via* K-HMDS is depicted in **Figure 5.23**, whilst the optimized structures for transition states for the formation of 1,4-bisphosphinated product are illustrated in **Figure 5.24**.

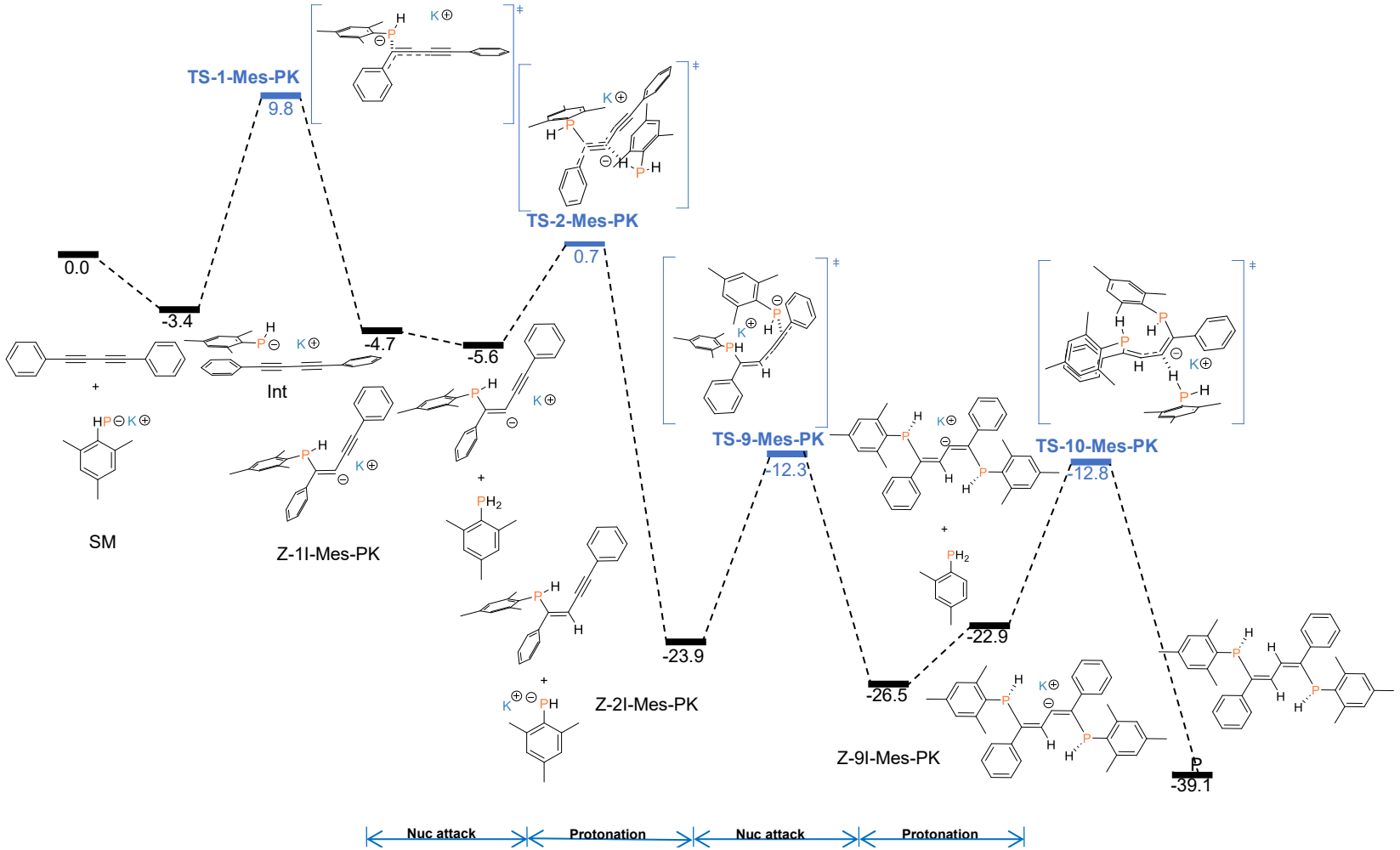

Figure 5.23.: Computed Gibbs energy profile in THF (ΔG_{THF} kcal mol^{-1}) at 298K for potassium-mediated bishydrophosphination of diphenylbutadiyne for the formation of 1,4-bisphosphination product, using K-HMDS catalyst at the B3LYP-D3/def2-TZVP/SMD(THF)//B3LYP-D3BJ/6-31G(d,p)/SMD(THF) level of theory.

TS-1-Mes-PK **TS-2-Mes-PK**

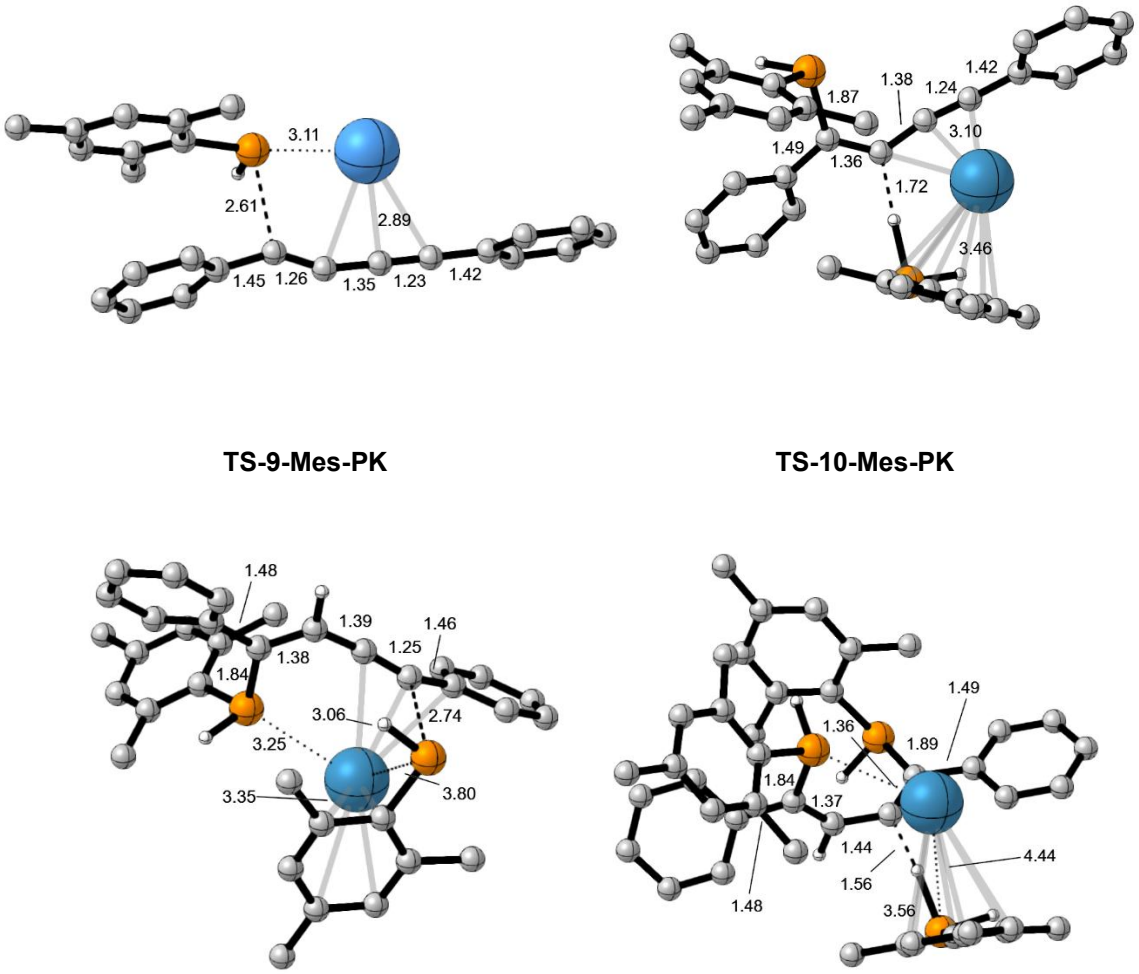

TS-9-Mes-PK **TS-10-Mes-PK**

Figure 5.24.: Optimized structures for transition states for the 1,4-bisphosphination product. Certain H atoms are omitted for clarity reasons. Distances are shown in Å.

As illustrated in **Figure 5.9** and **5.21** this nucleophilic attack (**TS-1-Mes-PK**) will proceed with an energy barrier of 13.2 kcal mol^{-1} whilst the subsequent protonation (**TS-2-Mes-PK**) step will ensue with an energy barrier of 6.3 kcal mol^{-1}.

The ensuing step, the second nucleophilic attack, necessitates an energy barrier of 11.6 kcal mol^{-1} (**TS-9-Mes-PK**), which is comparable to the 1st nucleophilic attack. However, the deprotonation step which would be the following step in the formation of the phosphole for all three-alkali cations, required smaller or almost equivalent energy barrier to be overcome (ranging from 7.6 to 11.4 kcal mol^{-1}) depending on the implemented alkali cation. It should be noted that the introduction of potassium mesityl phosphanide for this step as in the case for the deprotonation step is not

necessary as this molecule was formed in the proceeding step of protonation. Thus, the system will not need to “pay energetic tax” for introduction of another molecule and subsequent activation of the second C≡C triple bond. As depicted in **Figure 5.22**, in this TS, the metal cation will preferably interact with both phosphorous atoms simultaneously and with the C-C conjugated system. The proceeding step i.e., protonation is thermodynamically disfavoured, as the sole introduction of another mesitylphosphinemolecule in the system increases the energy by 3.6 kcal mol^{-1} (**TS-10-Mes-PK**). The energetic step for the protonation has an energy barrier of 13.7 kcal mol^{-1}. Notably, the sole interaction of the potassium cation in the TSs with any aryl rings will be only in the last protolysis step, whilst in the rest the main interaction will be with the C≡C triple bond.

The final 1,4-bisphosphination product may be found at -39.1 kcal mol^{-1} bellow separated reactants, making the formation of this product exergonic. However, this product is less thermodynamically stable comparatively to the phosphole (-55.4 kcal mol^{-1}).

The highest calculated energy barrier for the bishydrophosphination pathway is 13.7 kcal mol^{-1}, while for the phosphole pathway, it is 21.7 kcal mol^{-1}. We conducted additional calculations to determine if introducing three or four explicit THF molecules to solvate the cation would reverse this trend, but the results showed no discernible change in the trend. These findings indicate that the formation of the phosphole, compared to the 1,4-bisphosphination product, is governed by the thermodynamic factor. Therefore, lowering the reaction temperature and extending the reaction time to promote kinetic control could potentially alter the resulting product of the reaction.

5.3. Conclusions

To overcome the adverse entropic impact and to approach two electron-rich molecules, the addition of phosphanes across diynes necessitates a catalyst. Catalysis with s-block metal reagents is a well-established method for activating the phosphinepartner by generating the more reactive form i.e., metal mesitylphosphanide.[23,47,48] The bis(trimethylsilyl)amides (M-HMDS) of alkali metals were chosen as catalysts in the addition of mesitylphosphineacross diphenylbutadiyne.

The objectives of this Chapter included the elucidation of the chemo- and regioselective outcome during catalytic P-C bond formation across 1,4-diphenylbutadiyne, clarifying modes of action for the alkali metal ions during the reaction by means of experimental and mechanistic studies and proposing a mechanism by which the cyclization might be proceeding *via* DFT means.

Experimental results showed that Li-HMDS cannot mediate the reaction. Reactivity increased with heavier congeners, with K-HMDS being the most reactive and Na-HMDS in between. Moreover, only one product (1-mesityl-2,5-diphenyl phosphole) was formed regardless of the alkali cation present in the catalyst. The crystal structure of 1-mesityl-2,5-diphenyl phosphole is akin to the already known structure of 1,2,5-triphenyl phosphole.[30,49]

Before initiating the computational study of the proposed mechanism for phosphole formation, we analyzed the formation and possible deactivation of the active species M-P(H)Mes. Following the dissociation of dimeric M-HMDS catalysts, a P-to-N proton transfer generates the phosphanide and H-HMDS. This reaction is exergonic for all three cations; however, the barrier for lithium (15.2 kcal mol^{-1}) is almost twice that of sodium and potassium (8.7 and 7.8 kcal mol^{-1}, respectively). Alkali metal mesitylphosphanides in THF can be described as contact ion pairs. The formation of oligomeric structures from alkali metal phosphanides has been reported. [38–41] We investigated the possibility of dimerisation of the three-alkali metal mesityl phosphanides, being the easiest for the lithium system.

We also explored the most favourable interaction amongst the metal cation (from the active catalytic species) and the diyne. We found that all the cations in the

active catalytic species will predominantly interact with the diyne system rather than with the phenyl moieties.

A comparative analysis of the alkali-catalysed hydrophosphination of diynes, reveals, besides sharing a common general mechanism the energy barriers take place with similar reaction barriers. Our proposed mechanism begins with the formation of the active species, followed by a nucleophilic attack onto C_1. This is succeeded by a protonation step, deprotonation, another nucleophilic attack onto C_4 to generate the five-membered ring, and finally, another protonation step. It should be noted that, despite numerous attempts, we were not able to attain a step which would induce a protonation and simultaneous metallation at the phosphorous atom. Consequently, we concluded that the most probable pathway for this step is a stepwise protonation and then consecutive deprotonation/metalation. According to the computational results for the first protonation step and subsequent deprotonation step (regardless of the alkali cation implemented), it's uncertain which is the protonating agent: H-HMDS or $MesPH_2$. The energy barriers are very close in value. Therefore, it's likely that in the reaction mixture, we have a combination of both protonating and deprotonating agents, simultaneously fulfilling their roles.

The reactivity trend of alkali cations mirrors the one observed for phosphineoxides with phenylacetylene (see **Chapter 4**). Notably, DFT calculations confirmed the same pattern between the alkali metals' chemical hardness and their catalytic capacity as observed experimentally.[22,50] The computed barriers for all the step of the addition of mesitylphosphineacross diphenyllbutadiyne depending on the alkali metal of the utilised bis(trimethylsilyl)amide catalyst, are summarized in **Table 5.4**. For the three cations the step involving the highest barrier and, therefore, the RDS, is the cyclization step. For this step the barrier for the sodium system is 3.1 kcal mol^{-1} higher than for the potassium one, justifying in this way the experimental behaviour of both cations (**Table 5.1)**.

Table 5.4.: Computed barriers in THF ($\Delta\mathbf{G}^{\ddagger}$, kcal mol^{-1}) at 298 K for the addition of mesitylphosphineacross diphenylbutadiyne depending on the alkali metal of the utilised bis(trimethylsilyl)amide catalyst (M-HMDS; M = Li, Na and K) and for the bare anion case, at the B3LYP-D3/def2-TZVP/SMD(THF)//B3LYP-D3BJ/6-31G(d,p)/SMD(THF) level of theory.

Entry	Metal	$\Delta\mathbf{G}^{\ddagger}$				
		1st Nuc attack	1st Protonation	Deprotonation	Cyclization	2nd Protonation
1	Li	17.7	6.0	11.4	21.5	5.9
2	Na	11.9	10.2	9.1	24.6	9.2
3	K	13.2	6.3	7.6	21.7	7.2
4	/[a]	11.7	6.0	3.2	17.9	1.7

[a] No cation in the computed system

However, the barriers for potassium and lithium are very similar, despite the reaction does not proceed with lithium. Calculations indicate that, if the active LI-P(H)Mes is formed, it should catalyse the reaction, suggesting that the issue with lithium should be related with the generation of the active species and the concentration of this species in the solution medium (THF). Indeed, for lithium HMDS deaggregation is much less favourable and the concentration of monomer in solution should be much smaller (Chapter 4), the P- to N- proton transfer has the highest barrier, and lithium phosphanide has the less endergonic dimerisation reaction. All together, these results should entail a decreased concentration of the lithium active species in solution.

By computing the reaction without any alkali metal cation, we found that, in this situation all the barriers are lower than with cation. Particularly, we got the lowest barrier for the RDS cyclization step in this situation. That means that the cation, although required for the formation of the active species, is then detrimental for the reaction itself because it decreases the nucleophilicity of the phosphorous centre of the phosphanide.

Additional DFT calculations provided evidence that the double addition of phosphineacross 1,4-diphenylbutadiyne has a lower barrier than the cyclization. However, the double-added product is less thermodynamically favoured than the phosphole. This could be the factors influencing the chemoselective outcome. The other possible

outcomes of twofold addition were not explored into depth as the energy barrier for the addition across C_2 was determined to be higher by 7.5 kcal mol^{-1} than onto C_1.

Overall, this investigation provided additional proof that the alkali cations play an important role in altering the bonding, structure, and the outcome of the reactions, due to the magnitude of the cation-π interactions. Thus, confirming that these cations are not only “spectator” species. Consequently, from now on, the size and the hardness of the metal cation should be taken into consideration when discussing and planning phosphole synthesis.

Bibliography:

1. Banerjee, I., Harinath, A. & Panda, T. K. Alkali Metal Catalysed Double Hydrophosphorylation of Nitriles and Alkynes. *Eur J Inorg Chem* **2019,** 2224–2230 (2019).
2. Banerjee, I. & Panda, T. K. Recent advances in the carbon–phosphorus (C–P) bond formation from unsaturated compounds by s- and p-block metals. *Org. Biomol. Chem.* **19,** 6571–6587 (2021)
3. Bange, C. A. & Waterman, R. Challenges in Catalytic Hydrophosphination. *Chem. Eur. J.* **22,** 12598–12605 (2016)
4. Lau, S., Hood, T. M. & Webster, R. L. Broken Promises? On the Continued Challenges Faced in Catalytic Hydrophosphination. ACS Catal. 12, 10939–10949 (2022).
5. Al-Shboul, T. M. A., Görls, H. & Westerhausen, M. Calcium-mediated hydrophosphination of diphenylethyne and diphenylbutadiyne as well as crystal structure of 1,4-diphenyl-1,4-bis(diphenylphosphanyl)buta-1,3-diene. *Inorg. Chem. Commun.* **11,** 1419–1421 (2008).
6. Gorrell, I. B. Chapter 2. Alkali and alkaline earth metals. *Annu. Rep. Prog. Chem., Sect. A* **91,** 3 (1994).
7. Eleutério, R. V., Simão, L. & Hotza, D. Alkali-activated materials for catalytic applications: A state-of-the-art review. *Materials Science and Engineering: B* **299,** 117007 (2024).
8. Magre, M., Szewczyk, M. & Rueping, M. s-Block Metal Catalysts for the Hydroboration of Unsaturated Bonds. *Chem. Rev.* **122,** 8261–8312 (2022).
9. Kuciński, K. & Hreczycho, G. Hydrosilylation and hydroboration in a sustainable manner: from Earth-abundant catalysts to catalyst-free solutions. *Green Chem.* **22,** 5210–5224 (2020).
10. Zhang, L., Bai, S. & Zheng, L. Magnesium-Catalyzed Regioselective Hydrophosphinylation of Alkenes with Diarylphosphine Oxides. *Organometallics* **42,** (2023).
11. Platten, A. W. J., Borys, A. M. & Hevia, E. Hydrophosphinylation of Styrenes Catalysed by Well-Defined s-Block Bimetallics. *ChemCatChem* **14,** e202101853 (2022).
12. Moglie, Y., González-Soria, M. J., Martín-García, I., Radivoy, G. & Alonso, F. Catalyst- and solvent-free hydrophosphination and multicomponent hydrothiophosphination of alkenes and alkynes. *Green Chem.* **18,** 4896–4907 (2016).
13. Deschamps, E., Ricard, L. & Mathey, F. ChemInform Abstract: Toward Polyphospholes: Synthesis and Structure of an α-Linked Quaterphosphole. *ChemInform* **25,** (2010).
14. Matano, Y. in *Organic Redox Systems* (ed. Nishinaga, T.) 477–501 (Wiley, 2016).
15. Bachrach, S. M. & Perriott, L. M. Theoretical exammation of the Diels–Alder reaction of 1,3-butadiene with cyclopentadiene and 2 *H* -phosphole. *Can. J. Chem.* **74,** 839–850 (1996).
16. Bachrach, S. M. & Perriott, L. Relative Energies of Methyl- and Vinylphospholes. *J. Org. Chem.* **59,** 3394–3397 (1994).
17. Delaere, D., Dransfeld, A., Nguyen, M. T. & Vanquickenborne, L. G. Theoretical Study of the Structure−Property Relationship in Phosphole Monomers. *J. Org. Chem.* **65,** 2631–2636 (2000).
18. Roesler, F., Bruhn, C. & Pietschnig, R. Asymmetrically Substituted Phospholes as Ligands for Coinage Metal Complexes. *Molecules* **27,** 3368 (2022).

19. Roesler, F., Kovács, M., Bruhn, C., Kelemen, Z. & Pietschnig, R. Phosphetes via Transition Metal Free Ring Closure – Taking the Proper Turn at a Thermodynamic Crossing. *Chem. Eur. J.* **27,** 9782–9790 (2021).

20. Roesler, F., Kovács, M., Bruhn, C., Kelemen, Z. & Pietschnig, R. Moving on from Silicon to the Heavier Tetrels: Germyl- and Stannyl-Substituted Phosphole Derivatives. *Organometallics* **42,** 793–802 (2023).

21. Novas, B. T. & Waterman, R. Metal-Catalyzed Hydrophosphination. *ChemCatChem* **14,** e202200988 (2022).

22. Fener, B. E., Schüler, P., Ueberschaar, N., Bellstedt, P., Görls, H., Krieck, S. & Westerhausen, M. Scope and Limitations of the s-Block Metal-Mediated Pudovik Reaction. *Chem. Eur. J.* **26,** 7235–7243 (2020).

23. Krieck, S. & Westerhausen, M. Kudos and Renaissance of s-Block Metal Chemistry. *Inorganics* **5,** 17 (2017).

24. Ishidoshiro, M., Matsumura, Y., Imoto, H., Irie, Y., Kato, T., Watase, S., Matsukawa, K., Inagi, S., Tomita, I. & Naka, K. Practical Synthesis and Properties of 2,5-Diarylarsoles. *Org. Lett.* **17,** 4854–4857 (2015).

25. Mattmann, E., Mathey, F., Sevin, A. & Frison, G. De-aromatizing Phosphole. *J. Org. Chem.* **67,** 1208–1213 (2002).

26. Josa, D., Peña-Gallego, A., Rodríguez-Otero, J. & Cabaleiro-Lago, E. M. A MP2 and DFT study of the aromatic character of polyphosphaphospholes. Is the pyramidality the only factor to take into consideration? *J Mol Model* **17,** 1267–1272 (2011).

27. Burganov, T., Katsyuba, S., Zagidullin, A., Oshchepkova, E., Miluykov, V., Monari, A. & Assfeld, X. Theoretical study of the excited state properties of luminescent phospholes. *Dyes Pigm.* **164,** 363–371 (2019).

28. Katritzky, A. R. *Comprehensive heterocyclic chemistry III*. (Elsevier, 2008).

29. Bart, J. C. J. Structure of the non-stabilized phosphonium ylid methylenetriphenylphosphorane. *J. Chem. Soc., B:* 350 (1969).

30. Ozbirn, W. P., Jacobson, R. A. & Clardy, J. C. Crystal and molecular structure of 1,2,5-triphenylphosphole. *J. Chem. Soc. D* 1062 (1971).

31. Daly, J. J. 729. The crystal and molecular structure of triphenylphosphorus. *J. Chem. Soc.* 3799 (1964).

32. Winter, M. J. *Chemical bonding*. (Oxford University Press, 1994).

33. Atkins, P. W. & De Paula, J. *Physical chemistry*. (W.H. Freeman, 2010).

34. Housecroft, C. E. *Inorganic chemistry*. (Pearson, 2018).

35. Mulvey, R. E. & Robertson, S. D. Synthetically Important Alkali-Metal Utility Amides: Lithium, Sodium, and Potassium Hexamethyldisilazides, Diisopropylamides, and Tetramethylpiperidides. *Angew Chem Int Ed* **52,** 11470–11487 (2013).

36. Ojeda-Amador, A. I., Martínez-Martínez, A. J., Kennedy, A. R. & O'Hara, C. T. Structural Studies of Cesium, Lithium/Cesium, and Sodium/Cesium Bis(trimethylsilyl)amide (HMDS) Complexes. *Inorg. Chem.* **55,** 5719–5728 (2016).

37. Neufeld, R., Michel, R., Herbst-Irmer, R., Schöne, R. & Stalke, D. Introducing a Hydrogen-Bond Donor into a Weakly Nucleophilic Brønsted Base: Alkali Metal Hexamethyldisilazides (MHMDS, M=Li, Na, K, Rb and Cs) with Ammonia. *Chem. Eur. J.* **22,** 12340–12346 (2016).

38. Reich, H. J. & Dykstra, R. R. Solution Structure of Lithium Benzeneselenolate and Lithium Diphenylphosphide: NMR Identification of Cyclic Dimers and Mixed Dimers. *Organometallics* **13,** 4578–4585 (1994).

39. Driess, M., Huttner, G., Knopf, N., Pritzkow, H. & Zsolnai, L. Novel Alkali Metal Phosphanide Aggregates. *Angew. Chem. Int. Ed. Engl.* **34,** 316–318 (1995).

40. Smith, J. D. Phosphanides of the Heavier Alkali Metals. Angew. Chem. Int. Ed. **37,** 2071–2073 (1998).

41. Izod, K., Evans, P. & Waddell, P. G. Desolvation and aggregation of sterically demanding alkali metal diarylphosphides. *Dalton Trans.* **46,** 13824–13834 (2017).

42. Rae, A., Byrne, K. M., Brown, S. A., Kennedy, A. R., Krämer, T., Mulvey, R. E. & Robertson, S. D. Sigma/pi Bonding Preferences of Solvated Alkali-Metal Cations to Ditopic Arylmethyl Anions. Chem. Eur. J. **28,** (2022).

43. Davidson, M. G., Garcia-Vivo, D., Kennedy, A. R., Mulvey, R. E. & Robertson, S. D. Exploiting σ/π Coordination Isomerism to Prepare Homologous Organoalkali Metal (Li, Na, K) Monomers with Identical Ligand Sets. *Chem. Eur. J.* **17,** 3364–3369 (2011).

44. Streitwieser, A., McKeown, A. E., Hasanayn, F. & Davis, N. R. Basicity of Some Phosphines in THF. *Org. Lett.* **7,** 1259–1262 (2005).

45. Pöttgen, R., Hönle, W. & Von Schnering, H. G. in *Encyclopedia of Inorganic Chemistry* (eds. King, R. B., Crabtree, R. H., Lukehart, C. M., Atwood, D. A. & Scott, R. A.) (Wiley, 2005).

46. Reichardt, C. & Welton, T. *Solvents and Solvent Effects in Organic Chemistry*. (Wiley, 2010).

47. Bevern, D., Görls, H., Krieck, S. & Westerhausen, M. Synthesis, Structure, and Stability of Lithium Arylphosphanidyl-diarylphosphineOxide. Z. Anorg. Allg. Chem. **646,** 948–958 (2020).

48. Dorow, R. C. C., Liebing, P., Görls, H. & Westerhausen, M. Coordination chemistry of alkali metal dimesityl-thio- and dimesityl-selenophosphinites $[(L)_2A\text{-}EPMes_2]_2$ (A = Li, Na, K; E = S, Se; L = THF, THP) and $[(18C6)K\text{-}SPMes_2]$. *Dalton Trans.* **53,** 5711–5720 (2024).

49. Kumaravel, M., Mague, J. T. & Balakrishna, M. S. Chalcogenide derivatives of 1,2,5-triphenyl-1H-phosphole: structure and photophysical properties. *Tetrahedron Lett.* **55,** 2957–2961 (2014).

50. Härling, S. M., Fener, B. E., Krieck, S., Görls, H. & Westerhausen, M. Potassium Dimesitylphosphinite Catalyzed Intermolecular Hydrophosphorylation of Alkynes. *Organometallics* **37,** 4380–4386 (2018).

Chapter 6: [2+2] Homodimerization in P(V) derivate of 1,2,5-trisubstituted phosphole oxides

Results from a combined experimental and computational study on the oxidation and subsequent [2+2] photodimerization of phospholes will be discussed in the following chapter. This study explores how oxidation of 1-mesityl-2,5-diphenyl-1H-phosphole alters its electronic structure, enabling subsequent light-induced [2+2] photodimerisation. The experimental procedures, computational analyses, data evaluation have been conducted by me unless otherwise stated.

6.1. Introduction

Hitherto, chalcogen derivatives of phospholes are known adducts, thus upon a successful formation of the 1-mesityl-2,5-diphenyl-1H-phosphole we decided to add an additional topic to this thesis: oxidation of 1-mesityl-2,5-diphenyl-1H-phosphole.[1–5] We decided on this additional topic as to determine how the addition of a chalcogen element would influence the properties of 2,5-disubstituted phospholes. Albeit we were trying to synthesize solely the phosphole oxide derivative we serendipitously synthesized "head-to-tail" dimer of the phosphole oxide *via* a formally forbidden [2+2] cycloaddition (see **Scheme 6.1**).

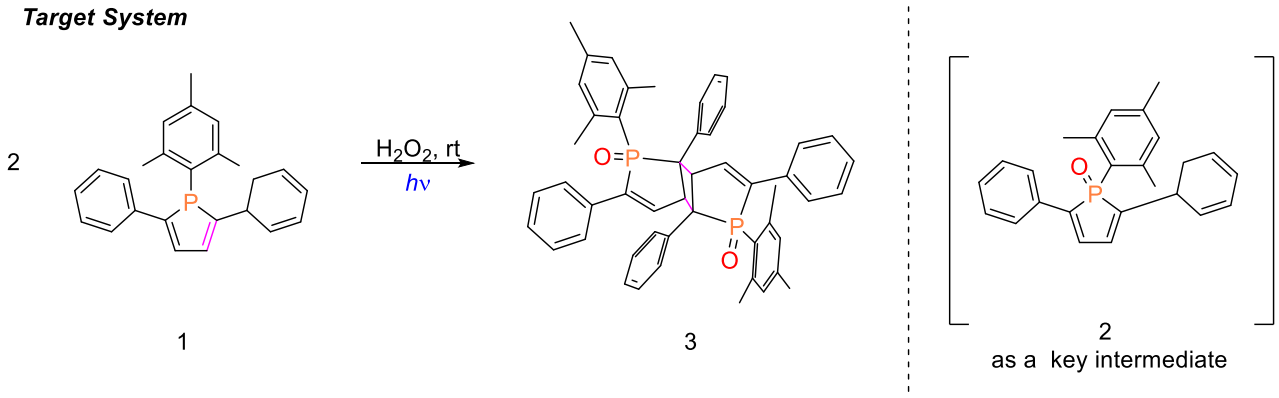

Scheme 6.1: Oxidation and dimerisation of 1-mesityl-2,5-diphenyl phosphole examined in this study.

In light of the unexpected formation of the bis(phosphole)dioxide, we decided to conduct computational calculations to gain a more comprehensive understanding of the detailed mechanism by which the [2+2] photocycloaddition of phosphole oxide proceeds. These calculations aimed to provide insights into the electronic and steric factors governing the reaction pathway. Additionally, we conducted experimental testing to determine the properties of both the newly formed [2+2] adduct and its precursor, the phosphole oxide.

Thermal or light-induced [2+2] dimerisation processes have traditionally been limited to phospholes and phosphole derivatives coordinated to metals.[6–11] In 1969 Nelson *et al.* first reported on the formation of a [2+2]-dimer by irradiating a 1,2,5-

triphenylphosphole, marking a significant milestone in the study of phosphole reactivity. .[6] From the initial data, the stereochemistry of the cyclobutane ring and the ''head-to-tail'' orientation of the dimer couldn't be determined (see **Scheme 6.2**).

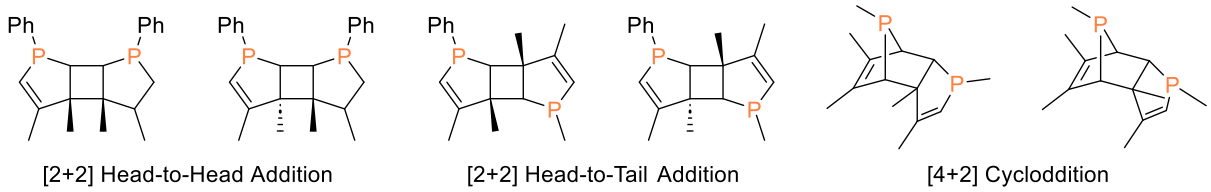

Scheme 6.2: Possible isomers generated *via* cycloaddition from photocycloadditions of $[(\eta^5\text{-}C_5H_5)Ru(DMPP)_2L]PF_6$ complexes; Adapted from ref [12]

Although there have been several reports of [2+2] dimers involving different phosphole chalcogens, the study of phosphole oxide dimers has been relatively limited. Marinetti and Voituriez in 2012 reported the first metal-free [2+2] photocyclizations using non-substituted helical phosphoindole oxides.[13] A substituted helical phosphinamide in the C_2 position was recently investigated, yielding a head to tail [2+2] dimer under sunlight. The same reaction proceeded in crystalline state under X-ray radiation.[14] In 2021, Arp *et al.* also reported an accidental formation of a dimer of phosphole oxide.[15] In their case they were aiming to reduce the weight and widen the spectrum of applicable phosphineoxide carriers. They treated 1,2,5-triphenylphosphole with the water adduct of di(hydroperoxy)adamantane and instead of the predicted phosphole oxide adduct, a [2+2] cycloaddition ensued. The reported structure of 1,2,5-triphenylphosphole oxide dimer has akin stereochemistry to the reported dimer for the parent phosphole. In 2019 Bourez *et al.* showed that the oxidation of P(V) derivatives of 2,4-disubstituted phospholes can lead to either [4+2] or [2+2] dimerisation products.[16] These findings broaden the understanding of the reactivity and dimerisation behaviour of phosphole oxide derivatives, revealing the potential for diverse bonding interactions and providing new pathways for the synthesis of novel phosphole-based materials.

Therefore, we opted to conduct both experimental and computational studies on the oxidation of 1-mesityl-2,5-diphenyl-1H-phosphole and its subsequent dimerisation. This chapter will commence with an explanation of the experimental results,

followed by a discussion of the computational findings. Concerning the DFT calculations, we will first elucidate the oxidation mechanism and subsequently delve into the mechanism for [2+2] photocycloaddition. For comparative purposes we have also computed the [4+2] Diels-Alder cycloaddition. Each of the main sections will be divided into several subsections. It should be noted that unless specifically stated otherwise under parent phosphole or solely phosphole we mean 1-mesityl-2,5-diphenyl-1H-phosphole. Phosphole oxide signifies 1-mesityl-2,5-diphenyl-1H-phosphole 1-oxide, while the [2+2] adduct represents 1,4-dimesityl-2,3b,5,6b-tetraphenyl-3a,3b,6a,6b-tetrahydrocyclobuta[1,2-b:3,4-b']bis(phosphole) 1,4-dioxide.

6.2. Experimental section

In this section of the thesis, we will focus on presenting our experimental results and the accompanying scientific discussion for the formation of 1-mesityl-2,5-diphenyl-1H-phosphole oxide and bis(phosphole)1,4-dioxide.

6.2.1. Synthesis of 1-mesityl-2,5-diphenylphosphole 1-oxide

I carried out the synthesis, data collection, and data analysis, whereas Benjamin Fener from the Westerhausen group managed the crystallization process and gathered supplementary data on the properties of 1-mesityl-2,5-diphenylphosphole 1-oxide.

Notably, for this section, we exclusively used K-HMDS as the catalyst, as it demonstrated the best conversion in the previous chapters. To ensure reliable results, freshly prepared potassium mesityl phosphinate was utilised likewise in **Chapter 5**. At room temperature, 5 mol% of the amide was combined with mesityl phosphine in THF, followed by a slight excess of 1,4-diphenylbutadiyne. After one-hour, quantitative conversion was confirmed using ^{31}P NMR. H_2O_2 was then added as an oxidizing agent to the mixture at room temperature in the dark. The formation of phosphole oxide was confirmed using ^{31}P NMR. No side products observed in the NMR spctrums. **Scheme 6.3** depicts the formation of phosphole oxide.

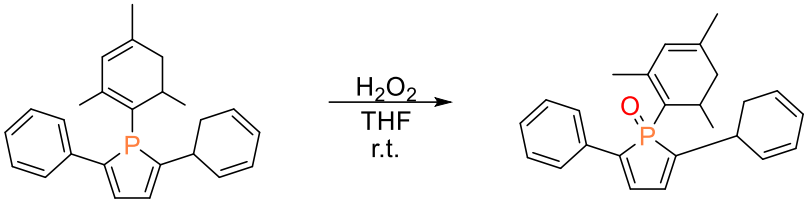

Scheme 6.3: Oxidation of 1-mesityl-2,5-diphenyl phosphole with hydrogen peroxide yielding 1-mesityl-2,5-diphenyl-phosphole oxide.

6.2.1.1. NMR data of 1-mesityl-2,5-diphenylphosphole 1-oxide

Selected NMR parameters of 1-mesityl-2,5-diphenylphosphole 1-oxide are discussed using the numbering scheme depicted in **Figure 6.3**. The $^{31}P\{^1H\}$ NMR, $^{13}C\{^1H\}$ NMR, and ^1H NMR spectra for 1-mesityl-2,5-diphenylphosphole oxide, are all depicted in **Figure 6.1**.

The chemical shift of the phosphorus atom, $\delta(^{31}P)$ = 45.8 ppm, lies in the same region as that of 1,2,5-triphenylphosphole 1-oxide ($CHCl_3$, 41.7 ppm). [17]

In accordance with its structure, the 1-mesityl-2,5-diphenylphosphole 1-oxide ($CDCl_3$, 400 MHz) ^1H NMR spectrum shows the expected signals for aromatic and methyl protons. The aromatic protons of the two phenyl groups at the 2- and 5-positions of the phosphole ring are represented by a multiplet between δ = 7.25-7.85 ppm that integrates for ten protons. The meta-protons C_3 and C_5 of the mesityl substituent on phosphorus are assigned a sharp singlet at δ = 6.72 ppm (2H).Three singlets in the aliphatic region at δ = 2.32, 2.25, and 2.12 ppm integrate for nine protons in total and are attributed to the methyl groups on the mesityl ring: the singlets at δ = 2.32 and 2.25 ppm (6H) correspond to the two equivalent ortho-methyl groups ,while the singlet at δ = 2.12 ppm (3H) is assigned to the para-methyl group.

In the $^{13}C\{^1H\}$ NMR spectrum (101 MHz, [D_8]-THF), multiplet signals between δ = 126-140 ppm correspond to the aromatic carbons of the two phenyl substituents and the mesityl ring. The mesityl ipso-carbon bonded to phosphorus C_1 typically appears downfield, near δ ≈ 138-140 ppm, due to deshielding from the electron-

withdrawing phosphole oxide moiety. The signal at δ ≈ 82 ppm is characteristic of the phosphole ring's sp^2-hybridised positions. Additional peaks around δ = 21-22 ppm maybe be attributed to the methyl groups of the mesityl substituent: the ortho-methyls and the para-methyl, which may appear as two separate signals due to slight magnetic non-equivalence.

A)

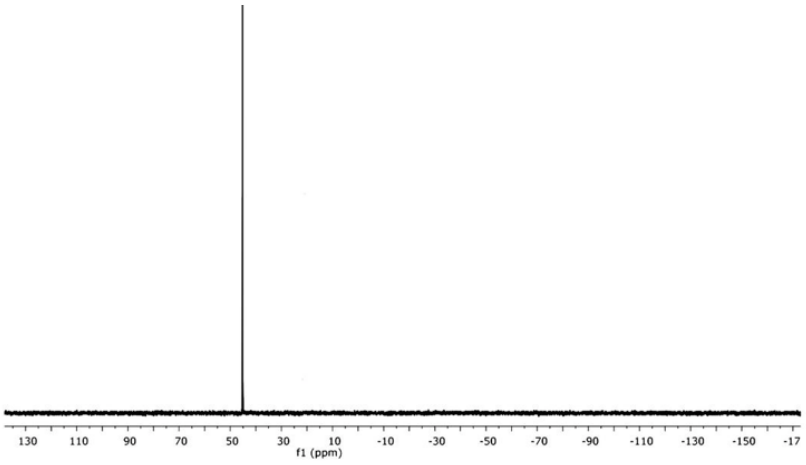

B)

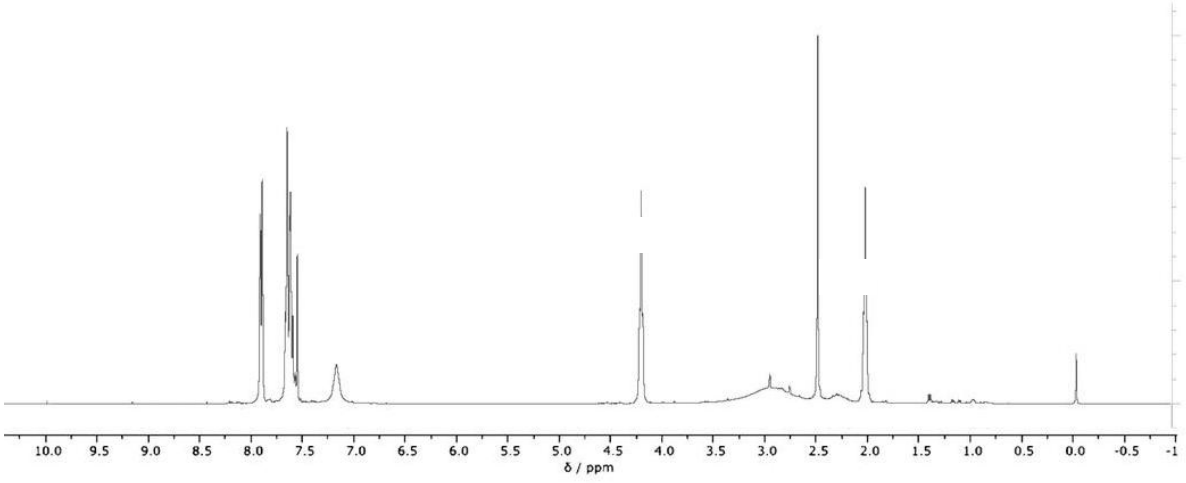

C)

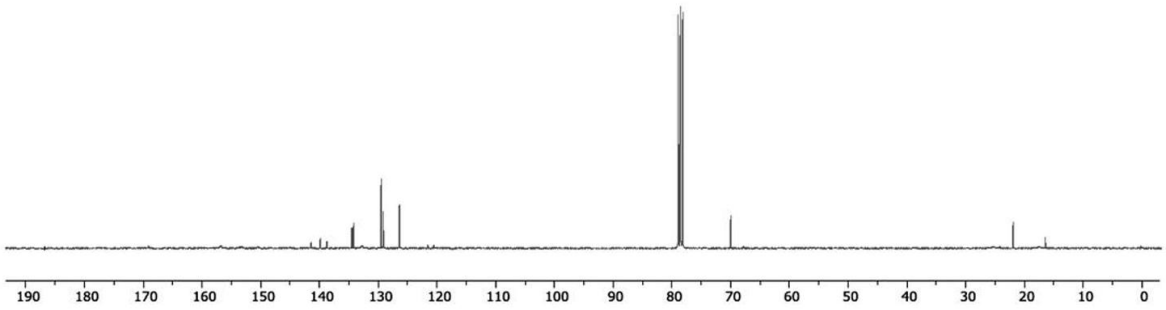

Figure 6.1.: A) ^{31}P {H} NMR **B)** ^{1}H NMR and **C)** $^{13}C\{H\}$ NMR spectra monitored at 162, 400, and 101 MHz, respectively, for 1-mesityl-2,5-diphenylphosphole oxide in [$CDCl_3$]-THF at room temperature.

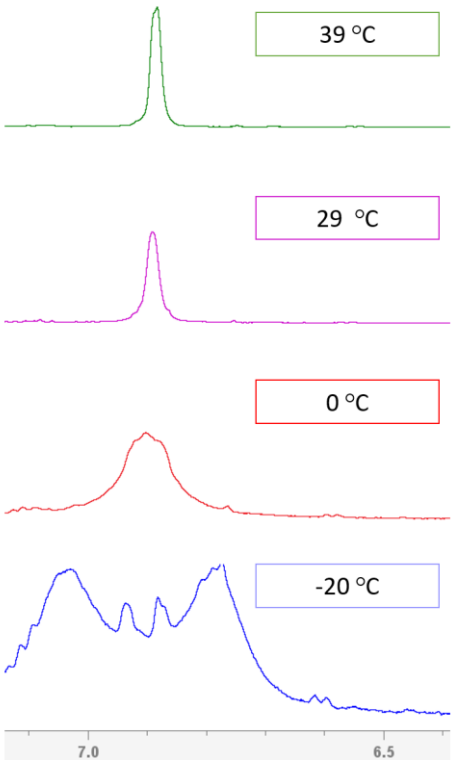

Figure 6.2.: Temperature-dependent ^{1}H NMR spectra (400 MHz, $CDCl_3$) of 1-mesityl-2,5-diphenylphosphole 1-oxide at different temperatures.

The rotational barrier was determined to be 41 kJ mol^{-1} based on the coalescence temperature (T_c = 253 K) seen in the ^1H NMR spectra of ortho-methyl groups. The hydrogens live in different chemical environments at lower temperatures because of the slow rotation around the phosphole's P-C bond. Because their chemical environments do not overlap, each hydrogen has a distinct peak in the ^1H NMR spectrum. The hydrogen atoms exchange their environments more quickly as the temperature rises because the rotation around the P-C bond speeds up. Once the exchange rate surpasses the NMR time scale, the peaks progressively merge into a single average peak, signifying that the hydrogens are in the same averaged chemical environment.

6.2.1.2. Crystal structure of 1-mesityl-2,5-diphenylphosphole 1-oxide

For 1-mesityl-2,5-diphenyl-1H-phosphole oxide, we successfully obtained single crystals suitable for XRD analysis. The oxidised phosphole crystalized in the monoclinic group P $2_1/n$, akin to the parent phosphole (see **Chapter 5**). The molecular structure and numbering scheme of P-methyl-2,5-diphenyl-phosphole oxide are illustrated in **Figure 6.3**.

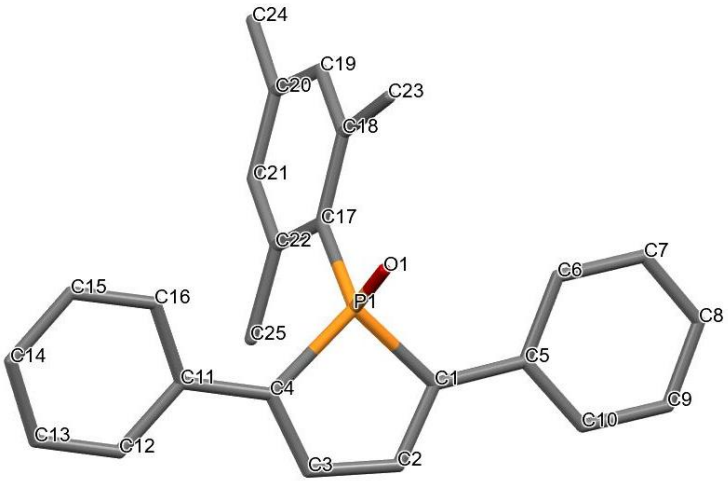

Figure 6.3.*:* Molecular structure in the solid state and atom labelling of 1-mesityl-2,5-diphenylphosphole 1-oxide. H atoms are omitted for clarity reasons. Selected bond lengths (Å): P1-O1 1.492(2), P1-C1 1.827(3), P1-C4 1.820(3), P1-C17 1.823(3), C1-

C2 1.344(4), C1-C5 1.459(5), C2-C3 1.455(5), C3-C4 1.345(4), C4-C11 1.459(5). Selected bond angles (°): O1-P1-C1 113.48(14), O1-P1-C4 113.72(14), O1-P1-C17 112.92(13), C4-P1-C1 92.71(15), C4-P1-C17 111.87(14), C1-P1-C17 110.54(14), C2-C1-P1 107.4(2), C2-C1-C5 126.6(3), C5-C1-P1 125.7(2), C1-C2-C3 116.0(3), C4-C3-C2 116.3(3), C3-C4-P1 107.4(2), C3-C4-C11 126.5(3), C11-C4-P1 126.0(2), C18-C17-P1 119.9(2), C22-C17-P1 120.7(2).

As depicted in **Figure 6.3**, the two phenyl substituents on C2 and C5 are not coplanar with the heterocyclic core (P1-C1-C2-C3-C4). The exocyclic P1−C17 bond distance is 1.823(3) Å whilst, the endocyclic C1-C2 distances is 1.344(4) and C_3-C_4 is 1.345(4) Å. In comparison with the analogous bond length in the parent phosphole there is a de*via*tion almost no de*via*tion (0.02 Å ; 1-mesityl-2,5-diphenyl-1H-phosphole; P1−C17 1.8291 (16) Å , C1-C2 1.363(2) Å and C_3-C_4 1.369(2) Å).[1] However, comparatively to the smaller but akin 1,2,5-triphenylphosphole oxide, the bond length are almost identical with a mean bond de*via*tion of 0.01 Å (P1−C17 1.4927(10) Å , C1-C2 1.3547(16) Å and C3-C4 1.3513(18) Å). Moreover, the distances between P1-C1 1.827(3) Å, P1-C4 1.820(3) Å and P1-C17 1.823(3) Å are very similar thus, it may be concluded that the delocalization is uniform. The O atom lies at a torsion angle of 123.19° with respect to C_2 and the mesityl substituent lies on a torsion angle of 128.87° to the heterocyclic core. The P=O bond length (1.492(2) Å) is similar to that in simple unstrained diarylphosphineoxides ($Mes_2P(O)H$: 1.485 (13) Å ; $Ph_2P(O)H$: 1.488(11) Å) and similar phosphole oxide (1,2,5-triphenylphosphole oxide 1.4927(10) Å).[1,16,18] However, it should be noted that the minor shortening of the P=O bond may be attributed to the hyperconjugation from the negatively charged oxygen atom into the antibonding σ*(P−C). [19]

Intermolecular interactions such as π–π stacking and hydrogen bonding may influence the crystallization process regardless of their small energetic value. **Figure 4** depicts the lateral views, of phosphole oxide. The distances of 2.534 Å and 2.807 Å and respective angles of 126.56° and 114.95° illustrate the existence of the hydrogen bonding (C-H···O-P) amongst the two independent molecules of phosphole oxide. These values are in accordance with the criteria for moderate hydrogen bonding of (< 2.9 Å and >90°).[20] Furthermore, no π- π stacking interaction was observed for this chalcogen phosphole which is in accordance with the literature.[16]

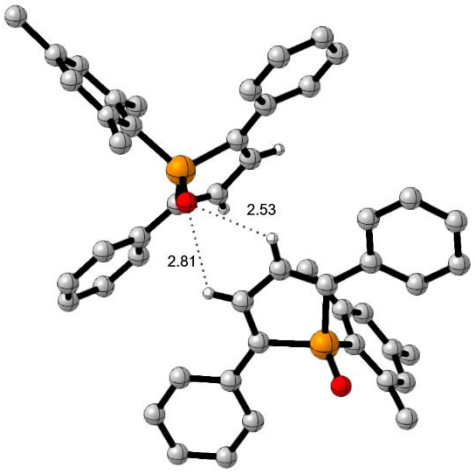

Figure 6.4.: Lateral views of the packing of **1**-mesityl-2,5-diphenylphosphole 1-oxide in crystalline phase. The hydrogen bonding between C-H···O-P has been depicted with bond distance of Å and their respective angles in degrees (°). Certain H atoms are omitted for clarity reasons.

Having analysed the NMR data and the XRD structure of the newly formed phosphole oxide we will now continue discussing the synthesis, NMR data and the XRD structure of the [2+2] adduct.

6.2.2. Synthesis of [2+2] adduct of 1-mesityl-2,5-diphenylphosphole 1-oxide

We initially synthesized this product serendipitously while attempting to form only the oxide version of the parent phosphole, following the same protocol described in **Section 6.2.1**, with the exception that the H_2O_2 addition was done under sunlight (see **Scheme 6.4)**. The formation of [2+2] adduct of 1-mesityl-2,5-diphenylphosphole 1-oxide as a sole product was verified *via* ^{31}P NMR.

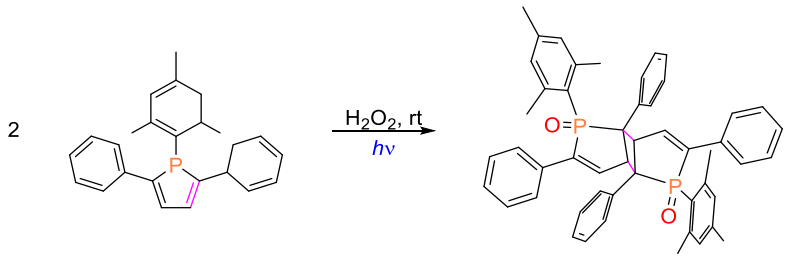

Scheme 6.4: Oxidation and subsequent dimerisation of 1-mesityl-2,5-diphenyl phosphole under light yielding the [2+2] adduct of 1-mesityl-2,5-diphenylphosphole 1-oxide.

6.2.2.1. NMR data of [2+2] adduct of 1-mesityl-2,5-diphenylphosphole 1-oxide

A numbering scheme that is in line with the atom labelling in the molecular structure is used to discuss a few of the [2+2] dimer's NMR parameters (**Figure 6.6**). No corresponding ^{31}P NMR chemical shift was reported by Arp *et al.* in their study.[15]

^{31}P NMR spectrum shows a single sharp resonance at δ 66.3 ppm, indicating that the two phosphorus centers are in nearly equivalent environments and that any potential P–P coupling is not resolved, likely due to fast conformational averaging. In the ^{1}H NMR spectrum aromatic peaks are depicted between δ 6.5-8.0 ppm which is consistent with the presence of multiple phenyl and mesityl rings. A single sharp singlet appears between δ 2.0-2.4 ppm, corresponding to the mesityl substituent. While the crystal structure clearly shows an asymmetric molecular geometry, the observation of only one methyl resonance suggests that the methyl environments are magnetically equivalent on the NMR timescale, likely due to rapid rotation around the P-C(aryl) bond or coincidental chemical shift overlap. In the aliphatic region, additional peaks between δ 3.0-4.0 ppm may be attributed to the newly formed sp^3-hybridized carbons of the four-membered ring. The ^{13}C NMR spectrum supports these findings, with peaks for aromatic carbons (δ 120-140 ppm), methyl carbons (~20 ppm), and aliphatic ring carbons (δ 30-50 ppm). The structure of the [2+2] cycloaddition adduct of 1-mesityl-2,5-diphenylphosphole 1-oxide was confirmed by ^{1}H and ^{13}C NMR spectroscopy.

A)

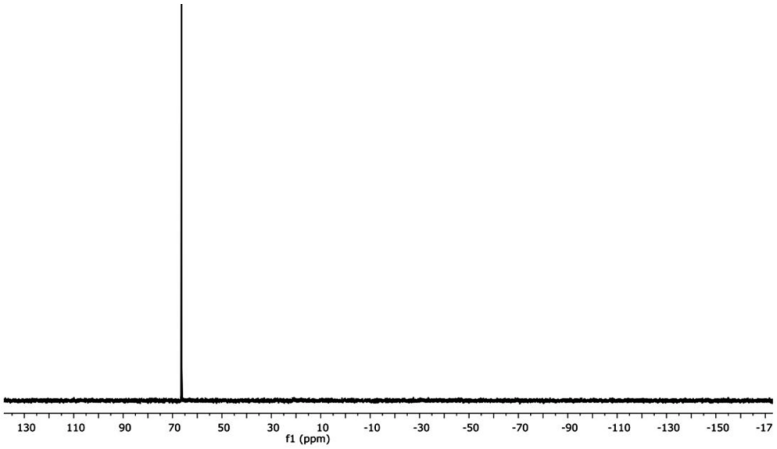
130 110 90 70 50 30 10 -10 -30 -50 -70 -90 -110 -130 -150 -17
f1 (ppm)

B)

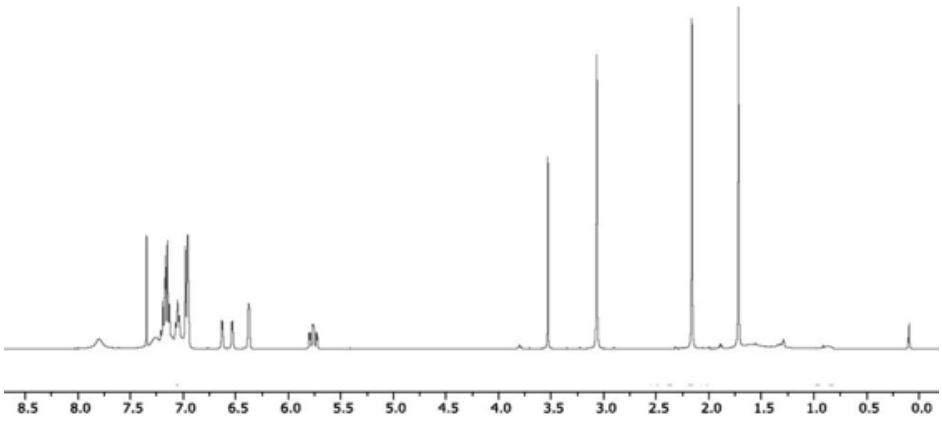
8.5 8.0 7.5 7.0 6.5 6.0 5.5 5.0 4.5 4.0 3.5 3.0 2.5 2.0 1.5 1.0 0.5 0.0

C)

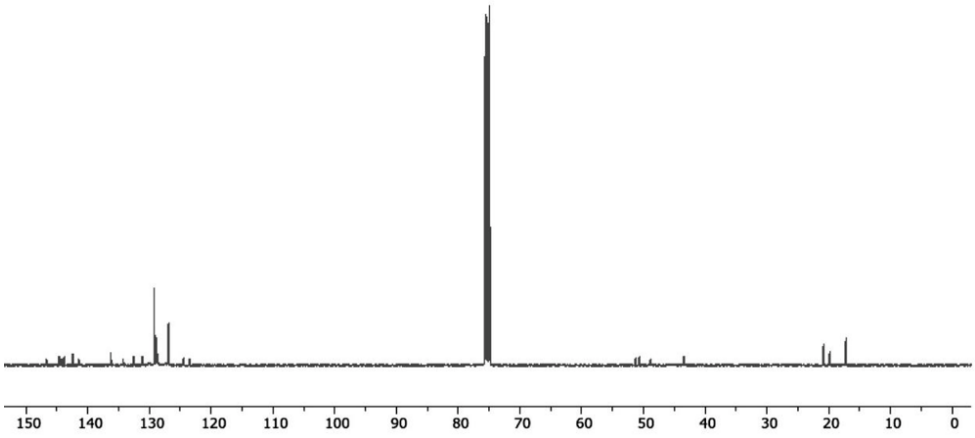

Figure 6.5.: A) ^{31}P {H} NMR **B)** ^{1}H NMR and **C)** ^{13}C{H} NMR spectra monitored at 162, 400, and 101 MHz, respectively, for [2+2]photodimer in [D_8]-THF at room temperature.

6.2.2.2. Crystal structure of [2+2] adduct of 1-mesityl-2,5-diphenylphosphole 1-oxide

For the dioxide adduct, we also successfully obtained single crystals suitable for XRD analysis. This compound crystalized in triclinic space group, $P\bar{1}$ thus has a unit cell symmetry of C_i. The molecular structure and the numbering scheme of bis(phosphole) 1,4-dioxide are depicted in **Figure 6.6**.

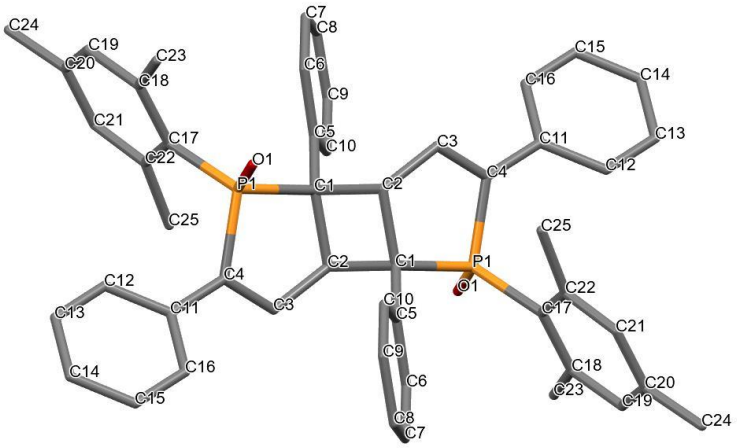

Figure 6.6.: Molecular structure and atom labelling scheme of 1,4-dimesityl-2,3b,5,6b-tetraphenyl-3a,3b,6a,6b-tetrahydrocyclobuta[1,2-b:3,4-b']bis(phosphole) 1,4-dioxide. H atoms are omitted for clarity reasons. Selected bond lengths (Å): P1-O1 1.4901(9), P1-C1 1.8602(13), P1-C4 1.7963(14), P1-C17 1.8169(13), C1-C2 1.5594(18), C1-C2^1 1.5941(17), C1-C5 1.5088(18), C2-C3 1.5028(19), C3-C4 1.3380(19), C4-C11 1.4775(19). Selected bond angles (°): O1-P1-C1 112.37(5), O1-P1-C4 112.35(6), O1-P1-C17 113.29(6), C4-P1-C1 95.04(6), C4-P1-C17 111.34(6), C17-P1-C1 111.11(6), C2-C1-P1 105.30(9), C2^1-C1-P1 111.19(8), C2-C1-C2^1 89.11(9), C5-C1-P1 113.58(9), C5-C1-C2 122.01(10), C5-C1-C2^1 113.10(10), C1-C2-C1^1 90.89(9) , C3-C2-C1^1 111.99(10), C3-C2-C1 109.95(10), C4-C3-C2 118.88(12), C3 -C4-P1 110.72(10), C3-C4-C11 126.45(13), C11-C4-P1 122.15(10), C6-C5-C1 117.7(11), C10-C5-C1 123.47(12), C18-C17-P1 120.50(9), C22-C17-P1 120.29(10).

As illustrated in **Figure 6.6** the [2+2] cycloaddition yields a “head-to-tail” arrangement with regards to the substituents on the cyclobutene ring and phosphole oxide units (see **Scheme 6.2**). Thus far, the best to our knowledge in the literature there only a handful of other structurally characteristic compounds with this similar arrangement for oxidised P(V) derivatives.[7,13,14,16]

In our case the cyclobutane ring is essentially rectangular with angles C2-C1-C2^1 of 89.11(9)° and C1-C2-C1^1 of 90.89(9)°. Moreover this ring has a slightly non-planar configuration as the dihedral angle C1-C2-C2^1-C1^1 is 6.44°. The dimerization will induce a change in C-P and C-C bond lengths in phosphole oxide unit as C1 and

C2 change their hybridization from sp^2 to sp^3 (see **Figure 3** and **6**). This change in bond length is most significant for C1-C2 which changes from 1.34 Å to 1.56 Å, for C1-C5 from 1.46 Å to 1.51 Å and for P1-C1 which changes from 1.83 Å into 1.86 Å from the monomer to dimer respectively. The rest of the bonds either show an insignificant change of 0.02 Å or no change at all. The elongation of the C1-C5 bond length is most likely prompted by a steric effect upon the formation of the C1-C2 bond. The change in the both lengths is within the parameters for characteristic single bonds amongst sp^2-hybridized carbon atoms and sp^2-hybridized carbon and phosphorus. [22–24]

From the scarcely similar reported structures, ours is most akin to the one reported to Arp *et al.*, hence we will compare it to this one.[15] As a reminder the phosphole oxide which dimerized in their case in the 1,2,5-triphenylphosphine oxide. Despite both dimerizations proceeding in a head-to-tail addition, the two molecules don't have the same stereochemistry. In our case the two P=O groups in the molecule are pointing to opposite sides of the ring system, whilst in theirs this is not the case.[15] Interestingly, there is no significant (> 0.02 Å) difference between the bonds in the two [2+2] adducts. Hence, it may be deduced that the substitution of phenyl by a mesityl substituent in position 1, despite increasing the steric bulk, will have no influence over the bond lengths in the [2+2] adduct. Moreover, they also observed formation of two hydrogen bonds to P=O groups by each bridging a solvent molecule of DCM. We didn't observe anything similar in our case.

After experimental exploration of the oxidation of the parent phosphole yielding mesityl-2,5-diphenyl-2,3-dihydro-1H-phosphole oxide and the [2+2] adduct, along with detailed structural analysis them, our focus shifts towards computational investigation. Our aim was to elucidate the mechanisms underlying the formation of these two products and understand the factors influencing their outcome.

6.3. Computational section

This Section is divided into multiple subsections in which we analyse the Gibbs energy profiles for the formation of the phosphole oxide and the [2+2] adduct, along

with their properties, and we will analyse the formation of one of the possible Diels-Alder products.

6.3.1. Computational details

6.3.2. Mechanism for formation of 1-mesityl-2,5-diphe-nylphosphole 1-oxide

The first step in the dimerisation of phosphole oxide implies the formation of the phosphole oxide by oxidation of phosphole with hydrogen peroxide. The computed Gibbs energy diagram for the formation of 1-mesityl-2,5-diphenyl-1H-phosphole oxide is depicted in **Figure 6.7**; **part A**, whilst **part B** depicts the optimized structure for the corresponding transition state. Exploration of the potential energy surface for the formation of phosphole oxide revealed that it proceeds in one step, through transition state **TS-O**.

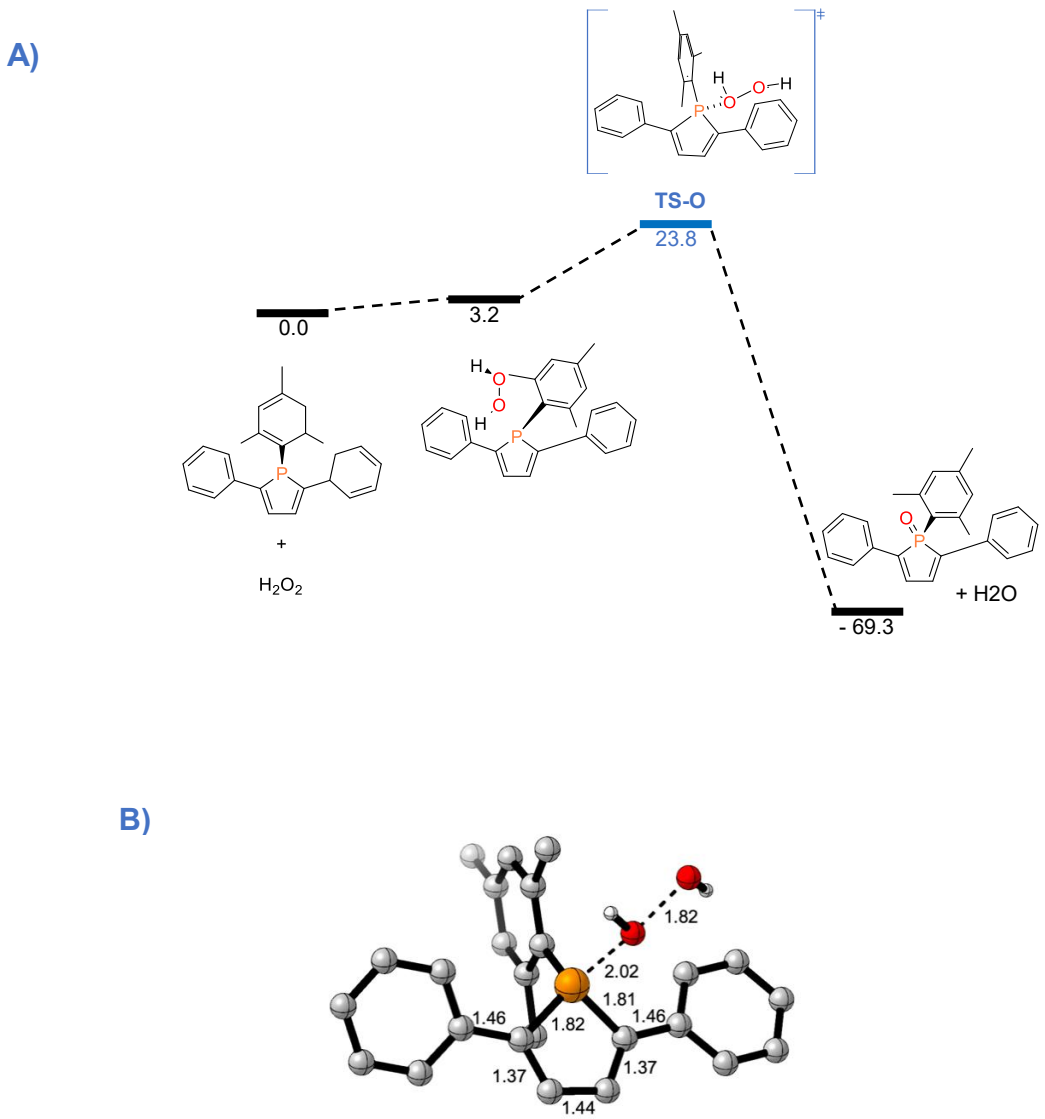

Figure 6.7.: Part A) Computed Gibbs energy profile in THF (ΔG_{THF} kcal mol^{-1}) at 298 K for oxidation of 1-mesityl-2,5-diphenyl-1H-phosphole, using H_2O_2 as an oxidizing agent at the B3LYP-D3/def2-TZVP/SMD(THF)//B3LYP-D3BJ/6-31G(d,p)/SMD(THF) level of theory. **Part B**) Optimised structure for the transition state involved in the mechanism for formation of oxidised phosphole oxide. Certain H atoms are omitted for clarity reasons. The distances presented are given in Å.

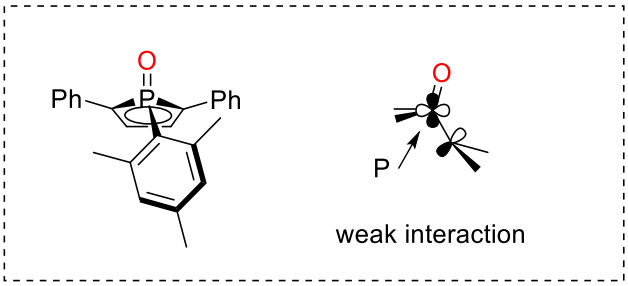

Scheme 6.5: Interaction of orbitals upon oxidation. Adapted from ref [27].

We suggested that dimerisation of phosphole oxides proceeds through a photochemical process to form the [2+2] adduct. Before entering into the study of the mechanism for the light induced formation of the [2+2] adduct, we will analyse in the two ensuing sections first the electronic structure of phosphole oxide and then the optical and photophysical properties of phosphole oxides. Understanding the ground state of the phosphole oxide is essential for comprehending its behaviour in the excited state. This knowledge provides a baseline for analysing how the molecule interacts with light, undergoes photochemical transformations, and ultimately forms various adducts, and including the formation of the [2+2] adduct. By examining both the ground and excited states, we can gain deeper insights into the reaction mechanisms and the factors influencing the efficiency and selectivity of these photochemical processes.

6.3.2.1. Frontier molecular orbital analysis of precursors and the [2+2] cycloadduct

To analyse the electronic structure of the precursors we calculate their frontier molecular orbital i.e., HOMO (highest occupied molecular orbital) and LUMO (lowest unoccupied molecular orbital) orbitals. The HOMO-LUMO gap correlates the observed reactivity of phosphole and its oxide derivative to their electronic characteristics. This gap is a crucial parameter that influences how these molecules interact with other species. A smaller HOMO-LUMO gap typically indicates higher reactivity, as electrons can be more easily excited or transferred, while a larger gap suggests lower reactivity and greater stability. By analysing the HOMO-LUMO gap, we can gain insights into the chemical behaviour, stability, and potential applications of phosphole compounds and their derivatives. We will first discuss the frontier molecular orbitals (FMO) of the parent phosphole and the oxide as illustrated in **Figure 6.8**.

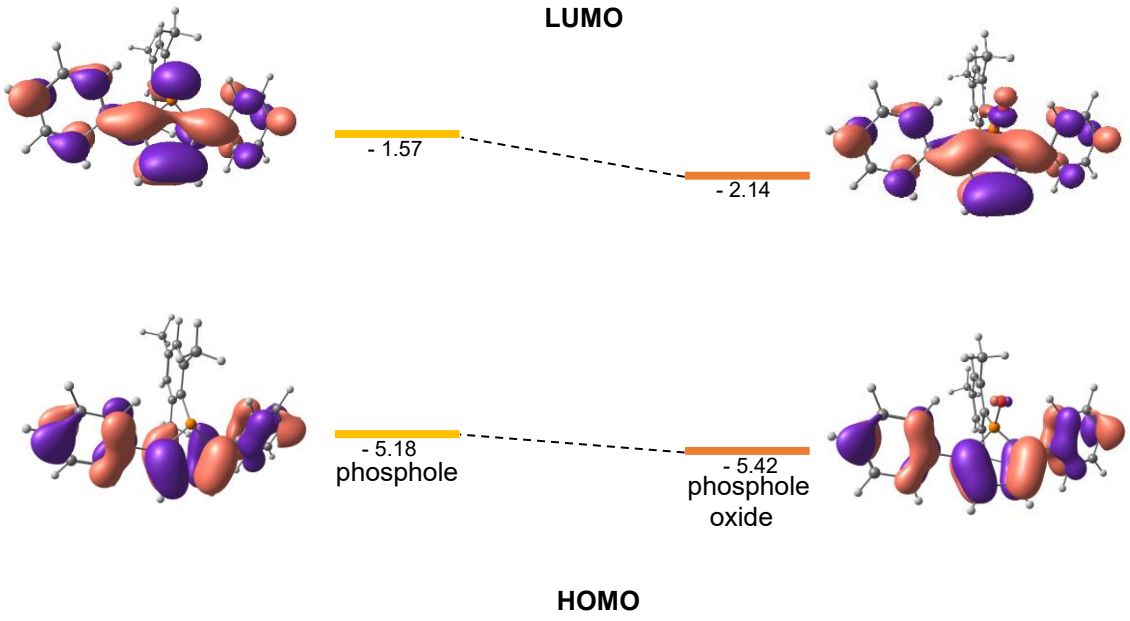

Figure 6.8.: Frontier molecular orbitals of the parent phosphole (yellow) and the phosphole oxide (orange) and their respective energies in [eV] calculated at the B3LYP-D3/def2-TZVP/SMD(THF)//B3LYP-D3BJ/6-31G(d,p)/SMD(THF) level of theory.

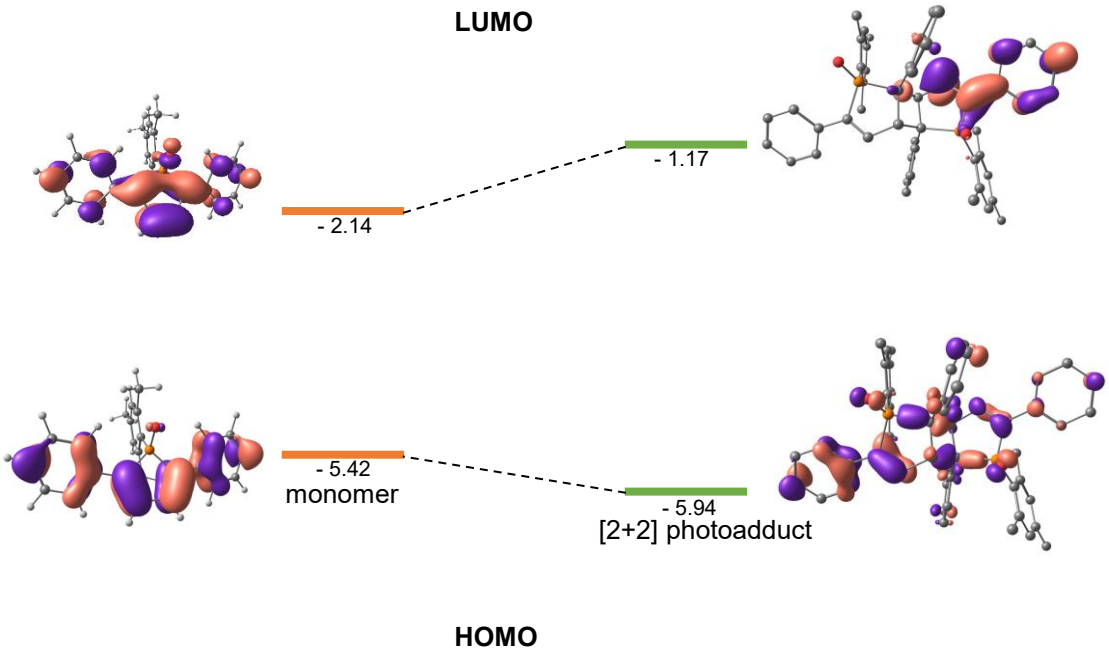

Figure 6.9.: HOMO (bottom) and LUMO (top) of the phosphole oxide (orange) and [2+2] cycloadduct (green) and their respective energies in [eV] calculated at the B3LYP-D3/def2-TZVP/SMD(THF)//B3LYP-D3BJ/6-31G(d,p)/SMD(THF) level of theory.

6.3.2.2. Photophysical studies

UV-Vis spectroscopy was used to examine the absorption spectra of 1-mesityl-2,5-diphenyl-1H-phosphole (A), 1-mesityl-2,5-diphenyl-1H-phosphole oxide (B), and the [2+2] cycloaddition adduct of 1-mesityl-2,5-diphenyl-1H-phospholeoxide (C), which were all dissolved in chloroform. These measurements reveal important information about the electrical transitions inside each molecule, which influence the conversion process from phosphole oxide to the [2+2] dimer alter on. **Figure 6.10** depicts the experimental UV-Vis absorption spectra of 1-mesityl-2,5-diphenyl-1H-phosphole (A), 1-mesityl-2,5-diphenyl-1H-phosphole oxide (B), and the [2+2] cycloaddition adduct of 1-mesityl-2,5-diphenyl-1H-phospholeoxide (C), in chloroform solvent. The discrepancies in their absorption patterns reflect structural and electrical changes caused by oxidation and subsequent cycloaddition,

1) 1-mesityl-2,5-diphenyl-1H-phosphole

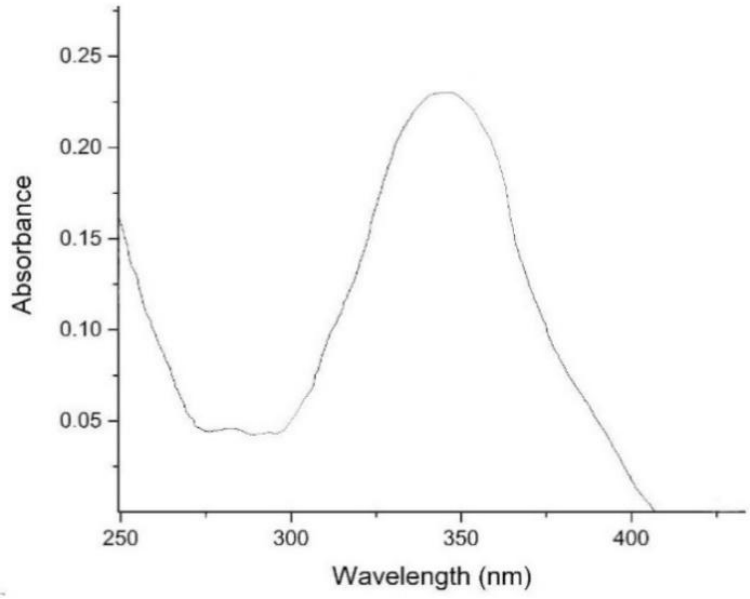

2) 1-mesityl-2,5-diphenyl-1H-phosphole oxide

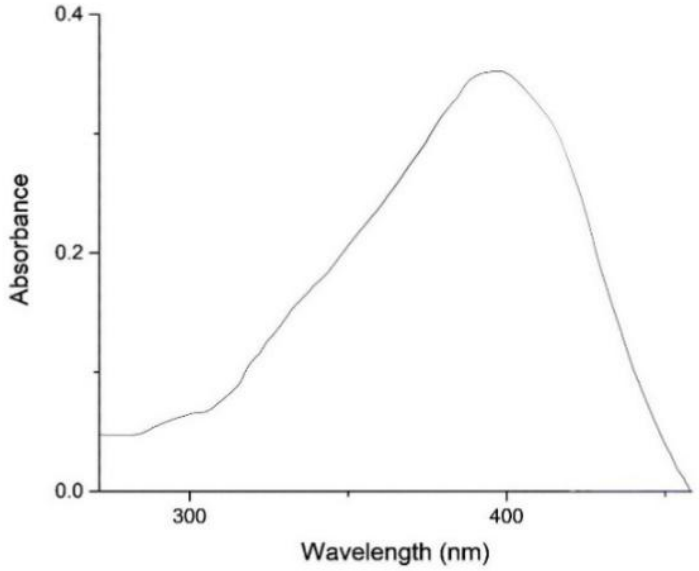

3) [2+2] adduct

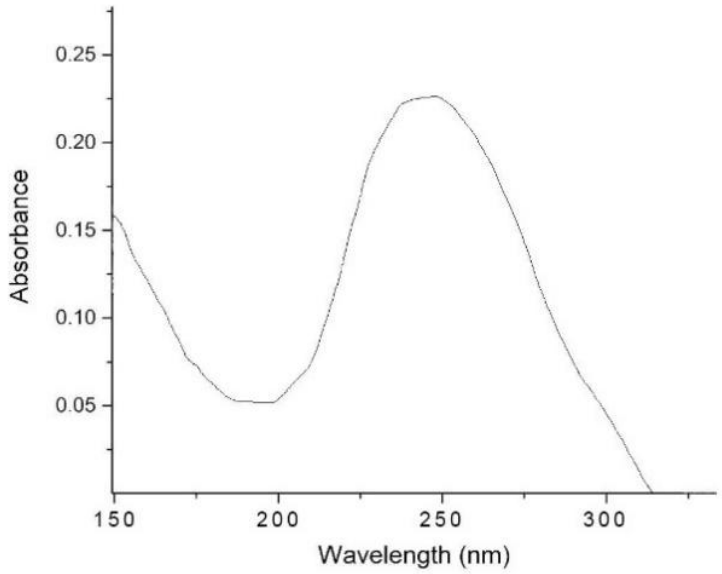

Figure 6.10.: Experimentally attained UV-Vis spectrums for phosphole **(A)**, phosphole oxide **(B)** and the [2+2] adduct **(C)** in chloroform solvent.

Table 6.1 compiles comprehensive optical characteristics such as absorption maxima (λ_{max}), molar absorptivities, and band gaps to compare the attributes of the examined products to those of related compounds. All data were obtained in chloroform solution under air conditions to ensure consistency and applicability to usual experimental settings.

Table 6.1.: Optical properties of products and akin compounds (The data were collected in chloroform solution under air conditions).

Entry	Compound	λ_{abs} [C] [nm]	Ref.
1	1,2,5-triphenyl-1H-phosphole	375	40
2	1,2,5-triphenyl-1H-phosphole oxide	394	17
3	1-mesityl-2,5-diphenyl-1H-phosphole	350	this thesis
4	1-mesityl-2,5-diphenylphosphole-1H-oxide	397	this thesis
5	[2+2] adduct	255	this thesis

Measured in solutions under air conditions. [C] Absorption maxima. [17,40]

The values at which the peaks can be found correspond to the purple/blue colour of the electromagnetic spectrum; hence, we see these compounds having the complementary colour of yellow. We attained confirmation of the transformation from

phosphole oxide to [2+2] adduct by conducting ^{31}P NMR testing on phosphole oxide before and after being irradiated under the same light (λ=380 nm) as the other experiments. NMR measurements presented that this does indeed occurs.

Time dependent-DFT calculations, using the CAM-B3LYP functional and the DEF2TZVP basis set, were performed to analyse the electronic transitions responsible for the UV-vis spectra of all the compounds in **Table 6.3**. The absorption spectra of the compounds in chloroform were computed with TD-DFT calculations using the optimized ground state (S_0) geometries of these species. The results are summarized in **Table 6.2** and **Figure 6.11**.

Table 6.2.: Selected parameters for the vertical excitation (UV-vis absorptions) in chloroform of compounds **1**-**5** in **Table 6.1**. Calculated by TD-DFT//CAM-B3LYP-D3BJ/DEF2TZVP, based on their optimized ground state geometries.

Compound	Electronic transition	Excitation energy (eV; nm)	f[a]	Composition[b]	Experiment λ_{abs} max (nm)
1	$S_0 \rightarrow S_1$	3.24; 382	0.646	H →L	374
2	$S_0 \rightarrow S_1$	2.98; 416	0.561	H →L	394
3	$S_0 \rightarrow S_1$	3.30; 376	0.644	H →L	376
4	$S_0 \rightarrow S_1$	2.96; 419	0.523	H →L	397
5	$S_0 \rightarrow S_1$	4.64; 267	0.604	H →L	255

[a] Oscillator strength

[b] H stands for HOMO and L stands for LUMO

The TD-DFT calculations reasonably reproduce the experimental absorption maxima, with maximal de*via*tions (ΔE_{abs}, see **Table 6.4**) of less or close to ~0.15 eV.

1) 1,2,5-triphenyl-1H-phosphole

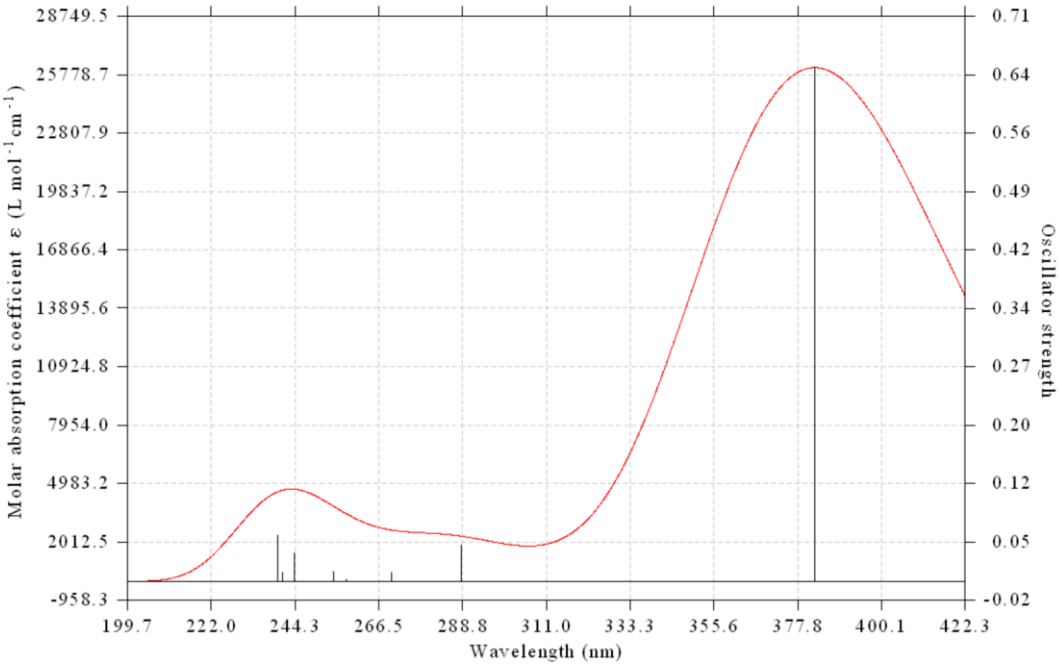

2) 1,2,5-triphenyl-1H-phosphole oxide

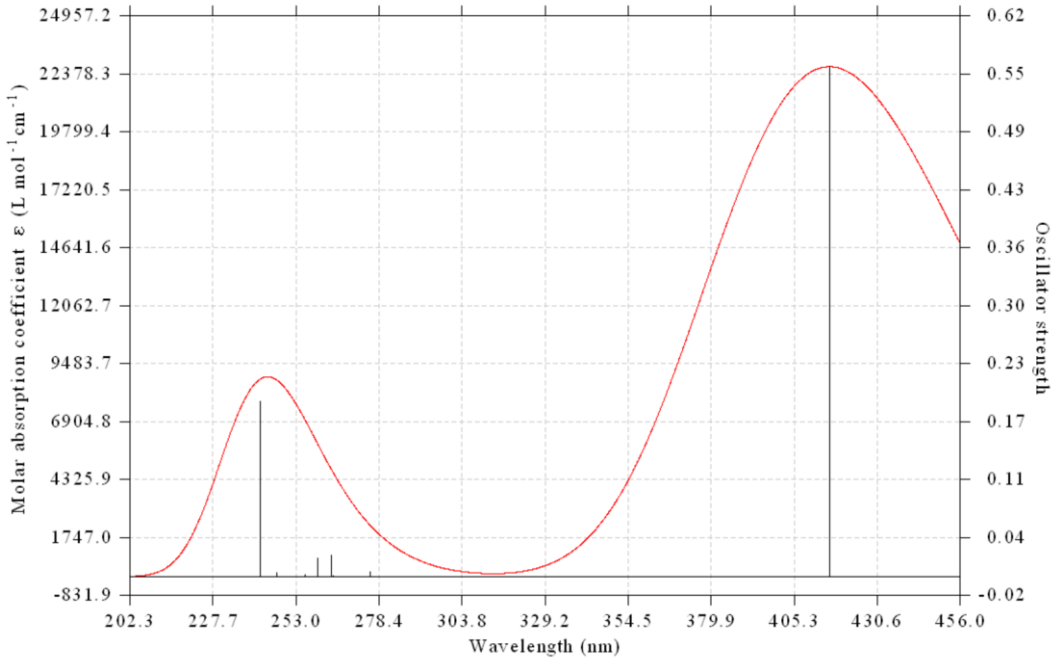

3) 1-mesityl-2,5-diphenylphosphole

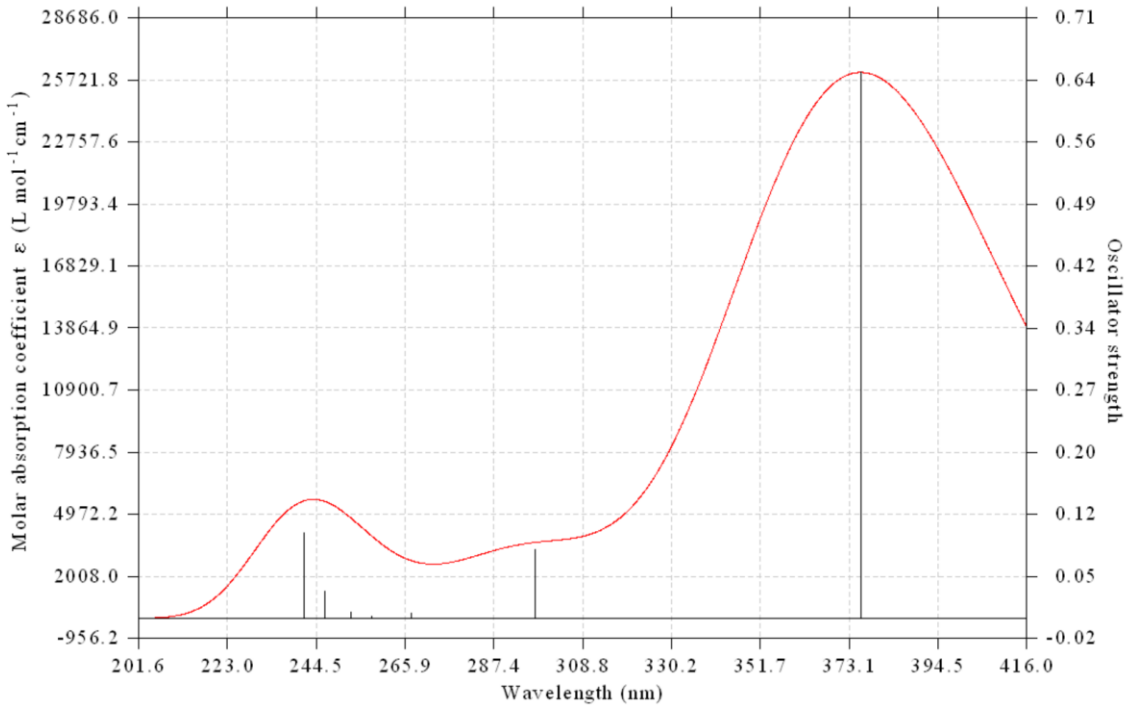

4) 1-mesityl-2,5-diphenylphosphole oxide

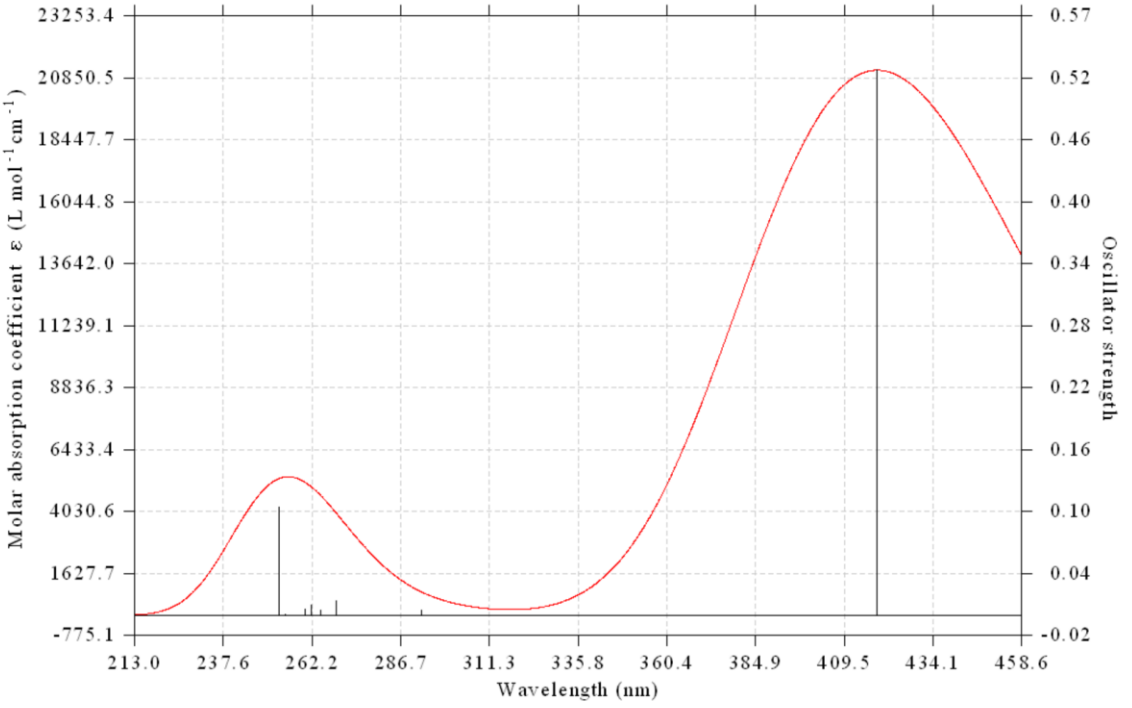

Figure 6.11.: UV-Vis Absorption spectrum for complexes **1-4** (**Table 6.4**) in chloroform solvent, at the TD-DFT CAM-B3LYP/DEF2TZVP level of theory.

These absorption peaks may be attributed to π–π∗ transitions within the conjugated system, with minor contribution from the phosphorous substituents. Since the 1,4-diphenylbutadiyneand mesityl phosphinedo not have an associated band in that region it may be concluded that the bands are descriptive of the phosphole moiety in the three compounds.[41]

For all the compounds the maximum absorption and emission peaks result to be HOMO → LUMO in nature and involve the same kind of orbitals: they are built on the π-system, mainly located on the phosphole ring and with contribution of the aryl groups of mesityl substituents (**Figure 6.9**). In the phosphole oxides, the oxygen orbitals contribute to the LUMO, but no to the HOMO. Both with phenyl and mesityl substituents at phosphorous phosphole oxidation induces a bathochromic shift (**Table 6.4**).

Having explored the electronic structure and optical properties of the phosphole, phosphole oxide, we now proceed to explore the formation of the [2+2] homodimer.

6.3.3. Mechanism for [2+2] photodimerisation of P(V) derivate of 2,5 disubstituted phosphole

The possible reaction pathways for [2+2] photodimerisation have been reviewed in a multitude of textbooks and reviews of photochemistry.[42–47] [48]Visible light photocatalysis of [2+2] cycloadditions have been reported.[49,50] The pathway that will be presented in this thesis incorporates a light-induced excitation of the phosphole oxide from the ground state (S_0) to the first excited singlet state (S_1), with ulterior evolution to a more stable triplet biradical (T_1). The ensuing addition of this biradical to another molecule of phosphole oxide yields the product of [2+2] photodimerization. **Scheme 6.6** summarizes the proposed photocatalytic cycle for the formation of [2+2] adduct.

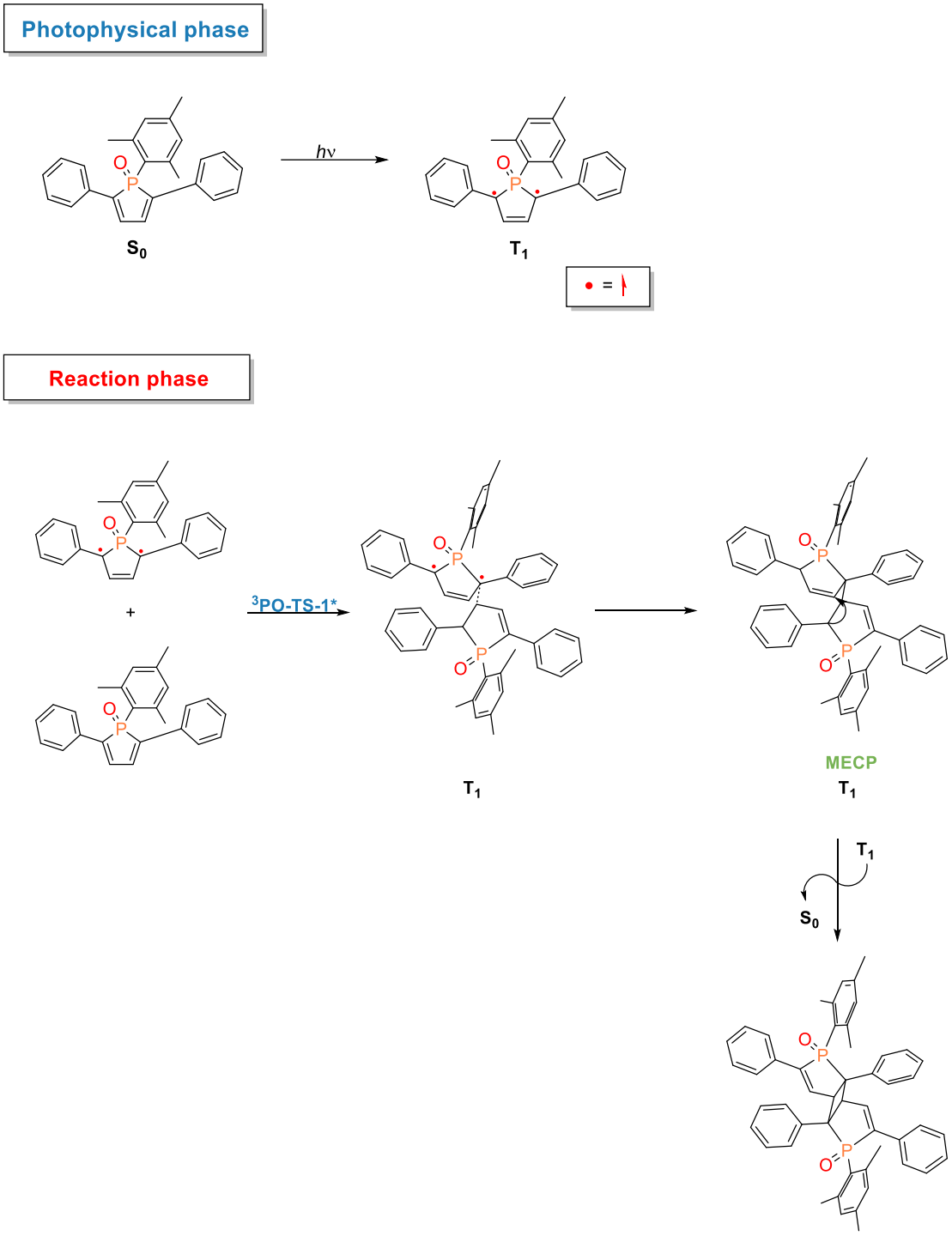

Scheme 6.6: Proposed reaction mechanism for the formation of [2 +2] adduct. The unpaired electrons are expressed with red dots.

Two main steps can be singled out in the reaction mechanism. In the first one, the photophysical phase, a highly reactive intermediate is generated from the

phosphole oxide by absorption of light. Then, in the reaction phase, this intermediate reacts with another molecule of phosphole oxide forming the [2+2] homodimer.

Time-dependent density functional theory (TD-DFT) was employed to characterize the photochemically induced excitation of the phosphole oxide, which happens upon absorption of light quanta (see **Figure 6.12**).

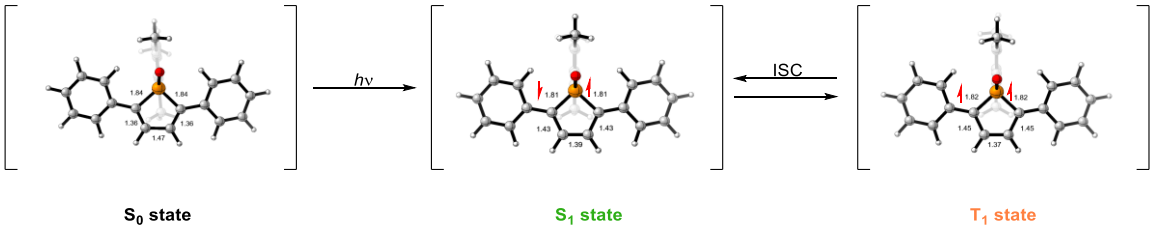

Figure 6.12.: Optimized structures for S_0, S_1 and T_1 (from left to right) involved in the [2+2]-cycloaddition *via* light excitation leading to the [2+2]-cycloaddition product. The unpaired electrons are expressed with red arrows. Distances are shown in Å.

The reaction commences with excitation of one molecule of the phosphole oxide, that absorbs light to be promoted from the singlet ground state (S_0) to the first singlet excited state **^{1}PO-1*** (S_1), that evolves to the more stable triplet species (T_1). S_1 can be reached with an excitation of 2.82 eV (B3LYP-D3BJ/6-31G(d,p)/SMD(THF) level of theory), feasible under visible light irradiation. The triplet state T_1 lies below S_1, at 1.52 eV. The optimised structures of the excited species which participate in the mechanism are depicted in **Figure 6.12**. The excitation *via* light is possible in our case as excitation of conjugated dienes like ours may be done *via* a commercially available irradiation source (λ≥250nm).[51,52] Additionally, as stated above in the absence of light/irradiation the reaction does not proceed with the formation of the [2+2] adduct (see **Section 6.1.1.**).

The **^{1}PO-1*** then undergoes an additional intersystem crossing process (ISC) to generate the much more stable intermediate in the triplet state **^{3}PO-I-1*** that will be the reactive intermediate in the [2+2] addition. In **Figure 6.12** we can see that the S_1 species presents noticeable structural differences with respect to the ground state geometry: it has one double bond in the phosphole ring instead of two i.e., the distances C1-C2 and C3-C4 are elongated by 0.07 Å, whilst the C2-C3 distance is shortened by

0.08 Å in comparison to the S_0 state. The configuration of the T_1 state is similar to the configuration of the S_1 state, with elongation and shortening of 0.02 Å for C1-C2 and C3-C4 and C2-C3 distance respectively. The value of these distances in **^{3}PO-I-1*** (1.45, 1.45 and 1.37 Å, respectively), when compared to the corresponding distances in the ground state (1.36, 1.36 and 1.46 Å, respectively) highlight the changes in the electronic structure induced by the excitation. This species is a biradical, with two unpaired electrons at C1 and C4 carbon atoms of the ring, as can be appreciated in the spin density map of **^{3}PO-I-1** (see **Figure 6.13**). P=O distance does not change with the excitation (1.51 Å). This phosphole oxide which is biradical is the one which will later on participate in the dimerisation process.

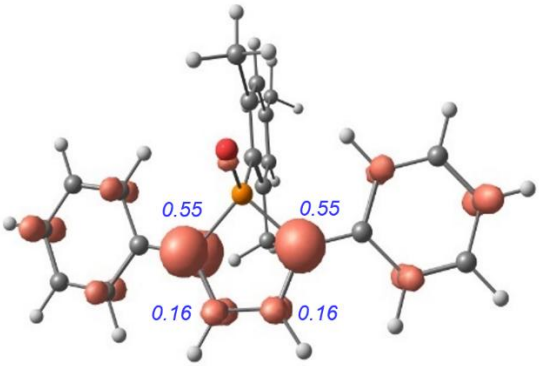

Figure 6.13.: Surface contour of the total SCF spin density for the triplet state of phosphineoxide (**^{3}PO-I-**1) at the B3LYP-D3/def2-TZVP/SMD(THF)//B3LYP-D3BJ/6-31G(d,p)/SMD(THF) level of theory. In blue, Mulliken spin densities in the phospohole ring.

The triplet excited intermediate **^{3}PO-I-1** then may proceed with a C-C stepwise bond formation reacting with a molecule of phosphole oxide. The reaction will proceed *via* a non-concerted manner, and it will generate a stereospecific product. **Figure 6.14** contains the computed Gibbs energy diagram for this reaction. The attack of a radical carbon of **^{3}PO-I-1** to a double bond of the diene-like phosphole forms the first C-C bond of the cyclobutene ring. This step has a feasible energy barrier of 16.2 kcal mol^{-1} (**^{3}PO-TS-1***) and generates a biradical intermediate with an unpaired electron in each phosphole ring, **^{3}PO-I-1***(10.6 kcal mol^{-1}). The C-C distances decreased from 2.19 Å in **^{3}PO-TS-1*** to 1.63 Å in **^{3}PO-I-1***, suggesting that the first C-C bond was formed.

After the formation of the first C-C bond, the two unpaired electrons system will proceed with an intersystem crossing process (ISC) from the triplet to the singlet potential energy surface, to form the second C-C bond of cyclobutane and generate the [2+2] product in the singlet state. We have computed the Minimum Energy Crossing Point (**MECP**) for the spin crossover units from the triplet to the closed singlet spin state, which lies at 12.2 kcal mol^{-1} above ^{3}**PO-1*** and ^{1}**PO-1**. After crossing the **MECP** the [2+2] photodimerisation product ^{1}**PO-P-1** is formed in the singlet hypersurface. The reaction gives the head-to-tail adduct, probably by steric reasons.

From the Gibbs energy diagram, it can be concluded that overall, the light induced [2+2] dimerisation in P(V) derivate is an exergonic process by -20.8 kcal mol^{-1}. The formation of the first C-C bonds is the most energy-intensive stage in this reaction, (^{3}**PO-TS-1***; **Figure 6.14**), with an energy barrier of 16.2 kcal mol^{-1} in reference to ^{3}**PO-1*** and ^{1}**PO-1**. The structures of the transition state and minimum energy crossing point associated with this reaction mechanism are depicted in **Figure 6.15**.

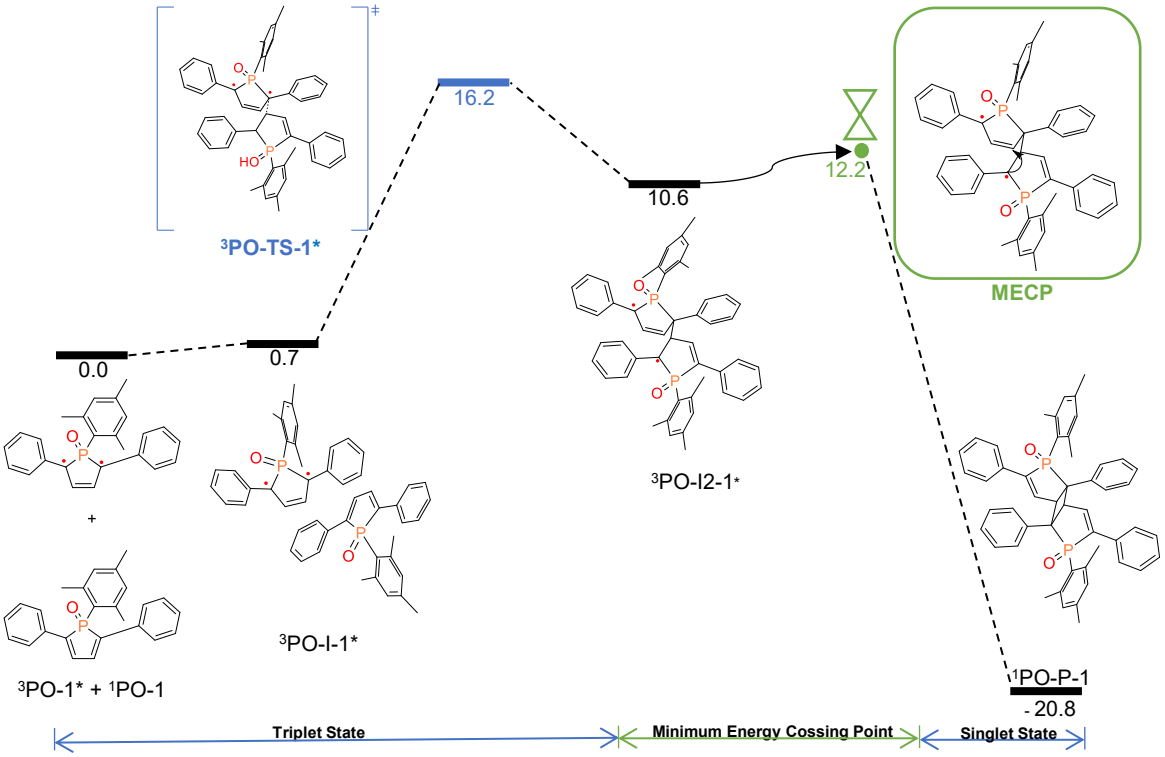

Figure 6.14.: Computed Gibbs energy diagram in THF (ΔG_{THF}/kcal mol^{-1}) at 298 K for light induced formation of [2+2] cycloaddition product at the B3LYP-D3/def2-TZVP/SMD(THF)//B3LYP-D3BJ/6-31G(d,p)/SMD(THF) level of theory.

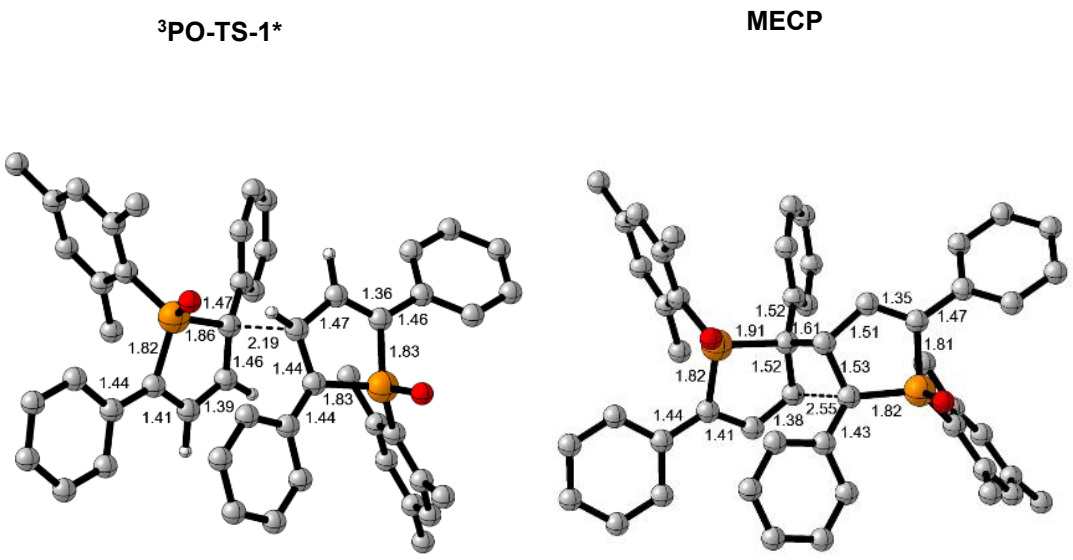

Figure 6.15.: Selected optimised structures for the transition state (left) and the minimum energy crossing point (right) involved in the formation of [2+2] photodimerisation product. Certain H atoms are omitted for clarity reasons. The distances presented are given in Å.

6.3.4. Mechanism for formation of Diels-Alder adduct

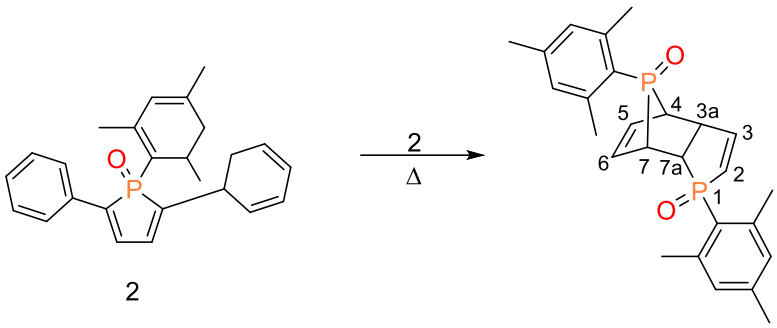

2

Scheme 6.7: General Scheme for formation of a possible Diels Alder adduct.

Figure 6.16, **part A** depicts the computed Gibbs energy diagram for the formation of the DA adduct, whilst **part B** depicts the optimised structure for the transition state.

A)

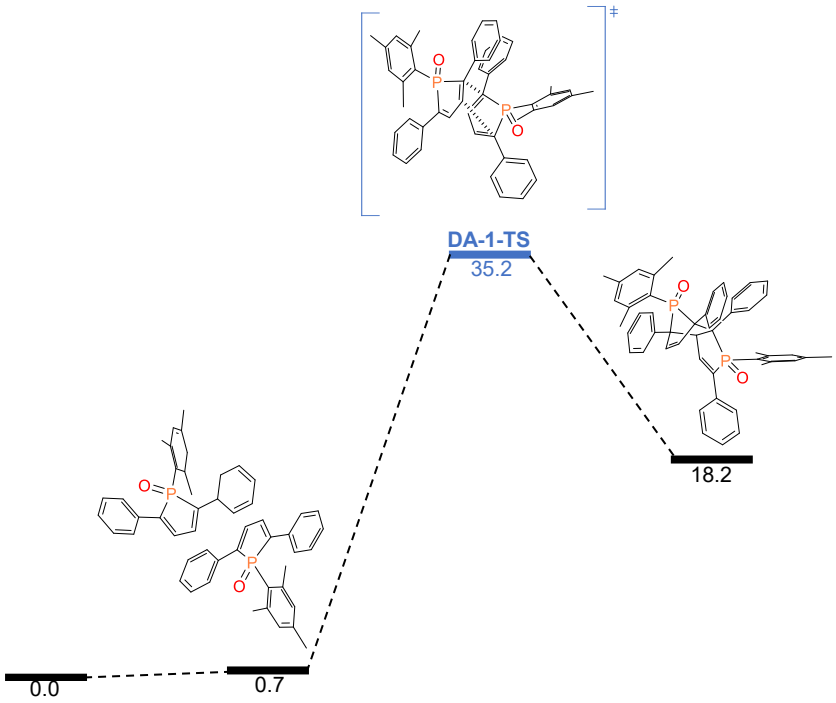

B)

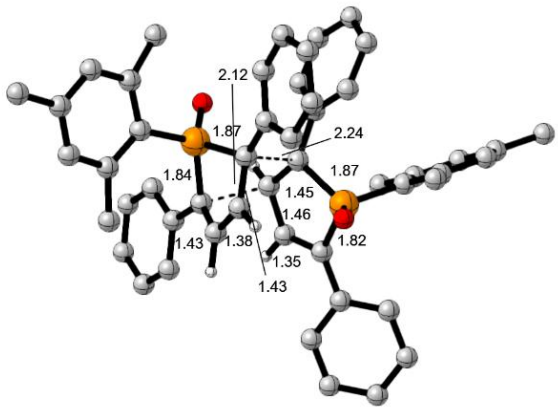

Figure 6.16.: Part A) Computed Gibbs energy diagram in THF (ΔG_{THF} kcal mol^{-1}) at 298 K for formation of Diels-Alder adduct of 1-mesityl-2,5-diphenyl-1H-phosphole oxide at the B3LYP-D3/def2-TZVP/SMD(THF)//B3LYP-D3BJ/6-31G(d,p)/SMD(THF) level of theory. **Part B)** Optimised structure for the transition state for formation of the DA adduct. Certain H atoms are omitted for clarity reasons. The distances presented are given in Å.

According to our calculations, the Diels–Alder addition which we assessed necessitates an energy barrier of 35.2 kcal mol^{-1} to proceed (**DA-1-TS**). The addition is concerted and only slightly asynchronous, in the transition state the two C-C bonds being formed have similar distances (2.12 and 2.24 Å). This addition is endergonic and will generate 1,8-dimesityl-2,4,7,7a-tetraphenyl-3a,4,7,7a-tetrahydro-4,7-phosphanophosphindole 1,8-dioxide (DA adduct) at 18.2 kcal mol^{-1} above separated reactants. Both the high barrier and the endergonic character of the reaction disfavours the formation of the [4+2] adduct.

Hitherto, it is known that Diels-Alder reaction are controlled by both kinetic and thermodynamic factors.[22,50] The generated adduct for this TS is an endo isomer. Despite the more hindered transition state, the formation of the endo isomer is preferred over the exo isomer according to previous studies conducted on Diels-Alder reactions of phospholes.[46,47,49] This preference can be attributed to the stabilizing interaction in the endo transition state between the extended π-orbitals on the HOMO of one phosphole oxide, acting as the diene, and the π-orbitals of the other phosphole oxide, acting as the dienophile. Even though this “secondary orbital overlap“ is not bond forming, it is enough to be compensated for the higher steric hinderance, rendering this TS more favourable. Moreover, due to the distance between the π-orbitals amongst the diene and the dienophile in the TS, which renders the exo adduct, the secondary overlap is not possible. Hence, we focused in our further discussing only on the endo addition.

The oxygen atoms from the P=O group in the yielded product are projected towards the centre of the system. In the DA product the distance between the newly formed C-C bonds is 1.61 Å which correspond to elongated C-C bonds from sp^2 hybridized atoms. The bond distances between C_6 - C_7 and C_4-C_5 are elongated from 1.36 Å to 1.51 Å from monomeric species to the DA product, respectively, thus converting these bonds from double to single bonds. The opposite trend may be detected for the distance between C_5 and C_6 as the distances shortens from 1.46 to 1.34 Å. Additionally, the bond length C_{7a}-C_{3a} is also elongated from 1.46 to1.587 Å in the adduct. In comparison to similar compounds, this adduct has slightly shorter bond lengths.[2]

6.4. Conclusions

In this chapter, we presented the experimental findings on oxidation of phosphole and subsequent [2+2] photodimerisation and computational investigation on the possible mechanism by which these two reactions proceed.

We were able to determine experimentally that the outcome of the introduction of the chalcogen atom into the phosphole oxide unit will depend on whether the reaction proceeds under light or not. In the case of absence of light, the reaction stops with the formation of the phosphole oxide. However, in the presence of light the reaction might proceed with subsequent [2+2]photodimerization.

The introduction of the chalcogen atom to the parent phosphole reduces the pyramidally of the phosphorous atom and as such transforms the parent phosphole from slightly aromatic into antiaromatic compound. Moreover, the oxidation induced a downfield shift in the ^{31}P NMR spectrum. The [2+2] adduct will introduce a further downfield shift in the ^{31}P NMR spectrum.

As the formation of the head-to-tail [2+2] adduct only proceeded under light and was hindered in darkness, we were able to propose that this reaction is a photo induced [2+2] photodimerization. The conversion of the phosphole oxide into the [2+2] adduct was observed experimentally by an isosbestic point and subsequently confirmed by ^{31}P NMR.

We found by DFT calculations that the oxidation step would proceed *via* a single step with H_2O_2 as the oxidizing agent. We estimated that this step will necessitate an energy barrier of 23.8 kcal mol^{-1} to proceed. The yielded phosphole oxide was determined to lay at -69.3 kcal mol^{-1} bellow separated reactants, thus making this step very exergonic.

Before exploring a mechanism for the formation of the [2+2] adduct, we were able to confirm that the addition of the chalcogen atom indeed lowers the LUMO orbital and induces a red shift into the UV-Vis spectrum. Moreover, we were able to determine that this lowering of the LUMO orbital provides the conditions prerequisite for the subsequent [2+2] addition to ensue. We studied by means of Time-Dependent DFT calculations (TD-DFT) the UV-visible spectra of phospholes and phosphole oxides. We estimated that the phosphole oxide is initially excited from the ground singlet state (S_0)

to the first singlet excited state (S_1) with 2.82 eV of energy, which is possible under visible light. A subsequent transition to a more stable triplet state (T_1) at 1.52 eV *via* intersystem crossing (ISC) takes place. The T_1 state's configuration is similar to S_1 state, with bond length changes of 0.02 Å due to altered electron delocalization. This triplet state has a biradical nature, with unpaired electrons on C1 and C4 which may react with another phosphole to form the first C-C bond in the triplet state, necessary for the formation of the [2+2] adduct. The system then transitions back to the singlet state, forming the second C-C bond to form the four-membered ring. We estimated that overall, light-induced [2+2] dimerisation of the P(V) derivative is exergonic by -20.8 kcal/mol, with the formation of the first C-C bond being the most energy-intensive step, requiring 16.2 kcal/mol.

Furthermore, we also estimated that the formation of the endo-7-phosphanorborane *via* Diels-Alder reaction, necessitates in the instance of 1-mesityl-2,5-diphenyl-1H-phosphole an energy barrier of 35.2 kcal mol^{-1}. This is consistent with the experimentally notion that formation of no such product was observed at room temperature. Moreover, we estimated this process to be endergonic.

Overall, this work paints a detailed picture of the reaction mechanism associated with the oxidation of phospholes *via* H_2O_2 as oxidant, including the major factors which govern further reactivity entailing the subsequent [2+2] photodimerisation of phosphole oxides.

Bibliography

1. Veinot, A., Ramgoolam, K., Giffin, N. & Masuda, J. Crystal Structure of Bis(2,4,6-trimethylphenyl)-phosphine Oxide. *Molbank* **3,** (2017).
2. Keserű, G. M. & Keglevich, G. Stereospecific cyclodimerization of 1-methylphosphole 1-oxide: a theoretical study. J. Organomet. Chem. **586,** 166–170 (1999).
3. Mathey, F. The organic chemistry of phospholes. *Chem. Rev.* **88,** 429–453 (1988).
4. Quin, L. D. & Wu, X.-P. Products derived from oxidations of 3,4-dimethyl-1-phenylphosphole-1-oxide: A 3-phenyl-5,6-dimethyl-2,3-oxaphosphabicyclo[2.2.2]octene-3-oxide derivative as a precursor of phenyl metaphosphonic anhydride. *Heteroat. Chem.* **2,** 359–367 (1991).
5. Hissler, M., Lescop, C. & Réau, R. Coordination chemistry of phosphole ligands: From supramolecular assemblies to OLEDs. *C. R.Chim.* **11,** 628–640 (2008).
6. Barton, T. J. & Nelson, A. J. Heterocyclopentadiene photochemistry. *Tetrahedron Lett.* **10,** 5037–5040 (1969).
7. Duffy, M. P., Lin, Y., Ting, L. Y. & Mathey, F. Intramolecular [4+2] versus [2+2] cycloadditions in P–X–P-linked biphospholes (X = O, S). *New J. Chem.* **35,** 2001 (2011).
8. Wilson, W. L., Fischer, J., Wasylishen, R. E., Eichele, K., Catalano, V. J., Frederick, J. H. & Nelson, J. H. Thermal Coupling Reactions of 1-Phenyl-3,4-dimethylphosphole within the Coordination Sphere of Palladium(II). *Inorg. Chem.* **35,** 1486–1496 (1996).
9. Deschamps, E., Ricard, L. & Mathey, F. Toward Polyphospholes: Synthesis and Structure of an α-Linked Quaterphosphole. *Angew. Chem. Int. Ed. Engl.* **33,** 1158–1161 (1994).
10. Santandrea, R. P., Mensing, C. & Von Schnering, H. G. Chemistry and structural chemistry of phosphides and polyphosphides. 45. The thermal decomposition and thermodynamic properties of the alkali metal pho. *Thermochim. Acta* **117,** 261–270 (1987).
11. Katritzky, A. R. *Comprehensive heterocyclic chemistry III*. (Elsevier, 2008).
12. Ji, H., Nelson, J. H., DeCian, A., Fischer, J., Li, B., Wang, C., McCarty, B., Aoki, Y., Kenney, J. W., Solujic, L. & Milosavljevic, E. B. [2 + 2] Photocycloadditions of [(η5-C5H5) Ru(DMPP)2L]PF6 complexes. J. Organomet. Chem **529,** 395–408 (1997).
13. Yavari, K., Retailleau, P., Voituriez, A. & Marinetti, A. Heterohelicenes with Embedded P-Chiral 1 *H* -Phosphindole or Dibenzophosphole Units: Diastereoselective Photochemical Synthesis and Structural Characterization. *Chem. Eur. J.* **19,** 9939–9947 (2013).
14. Demmer, C. S., Aillard, P., Febvay, J., Retailleau, P., Voituriez, A. & Marinetti, A. Photochemical [2+2] Cyclization of Helical Phosphinamides in Solution and in the Solid State. *ChemPhotoChem* **1,** 535–538 (2017).
15. Arp, F. F., Ashirov, R., Bhuvanesh, N. & Blümel, J. Di(hydroperoxy)adamantane adducts: synthesis, characterization and application as oxidizers for the direct esterification of aldehydes. *Dalton Trans.* **50,** 15296–15309 (2021).
16. Bousrez, G., Nicolas, E., Martinez, A., Chevreux, S. & Jaroschik, F. [4+2] versus [2+2] Homodimerization in P(V) Derivatives of 2,4-Disubstituted Phospholes. *Heterot. Chem.* **2019,** 1–10 (2019).
17. Kumaravel, M., Mague, J. T. & Balakrishna, M. S. Chalcogenide derivatives of 1,2,5-triphenyl-1H-phosphole: structure and photophysical properties. *Tetrahedron Lett.* **55,** 2957–2961 (2014).
18. Härling, S., Greiser, J., Al-Shboul, T. M. A., Görls, H., Krieck, S. & Westerhausen, M. Calcium-mediated Hydrophosphorylation of Organic Isocyanates with DiphenylphosphineOxide. *Aust. J. Chem.* **66,** 1264 (2013).

19. Gilheany, D. G. No d Orbitals but Walsh Diagrams and Maybe Banana Bonds: Chemical Bonding in Phosphines, Phosphine Oxides, and Phosphonium Ylides. *Chem. Rev.* **94,** 1339–1374 (1994).
20. Arunan, E., Desiraju, G. R., Klein, R. A., Sadlej, J., Scheiner, S., Alkorta, I., Clary, D. C., Crabtree, R. H., Dannenberg, J. J., Hobza, P., Kjaergaard, H. G., Legon, A. C., Mennucci, B. & Nesbitt, D. J. Definition of the hydrogen bond (IUPAC Recommendations 2011). *Pure Appl. Chem* **83,** 1637–1641 (2011).
21. Mucsi, Z. & Keglevich, G. Why are Phosphole Oxides Unstable? The Phenomenon of Antiaromaticity as a Destabilizing Factor. *Eur J Org Chem* **2007,** 4765–4771 (2007).
22. Ishidoshiro, M., Matsumura, Y., Imoto, H., Irie, Y., Kato, T., Watase, S., Matsukawa, K., Inagi, S., Tomita, I. & Naka, K. Practical Synthesis and Properties of 2,5-Diarylarsoles. *Org. Lett.* **17,** 4854–4857 (2015).
23. Hocking, M. B., Preston, D. M. & Zink, J. I. Triboluminescence of 1,2,5-triphenylphosphole and related compounds. *J. Lumin*. **43,** 309–322 (1989).
24. Poplata, S., Tröster, A., Zou, Y.-Q. & Bach, T. Recent Advances in the Synthesis of Cyclobutanes by Olefin [2 + 2] Photocycloaddition Reactions. *Chem. Rev.* **116,** 9748–9815 (2016).
25. Sarkar, D., Bera, N. & Ghosh, S. [2+2] Photochemical Cycloaddition in Organic Synthesis. *Eur J Org Chem* **2020,** 1310–1326 (2020).
26. Sicignano, M., Rodríguez, R. I. & Alemán, J. Recent Visible Light and Metal Free Strategies in [2+2] and [4+2] Photocycloadditions. *Eur J Org Chem* **2021,** 3303–3321 (2021).
27. Alcaide, B., Almendros, P. & Aragoncillo, C. Exploiting [2+2] cycloaddition chemistry: achievements with allenes. *Chem. Soc. Rev.* **39,** 783–816 (2010).
28. Atkins, P. W. & De Paula, J. *Physical chemistry*. (W.H. Freeman, 2010).
29. Persico, M. & Granucci, G. *Photochemistry*. (Springer International Publishing, 2018).
30. Alonso, R. & Bach, T. A Chiral Thioxanthone as an Organocatalyst for Enantioselective [2+2] Photocycloaddition Reactions Induced by Visible Light. *Angew Chem Int Ed* **53,** 4368–4371 (2014).
31. Lu, Z. & Yoon, T. P. Visible Light Photocatalysis of [2+2] Styrene Cycloadditions by Energy Transfer. *Angew Chem Int Ed* **51,** 10329–10332 (2012).
32. Zou, Y.-Q., Duan, S.-W., Meng, X.-G., Hu, X.-Q., Gao, S., Chen, J.-R. & Xiao, W.-J. Visible light induced intermolecular [2+2]-cycloaddition reactions of 3-ylideneoxindoles through energy transfer pathway. *Tetrahedron* **68,** 6914–6919 (2012).
33. Baumgartner, T. Insights on the Design and Electron-Acceptor Properties of Conjugated Organophosphorus Materials. *Acc. Chem. Res.* **47,** 1613–1622 (2014).
34. Soengas, R. G. & Rodríguez-Solla, H. Modern Synthetic Methods for the Stereoselective Construction of 1,3-Dienes. *Molecules* **26,** 249 (2021).
35. Fleming, I. *Molecular Orbitals and Organic Chemical Reactions*. (Wiley, 2010).
36. Clayden, J., Greeves, N. & Warren, S. *Organic chemistry*. (Oxford university press, 2012).
37. Dinadayalane, T. C., Geetha, K. & Sastry, G. N. Ab Initio and Density Functional Theory (DFT) Study on [1,5] Sigmatropic Rearrangements in Pyrroles, Phospholes, and Siloles and Their Diels−Alder Reactivities ′. *J. Phys. Chem. A* **107,** 5479–5487 (2003).
38. Dinadayalane, T. C., Gayatri, G., Sastry, G. N. & Leszczynski, J. Competitive Diels−Alder Reactions: Cyclopentadiene and Phospholes with Butadiene. *J. Phys. Chem. A* **109,** 9310–9323 (2005).
39. Tomioka, H., Miura, S. & Izawa, Y. Synthesis and photochemical reaction of diels-alder adduct of phosphole oxide and cyclopentadiene. *Tetrahedron Lett.* **24,** 3353–3356 (1983).

Chapter 7: General Conclusions

At the end of each chapter, detailed conclusions for each of the explored reactions in this thesis was presented. Hence, only the general conclusion gained from these investigations will be summarised herein.

The primary aim of this work was to explore the factors influencing alkali metal-mediated reactions detailed in the publication “Scope and Limitations of the s-Block Metal-Mediated Pudovik Reaction” and to examine the alkali metal-mediated addition of mesityl phosphineto 1,4-diphenylbutadiyne, employing the same catalyst as in the earlier study. An additional goal that emerged during the course of the research was the oxidation of the newly formed phosphole and the subsequent formation of the [2+2] photo cycloadduct. Both the Pudovik and the hydrophosphination reactions imply the approach of a base lone pair to an electron-rich π-system of an unsaturated bond. Moreover, these reactions necessitate the use of a catalyst to overcome the adverse entropic impact and the approach of two electron-rich molecules. Both of the analysis were conducted using alkali metal hexamethyldisilazanides (M-HMDS) as catalysts.

In both hydrophopshorylation and hydrophopshination, our calculations indicate that alkali metal diarylphosphinites and alkali metal phopshonates (M-P(H)R and M-OPR_2, where M = Li, Na, and K) possess enough nucleophilicity to function as the active species, facilitating the formation of P-C bonds in these addition reactions. Notably, in both instances the same reaction trend was observed, with that the metal cations play an important role as the conversion showed dependence on the softness and the radius of the metal ions.

From both sets of calculations, we were able to determine that the influence of the alkali metal cation on the addition process is relatively minor, casing only slight variations in the nucleophilicity of the active species. The formation of the active species proceeded *via* deprotonation of either the phosphine oxide or the phosphine by alkali metal hexamethyldisilazanides (M-HMDS). Notably, the degree to which the active species formation will be successful will vary due to simultaneous deactivation processes, such as dismutation and aggregation, which diminishes the concentration of catalytically active species in the reaction mixture.

For both aforementioned reactions, while the computed energy barriers for the addition reactions involving the three cations are comparable, experimental observations indicate that Li-HMDS fails to facilitate both of them. This discrepancy appears to stem not from the reaction mechanisms themselves but from challenges in generating the active species Li-$OPMes_2$ and Li-P(H)Mes, respectivly. DFT calculations confirmed the correlation between alkali metal cations' chemical hardness and their catalytic capacity, as observed experimentally.

In the alkali-mediated Pudovik reaction, all reactions yielded the anti-Markovnikov product, with regioselectivity driven by the π-withdrawing nature of the phenyl group, which enhances electrophilicity and facilitates nucleophilic attack. DFT calculations revealed that the Z isomer is kinetically preferred, while the E isomer is thermodynamically favoured, and an isomerization step from pro-Z to pro-E was proposed to explain the observed stereoselectivity. Our calculations showed a significant dependence on the P-bound substituent. Our investigation of the bishydrophosphorylated product formation revealed that for R = Ph, the second addition proceeds with low energy barriers and is thermodynamically favoured, while for R = Mes, steric effects lead to higher barriers and the *E-isomer* being more stable. Additionally, we found that in the protonation steps and the second nucleophilic attack, the alkali cation prefers to bind with oxygen atoms from neighbouring molecules, which lowers the energy barrier for the protonation steps.

Notably in the alkali metal-mediated hydrphopshorylation, the RDS is the cyclization. In the sodium case this step necessitates 3.1 kcal mol^{-1} more energy than in the potassium case, which aligns with the experimental observations. Our calculations without any alkali metal cation present showed interesting results as the energy barriers for all the cases were lower, particularly for the RDS, indicating that whilst the cation is necessary for the formation of the active species it does not play a significant role in the mechanism itself. Interestingly, our calculations also revealed that the double addition necessitates a lower energy barrier than for the cyclization reaction, however the product is less thermodynamically favoured.

Finally, we investigated experimentally and theoretically the oxidation of the 1-mesityl-2,5-diphenylphosphole the subsequent [2+2] photodimerization. Experimentally, we observed that in the absence of light, the reaction halts at the phosphole oxide

stage, while light promotes the [2+2] photodimerisation of phosphole oxides. DFT calculations revealed that the oxidation step, facilitated by H_2O_2, generates the highly exergonic [2+2] adduct. Notably, utilising TD-DFT calculations we determined that the introduction of a chalcogen atom lowers the LUMO and induces a red shift in the UV-Vis spectrum, which is crucial for the [2+2] photodimerization. Overall, our work suggests a comprehensive understanding of the mechanisms governing the oxidation phospholes and subsequent photodimerisation of phosphole oxides.

This thesis combines both experimental studies and computational calculations to explore the reaction mechanisms of s-block metal-promoted hydrophosphorylation and hydrophosphonylation. The use of DFT calculations allowed for the characterization of reaction intermediates and transition states, providing detailed insights into the outcomes of these reactions. In addition to the computational work, experimental studies on hydrophosphonylation were also conducted, expanding on the overall understanding of the processes.

While s-block metal-promoted processes have received less computational attention compared to transition-metal-catalysed reactions, this study highlights the difficulties in modelling these reactions, particularly concerning issues like speciation and solvation. The results presented in this thesis highlight that integrating computational methods with experimental data is crucial for investigating the mechanisms of homogeneous catalytic reactions. The experimental studies serve to validate and enhance the computational findings. This integrated approach has led to a more comprehensive understanding of s-block metal-promoted catalytic processes.

8 Experimental Section

8.1. General remarks

All the reaction steps for the synthesis of the 1,4-Diphenyl-2,3-bis(diphenylphosphoryl)buta-1,3-diene, 1-mesityl-2,5-diphenyl-1H-phosphole, 1-mesityl-2,5-diphenyl-1H-phosphole oxide and bis(phosphole) 1,4-dioxide were conducted under nitrogen atmosphere by application of standard Schlenk techniques including absolute and oxygen free-solvents. The solvents (THF, n-hexane, n-pentane, diethyl ether and toluene were dried over sodium and benzophenone, degassed, and saturated with nitrogen using standard methods. $CDCl_3$ was dried over CaH_2, whilst C_6D_6 was dried over sodium, followed by distillation under atmosphere of reduced pressure but saturated nitrogen. The $^{13}C\{^1H\}$-NMR and ^1H NMR spectra were referred to the external standard of trimethylsilane and the chemical shifts were ascribed to the residual signals from the used deuterated NMR solvent. The ^{31}P NMR spectra were ascribed to the aq. phosphoric acid as external standard. ^1H, ^{31}P and $^{13}C\{1H\}$ NMR spectra were recorded on Bruker Avance III 400 and Fourier 300 spectrometers.The Figures of the NMR spectra were created with either MestReNova or with TopSpin programs. The multiplicities found in ^1H NMR and ^{31}P NMR spectra were assigned as: singlet (s), doublet (d), double doublet (dd), triplet (t), triplet of doublet (td), doublet of multiplet (dm), multiplet (m), doublet of doublet of doublet (ddd) and doublet of triplet of triplet (dtt). In the Figures the observed related coupling constants were also depicted as $^nJ_{A,B}$ (coupling between nuclei A and B *via* n-bonds).

Mass spectra data was collected on the Finnigan MAZ95XL and Finnigan MAT SSQ 710 system. The measurement for the IR spectrum were conducted on. Perkin Elmer System 2000 FTIR The melting points were collected on Reichert-Jung apparatus type 302102. The UV-Vis spectra were collected on Agilent HP 8453 spectrometer using HPLC quality solvents and 1cm quartz high precision cuvettes from Hellma Analytics.

The crystal structure of the newly discovered compounds was determined on a Nonius KappaCCD diffractometer utilizing graphite-monochromated Mo-Kα radiation (λ= 0.710 73 Å).

The substrates that were purchased from commercial sources (Alfa Aesar, Merck or Sigma-Aldrich) were used without further purification. The yields given were optimized.

Synthesis of 2,4,6-Trimethylphenyl PhosphineMesPH$_2$

This compound was synthesised by method which was developed by Damian Bevern in the group of Westerhausen.

3.2 g (132 mmol) Magnesium turnings were added to a three-neck flask and suspended with 60 mL THF. To the suspension 2-bromo-1,3,5,- trimethylbenzene (10 mL, 11.15 g, 56.0 mmol) was added gradually with a syringe while continuously stirring. Upon 5 min at room temperature the reaction began, and the solvent mixture stated to reflux. The solution mixture was left under reflux for 2 h upon which it yielded a dark grey solution with some leftover magnesium at the bottom of the flask. Afterwards a titration was conducted with an acid to determine the conversion rate. Upon which the Grignard-reagent (cooled down to −20 °C) was added dropwise to a solution of PCl_3 (13 mL, 20.4 g, 148.6 mmol) in 20 mL THF that has been cooled down to −60 °C. 30 minutes upon completion of the previous step, the mixture was allowed to reach room temperature and then was left to be stirred overnight. The volatiles were removed the following day by a distillation under vacuum. Using 20 mL n-pentane each time the residual solid was extracted. Upon which the solvent was changed to 10 mL Et_2O. For reduction, the phosphoroushalide was added to a suspension of $LiAlH_4$ (1.57 g, 41 mmol) and 60 mL Et_2O. Before extracting the required phosphane, the excess LiAlH4 was quenched with degassed water. The phosphinewas refined by vacuum distillation (75 °C - 80 °C) after separation from the solvent yielding a colourless oil with foul smell (3.0g 20mmol, 40 %). The side product generated by this reaction is Mes_2PH and it may be removed by a continued vacuum distillation. Additional physical data was not collected as this is a well-known compound. Physical data of $MesPH_2$:

^{31}P NMR (162MHz, C_6D_6, 297K) = -156.0

^{1}H NMR (400 MHz, C_6D_6 , 297 K): δ = 6.70 (d, 4JP,H = 2.3 Hz, 2H, meta-H), 3.60 (d, 1JP,H = 203.7 Hz, 2H, -PH2), 2.21 (d, 4JP,H = 1.87 Hz, 6H, ortho-CH_3), 2.09 (s, 3H, para-CH3).

^{13}C{^{1}H} NMR (100.62 MHz, C_6D_6 , 297 K): δ = 141.3 (d, 2JP,C = 10.8 Hz, ortho-C), 137.4 (s, para-C), 129.2 (d, 3JP,C = 2.6 Hz, meta-C), 125.3 (d, 1JP,C = 12.0 Hz, ipso-C), 23.5 (d, 3JP,CJ = 9.6 Hz, ortho-CH_3), 21.3 (s, para-CH_3)

General protocol for catalytic studies for alkali metal-mediated hydrophosphination

In a Schlenk flask mesityl phosphine(200 mg, 1.0 equiv) was dissolved in THF (5 mL). To the flask M-HMDS (M – Li, Na, K) solution in THF (5 mol%) was added slowly by a syringe and the reaction mixture was left to be stirred for a couple of minutes at room temperature. In the reaction vessel in one go 1 4-diphenylbutadiyne (132.91 mg, 657.13 µmol, 1.0 equiv.) was added. The reaction mixture was left to be stirred for one hour. The conversion was tracked using ^{31}P NMR spectroscopy.

Synthesis of 1-mesityl-2,5-diphenyl-1H-phosphole

Mesityl phosphine (200 mg, 1.31mmol, 1.0 equiv) was added into a Schlenk flask and K-HMDS (0.013 g, 65.71µmol, 0.05 equiv) dissolved in THF was added *via* a syringe. THF was added until the solution mixture reached 5ml. The newly formed solution presented with a pale-yellow colour upon which the solution mixture was left to stir for five minutes at room temperature. To the solution diphenylbutadiyne (265 mg, 1.31mmol, 1.0 equiv) was added while slowly stirring. The reaction mixture was stirred for 1h. In the meanwhile, the reaction mixture turned deeper yellow. Upon completion the reaction mixture was quenched with degassed methanol. The conversion into the phosphole was tracked *via* ^{31}P NMR. All the solvents were removed and the newly formed phosphole was washed three times with 4ml n-hexane. Upon washing the phosphole was crystallised from a mixture of n-Hexane: methanol: THF = 1: 0.5 :

2. The phosphole crystalized over the night forming yellow crystals with yield of 80%. Physical data of: **IR** (ATR)$\tilde{\nu}$ [cm^{-1}]: 3020 (w), 2967 (w), 1069 (w), 1449(w), 1420(w), 1396(w), 1161 (m), 1071(b), 787 (s), 767 (m), 687 (m), 624 (s). **MS(ESI)**: m/z (%) =. **Elemental analysis** ($C_{25}H_{23}P$): calc. C 84.72%, H 6.54%; found: C 84.06.64%, H 6.26%. **MP**.:128.3-130.1 °C

^{31}P NMR (162 MHz, $CDCl_3$, 297 K): δ = -7.55 ppm

^{1}H NMR (400 MHz, [D_8]-THF, 297 K):
δ = 7.64-7.77 (m, 6H, Ar-H), 7.47 (tdd, 2H, Ar-H, J = 7.8, 1.5, 1.1 Hz), 6.92-7.06 (m, 6H, Ar-H), 2.27 (s, 6H, o-CH_3), 2.23 (s, 3H, p-CH_3);

^{13}C{^{1}H} NMR (101 MHz, [D_8]-THF, 297 K):
δ = 138.6 (s, C20, q-C mesityl), 137.7 (s, C17, q-C mesityl), 136.6 (s, C4, q-C), 135.9 (s, C14, q-C), 134.8 (s, C12, q-C), 130.3 (s, C15, Ph-C), 129.9 (s, C10, Ph-C), 129.7 (s, C11, Ph-C), 128.6 (s, C13, Ph-C), 110.1 (s, C2/C3, phosphole ring), 23.3 (s, C24, p-CH_3 mesityl), 19.2 (s, C23/C25, o-CH_3 mesityl).

Synthesis of 1-mesityl-2,5-diphenyl-1H-phosphole oxide

Mesityl phosphine (200 mg, 1 .31mmol, 1.0 equiv) was added into a Schlenk flask and K-HMDS (0.013 g, 65.71µmol, 0.05 equiv) dissolved in THF was added though syringe. THF was added until we reached 5ml of solution mixture (light yellow colour). The solution mixture was left to stir for five minutes at room temperature. To the solution diphenylbutadiyne (265 mg, 1.31mmol, 1.0 equiv) was added while slowly stirring. The reaction mixture was stirred for 1h upon which the reaction mixture turned deeper yellow. Upon which the reaction mixture was quenched with degassed methanol. The conversion into the phosphole was tracked *via* ^{31}P NMR. After confirmation of formation of desired phosphole the Schlenk flask is wrapped in aluminium foil to prevent light irradiation. H_2O_2 (3mL, 35%, 34.57mmol) was added to the reaction mixture and the biphasic mixture was stirred vigorously. After 3h we confirm the conversion into the phosphole oxide *via* ^{31}P and ^{31}P{H} NMR. THF is removed is removed under vacuum and the newly formed phosphole oxide is extracted using chloroform 10 x 3ml. Upon the extraction the solvent is removed and the phosphole oxide is

washed three times with 4ml n-hexane. The phosphole oxide is crystalized from a mixture of n-hexane: methanol: THF = 1: 2: 5. Physical data of 1-mesityl-2,5-diphenyl-1H-phosphole oxide: **MP**: 128.3-130.1 °C, **IR** (ATR)$\tilde{\nu}$ [cm^{-1}]: 3024 (), 2962 (w), 1064 (w), 1446(w), 1406(w), 1392(w), 1259 (s), 1169 (m), 1066(b), 794 (s), 756 (m), 684 (m), 635 (s). m/z: 354.1537 (100.0%), 355.1571 (27.0%), 356.1604 (3.5%)

^{31}P NMR (162 MHz, $CDCl_3$, 297 K): δ = 46.3 ppm

^{1}H-NMR (400 MHz, $CDCl_3$, 297 K):
δ = 7.50 (dddd, 2H, Ar-H, J = 7.9, 7.6, 1.8, 0.4 Hz), 7.40 (dddd, 2H, Ar-H, J = 7.9, 1.9, 1.7, 0.4 Hz), 7.32 (tt, 2H, Ar-H, J = 7.6, 1.7 Hz), 7.25 (d, 6H, Ar-H, J = 1.9 Hz), 6.88 (d, 2H, Ar-H, J = 1.1 Hz), 2.37 (s, 3H, p-CH_3), 2.31 (s, 6H, o-CH_3), 2.26-2.42 (m, 9H, methyl region)

^{13}C{^{1}H}-NMR (101 MHz, $CDCl_3$, 297 K):
δ = 138.6 (s, C20, q-C mesityl), 137.7 (s, C17, q-C mesityl), 136.6 (s, C4, q-C), 135.9 (s, C14, q-C), 134.8 (s, C12, q-C), 130.3 (s, C15, Ph-C), 129.9 (s, C10, Ph-C), 129.7 (s, C11, Ph-C), 128.6 (s, C13, Ph-C), 110.1 (s, C2/C3, phosphole ring), 23.3 (s, C24, p-CH_3 mesityl), 19.2 (s, C23/C25, o-CH_3 mesityl).

Synthesis of 1,4-dimesityl-2,3b,5,6b-tetraphenyl-3a,3b,6a,6b-tetrahydrocyclobuta[1,2-b:3,4-b']bis(phosphole) 1,4-dioxide

Mesityl phosphine(200 mg, 1 .31mmol, 1.0 equiv) was added into a Schlenk flask and K-HMDS (0.013 g, 65.71µmol, 0.05 equiv) dissolved in THF was added though syringe. THF was added until mixture of the solution reached 5ml. The solution had light yellow colour. The solution mixture was left to stir for five minutes at room temperature. To the solution diphenylbutadiyne (265 mg, 1.31mmol, 1.0 equiv) was added while slowly stirring. The reaction mixture was stirred for 1h upon which the reaction mixture turned deeper yellow. Upon which the reaction mixture was quenched with degassed methanol. The conversion into the phosphole was tracked *via* ^{31}P NMR. H_2O_2 (3mL, 35%, 34.57mmol) was added to reaction solution and the solution was left to stir. The addition of the hydrogen peroxide should be done under sunlight in this instance. Upon 24h we confirm the conversion into the 1,4-dimesityl-2,3b,5,6b-tetraphenyl-3a,3b,6a,6b-tetrahydrocyclobuta[1,2-b:3,4-b']bis(phosphole) 1,4-dioxide *via*

^{31}P. THF is removed is removed under vacuum and the newly formed phosphole oxide is extracted using chloroform 8 x 4ml. Upon the extraction the solvent is removed and the phosphole oxide is washed three times with 4ml n-hexane. The phosphole oxide is crystalized from a mixture of n-Hexane: methanol: THF = 1: 2: 5. The 1,4-dimesityl-2,3b,5,6b-tetraphenyl-3a,3b,6a,6b-tetrahydrocyclobuta[1,2-b:3,4-b']bis(phosphole) 1,4-dioxide crystalized over the week forming yellow crystals suitable crystals for single crystal s-ray diffraction with yield of (408.11 mg , 1.10mmol, 84%). Notably in the crystal structure 2 molecules of methanol crystallised within the structure. Physical data of: **MP** = 212.1-213.3 ◦C. **IR** (ATR)$\tilde{\nu}$ [cm^{-1}]: 3026 (), 2969 (w), 1053 (w), 1457(w), 1412(w), 1385(w), 1259 (s), 1158 (m), 1072(b), 798 (s), 766 (m), 693 (m), 640 (s). **MS(ESI)**: m/z (%) =. **Elemental analysis** ($C_{52}H_{54}O_4P_2$): calc. C 81.06%, H 6.26%; found: C 79.64%, H 6.17%. This difference arises due to incorporation of (MeOH) solvent molecules within the crystal structure.

^{31}P NMR (162 MHz, $CDCl_3$, 297 K): δ = 66.3ppm

^{1}H NMR (400 MHz, $CDCl_3$, 297 K): δ = 7.50 (dddd, 2H, Ar-H, J = 7.9, 7.6, 1.8, 0.4 Hz), 7.40 (dddd, 2H, Ar-H, J = 7.9, 1.9, 1.7, 0.4 Hz), 7.32 (tt, 2H, Ar-H, J = 7.6, 1.7 Hz), 7.25 (d, 6H, Ar-H, J = 1.9 Hz), 6.87 (d, 2H, Ar-H, J = 1.1 Hz), 3.78 (dd, 2H, CH–CH, cyclobutane, J = 10.2, 6.1 Hz), 3.12 (dd, 2H, CH–CH, cyclobutane, J = 10.2, 6.1 Hz), 2.29 (s, 3H, p-CH_3), 2.28 (s, 6H, o-CH_3).

^{13}C ^{1}{H} NMR (101 MHz, $CDCl_3$, 297 K): δ = 145.2 (C20, q-C, mesityl), 140.6 (C17, q-C, mesityl), 138.9 (C14, q-C, phenyl), 135.4 (C12, q-C, phenyl), 132.7 (C15, CH, phenyl), 130.4 (C10, CH, phenyl), 129.9 (C11, CH, phenyl), 128.7 (C13, CH, phenyl), 126.5 (C16, CH, mesityl), 111.3 (C2/C3, phosphole ring), 48.6 (C8/C9, CH, cyclobutane ring), 39.4 (C7/C10, CH, cyclobutane ring), 21.3 (C24, p-CH_3, mesityl), 19.2 (C23/C25, o-CH_3, mesityl).

Appendix:

Crystallographic data for the X-ray structure determinations of compounds

Table A1.: Crystallographic data for the X-ray structure determinations of compounds.

Compound	**Phosphole**	**Phosphole oxide**	**[2+2] adduct**
empirical formula	$C_{25}H_{23}P$	$C_{29}H_{31}O_2P$	$C_{52}H_{54}O_4P_2$
formula weight	354.40	442.51	804.89
temperature [K]	120.0	120.0	120.0
crystal system	monoclinic	monoclinic	triclinic
space group	$P2_1/c$	$P2_1/n$	P-1
unit cell dimensions:			
a [Å]	10.417(2)	29.845(2)	8.3253(9)
b [Å]	9.0952(18)	8.0488(5)	10.8850(12)
c [Å]	20.942(4)	29.980(2)	13.2519(13)
α [°]	90	90	68.964(3)
β [°]	103.75(3)	96.390(3)	73.306(3)
γ [°]	90	90	74.499(3)
V [Å^3]	1927.3(7)	7157.2(9)	1055.4(2)
Z	4	12	1
ρ_{calc} [Mg/m^3]	1.221	1.232	1.266
μ [mm^{-1}]	0.148	0.139	0.150
F(000)	752.0	2832.0	428.0
crystal size [mm^3]	0.11 × 0.09 × 0.08	0.21 × 0.17 × 0.09	0.29 × 0.09 × 0.08
Θ range [°]	4.004 to 54.926	1.826 to 56.564	4.078 to 63.212
index range (h, k, l)	−13, 13; −11, 11; −27, 27	−39, 39; −10, 10; −39, 39	−12, 11; −15, 15; −19, 15
reflections collected	15016	90500	13145
independent reflections	4392	17770	6244
R(int)	0.0349	0.0467	0.0216
max. and min. transmission	and	0.4305 and 0.4023	
data/restraints/parameters	4392/0/238	17770/170/966	6244 / 19 / 288
goodness-of-fit on F^2	1.103	1.189	1.030
R indices (final) [$I > 2\sigma(I)$]			
R_1	0.0455	0.0959	0.0427
wR_2	0.1009	0.1864	0.1008
R indices (all data)			
R_1	0.0530	0.1189	0.0588
wR_2	0.1050	0.1967	0.1121
largest diff. peak and hole [eÅ^{-3}]	0.35 and -0.27	0.89 and -0.48	0.38 and -0.39

Publications:

P1: Bozhinovska, I.; Ujaque, G.; Westerhausen, M.; Lledós, A. Understanding alkali-metal driven hydrophosphorylation: mechanism and challenges in the Pudovik reaction. Catal. Sci. Technol., 2025, 15, 3888–3905.

P2: Chan, C.; Alsalem, L. F.; Almalki, M.; Bozhinovska, I.; Hayward, J. S.; Williams, S. S.; Bartley, J. K. Microwave-Assisted Degradation of Azo Dyes Using NiO Catalysts. Catalysts, 2025, accepted.

Oral communications:

OC1: Computational study of Pudovik reaction with s-block metal catalysts

Bozhinovska I.; Lledós A.; Westerhausen M.; Ujaque G.

International Workshop Cutting-Edge Homogenous Catalysis, May 4-6, **2021**, online Toulouse, France

OC2: Computational study of Pudovik reaction with s-block metal catalysts

Bozhinovska I.; Lledós A.; Westerhausen M.; Ujaque G.

2nd Network Workshop, May 4-6, **2021**, online Toulouse, France

OC3: Development of s-Block metal-mediated formation of phospholes: A combined experimental and DFT work

Bozhinovska I.; Lledós A.; Westerhausen M.; Ujaque G.

Doctoral Workshop, October 11-13, **2021**, online York, United Kingdom

OC4: S-block metal-mediated hydrophosphination of alkynes: New synthetic routes elucidated with DFT

Bozhinovska I.; Lledós A.; Westerhausen M.; Ujaque G.

2nd International Workshop Cutting-Edge Homogenous Catalysis, March 29-31, **2022**, Leipzig, Germany

OC5: Phospholes *via* S-block metal-mediated route: A combined experimental and DFT study

Bozhinovska I.; Lledós A.; Westerhausen M.; Ujaque G.

International School on Innovations in Homogeneous and Supported Homogeneous Catalysis, April 25-28, **2023**, Bucharest, Romania

Posters:

P1: Computational study of Pudovik reaction with s-block metal catalysts

Bozhinovska I.; Lledós A.; Westerhausen M.; Ujaque G.

International Workshop Cutting-Edge Homogenous Catalysis, May 4-6, **2021**, Toulouse, France

P2: S-block metal-mediated hydrophosphination of alkynes: New synthetic routes elucidated with DFT

Bozhinovska I.; Lledós A.; Westerhausen M.; Ujaque G.

2nd International Workshop Cutting-Edge Homogenous Catalysis, March 29-31, **2022**, Leipzig, Germany

P3: Development of s-Block metal-mediated formation of phospholes: A combined experimental and DFT work

Bozhinovska I.; Lledós A.; Westerhausen M.; Ujaque G.

Doctoral Workshop, May 26-27, **2022**, Barcelona, Spain

P4: Phospholes *via* S-block metal-mediated route: A combined experimental and DFT study

Bozhinovska I.; Lledós A.; Westerhausen M.; Ujaque G.

International School on Innovations in Homogeneous and Supported Homogeneous Catalysis, April 25-28, **2023**, Bucharest, Romania

P5: Computational study of alkali metal-catalysed Pudovik reaction

Bozhinovska I.; Lledós A.; Westerhausen M.; Ujaque G.

3rd International Workshop Cutting-Edge Homogenous Catalysis, January 15-17, **2024**, Montpellier, France

Affidavit

I hereby declare in lieu of oath and by my signature that I have written this thesis independently and without outside help. Contents and passages that originate from external sources and have been directly or indirectly adopted have been labelled as such. This thesis has been submitted in both Universities: Universitat Autònoma de Barcelona and Friedrich-Schiller-Universität as a joint thesis under cotutelle (International joint supervision).

Moreover, I declare that I have not used any additional literature other than that listed in the bibliography. This affidavit also extends to the diagrams and the illustrations presented herein.

Irina Bozhinovska